Author:
Paul, Aakash

Title:
Understanding the Effects of Environmental Conditions on the Failure of Bonded Joints

UNDERSTANDING THE EFFECTS OF ENVIRONMENTAL CONDITIONS ON THE FAILURE OF BONDED JOINTS

By

AAKASH PAUL

DEPARTMENT OF AEROSPACE ENGINEERING

UNIVERSITY OF BRISTOL

A dissertation submitted to the University of Bristol in accordance with the requirements of the degree of DOCTOR OF PHILOSOPHY in the Faculty of Engineering.

OCTOBER 2019

Word count: 53,870

ABSTRACT

Composites are widely utilised in aerospace structures, especially for the newer generation designs, due to their advanced properties such as high strength to weight ratios and durability. Understanding the failure of bonded joints with composite adherends is key for designers, particularly within the aerospace industry, for both a safe design and meeting the aircraft regulation standards. This thesis investigates both experimentally and numerically the effects of environmental conditions on the strength of Double Lap Joints (DLJ) with composite adherends, for different geometrical and loading conditions. The environmental conditions tested are at Room Temperature Dry (RTD), Hot Temperature Dry (HTD) and Hot Temperature Wet (HTW). The mechanical properties of both the adhesive and composite are characterised at these environmental conditions. DLJ tests for pristine, impacted and specimens with artificial defects are tested. Analytical models using simple calculations are used to determine the failure modes. Numerical model using Cohesive Zone Models (CZM) are used to predict and further understand the DLJ behaviour through sensitivity analyses.

During the characterisation tests, it is found that Mode I fracture energy increases whereas Mode II decreases with increasing temperature and moisture for both adhesive and composite. A distinct change in failure mechanism is also found with the influence of temperature and moisture. The effects of overlap length, adherend and adhesive thickness on the pristine DLJ strength at different environmental conditions are analysed and discussed. Following the pristine tests, the residual tensile strength after through-thickness impact and the effects of artificial defects (disbond) on the strength of DLJ are also studied. The impact is applied at RTD and followed by tensile tests at different environmental conditions. Disbond cases are represented by inserting an artificial defect in the bondline during the manufacturing process and is followed by tests at different environmental conditions. For all DLJ, increasing temperature and moisture had a significant effect on the strength, failure mechanisms and fracture surface.

ACKNOWLEDGEMENTS

First and foremost, I would like to express my heartfelt gratitude to my supervisors, Prof. Michael Wisnom and Dr. Xiaodong Xu for their immense support and dedication for the duration of my Ph.D., and also during my MEng. From my time as an undergraduate, their vast knowledge on the field, patience, motivation and guidance has been very inspiring and they have been great mentors for me to look up to. I would also like to thank them for giving me the opportunity to attend major conferences and meeting several experts within this field for very interesting discussions.

I am deeply grateful to Mitsubishi Heavy Industries (MHI) for this project as it has been a great opportunity to learn and apply my knowledge. Their guidance and feedback have been invaluable in helping us with this project.

I would also like to thank my colleagues and the technicians, for their guidance and support. Especially Ian Chorley, for helping and advising during the lab sessions and also being very understanding with my deadlines.

Finally, I would like to thank my family and friends for their great support and providing happy distractions during this time. My parents, Paul and Celly, and my sister, Alisha for their constant support, patience and encouragement throughout the Ph.D.

AUTHOR'S DECLARATION

I declare that the work in this dissertation was carried out in accordance with the requirements of the University's Regulations and Code of Practice for Research Degree Programmes and that it has not been submitted for any other academic award. Except where indicated by specific reference in the text, the work is the candidate's own work. Work done in collaboration with, or with the assistance of, others, is indicated as such. Any views expressed in the dissertation are those of the author.

SIGNED: .....Aakash Paul..... DATE: .....07/02/2020.....

LIST OF PUBLICATION AND REPORTS

CONFERENCE PAPERS

- A. Paul, X. Xu, M. R. Wisnom and T. Shimizu, "Residual Tensile Strength of Adhesively Bonded Double Lap Joints after Transverse Impact," in ASC 33rd Annual Technical Conference, 18th US-Japan Conference Materials, Seattle, 2018.

CONFERENCE PRESENTATIONS

- A. Paul, X. Xu, M. R. Wisnom and T. Shimizu, " The Effects of Environmental Conditions on The Strength of Double Lap Joints," in ICCM22, Melbourne, 2019.

REPORTS

- A. Paul, X. Xu, M. R. Wisnom, “Annual Report for Bristol - MHI Adhesively Bonded Structure Project”, issued on 17th March 2017.

- X. Xu, A. Paul, M. R. Wisnom, “Modelling Report for Bristol - MHI Adhesively Bonded Structure Project”, issued on 30th April 2017.

- X. Xu, A. Paul, M. R. Wisnom, “Annual Report for Bristol - MHI Adhesively Bonded Structure Project”, issued on 19th March 2018.

- X. Xu, A. Paul, M. R. Wisnom, “Final Report for Bristol - MHI Adhesively Bonded Structure Project”, issued on 11th March 2019.

TABLE OF CONTENTS

LIST OF TABLES

TABLE **PAGE**

LIST OF FIGURES

FIGURE **PAGE**

NOMENCLATURE

SLJ – Single Lap Joints

DLJ – Double Lap Joints

UD – Unidirectional Stacking Sequence

QI – Quasi-Isotropic Stacking Sequence

$\mathbf{G_c}$ – Total Fracture Energy

$\mathbf{G_{IC}}$ – Mode I Fracture Energy

$\mathbf{G_{IIC}}$ – Mode II Fracture Energy

$\mathbf{S_{33}}$ – Tensile Stress Component in the Through Thickness (Normal) Direction

$\mathbf{S_{13}}$ – Shear Stress Component in the Transverse Direction

$\mathbf{T_g}$ – Glass Transition Temperature

C.V. – Coefficient of Variation

DCB – Double Cantilever Beam

ENF – End Notch Flexure

RTD – Room Temperature Dry

HTD – Hot Temperature Dry

HTW – Hot Temperature Wet

$\mathbf{P_{max}}$ – Maximum Load at Failure

P5% - Load 5% Offset from the Initial Linear Response

NPC – Non Pre Cracked

PC – Pre Cracked

F1 – Fracture Controlled Failure

F2 – Strength Controlled Failure

CZM – Cohesive Zone Model

CHAPTER 1

INTRODUCTION

1.1 Aims and Objectives

The aim of this PhD thesis is to understand the failure of Double Lap Joints (DLJ) with composite adherends at different environmental conditions through both experimental and numerical analysis. To achieve this, the materials used, i.e. the adhesive and composite are characterised to understand how the mechanical properties and failure mode change at different environmental conditions. Following this, the DLJ of different geometries are tested at different environmental conditions to understand the DLJ performance. The effects of impact and artificial defects on the DLJ strength at different environmental conditions are also analysed. Numerical modelling is also conducted to predict the failure and to understand how the material mechanical properties influence the joint strength at different conditions, explaining the different trends observed.

This thesis is a result of the project funded by Mitsubishi Heavy Industries (MHI) with the aim of developing accurate strength prediction models for CFRP bonded joints at different environmental conditions. The project started in November 2016 running until March 2019, when the final report was delivered. Some results were presented at the ASC 2018 and ICCM 2019 conferences, as highlighted in the list of publications section.

1.2 Introduction to Adhesive Bonds

Joining similar or dissimilar materials is an integral part of the design process for an engineer. Conventional methods such as bolted and riveted mechanical joints exist, but adhesive joints are becoming more popular. An adhesive is defined as any substance that is applied on a surface, or on the surface of two separate items to bind them together and resist their separation [1]. It is defined as 'structural' when it has enough strength to transfer or share loads between highly stressed components. In engineering applications, using adhesive bonding techniques offers advantages compared to the traditionally mechanical fastening methods. These advantages are summarised by Adams et al. [2]

- High strength to weight ratio
- Reduced number of production parts leading to a simplified design
- Easier manufacturing of larger bond areas with minimum work force
- Excellent fatigue resistance
- Joining dissimilar materials – allowing for variations in coefficients of thermal expansion
- Excellent electrical and thermal insulation
- Improved aerodynamic smoothness

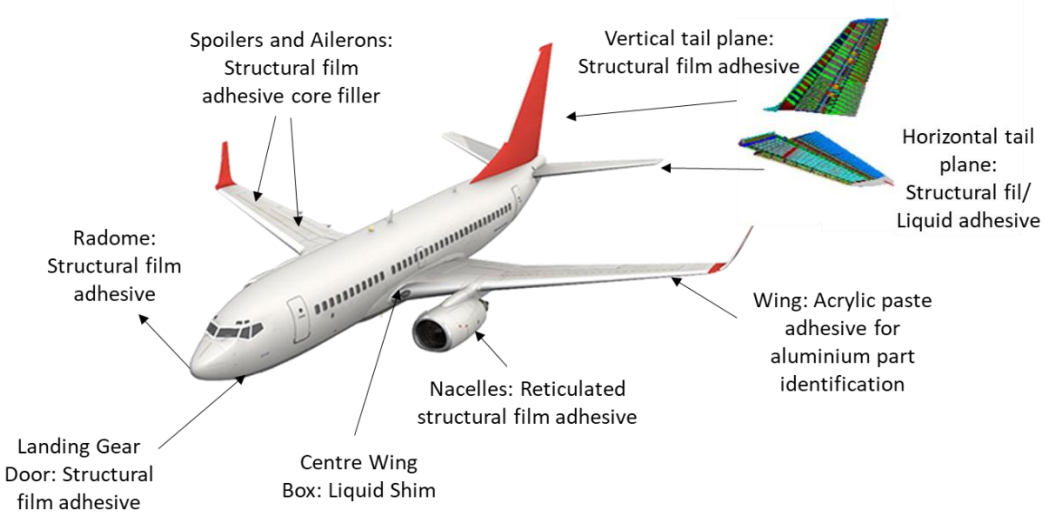

Figure 1.1 – Examples of adhesive bonding application *[3]*

Figure 1.1 shows some typical bonding applications for adhesives. Adhesive bonded structures with composite adherends are also used for civil aircraft manufacturing, particularly for control surfaces and horizontal and vertical tails. The combined advantages of the composite and the adhesive due to their advanced properties is very appealing to designers, especially with the emergence of newer aircraft using more composites. Newer generation aircraft such as the Boeing 787 and Airbus A350 utilise more than 50% of composite in their airframe structure.

Adhesive bonding can also be used in other engineering fields such as wind turbine blades and marine engineering. For wind blades, as the blades are primarily made from composites, the adhesive bonding with the composite structural parts and the different failure modes are of significant interest for designers. With the drive for lighter structures globally, understanding the failure and accurate prediction methods for CFRP bonded joints is of significant interest to engineers for the design of the next generation aircraft.

1.3 Introduction to Stress and Fracture Based Failure Criteria

This section describes the different loading types for a typical bonded joint. It also introduces the different terminologies for stress and fracture based criteria that are used to describe adhesive joint failure.

1.3.1 Different Types of Static In-Plane Loading in Adhesive Joints

The five basic loading cases for a typical adhesive joint are shown in Figure 1.2. The tension case (through-thickness direction) is when the forces are applied perpendicular to the plane of the joint and distributed across the entire bond area and adherends. In practice, a pure axial stress-state is hard to achieve because of peel or cleavage stresses developing from the eccentricity of loading. The stress distribution for the compressive loading application is opposite to the tension case. Shear failure is due to in-plane forces causing the adherend and adhesive to slide past each other. The shear forces are typically distributed along the whole bond-line. Cleavage and peel

forces are loads concentrated at the edges of the joint, pulling the adherends apart and occurs due to concentrated tensile forces acting on the bonded joint. Peel stresses occur for two flexible adherends, whereas cleavage forces occur for an adherend fixed at one end. A typical bonded joint is designed to withstand compressive and shear forces as adhesives are strongest under these conditions. For cases where the stress is distributed along the bond-line, a stress based criterion can be used to predict the failure. For cases where high concentrations of stresses occur, a fracture based criterion may be required.

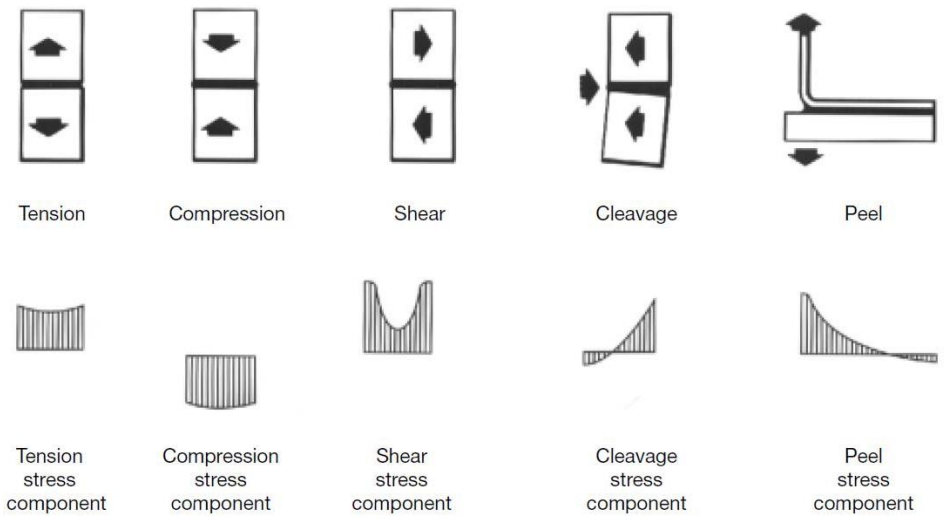

Figure 1.2 - Types of loading for an adhesive joint *[3]*

1.3.2 Adhesive Stress Based Criterion

An introduction into the basic stress based criteria for a lap joint is given in this section. Further information on stress based analytical models is discussed in Section 2.2.1. The simplest stress based analysis for a single lap joint (SLJ) assumes the adhesive to deform in shear and the other stress components in the DLJ do not affect the failure. A constant adhesive shear stress throughout the bondline and the adherend to be rigid are also assumed [2]. The average shear stress in the adhesive layer based on these assumptions can be obtained using Equation 1, where τ is the shear stress, P the applied load and A the bonded area. Although this analysis is limited due to several simplifications [4], it is still used to quote adhesive shear strength in ASTM and ISO standards [5].

$$\tau = \frac{P}{A} \qquad [1]$$

1.3.3 Fracture Based Criterion

This section introduces the concept of fracture mechanics and the terminologies used to define the modes of crack propagation. For some loading cases where stress discontinuities are present, the failure may be driven by fracture propagation. Using a linear elastic approach, the stresses at the vicinity of the crack tip will approach infinity no matter how small the applied load is. Linear Elastic Fracture Mechanics (LEFM) can describe the required loading condition to propagate an existing crack. Once the energy exceeds the critical amount of energy required to propagate a crack, new crack faces are formed. Figure 1.3 summarises the three different modes of fracture.

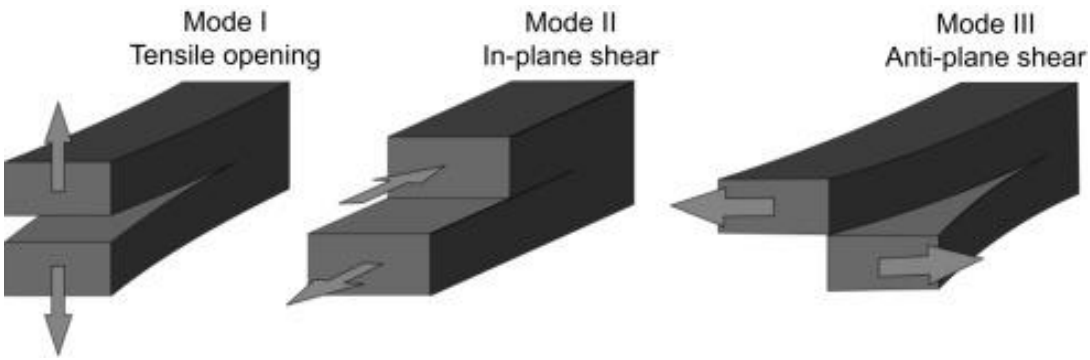

Figure 1.3 - Three modes of fracture *[5]*

As a crack extends, the amount of strain energy release rate must be equal or greater than the critical energy to create new surfaces. The material itself has a critical strain energy release rate (Gc), which is the energy required for the formation of new crack surfaces per unit crack face area, a material constant. The strain energy release rate, G is defined as the energy released per unit crack face area when the crack grows. When G is less than Gc there is no crack growth. When G is equal to Gc, stable crack propagation occurs. When G exceeds Gc, fracture will occur. The relation between G and crack length and the fracture resistance R-curve affect the stability of crack growth([6] [7]).

For certain bonded joint configurations, depending on the material and geometrical properties, the load required for crack propagation can be lower than the load at which

the joint would fail due to the shear stress. For bonded joints with composite adherends with a low fracture toughness, fracture becomes critical, hence the need for fracture based criteria to predict failure.

1.4 Outline of Thesis

The existing literature is analysed extensively in **Chapter 2.** In the experimental literature review section, the typical bonded joint failures are reviewed followed by the effects of adhesive thickness and impact on bonded joints. The modelling section reviews the analytical and numerical methods used for bonded joint prediction. This is followed by reviewing the effects of temperature and moisture on the mechanical properties of adhesives and composites.

Chapter 3 and **Chapter 4** investigate the effects of increasing adhesive thickness on the Mode I and Mode II fracture toughness at different environmental conditions experimentally. The failure mode changes with adhesive thickness, temperature and moisture for both Mode I and Mode II, between a cohesive failure within the adhesive and delamination within the surface 0° ply of the adherend. Why this occurs and the factors influencing it are analysed and discussed in these chapters

Chapter 5 introduces the pristine Double Lap Joints (DLJ) used to test at different environmental conditions. The manufacturing process and the typical specimen configurations used for testing are described. All experimental results looking into the effects of increasing adherend thickness, overlap length and adhesive thickness for the pristine DLJ with increasing temperature and moisture are briefly summarised. Based on the experiments, the different failure modes that are observed are introduced in this Chapter.

Following the experimental summary, analytical and numerical models for the pristine DLJ are introduced in **Chapter 6.** The analytical model is based on the shear strength and fracture energy criteria and is used to understand what controlled the failure for different DLJ cases. The numerical model used for the pristine DLJ failure prediction is introduced, using ABAQUS/Explicit with Cohesive Zone Modelling (CZM).

In the **Chapter 7**, the effects of environmental conditions on the strength of the DLJ with different geometries are discussed. An analytical model is applied to all cases to understand and determine the expected failure mode. Sensitivity analysis is also conducted using the numerical model to understand the critical material parameters

influencing the DLJ strength for different configurations. Based on the failure mode determined analytically, the material properties for the CZM are chosen and correlated to the experimental results.

Following the pristine joints, the residual strength after impact and the effects of artificial defects on the DLJ strength is analysed in **Chapter 8** for different environmental conditions. The effects of the DLJ strength with different impact energies and different disbond locations are analysed and discussed. Numerical simulations are used to understand the DLJ sensitivity to different CZM input material properties based on the characterisation test results.

Chapter 9 reports the conclusions of the thesis followed by possible future work.

CHAPTER 2

LITERATURE REVIEW

2.1 Failure in Adhesive Joints: Experimental

2.1.1 ASTM Standard definition

The different types of failures for adhesive/composite systems and the means of accurately characterising the failure is of interest for a designer. As per the ASTM standard D5573, the failure modes for a SLJ with composite adherends are shown in Figure 2.1. A brief description of each failure mode is given.

- **Adhesive Failure** – Also known as interfacial failure where the failure occurs at the adhesive/adherend interface (i.e. both surfaces visible from failure surface). This typically means the interfacial strength is weaker than the adhesive/adherend strength, for example due to poor surface treatments.
- **Cohesive Failure** – When the failure occurs within the adhesive (i.e. adhesive visible on both failure surfaces). This usually suggests that a good adhesive bond is obtained, and the failure is dominated by the adhesive properties. When this type of failure occurs close to the interface it is called **Thin-layered cohesive failure.**
- **Fibre-Tear Failure –** Failure that occurs within the matrix of the composite adherend, i.e. interlaminar failure within the composite. Hence, fibres are exposed on the failed surfaces. **Light fibre tear failure** is when the failure

occurs at the adherends close to the interface, leaving a thin layer of fibres exposed on the surface.

- **Stock-Break Failure –** The rupture of the composite adherend away from the bond-line.
- **Adhesive to Adhesion Promotor –** Adhesion promotors such as peel-plies are used to ensure high interfacial strength. This type of failure occurs at the adhesion promotor interface and adhesive. When the failure occurs at the promotor and adherend interface this is called **Adhesion promotor to substrate** failure.

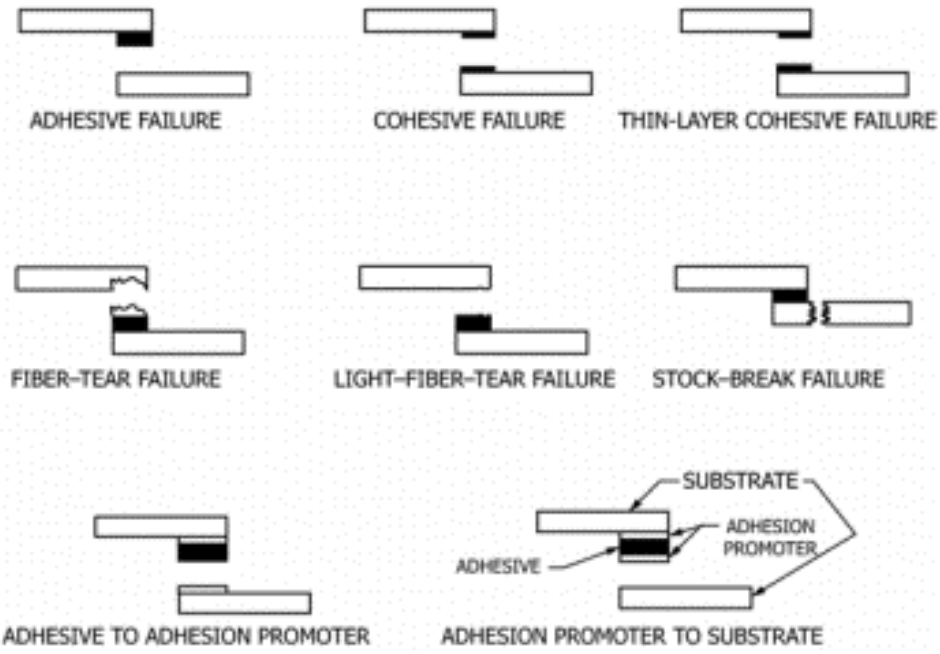

Figure 2.1 - Different failure modes for adhesively bonded joints (from ASTM standard D5573)

2.1.2 Typical Failure in Bonded Joints

The typical bonded joint failures have been studied by several authors and are summarised in this section. The different failure modes reported, effects of increased overlap length and adherend thickness on the joint strength are highlighted in this section.

The effects of different adherends on the failure mechanism for Double Lap Joints (DLJs) was considered in detail by Tsai and Morton [8] for Unidirectional (UD) and Quasi-isotropic (QI) stacking sequences. It was found for UD joints, the strain in the

longitudinal direction, ϵ_x was highest at the leading edge of the joint and almost zero at the trailing edge. The longitudinal forces in the adhesive are transferred to the outer adherend (strap, Figure 2.2) through shear stresses. High shear stresses and strain in the adhesive were found to be present at both ends of the DLJ, but relatively small at the centre of the overlap. The shear deformation was more significant for the QI joint. This was because the +/-45° plies created an in-plane stretching-shear coupling characteristic which resulted in inter-laminar shear stresses near and at the free edges due to the 3D stress state. The ϵ_x at the inner and outer adherends was higher for the QI laminates compared to the UD laminates due to the lower longitudinal stiffness. The authors also found that the adhesive peel stress distribution was not dependent on the material properties of the adherend except for a small region at the leading edge of the joint. The peel stresses were higher for the QI joints compared to the UD joints.

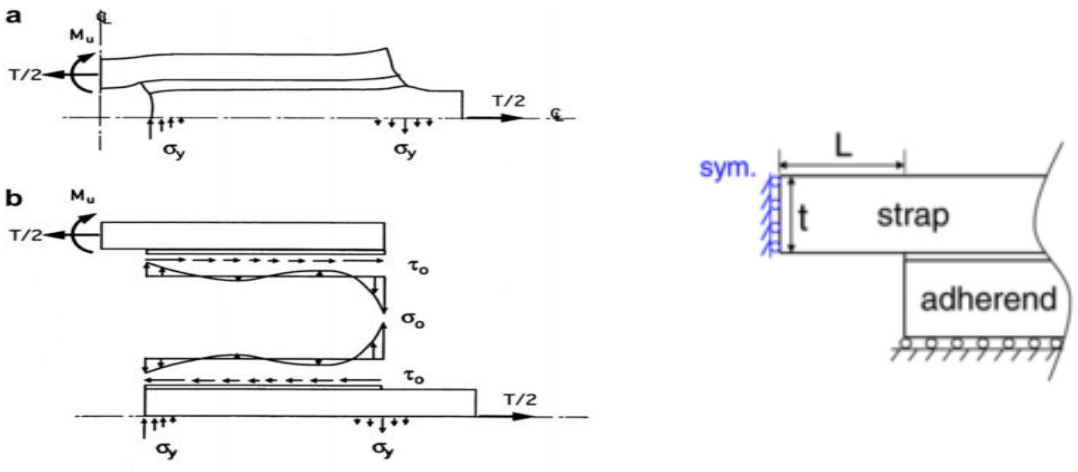

a) Free-body diagram of a quarter symmetry double lap joint

b) Gap schematic for a double lap joint *[8]*

Figure 2.2 - Free-body diagram of a quarter symmetry double lap joint *[8]*

The free-body diagrams of the DLJ are shown in Figure 2.2. When a tensile load is applied, compressive deformation in the transverse direction at the trailing edge of the inner adherend and a through-thickness tensile deformation at the outer adherend were found. The moment acting on the outer adherend, M_u is dependent on the stress in the longitudinal direction and decreases as the length of the outer adherend

increases. Increasing the outer adherend length (i.e. decreasing M_u) decreases the maximum shear stress on the adhesive and increases the maximum compressive peel stresses acting on the trailing edge of the inner adherend. The stresses at the edges of the outer adherend remain unaffected by increasing its length. It was found that if the ratio of L/t (Figure 2.2) was greater than 32, the effects of the moments were not critical, and the adhesive shear and peel stresses converged towards a uniform stress case.

The failure mechanisms observed by Tsai and Morton for the DLJ for UD and quasi-isotropic adherends are shown in Figure 2.3. The authors found that for UD joints, cohesive failure initiated at the leading edge of the joint. A mixed-mode of through-thickness tensile and shear failure at the interface was also observed, but the details of this failure were not explained. Delamination is a critical failure mechanism that occurs in composite materials. This type of failure arises due to the low through thickness strength of composites combined with high interlaminar tension or shear stresses. For the QI joints, delamination of the 0° ply at the surface (first ply) and a mixed-mode through-thickness tensile and shear failure was reported as the observed failure mechanisms.

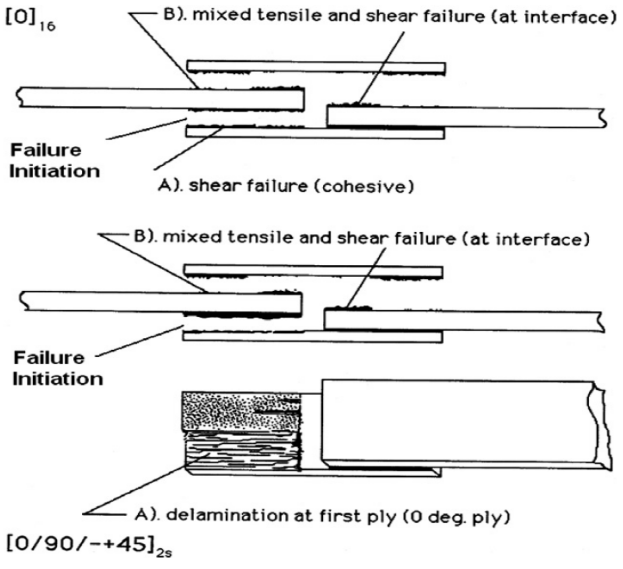

Figure 2.3 - Double lap joint failure mechanism *[8]*

A different failure mode for bonded joints compared to Tsai and Morton was reported by Leone et al. [9]. This was called double delamination, which was observed for some

Mode I and low mode mixity mixed-mode tests for adhesives with composite adherends. This type of failure was associated with a secondary delamination which developed in the composite ply adjacent to the adhesive as shown in Figure 2.4. Once the delamination in the composite was initiated, the propagation was unstable and prevented further damage propagation in the adhesive. The authors reported the crack propagation within the composite caused the bridge to stretch and then break the fibres. However, what controlled this failure was not clear.

Figure 2.4 - Example of double delamination *[9]*

Galliot et. al. [10] conducted in-plane impact testing on adhesively bonded carbon/epoxy laminate SLJs for velocities up to 4 m/s. For all tests, the failure occurred in the adherends and the adhesive layer always remained intact and the crack initiated at the end of the overlap, where the stresses were highest. The authors found that the strength of the bonded joints was dependent on the membrane and bending stiffness of the adherend, hence the effect of varying the stacking sequence was also investigated. QI stacking sequence with different surface plies were tested at high velocities. For all cases, the crack during failure initiated in the first layer of the laminates at the end of the overlap as a result of the tensile, shear and peel stress and then propagated through the adherend until catastrophic failure.

For the 0˚ surface ply case, after the fibres were broken, the crack propagated into the matrix following the fibre direction. The fracture was intra-laminar, and the crack propagated to the ends of the substrate leading the joint to split into two. For a 90˚ ply surface, the crack advanced through the matrix until it reached the next ply. For the 45˚ ply surface, the crack propagated along the fibre direction similarly to the 0˚ ply. Due to the orientation of the 45˚ ply, the crack was driven to the sides of the joint, hence the ply was not completely broken, and crack propagation occurred through the 45˚ surface ply. Figure 2.5 shows the typical failure process for the different surface

ply orientations. The images are taken during the failure process and are at an angle due to the eccentricity of the SLJ while loading.

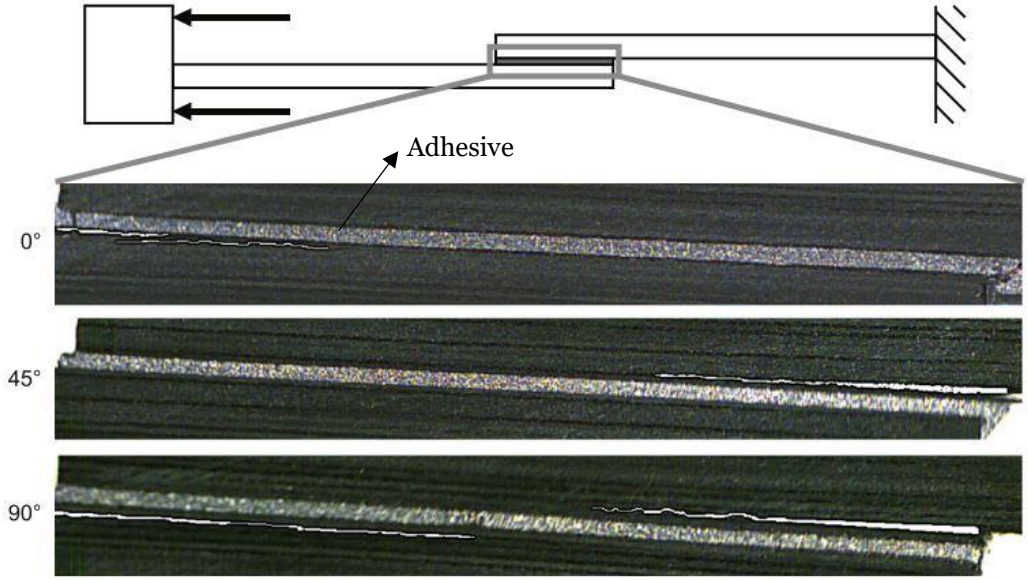

Figure 2.5 - Crack propagation for different surface ply orientations *[10]*

Li et al. [11] investigated the tensile performance for adhesively bonded carbon/fibre SLJ and DLJ to study the effects of lap length, adhesive and adherend thickness. The tests were conducted with a stacking sequence of $[45/0/-45/90]_s$. For SLJs, it was concluded that the ultimate failure load increased with the lap length, for which past 10 mm, the rate of increase decreased. For the shortest overlap length considered, a cohesive failure was reported and increasing the overlap length resulted in delamination from the surface 45° ply becoming the dominant failure mode. The authors suggested this was due to the increased peel stresses at the ends of the adherends with increased lap lengths. For the thickest adherend considered, a non-linear stress-strain response was reported due to the increased bending effect from the eccentric loading for the SLJ. Increasing the adherend thickness increased the ultimate failure load, but not in direct proportion. For DLJ using the same stacking sequence, it was found that both the joint strength and shear strength increased with adherend thickness. The failure mode observed for the DLJ was similar to the SLJ.

2.1.3 Adhesive Thickness Effects

There was been extensive work conducted on the influence of adhesive thickness on the bond-line failure. Peel tests using acrylic polymer adhesive with cellophane adherends were conducted by Gardon [12]. It was found that the peel force was proportional to the fracture energy, increasing with adhesive thickness. Tapered double cantilever beam (TDCB) tests on rubber-modified epoxy resin adhesives were studied by Bascom et al. [13]. They found that the maximum fracture energy was achieved when the bond thickness was similar to the diameter of the plastic zone formed ahead of the crack tip. Also, for TDCBs, as the bond-line thickness increased, the plastic dissipation and the fracture energy increased [14]. Kinloch and Shaw [15] found that the size of the damage zone was a factor in increasing the G_{IC} of adhesive joints. Using an elastic-plastic analysis of the stress field around the crack tip in an epoxy adhesive, Ikeda et al. [16] described the increase in the fracture toughness with adhesive thickness. Around the crack tip for a thinner adhesive layer, higher triaxial stress was found which decreased the fracture energy. Studying the crack tip showed that the rubber particles were almost at a spherical shape around the pre-crack tip, while those near the interface between the adhesive and adherend were ellipsoidal due to the constraint effects of the adherend. The ellipsoidal shape was also attributed to the shear caused by the residual stress from cure. Lee et. al. [17] reported that when the adhesive layer (rubber-modified epoxy) was less than 1.5 mm thick, with a metal adherend, a damage zone was observed near the interface. This zone significantly influenced the fracture toughness of the adhesive joint due to the stress shielding effect. This was when the stress around the pre-crack tip was reduced due to energy dissipation at the interface.

da Silva et. al. [18] investigated the Mode II fracture toughness as a function of the adhesive thickness (epoxy) with steel adherends. They concluded that the fracture toughness in Mode II increased with the adhesive thickness. The thickness influenced the mode II fracture toughness due to the natural failure process zone (FPZ) development as shown in Figure 2.6. The FPZ changed for different adhesive thickness due to the interaction with the adherends. It is known that the constraint of the stress field in the adhesive layer determines the plastic zone and hence affects the bond toughness ([13], [15]). For ductile adhesives, a non-linear plastic deformation was reported.

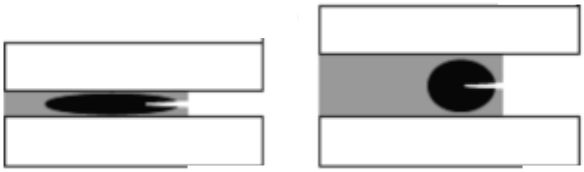

Figure 2.6- Fracture Process Zone for different Adhesive Thickness *[18]*

The fracture toughness of a thicker adhesive was higher than a thin adhesive specimen under pure loading mode, but the difference was less noticeable for mixed-mode loading [19]. The adherend thickness also influenced the fracture toughness of the adhesive where a thinner adherend resulted in a higher fracture toughness. This was due to bending in thin adherends leading to higher shear stresses and larger root rotations at the crack tip, promoting shear yielding, which increased plastic deformation in the adhesive [20].

Belnoue et. al. [21] conducted experiments on adhesively bonded IM7/8552 panels for ductile adhesives with the adhesive thickness varying from 0.25 mm to 1.5 mm (epoxy). Figure 2.7 and Figure 2.8 show the results for Mode I and Mode II with increasing thickness. It was seen that the thinner adhesives were more prone to adhesive failure (grey shading in the figures) whereas for the thicker adhesive, the failure was cohesive. Constraint effects from the adherend were also observed and reported by the authors. As the adhesive thickness is increased, more energy will be dissipated through the plastic straining resulting in an increased toughness. When the adhesive thickness was the same size as the plastic zone in the bulk material, the interaction of the plastic zone with the adhesive thickness was responsible for a slightly thinner but much longer plastic zone in comparison to what it would be in a bulk material, similar to what was observed by Bascom et al. [13]. When the adhesive thickness was increased further, the effects of the bond-line thickness were relaxed and the plastic zone was less constrained. As the adhesive thickness increased, the plastic zone progressively became shorter and deeper and its size started to decrease. For a thick enough adhesive, the plastic zone would develop as in the adhesive bulk material.

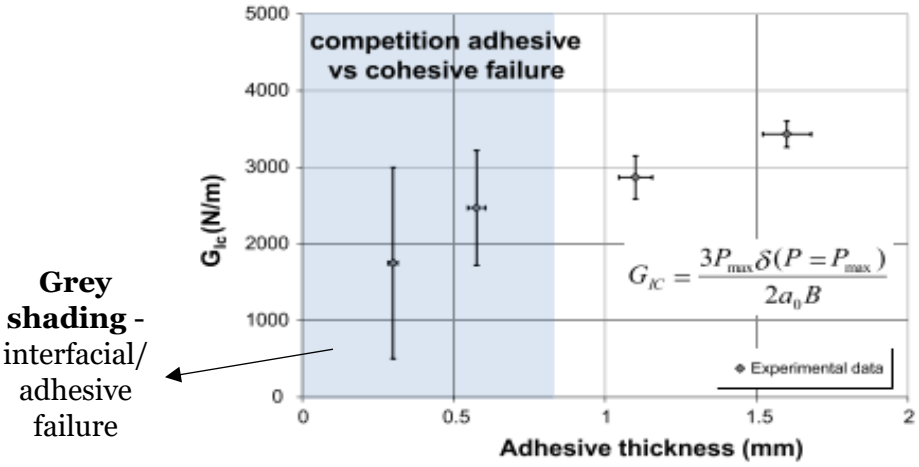

Figure 2.7 - Mode I vs adhesive thickness *[21]*

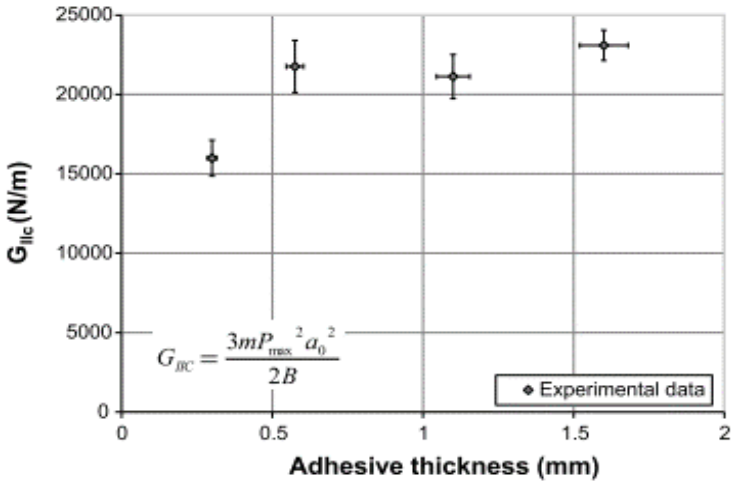

Figure 2.8 - Mode II vs thickness effects *[21]*

Next, the effects of increasing adhesive thickness for SLJ and DLJ were analysed. da Silva et. al. [22] conducted SLJ tests with varying adhesive (epoxy) thickness and properties. The three adhesives used were the EA9361 (very ductile), EA9321 (intermediate) and AV138 (very brittle). The overlap length was fixed at 25 mm, with high-strength steel used as the adherend. The results are shown in Figure 2.9. For the ductile and intermediate adhesives, the strengths decreased with increasing adhesive thickness, whereas for the brittle joint, the strengths were similar for the 0.2 mm and 0.5 mm cases, and then decreased for the 1 mm adhesive thickness. For all cases, the failure was cohesive and occurred close to the interface.

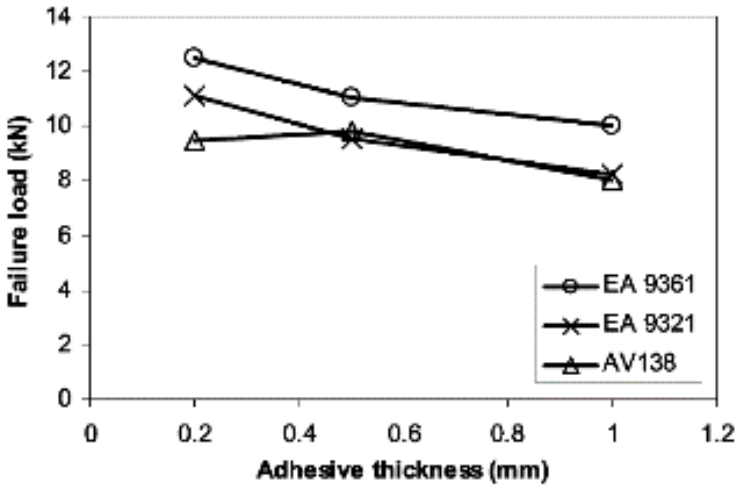

Figure 2.9 - Adhesive thickness vs failure strength for SLJ *[22]*

Davies et. al. [23] conducted a similar study on the adhesive bondline thickness effects on the joint strength using and Arcan fixture. The adhesive used was the Araldite 420 (epoxy) with aluminium 201 grade alloy substrates. For the thicker adhesives, significantly lower yield stress and failure strains were reported. The highest stress concentrations and edge effects were observed during tensile loading, while the lowest was under shear. Increasing the thickness increased the stress concentration, imperfections due to misalignment and the adhesive joint edge effects. It was highlighted that the stress gradients close to the free edges of the adhesive increased significantly with the joint thickness. Although the Arcan test fixture does not correspond directly to a double lap bonded joint case, the importance and implications of edge effects and misalignments are useful to consider.

2.1.4 Adhesive Failure under Impact and Disbond

Literature on the impact performance of adhesive joints with composite adherends has been limited compared to the static loading tests. As most adhesive joints are designed to carry in-plane loads, the failure mechanism that occurs during through-thickness impact applications and how this interacts with the in-plane failure is not well understood. Two types of impact applications were reported in the literature, impact applied in the in-plane and through-thickness directions.

Harris and Adams [24] conducted in-plane impact tests for SLJ with aluminium adherends. The authors explained that during impact loads, the energy absorption

comes from the deformation of the adherend material. Therefore, if the adherend was capable of large-scale plastic deformation, i.e. ductile, the joints can maintain sufficient strength under impact. It was also concluded that the strength of the joint did not vary between quasi-static or dynamic loading for this material configuration tested. Beevers and Ellis [25] found that for adhesives bonded with thin steel adherends, the ultimate strength under impact was higher than under quasi-static loading. This was due to the deformation and strain sensitivity of the steel adherends giving higher yield strengths under impact loading. Kihara et. al. [26] reported that that the fracture subject to in-plane impact was due to tensile stresses for low incident stresses (stress due to impact). For high incident stresses, fracture in the adhesive lap joint was due to the combination of shear and compression stress.

Higuchi et. al. [27] studied the stress wave propagation and stress distribution in adhesive butt joints of T-shaped metallic adherends subject to impact bending moments. The authors concluded that the maximum stress in the T-joint increased with the Young's modulus of the adherends, lap length and adherend thickness. Also, decreasing the adhesive thickness increased the maximum stress. The influence of the superposition length on the through-thickness impact response for single-strap adhesive joints was studied by Reis et. al. [28] These tests were conducted with metal adherends for three gap lengths (L_0) of 0, 10 and 20 mm. The testing configuration shown in Figure 2.10.

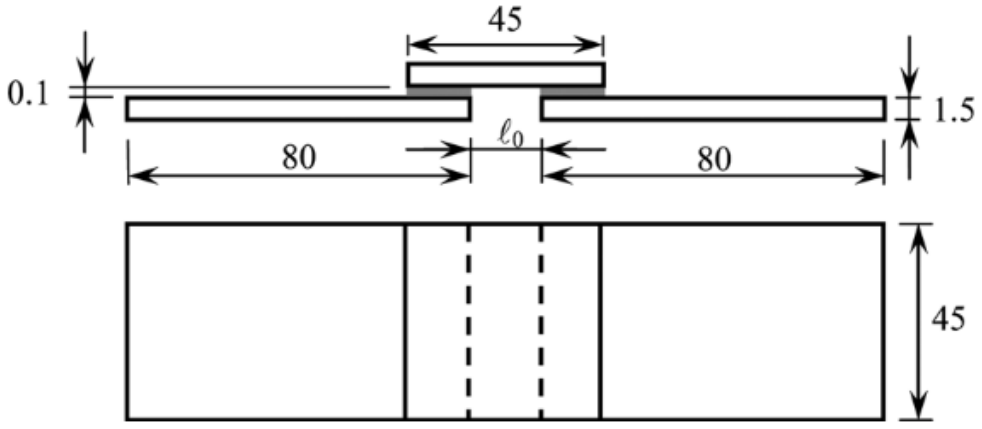

Figure 2.10 - Superposition Length Testing Configuration *[28]*

It was found that the larger L_o was, the higher the impact energies observed. For the larger L_o, the bonding area was lower and lower local deformation occurred. The case of L_o of 0 mm, i.e. zero gap gave the maximum peel stress and stress levels decreased with increasing L_o. The authors state that this was due to increased global stiffness with decreased L_o, lower plastic deformation of the metallic adherend and greater deformation of the adhesive.

Low velocity through thickness impact tests on single lap composite joints and the corresponding residual strength tests were carried out by Farrow et al. [29]. The single lap joint used had a reversed chamfered resin fillet for a 65 mm overlap length with a stacking sequence of $[45/0/0/\text{-}45/0/0/90/0]_s$ (as quoted). The specimen was a plate which was clamped at all edges. A Barely Visible Impact Damage (BVID) state was reported by the authors. No adhesive bond-line failure was reported, and delamination occurred at the 0°/90° and 0°/45° interfaces. From the tensile tests on the impacted specimens a 50% reduction in the static tensile strength was found, with complete delamination within the upper 0° ply closest to the bondline. It also showed the critical case occurred when impact was applied close to the leading edge of the joint. Vaidya et al. [30] provided a good summary for single lap joints under through-thickness impact. They stated that the peel stresses caused by the eccentricity of the loading path caused significant bending in the adherends, which was more critical to the joint performance than the shear stresses. The authors stated that the peel stresses arising from impact are more critical to failure due to the low through-thickness properties of the composite. The failure initiated under mixed-mode conditions compared to the in-plane test case where it was more shear dominated. This was also found from the numerical 2D FE analysis where the peak peel and shear stresses were found at the adhesive/adherend interfaces for SLJs [31]. Low velocity through-thickness impact tests were conducted by Kim et al. [32] on woven glass-epoxy SLJs bonded with adhesives. The authors stated that high shear stresses developed under the impact point forming localised debonding and interlaminar damage in the adherends. Debonding was also reported on the opposite side of the plate from the impact application due to high peel stresses. These failures were very difficult to detect visually, and a threshold impact energy was reported by the authors. Park et al. [33] analysed the effects of through-thickness high velocity impact tests on adhesively bonded composite SLJs using hailstones. The authors reported a threshold energy at which failure initiated for the composite joints. Past the threshold energy, the failure was catastrophic and delamination in the plies adjacent to the adhesive layer was the

dominant failure mode. Quasi-static 3-point tests were conducted on SLJs by Wu et al. [34] for which the load was applied across the width of the specimen. Initially, the load increased linearly with deflection. Due to the high peel stresses induced on the SLJ with the indentation force, cracks initiated at the edge of the SLJ which resulted in a load drop. The crack then propagated towards the ends of the joint until it failed completely. Nie et al. [35] also conducted low velocity impact on scarf joints. Matrix cracking, delamination and fibre breakage were the typical failure mechanisms that were observed. From the following tensile tests on the impacted scarf joints, peeling from the scarf tips was observed due to the effects of the bending stress under impact.

The influence of defect area within the adhesive on SLJ strengths were studied by Ribeiro et al [36]. The adhesive type had a significant influence on the SLJ strength, for which the brittle adhesive failed at the limiting stress due to the inability to undergo plastic deformation. The more flexible adhesive failed at stresses close to global yielding. Fatigue tests on SLJ with defects present at the adhesive/composite interface was investigated by Liu et al [37]. Using a peel ply surface treatment and surface 0° surface ply (QI), the initial crack propagated along the adhesive/composite interface followed by secondary cracks initiating and propagating at the opposite end. The fatigue disbond cases were subject to mixed-mode loading conditions.

2.2 Failure in Adhesive Joints: Modelling

2.2.1 Analytical Models

Having accurate failure prediction tools for adhesively bonded joint failure is critical for a safe design. Volkersen [38] proposed a simple shear lag model, being the first to develop an analytical solution for adhesively bonded joints. This was based on 1-D adherends and assumed shear deformation in the adhesive layer in the longitudinal direction and uniform stress through the thickness of the adhesive layer. It was essentially a shear spring that only transfers the longitudinal forces from the inner adherend to the outer adherend by shear. Then Goland and Reissner [39] considered both shear and transverse normal deformation in the adhesive layer for a joint consisting of two beams, predicting the shear stress distribution accurately. Figure 2.11a gives a typical adhesive shear stress distribution using the Volkersen and Goland & Reissner methods. Although these analyses provided advances in the stress analysis

for adhesive joints, there were limitations [40], such as not accounting for the variation of through thickness stresses in the adhesive.

Hart-Smith [41] considered the adhesive plasticity, giving analytical stress solutions for both linear elastic and elastic plastic adhesives. A typical stress distribution using Hart-Smith's analytical method is given in Figure 2.11b. To study the effects of adherend deflection on the adhesive shear stress distribution, Oplinger [42] developed a layered beam theory. Tsai [43] modified the analytical model for adherends with low transverse shear modulus such as composites, due to the large shear stresses present on the adherend surfaces.

Most theories are based on only strength dominated failure criteria. For predictions of more complex cases such as configurations with artificial defects, presence of adhesive fillets or when significant non-linearity is present for the adhesive, a more robust numerical prediction tool is required.

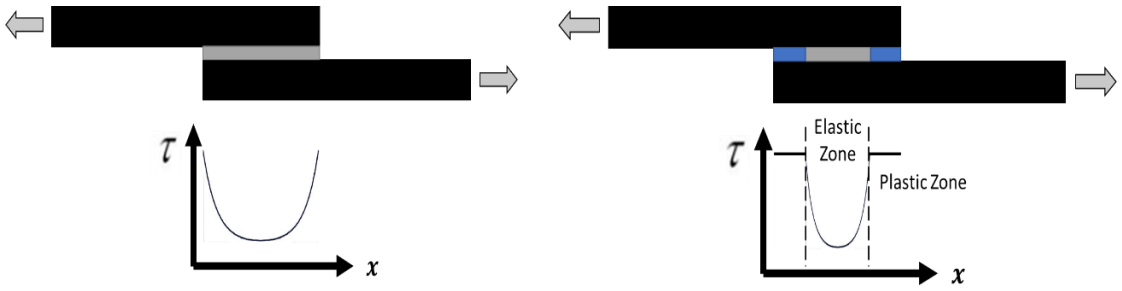

a) Volkerson b) Hart-Smith

Figure 2.11 – Simplified stress-strain distributions for adhesive joints

2.2.2 Numerical Models

For prediction of more complex bonded joint geometries and configurations, numerical methods using Finite Element (FE) models are popular. The classical approach using the continuum mechanics approach is comparing the material allowable values to the stresses and strain predicted using the FE models [2]. For brittle adhesives, Adams et al. [2] used the maximum principal stress criterion to predict the failure mode, which occurred at right angles to the direction of the maximum principal stress. For ductile adhesives, due to adhesive yielding and non-linearity, instead of a stress based criterion, a maximum principal strain based criterion was used to predict the joint strength [44]. These criteria are however

sensitive to the mesh size and how close to the singular point i.e. point of discontinuity/defect, accurate stress readings can be taken. A numerical failure criterion using the maximum shear stress against the bulk adhesive shear strength was also used extensively to predict joint strength ([45], [46]). However, this analysis works best for short and brittle adhesives and ignores the normal stresses acting on the joint.

Cracks are the most common defect that can arise in structures. Stress singularities are also present due to discontinuities within a structure. Hence, for certain bonded joint configurations, a failure criterion based on fracture mechanics is needed. As described in Section 1.3.3, LEFM can describe the required loading conditions to propagate an existing crack. For a more ductile material however, the non-linear zone ahead of the crack tip can become large compared to the crack length and an LEFM model cannot work effectively. LEFM also requires an initial crack to be present. The most common approach used in the literature for the prediction of bonded joint failure is the Cohesive Zone Model (CZM), overcoming the difficulties with LEFM. CZM assumes separation of the surfaces of the crack takes place resisted by cohesive traction [47]. CZM methods are used numerically to simulate interfacial fracture problems of adhesive joints. The CZM can be implemented on one or multiple interfaces in the bonded joint and can take mixed-mode loading ([48] [49]), rate dependent effects [50] and fatigue loading into account [51].

The simplest pure-mode traction-separation is the bi-linear softening law (Figure 2.12), which is defined by the strength, fracture toughness and the penalty stiffness. The bi-linear law is commonly used in adhesive joints. The interface strength sets the stress level at which the cohesive element will begin to soften, and the fracture toughness is the energy dissipated during the fracture process. The penalty stiffness term is set for the undamaged elements stiffness and must be defined to implement the cohesive law in a finite element framework. For zero thickness cohesive elements, this term is set to a high value to rigidly tie together the nodes across an undamaged interface and to prevent interpenetration [52]. For thicker cohesive elements, which can be used to represent a whole adhesive bondline, this term is also used to represent the adhesive compliance.

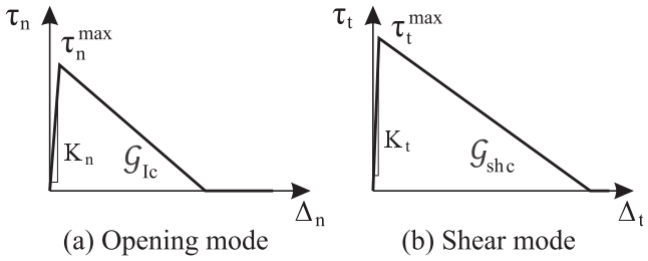

Figure 2.12 - Linear softening cohesive laws *[52]*

For thin adhesive layers, the typical approach is to represent the mechanical response of the adhesive fully using a traction separation law ([53] [54]). For thicker adhesives typically, the adhesive is modelled using elastoplastic solid elements and the CZM elements are placed adjacent to these elements ([20] [55]). Recently however, Sarrado et. al. [52] used CZM to represent a thick adhesive layer, modelling the initial elastic response, softening and failure successfully. For thicker adhesive modelling using the elastoplastic solids and CZM, Madhusudhana et al. [56] observed that the position of the crack and the thickness of the adhesive layer affect the plastic strain distribution due to the plastic yielding in the adhesive which could affect the traction-separation response.

Analysis of the traction-separation behaviour for Mode I and Mode II cohesive laws and fracture toughness was conducted by Sarrado et al. [57] for different adhesive and adherend thicknesses. The cohesive laws were characterised using experimental results. For Mode I, the cohesive law showed a steep profile both prior to and after damage initiation and this behaviour falls within the LEFM assumptions, meaning a relatively small FPZ in the DCB test ([58] [59]). For Mode II, a plateau was seen at the maximum traction values for the cohesive law. This indicated that the interface had undergone significant plastic deformation prior to damage propagation. This was in agreement with the larger plastic deformations under shear loads that adhesives have shown to exhibit [60]. The extent of plastic deformation was greater for the thick adhesive and thin adherend specimens [60]. Under mixed-mode loading, the effects of the adherends and adhesive thickness on the cohesive law was less pronounced. The fracture was Mode II dominant during the first stages of the crack growth and progressively changed to Mode I as the crack grew. For low load mixtures, the inter-laminar strength decreased rapidly whereas the fracture toughness increased together

with the plastic deformation before damage. The remaining interface traction increased with mode mixity.

2.3 Temperature and Moisture Effects

2.3.1 Effects of Moisture Absorption on Adhesives

Severe environmental conditions such as elevated temperature or humidity levels during the lifetime of an adhesively bonded joint can have a significant influence on the joint strength and properties. Several researchers have studied the effects of humidity on adhesively bonded metallic joints and concluded that exposure to high humidity for long periods of time can decrease the strength and fatigue performance [61]. High humidity leads to moisture uptake in the specimens.

Diffusion is defined as when matter is transported from one system to another through random molecular motions. The simplest diffusion model is Fick's Law [62]. Fick's first law states that the flux in the x-direction is proportional to the gradient concentration. For adhesives, two types of Fickian behaviours are possible. The first behaviour, Fickian sorption, Case I, is when the diffusion is much slower than the relaxation and the most common type of behaviour for adhesives [63]. The water uptake is directly proportional to the square root of the exposure time. The dual Fickian behaviour, Case II is when for a fully saturated and swollen component, the water uptake advances against the unpenetrated polymer. For this case the water uptake is proportional to the exposure time. Thinner adhesives are more susceptible to the dual Fickian behaviour. The first stage of absorption for the thinner adhesives occurs when the water occupies the free spaces in the adhesive. After this, only bound water is absorbed at a much slower rate in comparison to the first stage. Adhesives that do not follow the Fickian behaviour and are called non-Fickian.

The effects of moisture absorption included plasticisation, which occurs from the water occupying the free spaces in the adhesive. Moisture also affects the specimens through the water absorbed as bound water which forms hydrogen bonds within the adhesive polymer chain which lead to swelling and decrease in the joint strength and the glass transition temperature (Tg) [64]. Swelling causes the adhesive to be denser as the water is absorbed. This results in residual stresses in the adhesive layer, and enhances

the moisture diffusion in the joint([65] [63] [66]). Liljedahl et al. [67] stated that the strains induced by the swelling are larger than the strains induced due to thermal expansion mismatch. However, the absorbed water enhanced the creep behaviour of the adhesive, reducing the residual stresses.

Moisture absorption at high temperatures, approaching the adhesive Tg can lead to mass loss due to physical damage or chemical modification of the adhesive [68]. Liljedahl et al. [67] found that for a stressed bulk adhesive, the moisture diffusion and water absorption were significantly different to a free bulk adhesive sample which impacted the mechanical properties of the adhesive. If a saturated adhesive is exposed to dry environments, it can lose all the moisture absorbed. The cracks and crazes due to the aging process on the adhesive could however increase the speed of diffusion [69]. For metal adherends the adsorption (water molecules collected at the adherend surface but do not enter the solid interior) at the adhesive-adherend interface resulted in an interfacial failure. The moisture absorption at the interface was much faster than for a bulk adhesive [70]. The use of a low viscosity primer on a chemically treated adherend surface improved the joint strength, as the primer fills the gaps which would have been filled by moisture, causing hydration of the upper layers of the oxide [71].

2.3.2 Effects of Temperature and Moisture on the Mechanical Properties of Adhesives

Prolonged exposure to high temperatures also affects the adhesive strength and fracture properties. The yield strength and Young's modulus decrease with increasing temperature, however the ductility of the adhesive increase with temperature. Viscoelasticity and creep effects are also more significant due to the increased mobility of the adhesive polymer chains at high temperatures [64].

Hot temperature dry tests on modified epoxy adhesives were conducted by da Silva and Adams [72]. A decrease in both tensile and shear modulus and strength was reported with increased temperature. The adhesive becomes more ductile with increased temperatures, with higher strain to failure observed. A sharp fall in strength was also reported once the test temperature exceeded the Tg (155°C). Banea et al. ([73] [74]) conducted both G_{IC} and G_{IIC} characterisation tests for epoxy adhesives with metallic adherends at different temperatures. The G_{IC} increased slightly with temperature for the adhesive due to the increased ductility enhancing the plastic

deformation at the crack tip as shown in Figure 2.13a. However, once the Tg of the adhesive was approached a drop in G_{IC} was reported. For Mode II, a similar conclusion was found in that the G_{IIC} increased initially with increasing temperature due to the increased ductility of the adhesive and then decreased as the testing temperature approaches the Tg of the adhesive (Figure 2.13b). Chai et al [14] also backed this up, reporting that G_{IIC} decreased between $0.7 < T/Tg < 1$.

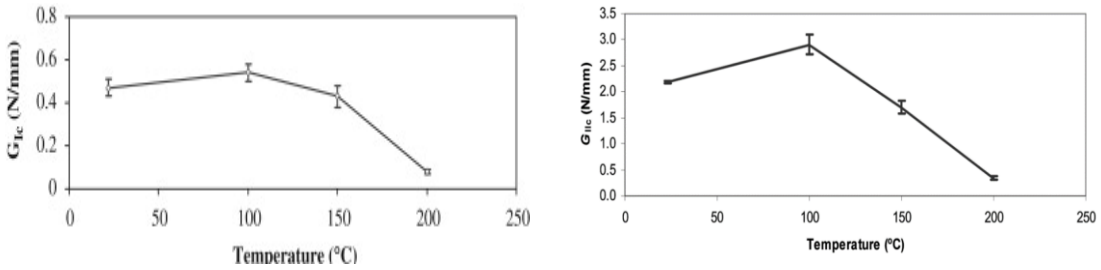

a) G_{IC} b) G_{IIC}

Figure 2.13 - Variation in G_C with increasing temperatures *[73] [74]*

The moisture content affects the mechanical properties of the adhesive, as has been reported by several authors. The tensile modulus and strength decrease linearly as a function of the moisture absorbed ([67] [75] [76]). The effects of humidity on adhesively bonded aluminium joints were studied by Costa et al. [77]. They found that a brittle adhesive absorbed more water compared to a ductile adhesive. Hence, during the mechanical testing for conditioned samples, a greater decrease in strength and stiffness was reported for the brittle adhesive. A greater decrease in Tg was also reported for the brittle adhesive compared to the ductile adhesive. The Tg was also affected by humidity as the mobility of the polymer chains within the adhesive was affected by the moisture absorbed [64]. Adhesives are typically designed to work below the Tg, where the adhesive tends to be stiff and strong. Above the Tg the adhesive is weak and flexible resulting in a loss of the joint strength.

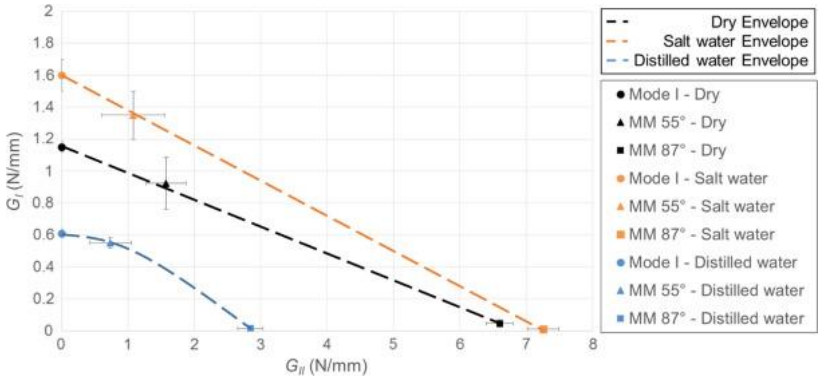

Figure 2.14 - Fracture envelope for different conditioning methods for adhesives *[78]*

Viana et al [79] conducted dog-bone tests on adhesives for samples conditioned for different time periods and at different temperatures. A significant decrease in strength was found as the moisture absorption caused plasticisation and increased ductility. For conditioned samples tested at a high temperature, a further decrease in strength was observed as the test temperature approached the Tg of the material. The authors also concluded that the tensile properties were not dependent on the aging time. The effects of moisture conditioning on the fracture toughness of adhesive with steel adherends was studied by Fernandes et al [78]. Considering two conditioning processes, the fracture toughness decreased for the distilled water conditioned samples and increased for the salt water environment as shown in Figure 2.14. This was attributed to the increased moisture absorption for the distilled water conditioning method compared to the saltwater method, which significantly decreases the Tg of the material to below the room temperature. As the saltwater specimens were tested above the Tg, the increase in toughness was due to plasticisation of the adhesive. The polymeric molecules in the adhesive rearranged themselves more easily, reducing its rigidity and, as a result, increasing its ductility.

Hot temperature dry and wet tests were conducted by Vaezie et al [80] with titanium adherends and polyimide adhesives. It was found that the G_{IC} increased with higher temperatures, up to 177°C when compared to the room temperature conditions. For the conditioned samples tested at high temperatures (hot temperature wet), the G_{IC} slightly decreased, but was within the scatter when compared to the room temperature dry case. A cohesive failure was reported for the Mode I tested samples. For the G_{IIC} cases however, an interfacial failure was obtained, with the G_{IIC} decreasing at high temperatures compared to room temperature. The G_{IIC} value further decreased with

adhesive specimens conditioned and tested at a high temperature. As interfacial failure occurred, the measured G_{IIC} was the interfacial toughness of the adherend/adhesive system.

2.3.3 Temperature and Moisture Effects on Composites

For adhesively bonded composite adherends, moisture degradation can be even more of an issue. The mechanical properties of the composites degrade with the moisture absorbed due to the plasticisation of the epoxy matrix or degradation of the fibre/matrix interface ([81], [82]). Carbon fibres do not absorb significant moisture, and the properties of the epoxy matrix are affected. Some fibres system such as Kevlar can absorb significant moisture [83].

The degradation of graphite/epoxy composites due to sea water immersion was studied by Grant and Bradley [84]. The transverse tensile strength decreased by 17%, and there was a change in failure mode from matrix cracking to interfacial failure. The change to interfacial failure was due to the reduction in radial residual compressive strength [85]. After curing the composite, compressive residual stresses form across the interface due to the cool down from high temperatures, providing mechanical friction. However, for a saturated specimen at higher temperatures, the effects of temperature and swelling in the matrix reduced the compressive residual stress, in turn reducing the effective interfacial strength. Above the Tg, the mechanical and physical properties of the composite were degraded considerably. The change of the epoxy Tg with moisture is therefore important to consider. [86].

High temperature tests on glass fibre composite systems were conducted by Li [87]. The longitudinal tensile modulus was relatively unaffected by the increase in temperature, while there was a decrease in the longitudinal tensile strength for a temperature range between room temperature and 70°C. A greater decrease compared to the longitudinal tensile tests was found in the longitudinal compressive strength. This was attributed to the degraded matrix properties affecting the fibre micro-buckling failure process. For tests in which the matrix dominated properties were significant, such as the shear and transverse tension, the modulus and strength decreased with increasing temperature. A further reduction in strength and modulus was found for hot temperature wet tests.

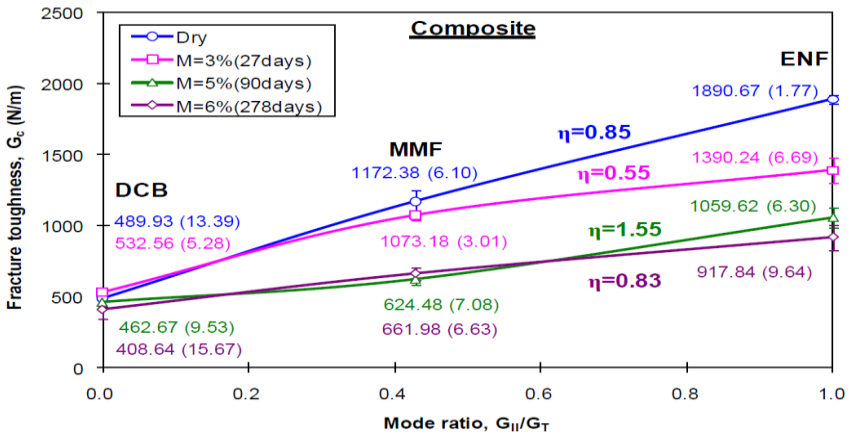

Figure 2.15 - Fracture envelope for different conditioning methods for composites *[88]*

Wong [88] conducted mechanical tests for composites at different absorbed moisture contents. The author concluded that the transverse strength properties for the composites degraded while in the longitudinal direction only a small decrease in strength was observed. For G_{IC}, no significant difference was reported with increasing moisture content, while G_{IIC} decreased as shown in Figure 2.15. Coronando et al. [89] concluded that for a carbon/epoxy system, increasing the testing temperature, to up 90°C increased the ductility of the composite. The increase in the G_{IC} was more noticeable for the fatigue test than the static test at higher temperatures.

2.4 Summary

Extensive work has been conducted on adhesive joints at RTD conditions, particularly for in-plane static loading. For SLJs bonded with composite adherends, the failure load increased and a change in failure mode was observed with increasing overlap length. Different failure modes were observed for adhesively bonded composite joints for different configurations, where for some cases the failure occurred within the surface composite ply. No conclusive explanation was given in the literature; hence the failure process and mechanisms are not well understood. The adhesive thickness effects on the fracture toughness were reported by several authors for metallic and composite adherends at RTD conditions. The general trend shows that fracture toughness increased with adhesive thickness under Mode I loading, whereas for Mode II a peak toughness value occurred at an intermediate thickness due to the interaction of the adhesive process zone with the adherends. For SLJs with metallic adherends the joint strength decreased with increasing adhesive thickness.

Literature for the impact performance of bonded joints was also analysed. Composite joints were found to be weaker under through-thickness impact loading compared to metallic joints due to the lower through-thickness properties of the composite. For most cases, the composite bonded joint had a threshold energy at which failure was initiated. The failure was also not visually observable. The effects of moisture and temperature on the mechanical properties of both adhesive and composites were also investigated from the literature review. It was found that different conditioning methods had different effects on the moisture absorbed by the adhesive. The presence of moisture decreased the Tg of the material for all types of conditioning process. The strength properties decreased, whereas the strain increased with increasing temperature and moisture content. The fracture toughness tests reported for the adhesives were conducted using metallic adherends and Gc was found to increase with temperature then decrease when the temperature approached the Tg of the material. With the presence of moisture, the failure was also reported to be more prone to interfacial failures for metallic adherends.

The literature review highlights the effects of the adhesive and composite at elevated temperatures and moisture conditions individually. This thesis aims to bridge the gap by analysing the effects of elevated temperature and moisture on bonded joints with composite adherends. Tests at RTD, HTD and HTW were conducted for DLJ without damage, impact damage and with artificial defects. The existing literature focuses mainly at RTD conditions for DLJ with and without damage, and this research expands this study at different environmental conditions. The literature also identified different failure modes for joints with composite adherends that were not well understood. This thesis explores the failure mechanisms with an aim to identify what controls the failure for different DLJ cases. The effects of adhesive thickness, interaction of the adhesive with composite adherends and changing failure modes for adhesive characterisation tests were also analysed at different environmental conditions. After the completion of the experimental results, a numerical failure prediction tool was created using existing CZM techniques. This tool was used to describe and understand the DLJ performance at the different conditions tested.

CHAPTER 3

CHARACTERISATION OF MODE I FRACTURE TOUGHNESS AND TENSILE STRENGTH

3.1 Introduction

Three different nominal adhesive thicknesses of 0.2mm. 0.4mm and 0.8mm were tested at Room Temperature Dry (RTD), Hot Temperature Dry (HTD) and Hot Temperature Wet (HTW) conditions to determine the Mode I (G_{IC}) fracture toughness value. For the 0.2mm nominal adhesive thickness case the insert, was placed in between the adhesive and adherend interface. For the 0.4mm and 0.8mm cases the insert was placed in between the adhesive layers. G_{IC} tests were according to the ASTM standard (ASTM D5528) for Mode I interlaminar fracture toughness of unidirectional fibre-reinforced polymer matrix composites using Double Cantilevered Beam (DCB) tests. The G_{IC} values were calculated using the Modified Beam Theory (MBT) using Equation 3.1.

$$G_I = \frac{3P\delta}{2b(a + |\Delta|)} \tag{3.1}$$

Where P, δ, b, a and Δ represent the load, displacement, specimen width, crack length and the correction factor. For tests where stable crack propagation was observed, Δ

was calculated using the least square plot of the cube of root of compliance, $C^{1/3}$ as a function of the delamination length. A typical example of the compliance graph and correction factor calculations is shown in Appendix A. The loading rate during the DCB testing was 2mm/min. Figure 3.1 shows the schematic for the DCB specimen according to the ASTM D5528 standard, where b is the specimen width, L the specimen thickness, h_f the specimen thickness and a_0 the delamination length. The DCB specimen edges were sprayed by white paint to help visually observe the crack propagation during loading. A ruler was also attached to measure the crack propagation. The typical DCB setup is shown in Figure 3.2.

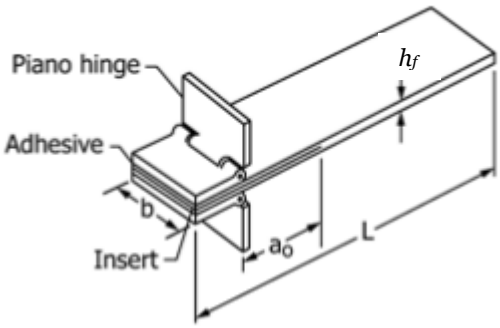

Figure 3.1 - Schematic of DCB according to ASTM D5528

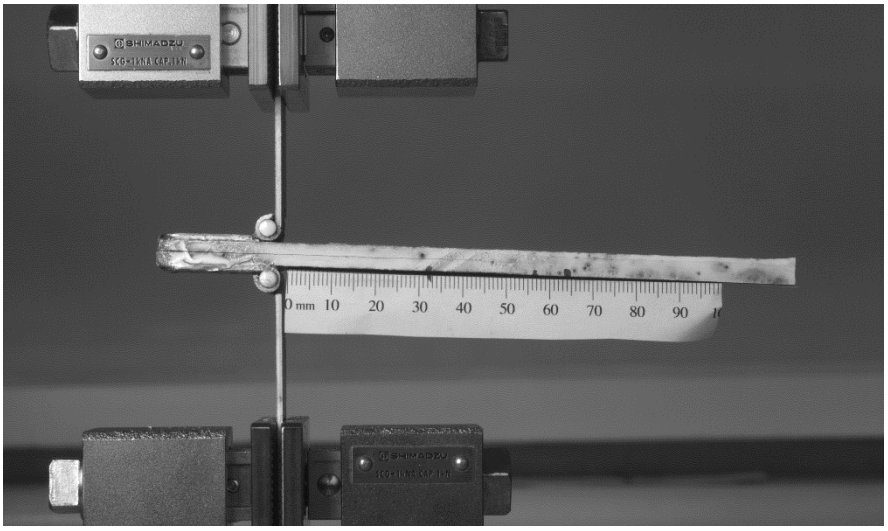

Figure 3.2 - DCB Test Setup

Piano hinges were bonded on either side of the specimen, such that the loading line of the DCB specimen was 25mm from the front edge of the specimen. A Shimadzu

universal machine was used to conduct the DCB test. The standard suggested that if the response was nonlinear, the G_{IC} can be calculated from the load 5% offset from the initial linear response (P5%). This P5% value should represent the lower bound value for the G_{IC} for cases where significant non-linearity is present. The G_{IC} based on P5% was reported for cases where non-linearity was present. For cases where the load does not deviate by 5% from the initial region before the load drop, G_{IC} based on P_{max} was reported. The actual adhesive thickness was based on the average value from the measurements of the adhesive thickness at three different locations.

The material for the composite adherends used was the IM7/8552 carbon/epoxy prepreg with a nominal thickness of 0.125mm and stacking sequence of $[0]_{20}$. The adhesive used was the Hexcel Redux 319 film adhesive with a nominal thickness of 0.2mm and no carrier. Using the same material configuration as the DCB tests under RTD, the HTD performance of the adhesive was tested to characterise the G_{IC}. For the HTD tests, the specimens were tested at 80°C using a thermal chamber. A thermocouple was attached to the specimens to ensure the specimen temperature was consistent with the nominal thermal chamber temperature. The HTW specimens were conditioned at 80°C at 85% Relative Humidity (RH) for 4 months. The specimens were weighed and reported before and after conditioning to understand the percentage weight increase (%wt) due to moisture absorption. At least 3 specimens for each configuration were tested for all DCB configurations. To determine the degree of variation in the experimental results, the Coefficient of Variation (CV) which is defined as the standard deviation divided by the mean was used and was given a percentage value. All tests were conducted using a screw-driven test machine in a universal thermal chamber.

The moisture conditioning process for both the adhesive and composite used for the Hot Temperature Wet (HTW) tests is also explained in detail in this chapter. The rate of moisture absorption and the standard used to characterise the process is discussed.

3.2 Characterisation Test Specimen Manufacturing

The manufacturing for the characterisation test specimens (G_{IC} and G_{IIC}) is explained in this section. A secondary bonding process was used. The layup of the IM7/8552 laminates was done first. The curing cycle for the laminates was in two stages. The autoclave was heated up to 125˚C at a ramp-up rate of 2˚C/min and held at this

temperature for 100 minutes, followed by a ramp to 185˚C at 2˚C/min and held for 165 minutes. The pressure was increased at 69kPa per minute to 690kPa, which was kept throughout the cycle. The adhesive was bonded using a secondary bonding technique. To achieve optimal bonding properties, surface treatment methods were used. A macroscopically rough surface was obtained by grit blasting, until the fibres were visible. The size of the grit used was 1.8 μm. Care was taken to ensure no debris were left after grit blasting by concentrated high pressure air and cleaning with a micro-fibre towel, as it can have a critical effect on the bond strength. Liquid degreasing with acetone was subsequently used to remove oils and other potential organic contaminants from the surfaces immediately prior to bonding. Following the surface preparation, the film adhesive was bonded on to the composite. The adhesive was cured at 175˚C for 1 hour at 690kPa. The ramp-up rate specified in the data sheet was 5˚C/min.

3.3 Moisture Conditioning

3.3.1 Introduction

The moisture uptake was recorded at 80°C at 85% relative humidity (RH) for the composite and adhesive according to the ASTM D5229 standard. The environmental chambers used were the Vötsch VC 7034 and the CM Envirosystems chambers. The samples were weighed using a universal weighing scale with a precision of 0.0001g. Before the initial reading the samples were dried at 105° C for 1 hour to ensure there was no significant moisture present in the samples. The moisture uptake readings were taken every week for the first 5 weeks, and then taken every fortnight for 4 months.

Equation 3.2 was used to measure the average moisture content, M. This is essentially the ratio of the current sample to the oven-dry material expressed as a percentage. W_i represents the current specimen mass and W_o represents the oven-dry specimen mass.

$$M\% = \frac{W_i - W_o}{W_o} * 100 \tag{3.2}$$

The average moisture content was measured and plotted against the square root of hours. According to the ASTM D5229 Standard, Equation 3.3 gives the diffusivity (D_Z) of a material, assuming moisture equilibrium, i.e. saturation has occurred.

There are two ways of defining the moisture equilibrium, absolute or effective. For absolute moisture equilibrium, there must be no changes in moisture content measured between two time periods. The effective moisture equilibrium allows a small specified change in the average moisture content in the material. The effective moisture equilibrium is a satisfactory definition for most engineering applications [ASTM D5229] and used for this research. It was defined as when the average moisture content does not change by 0.020% over two consecutive reference time period spans.

$$D_Z = \pi \left(\frac{h}{4M_m}\right)^2 \left(\frac{M_2 - M_1}{\sqrt{t_2} - \sqrt{t_1}}\right)^2 \tag{3.3}$$

h = average specimen thickness, mm

M_m = effective moisture equilibrium, %

$(M_2 - M_1)/(\sqrt{t_2} - \sqrt{t_1})$ = slope of moisture absorption in the initial and linear portion of curve, $\sqrt{seconds^{-1}}$

3.3.2 Specimen Configuration

Traveller specimens were placed in the environmental chamber to record the moisture absorption. The material for the composite was the IM7/8552 carbon/epoxy prepreg with a nominal thickness of 0.125mm and stacking sequence of $[45/90/-45/0]_{4s}$. The adhesive used was the Hexcel Redux 319 film adhesive with a nominal thickness of 0.2mm and no carrier.

For the adhesive, two traveller adhesive specimens bonded with aluminium were placed in the environmental chamber. The specimens were 100mm*20mm with a nominal adhesive thickness of 0.8mm (4 layers). Similarly, two composite traveller specimens of 100*20mm*4mm were placed in the environmental chamber to measure the moisture absorption. The moisture readings for the traveller specimens were taken for specimens placed in the Vötsch VC 7034 environmental chamber.

3.3.3 Results

Figure 3.3 shows the average moisture content for a typical adhesive and composite against the square root of time in hours for 4 months in the Vötsch VC 7034 environmental chamber. The wt% against sqrt(hours) for the composite started to saturate at about 0.9% wt. The adhesive continued to absorb moisture at the same rate during the 4 month period showing no indication of saturation. Using equation 2, the diffusivity for the composite was calculated as 5.2E-07 mm^2s^{-1}, as it achieved saturation. The diffusivity was not calculated for the adhesive as saturation was not achieved.

As the composite traveller sample reached 0.9% wt% within the 4 month period, it was agreed that considering the time constraints for the project that this was a sufficient degree of conditioning for the HTW experimental samples. The DCB, ENF and bonded joints have been conditioned for either 4 months or until the composite achieved 0.9% wt.

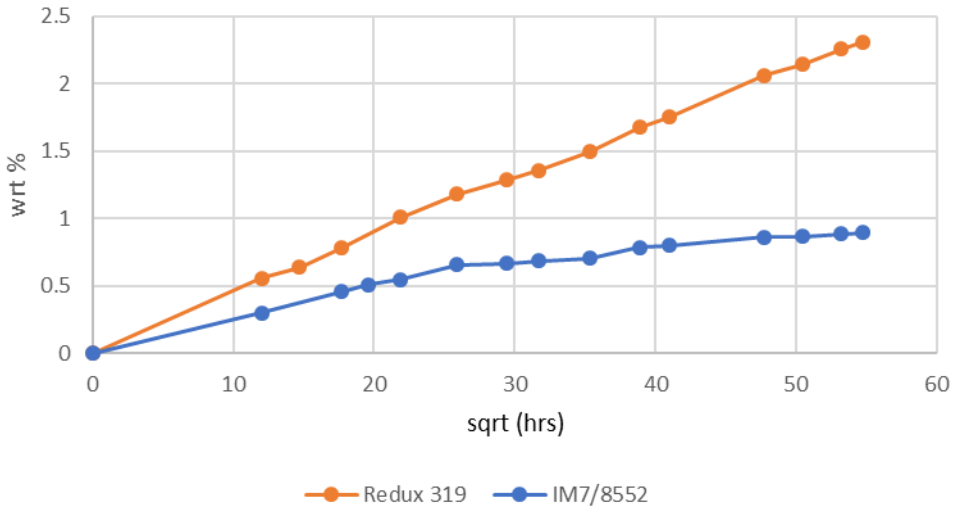

Figure 3.3 - %wt against square root hours for composite and adhesive traveller specimens

3.4 Mode I Fracture Energy: 0.2mm Nominal Adhesive Thickness

3.4.1 Experimental Configuration

Figure 3.4 shows the schematic for the 0.2mm nominal adhesive thickness (1 layer of film adhesive) DCB specimen, where *B*, the specimen width was 20mm, *h* the specimen half thickness was 2.5mm, *L* the specimen length was 140mm. These dimensions were held constant for all the DCB tests. The nominal adhesive thickness and actual measured adhesive thickness varied slightly due to leakage of the adhesive during the curing cycle, hence both nominal and actual thickness values were reported.

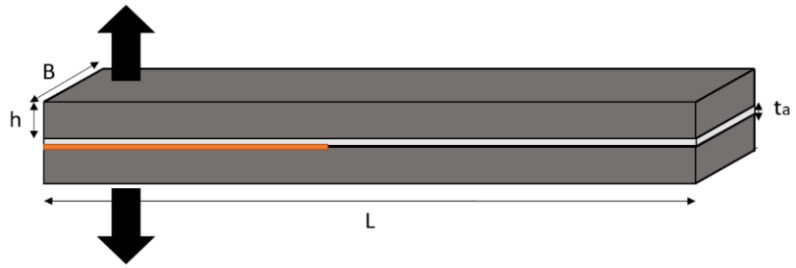

Figure 3.4 - Schematic of 0.2mm DCB specimen

The insert length was 65mm, with a thickness of 12μm. The material used for the insert was the Flomfilm 100 cast PTFE film. For the 0.2mm nominal adhesive thickness case, the PTFE film (highlighted in orange in Figure 3.4) was placed at the adherend/adhesive interface as shown in Figure 3.4. The initial loading was applied on the DCB specimen and the specimen was then unloaded. The second loading was defined as reloading, for which the new crack length was the initial insert length plus the crack growth that occurs during the initial loading. The G_{IC} was compared using the initial loading values for the adhesives. Reloading tests were only conducted at RTD conditions and are discussed in Appendix A.

3.4.2 Room Temperature Dry Case

The room temperature dry case was tested at 22°C. Figure 3.5 provides the load-displacement curves for the initial loading. The peak load was used for the G_{IC} calculation as the load-displacement graphs were linear.

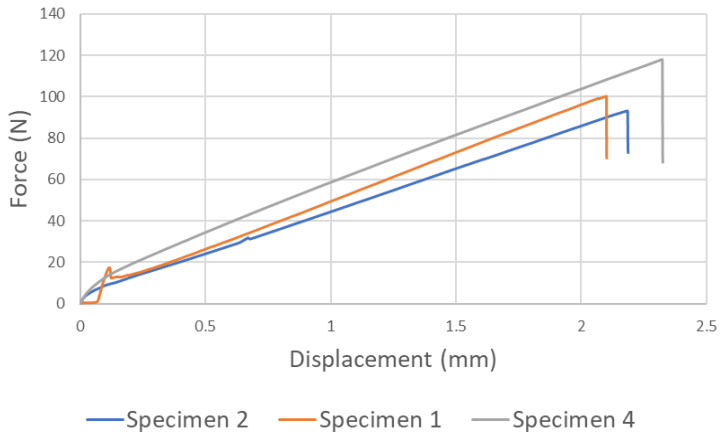

Figure 3.5- Force-displacement curve during initial loading for 0.2mm adhesive thickness at RTD conditions

The crack propagation was unstable, as seen from the sudden load drop in Figure 3.5. It was found during this process, that the crack jumps from the adhesive/composite interface into the surface 0˚ layer of the composite. The crack propagated about 10mm in the composite. Table 3.1 provides the initiation G_{IC} value.

The typical fracture surface and schematic is shown in Figure 3.6. The red dotted line indicates where the crack propagated to during the initial loading. As the composite 0˚ plies are visible on both fracture surfaces, it shows that the crack has propagated into the composite from the adhesive/composite interface.

Table 3.1 - 0.2mm nominal thickness Mode I test summary at RTD conditions based on initial loading

Specimen	**Adhesive Thickness (mm)**	**Initiation- G_{IC} (N/mm) (Pmax)**
1	0.18	0.315
2	0.13	0.302
4	0.17	0.424
Mean (*CV*)	**0.16** *(13%)*	**0.347** *(16%)*

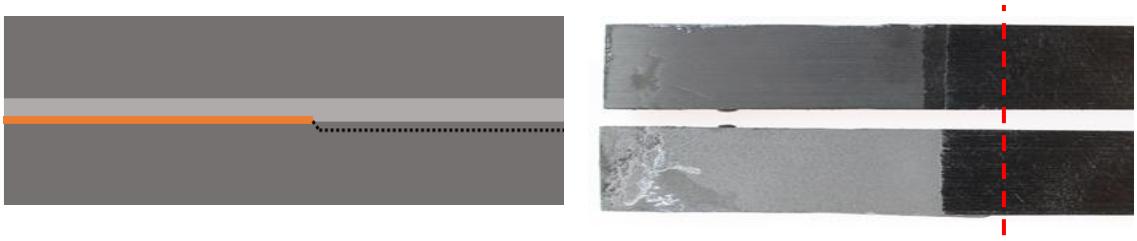

a) Failure Schematic b) Fracture surface

Figure 3.6 - Failure schematic and fracture surfaces for 0.2mm DCB specimens at RTD conditions

3.4.3 Hot Temperature Dry Case

The HTD specimens were tested at 80°C. Figure 3.7 shows the force displacement curves. Only the initial loading values are presented for this case as the crack propagated to the composite interface during the reloading test, similar to the RTD tests. To determine the composite HTD properties separate tests were conducted (Section 3.8). Due to the increased ductility of the adhesive at high temperatures, the G_{IC} based on the 5% load is reported. Table 3.2 shows the results for the 0.2mm nominal adhesive thickness case at HTD conditions.

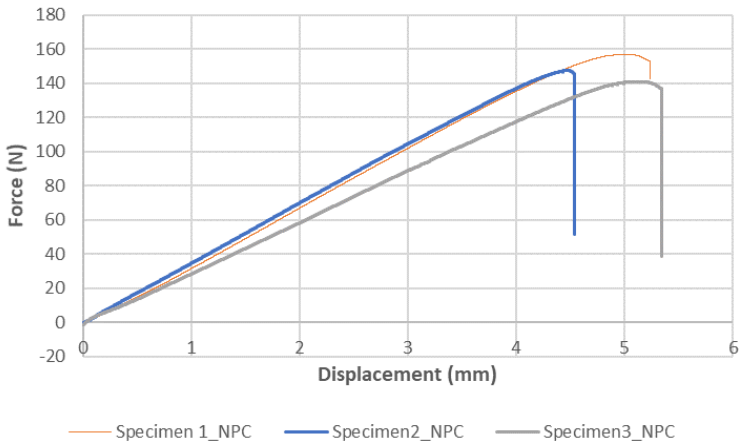

Figure 3.7 - Force-displacement curve during initial loading for 0.2mm adhesive thickness at HTD conditions

Table 3.2 - 0.2mm nominal thickness Mode I test summary at HTD condition based on initial loading

Specimen	Adhesive Thickness (mm)	Initiation- G_{IC} (N/mm) (P5%)
1	0.20	1.107
2	0.20	0.999
3	0.15	1.037
Mean *(CV)*	**0.18** *(12%)*	**1.055** *(3%)*

A significant increase in G_{IC} was observed with increasing temperature for the 0.2mm adhesive thickness case. Figure 3.8 shows the fracture surface and the failure schematic for the HTD configuration for the 0.2mm nominal adhesive thickness case and a difference in the failure mode was observed compared to the RTD case. For the RTD case, the crack propagated from the film insert to the composite at the maximum load. For the HTD case, the crack initially propagated into the adhesive, promoting a cohesive failure before unstable propagation into the composite. Therefore, the increase in the mode I fracture energy was due to the change in failure mechanism and the increased ductility of the adhesive at higher temperatures.

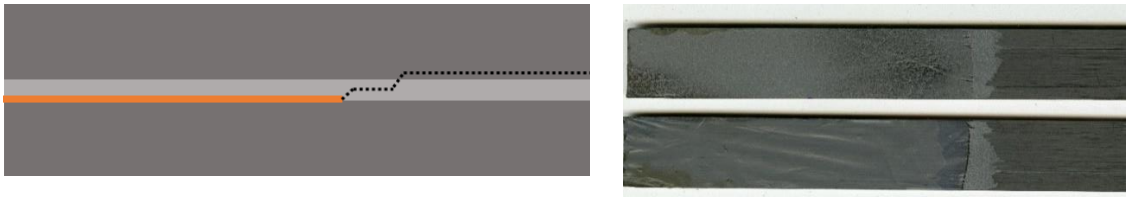

a) Failure Schematic b) Fracture Surface

Figure 3.8 - Failure schematic and fracture surfaces for 0.2mm DCB specimens at HTD conditions

3.4.4 Hot Temperature Wet Case

HTW tests were conducted on the DCB specimens at 80°C and with specimens conditioned at 80°C and 85% RH. The force displacement graph is shown in Figure 3.9. Unlike the previous loading for the RTD and HTD, a stable load drop and crack propagation was observed for the HTW case. The table of results is shown in Table 3.3.

The G_{IC} values were based on P5% due to non-linearity before the load drop. The %wt increase of the DCB specimens due to moisture was also recorded and is presented.

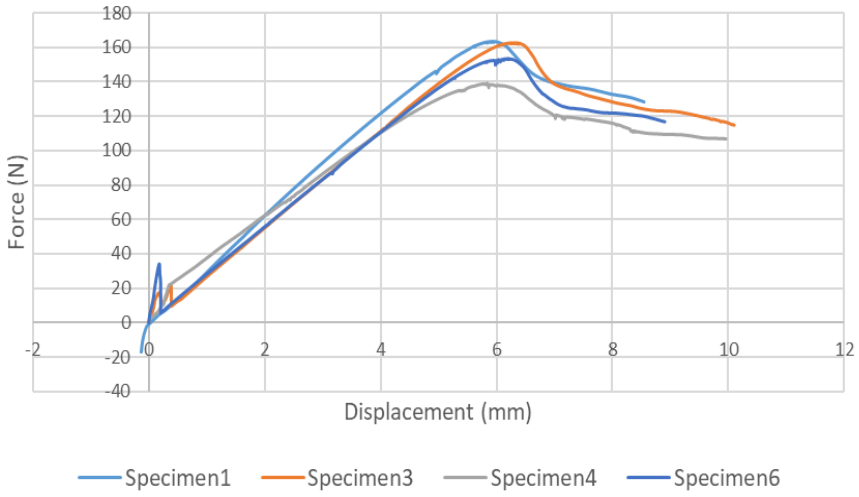

Figure 3.9- Force-displacement curve during initial loading for 0.2mm adhesive thickness at HTW conditions

Table 3.3 - 0.2mm nominal thickness Mode I test summary at HTW conditions based on initial loading

Specimen	**Adhesive Thickness (mm)**	**Initiation- G_{IC} (N/mm) (P5%)**	**%wt**
1	0.20	0.943	1.07
2	0.23	1.257	1.07
4	0.15	1.033	1.07
6	0.17	1.296	1.07
Mean *(CV)*	**0.19** *(16%)*	**1.132** *(13%)*	**1.07** *(0.2%)*

Analysing the fracture surface in Figure 3.10, a clear initial cohesive failure was observed for the HTW specimens, showing a difference to the fracture surfaces to the two previous conditions. A transition from a delamination dominated failure at RTD to adhesive dominated failure at HTW was observed. A small increase in G_{IC} at HTW compared to the HTD as shown in Figure 3.11. Both HTD and HTW conditions give a much higher G_{IC} compared to RTD. These results are analysed further in the discussion (Section 3.10)

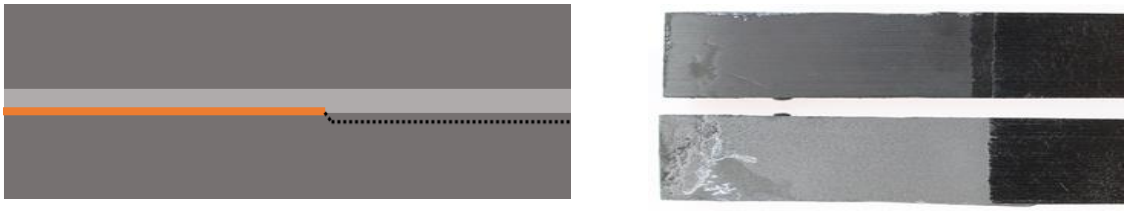

a) Failure Schematic b) Fracture Surface

1. RTD fracture surface and schematic

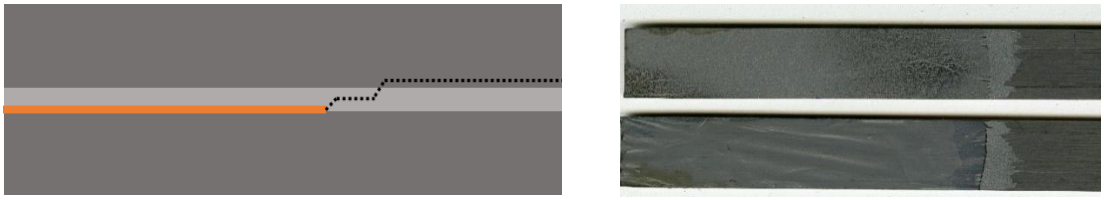

a) Failure Schematic b) Fracture Surface

2. HTD fracture surface and schematic

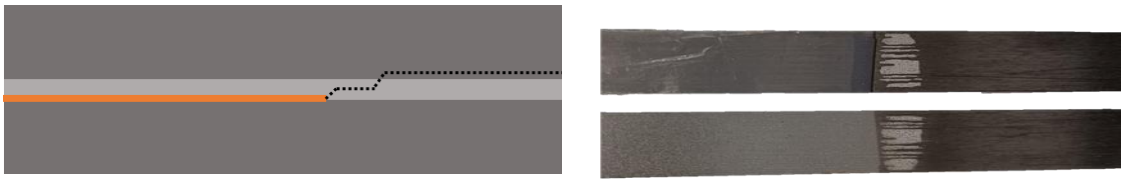

a) Failure Schematic b) Fracture Surface

3. HTW fracture surface and schematic

Figure 3.10 - Comparison of failure schematic and fracture surfaces for 0.2mm adhesive thickness

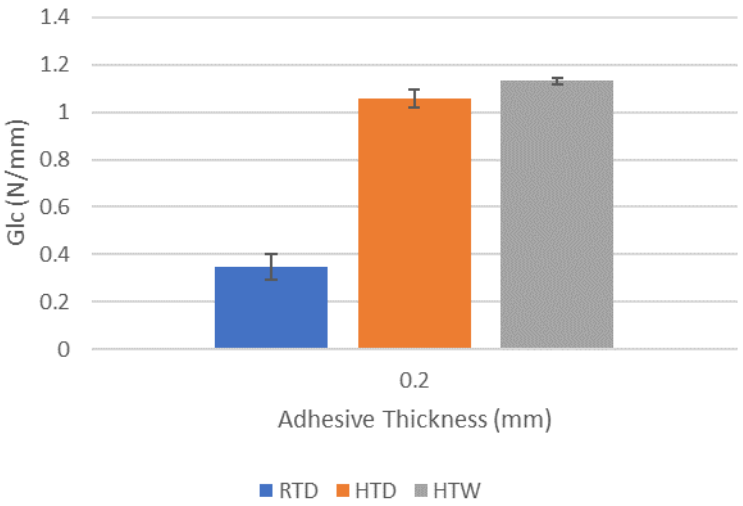

Figure 3.11 - Comparison of G_{IC} for RTD, HTD and HTW for 0.2mm adhesive thickness

3.5 Mode I Fracture Energy: 0.4mm Nominal Adhesive Thickness

3.5.1 Experimental Configuration

Following the 0.2mm nominal adhesive thickness case, the adhesive thickness was doubled. For the 0.4mm nominal adhesive thickness tests, the pre-implanted insert was inserted between two adhesive layers.

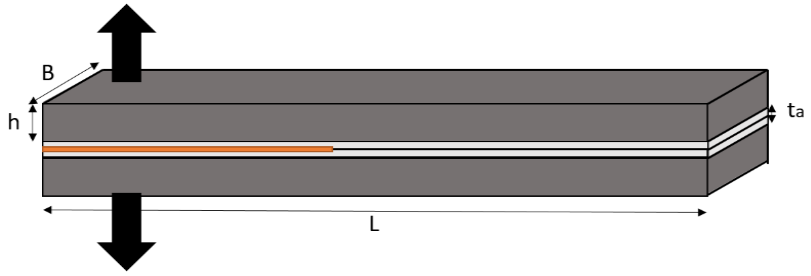

Figure 3.12- Schematic of 0.4mm DCB specimen

Figure 3.12 shows the schematic for this configuration. Wrinkles due to film insert were present for the thicker adhesive cases. These were formed during the curing process due to movement of the insert film placed in between the adhesive layers as a result of the low viscosity at higher temperatures. For the DCB tests these wrinkles were not believed to be critical due to the transverse load application.

3.5.2 Room Temperature Dry Case

Figure 3.13 shows the results for the 0.4mm adhesive thickness DCB specimen for the initial loading and reloading case. During the initial loading there was a sudden load drop at the maximum load resulting in unstable crack propagation. For the reloading tests, a stable crack growth was observed. Table 3.4 summarises the results for the RTD case.

The fracture surface in Figure 3.14 for the RTD case shows an initial region of cohesive failure before the crack propagated into the composite interface. The red dotted line in Figure 3.14 represents the end of the initial loading test and start of the reloading tests. For the reloading case, stable crack propagation occurred because the crack was in the

composite interface. Hence, the initial loading gave G_{IC} based on the adhesive properties.

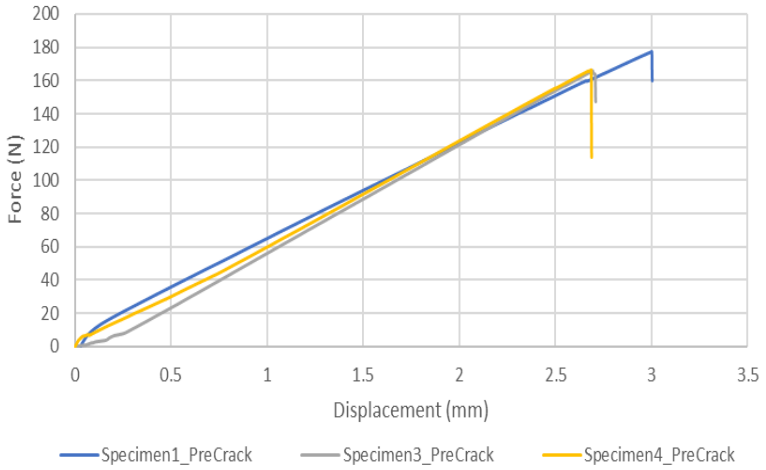

Figure 3.13 - Force-displacement curve during initial loading for 0.4mm adhesive thickness at RTD conditions

Table 3.4 - 0.4mm nominal thickness Mode I test summary at RTD conditions based on initial loading

Specimen	**Adhesive Thickness (mm)**	**Initiation- G_{IC} (N/mm) (P5%)**
1	0.41	0.951
2	0.40	0.812
4	0.39	0.799
Mean *(CV)*	**0.40** *(2%)*	**0.854** *(8%)*

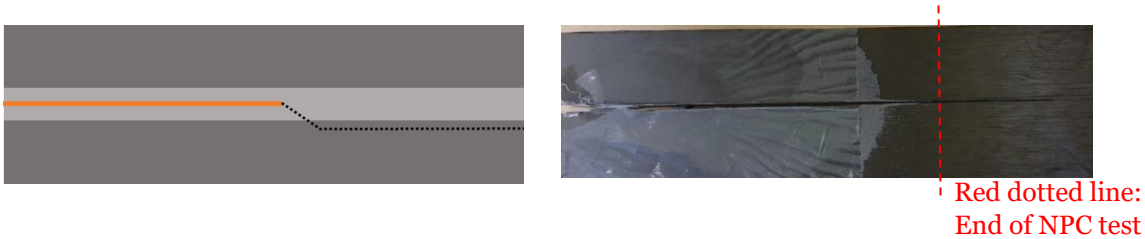

a) Failure Schematic b) Fracture Surface

Figure 3.14 - Typical failure schematic and fracture surfaces for 0.4mm nominal adhesive thickness DCB tests at RTD conditions

3.5.3 Hot Temperature Dry Case

The HTD specimens were tested at 80°C. Figure 3.15 shows the force displacement curves. A load drop at the peak load was observed, during which unstable crack propagation occurs, similar to the RTD case. Table 3.5 summarises the results for the 0.4mm nominal adhesive thickness case at HTD conditions for the initial loading.

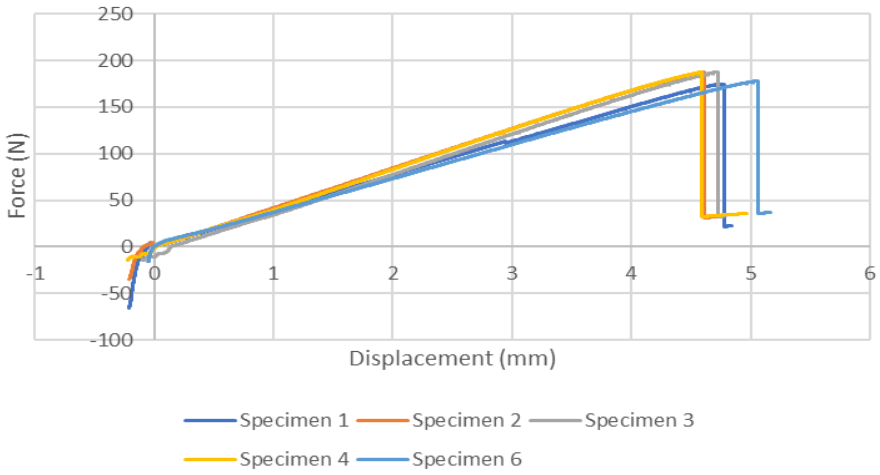

Figure 3.15 - Force-displacement curve for HTD 0.4mm adhesive thickness (Initial Loading)

Table 3.5 - 0.4mm nominal thickness Mode I test summary at HTD conditions based on initial loading

Specimen	Adhesive Thickness (mm)	Initiation- G_{IC} (N/mm) (P5%)
1	0.37	1.263
2	0.39	1.307
3	0.39	1.296
4	0.37	1.303
6	0.36	1.366
Mean *(CV)*	**0.38** *(4%)*	**1.307** *(3%)*

There was a significant increase in G_{IC} for the 0.4mm nominal adhesive thickness case at HTD compared to RTD. Figure 3.16 shows the fracture surface and mechanism for the HTD 0.4mm adhesive thickness case. Like the RTD case, during the unstable crack propagation from the initial loading, a small region of cohesive failure was seen before the crack migrated into the composite interface.

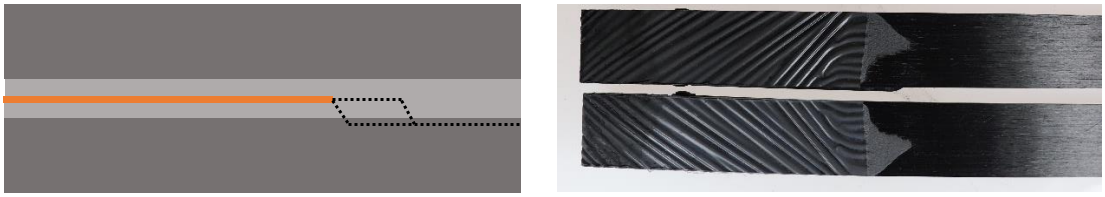

a) Failure Schematic b) Fracture Surface

Figure 3.16 - Typical failure schematic and fracture surfaces for 0.4mm nominal adhesive thickness DCB tests for HTD conditions

3.5.4 Hot Temperature Wet Case

The HTW tests were conducted on the DCB specimens. The force-displacement graph for the DCB samples at initial loading are shown in Figure 3.17. Compared to the RTD and HTD cases, the non-linearity in the force-displacement curve increased for the HTW conditions. The table of results is shown in Table 3.6. The %wt of the DCB specimens due to moisture was also recorded and presented.

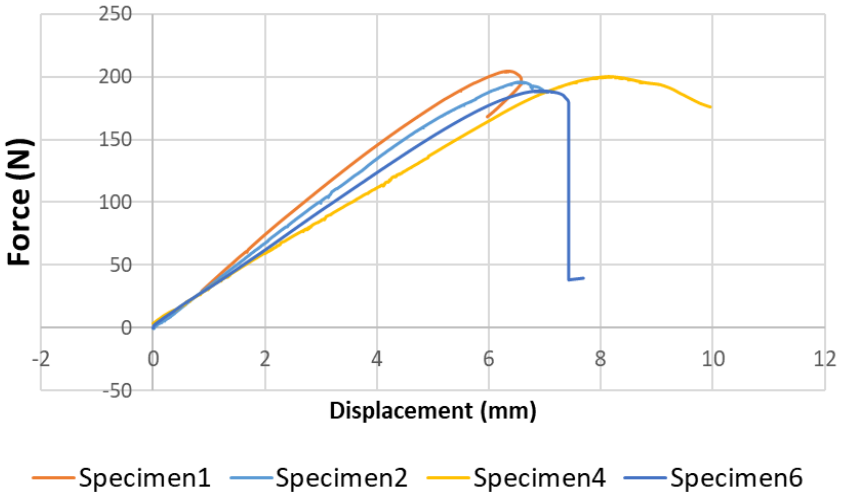

Figure 3.17- Force-displacement curve for HTW 0.4mm adhesive thickness (Initial Loading)

There is no significant difference in the G_{IC} value with increased moisture content. Figure 3.18 shows the fracture surface for the 0.4mm nominal adhesive thickness case for RTD, HTD and HTW conditions. Unlike the 0.2mm nominal adhesive thickness configuration, the failure mechanism was similar for the RTD, HTD and HTW conditions where an initial region of cohesive failure was followed by crack propagation into the adherend interface. The G_{IC} was therefore controlled by the adhesive for these cases. Figure 3.19 shows the effects of temperature and moisture for

the 0.4mm adhesive thickness. Consistent with the 0.2mm adhesive thickness case, the G_{IC} increased from RTD to HTD and HTW conditions.

Table 3.6 - 0.4mm nominal thickness Mode I test summary at HTW conditions based on initial loading

Specimen	Adhesive Thickness (mm)	Initiation- G_{IC} (N/mm) (P5%)	%wt
1	0.50	1.120	1.12
3	0.47	1.373	1.15
4	0.46	1.509	1.12
6	0.36	1.616	1.13
Mean *(CV)*	**0.45** *(12%)*	**1.405** *(13%)*	**1.13** *(1%)*

a) Failure Schematic b) Fracture Surface

1. RTD fracture surface and schematic

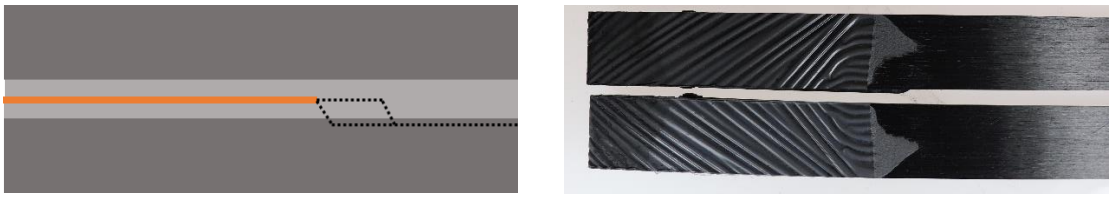

a) Failure Schematic b) Fracture Surface

2. HTD fracture surface and schematic

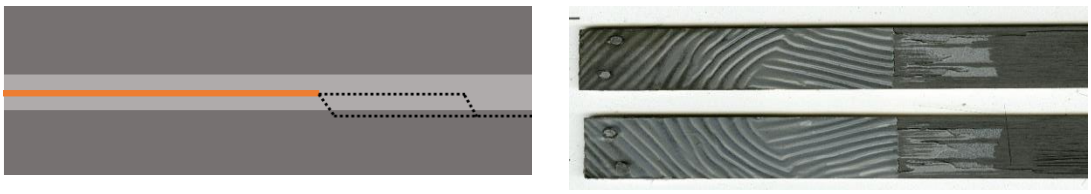

a) Failure Schematic b) Fracture Surface

3. HTW fracture surface and schematic

Figure 3.18 - Comparison of failure schematic and fracture surfaces for 0.4mm adhesive thickness

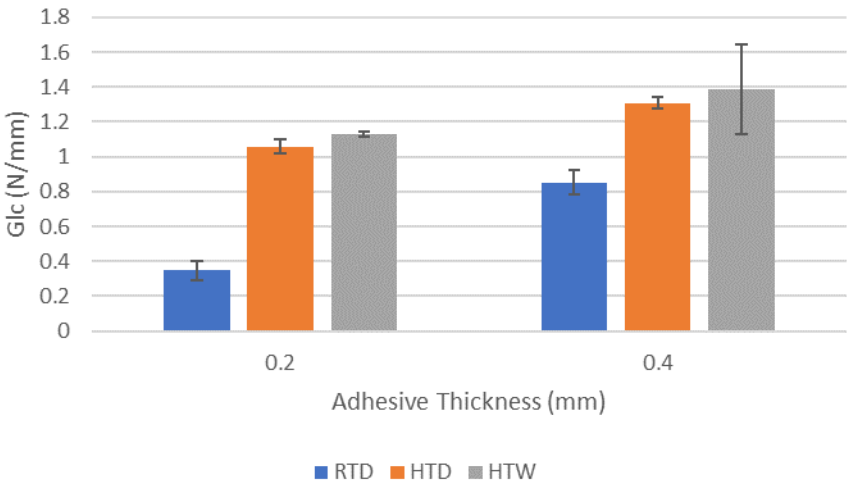

Figure 3.19 - Comparison of GIC for RTD, HTD and HTW for 0.2mm and 0.4mm adhesive thickness

3.6 Mode I Fracture Energy: 0.8mm Nominal Adhesive Thickness

3.6.1 Experimental Configuration

The 0.8mm adhesive thickness was manufactured by placing 2 layers of film adhesive either side of the insert. Figure 3.20 shows the schematic for the 0.8mm adhesive thickness DCB specimen.

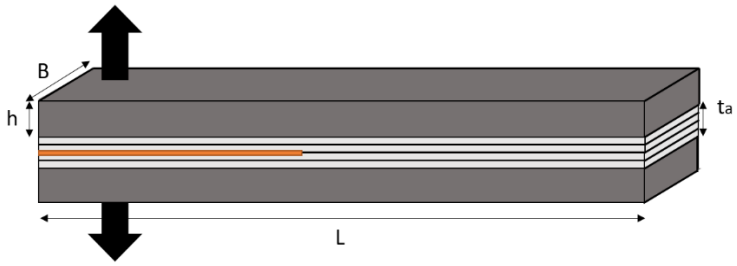

Figure 3.20 - Schematic of 0.8mm DCB specimen

3.6.2 Room Temperature Dry Case

3.21 provides the force displacement curves for the initial loading and reloading case. For the initial loading case, the force-displacement curves show a change in stiffness before an unstable crack propagation, indicating non-linearity for RTD conditions.

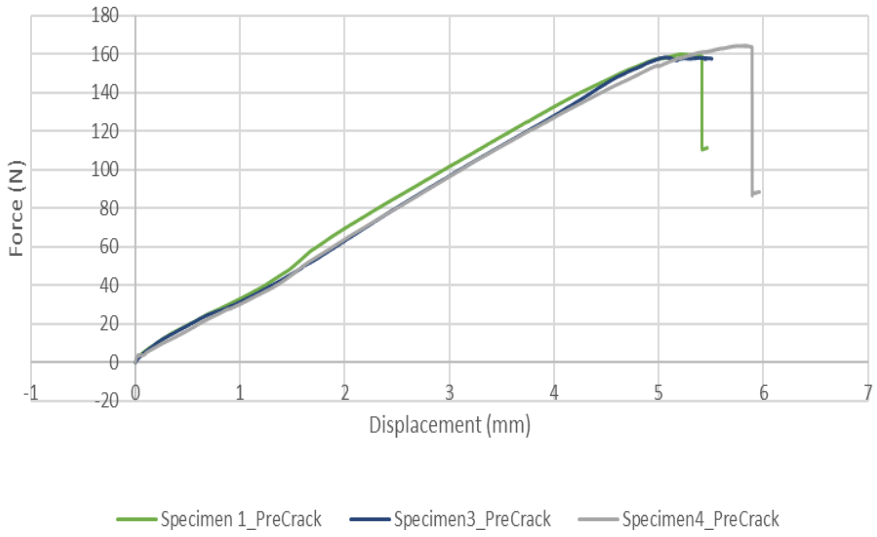

3.21 - Force-displacement curve during initial loading for 0.8mm adhesive thickness at RTD conditions

Table 3.7 - 0.8mm nominal thickness Mode I test summary at RTD condition based on initial loading

Specimen	Adhesive Thickness (mm)	Initiation- G_{IC} (N/mm) (P5%)
1	0.88	1.207
3	0.88	1.230
4	0.86	1.186
Mean *(CV)*	**0.85** *(6%)*	**1.211** *(2%)*

The experimental results are summarised in Table 3.7. Figure 3.22 shows the typical fracture schematic and surface for the 0.8mm case. During the initial loading, the crack propagated from the adhesive into the composite interface in an asymmetric pattern. The G_{IC} was therefore controlled by the adhesive. As the adhesive thickness increased the influence of the adhesive on the G_{IC} fracture surface increases for the RTD case. The red-dotted line on Figure 3.22, indicates the end of the initial loading and start of the reloading. The initial loading ends with the crack partially within the adhesive and

partially in the composite. This could have affected the G_{IC} obtained from the reloading case.

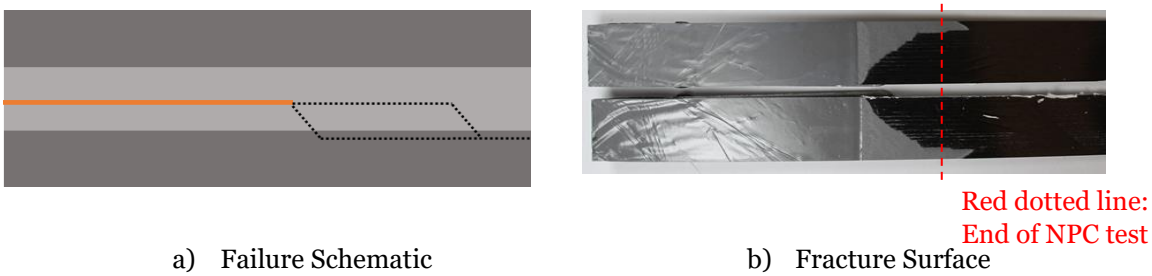

a) Failure Schematic b) Fracture Surface

Figure 3.22 - Typical failure schematic and fracture surfaces for 0.8mm nominal adhesive thickness DCB tests at RTD condition

3.6.3 Hot Temperature Dry Case

The HTD specimens were tested at 80°C. Figure 3.23 shows the force-displacement curves. Only the initial loading was considered for the 0.8mm adhesive thickness HTD case. A load-drop at the peak load resulting from unstable crack propagation was observed. Table 3.8 summarises the experimental results at HTD conditions. The G_{IC} increases with increasing temperature for the 0.8mm adhesive thickness case. There was no visible difference in the failure mechanism from analysing the fracture surfaces from Figure 3.24, where the failure was influenced by the adhesive properties.

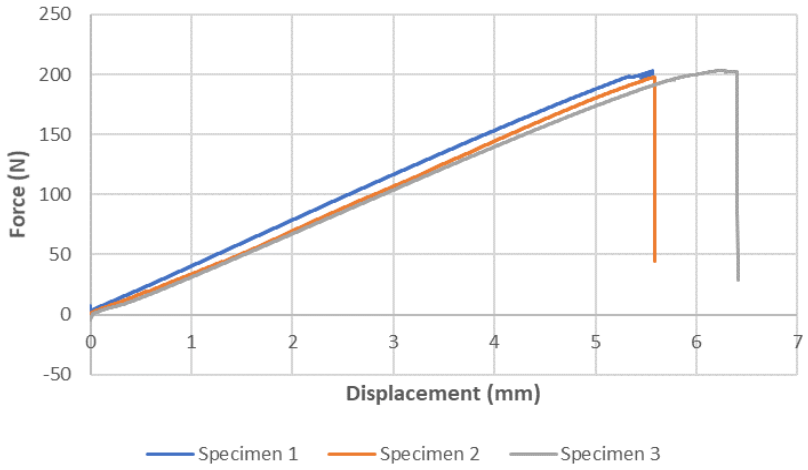

Figure 3.23 - Force-displacement curve for HTD 0.8mm adhesive thickness (Initial Loading)

Table 3.8 - 0.8mm nominal thickness Mode I test summary at HTD condition based on initial loading

Specimen	Adhesive Thickness (mm)	G_{IC} (N/mm) ($P_{5\%}$)
1	0.95	1.652
2	0.79	1.511
3	0.86	1.750
Mean *(CV)*	**0.86** *(7%)*	**1.637** *(6%)*

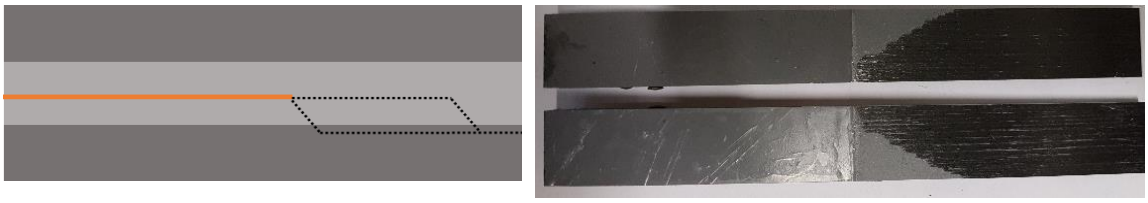

a) Failure Schematic b) Fracture Surface

Figure 3.24 - Typical failure schematic and fracture surfaces for 0.8mm nominal adhesive thickness DCB tests at HTD condition

3.6.4 Hot Temperature Wet Case

The force-displacement graph for the initial loading is shown in Figure 3.25. Consistent with the previous initial loading cases, unstable crack propagation occured at the maximum load which was represented by a load drop. The non-linearity also increased for the conditioned specimens tested at high temperature.

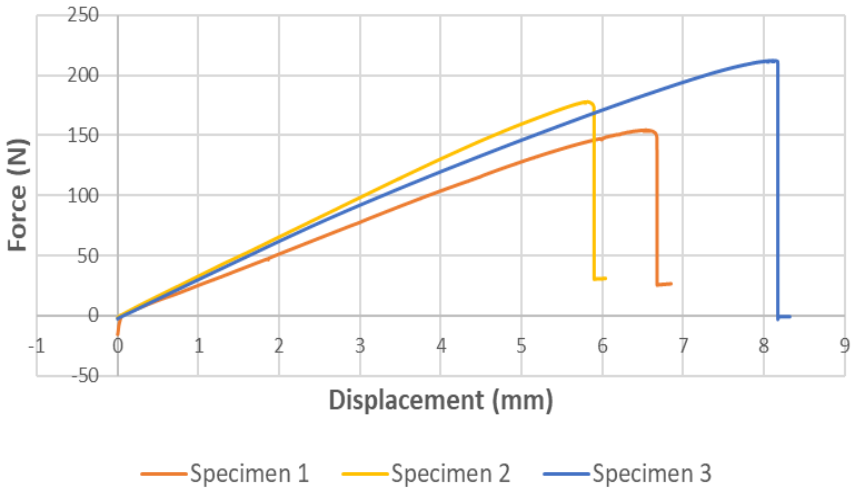

Figure 3.25 - Force-displacement curve for HTW 0.8mm adhesive thickness (Initial Loading)

Table 3.9 - 0.8mm nominal thickness Mode I test summary at HTW condition based on initial loading

Specimen	Adhesive Thickness (mm)	G_{IC} (N/mm) ($P_{5\%}$)	%wt
1	0.96	1.616	1.29
2	0.86	1.469	1.26
3	0.89	2.043	1.28
Mean *(CV)*	**0.90** *(5%)*	**1.709** *(14%)*	**1.28 (1%)**

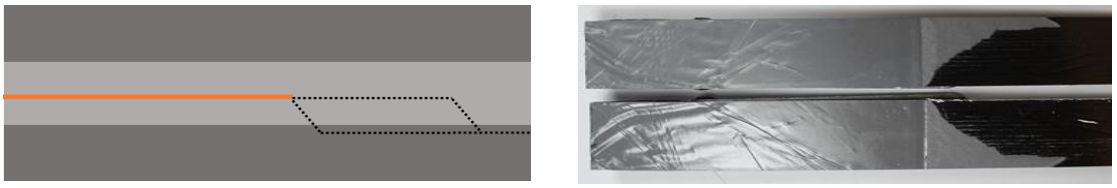

a) Failure Schematic b) Fracture Surface

1. RTD fracture surface and schematic

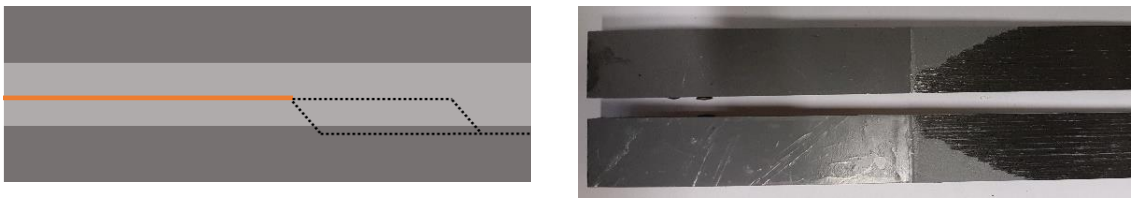

a) Failure Schematic b) Fracture Surface

2. HTD fracture surface and schematic

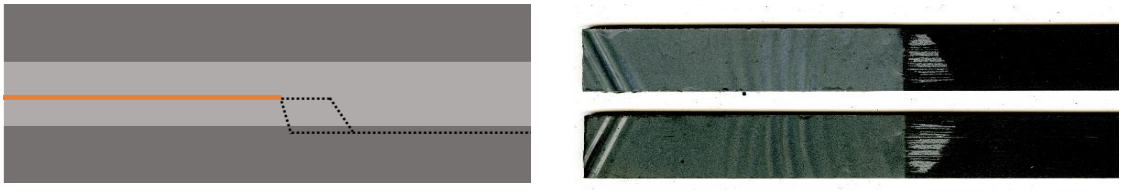

a) Failure Schematic b) Fracture Surface

3. HTW fracture surface and schematic

Figure 3.26 - Comparison of failure schematic and fracture for 0.8mm adhesive thickness

The experimental results are summarised in Table 3.9. The G_{IC} for the HTD and HTW conditions for the 0.8mm adhesive thickness were similar. Figure 3.26 shows the fracture surface for the 0.8mm nominal adhesive thickness case for RTD, HTD and HTW conditions. The asymmetric cohesive failure pattern from the initial loading test was consistent with all the environmental conditions tested. The G_{IC} was therefore

influenced by the adhesive for all these cases, similar to the 0.4mm adhesive thickness case.

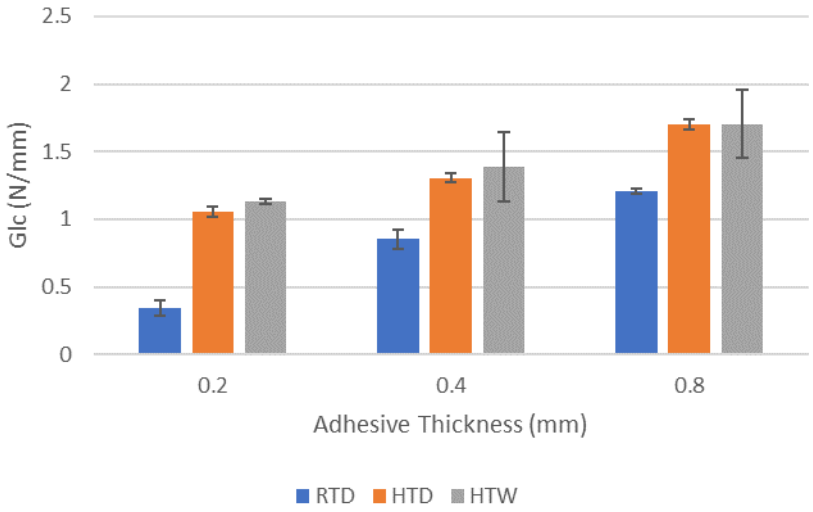

Figure 3.27 - Comparison of G_{IC} for RTD, HTD and HTW

Analysing the environmental effects on G_{IC} for the 0.8mm adhesive thickness in Figure 3.27 shows the G_{IC} increased with temperature and moisture compared to the RTD case. The HTD and HTW G_{IC} were similar.

3.7 Surface Treatment Effects

The surface treatment used for all characterisation and joint test configurations was by using grit blasting to achieve a macroscopically rough surface followed by liquid degreasing using acetone. It was found from previous research that the grit-blasting technique increased the critical strain-energy release rate due to the increased surface roughness, which for some cases changed the failure mode from interfacial to cohesive [90].

This section compares the effect of two different surface treatment methods on the G_{IC} and fracture surface of an adhesively bonded composite DCB specimen. The two surface treatments used were the grit blasted and peel ply techniques. The application of the peel ply was during the pre-preg lay-up process, whereas grit blasting occurred after the pre-pregs have been cured. The peel ply was applied as a surface layer on the

pre-preg. During cure the resin flows from the pre-preg into the gaps of the peel ply. The peel ply was then removed post cure just before applying the adhesive layer during the secondary bonding process. Ideally, a fresh epoxy surface that is chemically active should be obtained once the peel ply is removed. However, depending on the peel ply removal technique and material used, the peel ply could fracture or interlaminar failure within the composite could occur [91], which in turn affects the bond quality.

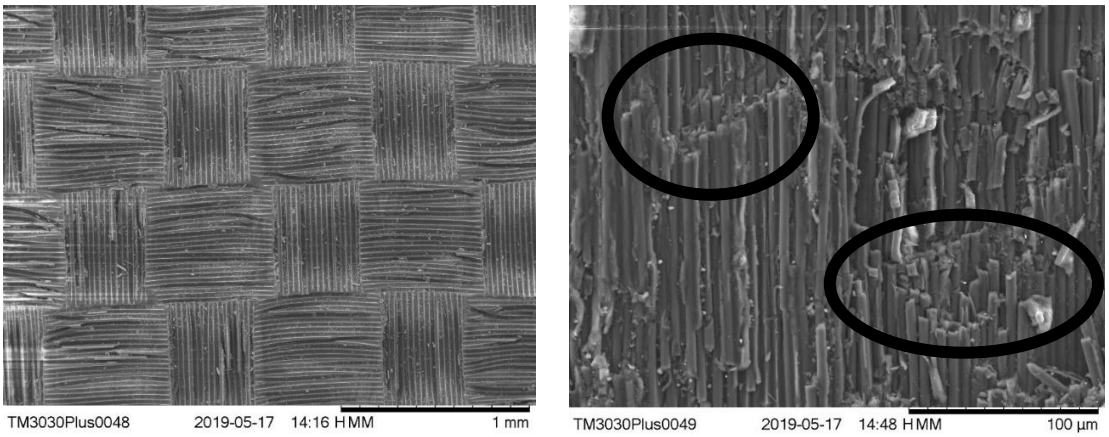

a) Peel ply b) Grit Blasted

Figure 3.28 - Comparison of different surface preparation

Figure 3.28 shows the Scanning Electron Microscope (SEM) images for the grit blasted and specimens after peel ply removal. The SEM image of the specimen after the removal of peel ply shows the undamaged 0° fibres, whereas the grit blasted surface shows multiple discontinuous fibres, meaning that these fibres were damaged during the grit blasting process. Hence, broken fibres were present on the adherend surface before the secondary bonding process when the specimens were grit blasted.

One DCB test using a peel ply surface treatment at RTD conditions for the 0.2mm adhesive thickness case was conducted. Only one specimen was tested as this was a qualitative study to understand the difference in failure mode between two surface treatment methods. The DCB test configuration was the same as described in the previous sections. The 0.2mm adhesive thickness case had the insert film placed in between the composite and adhesive at the interface. The fracture surface for both surface treated DCB specimens is shown in Figure 3.29. For the peel ply surface preparation, the crack propagation was along the adhesive/adherend interface, hence resulting in an interfacial failure. This was different to the grit blasted specimens,

where crack migration occurred into the 0° surface ply. This showed that without the good bond due to grit blasting the fibres, the interface between the composite and adhesive was the weakest path for the crack to initiate and propagate.

Although no solid conclusion could be drawn based on one specimen result, initial findings showed the G_{IC} for grit-blasted surface treatment was higher that the peel ply method, suggesting that the interface was weaker than the composite.

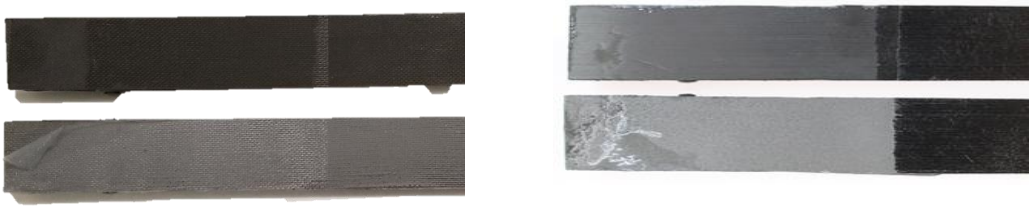

a) Peel ply b) Grit Blasted

Figure 3.29 - Fracture surface for different surface treatments

3.8 Mode I Fracture Energy: IM7/8552

3.8.1 Hot Temperature Dry Case

HTD DCB tests were conducted on IM7/8552 carbon/epoxy to understand how the G_{IC} changes with increased temperature. The insert film was placed within the mid-plane of the composite during the lay-up process. Figure 3.30 shows the DCB composite configuration used for testing. The specimen configuration was similar to the previous DCB tests, in which B was 20mm, specimen half-thickness, h was 2.5mm and the support length, *L* was 140mm. The insert length was 65mm and the layup for a half specimen was $[0]_{20}$.

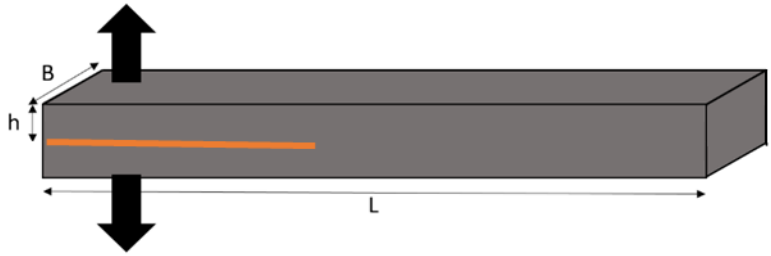

Figure 3.30 - Schematic of Composite DCB specimen

The same experimental conditions as for the adhesive G_{IC} tests was used for the composite G_{IC} tests, at 80°C. For the composites the G_{IC} was calculated using the reloading test data, as a stable crack propagation during the NPC test was achieved.

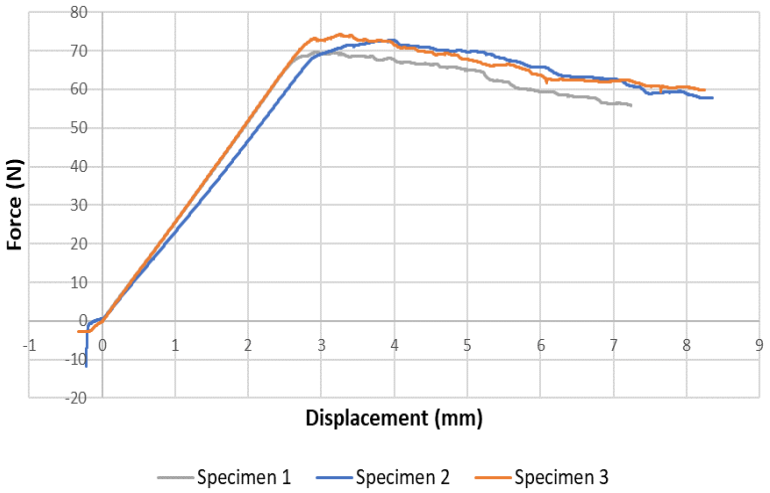

Figure 3.31 - Force-displacement curve for HTD IM7/8552 (Reloading)

Table 3.10 - IM7/8552 Mode I test summary at HTD condition

Specimen	**G_{IC} (N/mm) - Reloading**
1	0.242
2	0.263
3	0.274
4	0.232
Mean *(CV)*	0.253 *(7%)*

Figure 3.31 shows the force-displacement curves during the reloading tests and no significant non-linearity was observed for the HTD case. During the initial loading tests, the crack grew about 5mm stably before unloading. The load-displacement curve did not vary by 5% from the initial linear region before the maximum load, hence the P_{max} values are reported. Table 3.10 shows the G_{IC} results for the IM7/8552 specimens. The crack propagates from the insert film into the composite interface stably during the initial loading and reloading tests.

3.8.2 Hot Temperature Wet Case

HTW DCB tests were conducted on IM7/8552 for samples conditioned at 80°C and 85% RH, tested at 80°C, consistent with the other HTW cases. The force-displacement curves for the reloading tests are shown in Figure 3.32. Similar to the HTD case, stable crack propagation was observed past the maximum load. There was no significant non-linearity for the HTW case, therefore the G_{IC} based on P_{max} are reported.

The experimental results are summarised in Table 3.11. Figure 3.33 compares the G_{IC} for RTD, HTD and HTW cases for IM7/8552. The RTD value was obtained from literature [92]. Consistent with the trend observed for the adhesive G_{IC} with changing environmental conditions, there was an increase in G_{IC} with increasing temperature and moisture. This was due to the increased ductility and plasticisation of the adhesive at the HTD and HTW conditions. The increase in G_{IC} for the HTW condition was more significant for the IM7/8552 composite than for the adhesive.

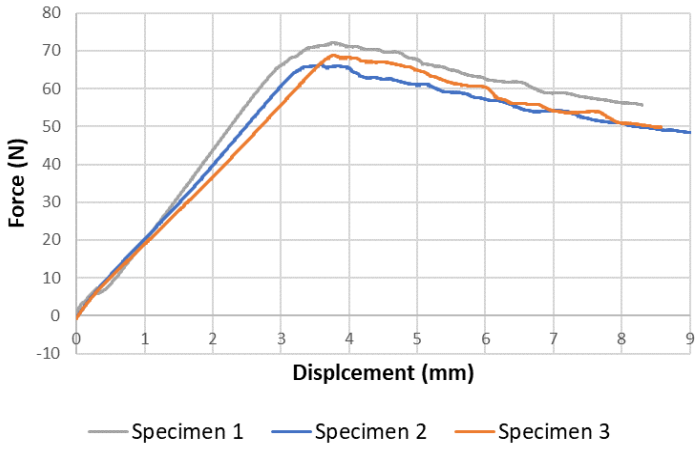

Figure 3.32 - Force-displacement curve for HTW IM7/8552 (Reloading)

Table 3.11 - IM7/8552 Mode I test summary at HTW condition

Specimen	**G_{IC} (N/mm) - Reloading**	**%wt**
1	0.332	0.96
2	0.352	0.96
3	0.335	0.97
4	0.322	0.96
Mean	0.335 *(3.2%)*	0.96 (0.5%)

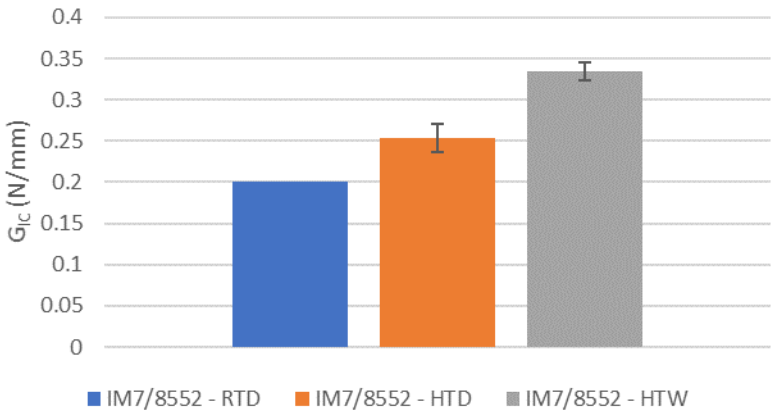

Figure 3.33 - Comparison of G_{IC} based of P_{max} for RTD, HTD and HTW for IM7/8552

3.9 Tensile Strength of Adhesive

3.9.1 Experimental Configuration

To understand the effects of temperature and moisture on the tensile strength of the bulk adhesive Redux 319, dog-bone specimen tests on the bulk adhesive were conducted according to ASTM D638. The schematic of the dog-bone specimen is shown in Figure 3.34

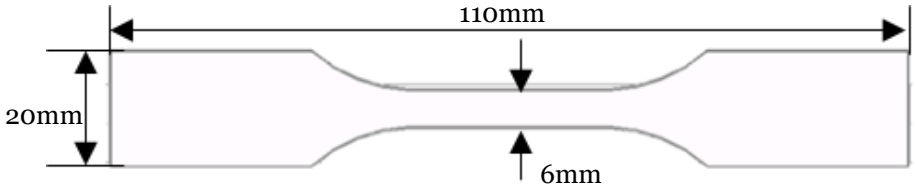

Figure 3.34 - Schematic of dog-bone tensile specimen

20 layers of film adhesive, each of 0.2mm nominal thickness were used to manufacture the bulk adhesive. The cure pressure for the bulk adhesive was 1.5kPa (within the range recommended by the manufacturer), which was different from the cure pressure for the characterisation and double lap joint specimens which were cured at 7kPa. The bulk adhesive was then machined after curing to a consistent thickness of 3mm and using a CNC machine, cut into the dog-bone specimens. A universal Shimadzu

machine was used for the testing at a loading rate of 0.5mm/minute. Non-contact measurements were taken to measure the strain during the tensile loading. Imetrum optical based video extensometer systems were used to measure the average strains during testing by tracking the relative vertical motion between two defined point in the gauge section of the dog-bone specimen.

3.9.2 Hot Temperature Dry Case and Hot Temperature Wet Case

The HTD and HTW specimens were tested at 80°C. The bulk adhesive HTW samples were conditioned at 80°C at 85% RH. Table 3.12

summarises the tensile test results for both the HTD and HTW cases. The 5% yield strength was taken when the stress-strain curve deviated from the initial linear response by 5%.

Table 3.12 - Bulk adhesive tensile strength under HTD and HTW conditions

	HTD	**HTW**
Ultimate Strength (MPa) (C.V.%)	58.5 (10%)	23.4 (7%)
5% Yield Strength (MPa) (C.V.%)	36.3 (9%)	7.47 (14%)
Young's Modulus (MPa) (C.V.%)	2232	1455 (16%)
wt%	-	3%
Number of Specimens	3	4

The RTD dog-bone tests for Redux 319 were conducted by Jeenjitkaew [93] who reported the Ultimate strength and Young's Modulus as 88MPa and 3762MPa (6%) respectively (*C.V%* for the strength was not given). Hence, a significant decrease in strength and Young's Modulus can be seen from RTD to HTD conditions. Comparing HTD and HTW results from Figure 3.35 and Figure 3.36 shows a significant decrease in tensile strength and increase in strain. As the HTW specimens absorb moisture, the glass transition temperature (T_g) of the material decreases. Therefore, the difference between the test temperature (80°C) and T_g changes for the HTD and HTW conditions. As materials approach the T_g, significant degradation of the material properties was reported in the literature. These results are consistent with the trends observed from the literature review.

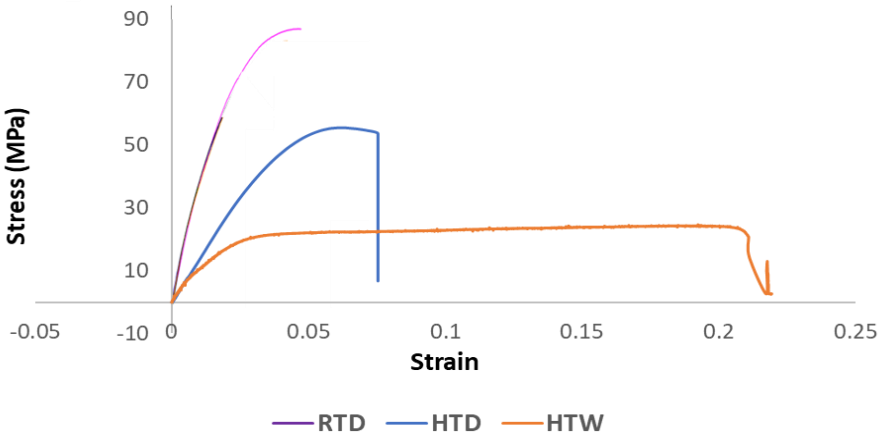

Figure 3.35 – Tensile Stress-Strain curves for Redux 319 at RTD, HTD and HTW conditions

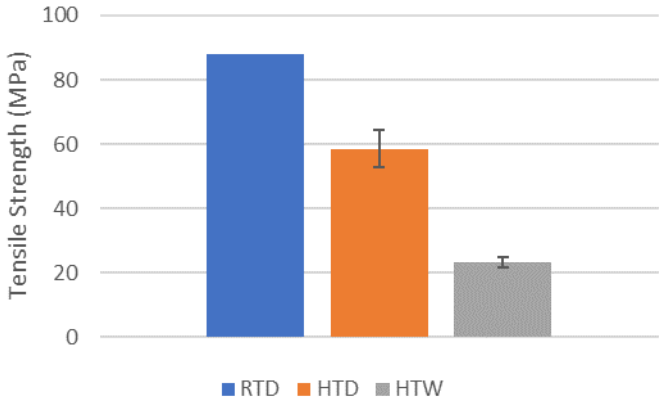

Figure 3.36 - Ultimate tensile strength of Redux 319 at RTD *[93]*, HTD and HTW

3.10 Summary of Environmental and Adhesive Thickness Effects on Mode I Fracture Toughness

Figure *3.37* compares the G_{IC} from the initial loading against the actual adhesive thickness for all environmental conditions. The data points in solid indicate cohesive failure, dashed lines mean an initial cohesive failure followed by delamination into the composite and empty bars indicate delamination within the composite. Large scatter on the measured adhesive thickness was present as the adhesive was unsupported (no nylon carrier for glue-line thickness control).

It can be seen for the initial loading case, as the adhesive thickness increased the G_{IC} increased for all environmental conditions, which is consistent with the literature. This

was due to more energy being dissipated in the process zone through increased plastic straining as a result of increased adhesive thickness [21]. A greater increase was seen for the RTD case between 0.2mm and 0.4mm nominal adhesive thickness case as the 0.2mm case was controlled by delamination within the composite. During the initial loading for all cases, after a region of cohesive failure the crack propagated unstably into the composite, hence the new crack tip was in the composite. Increasing temperature had a significant effect on the G_{IC} for all adhesive thicknesses considered. The increased ductility at higher temperatures gave a higher G_{IC} for the adhesive.

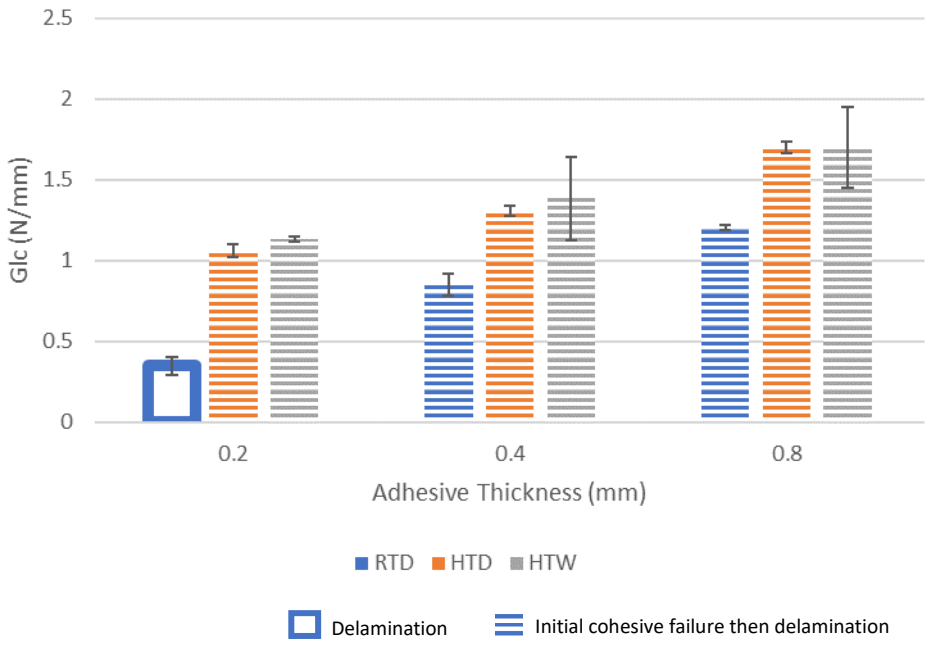

Figure 3.37 - Adhesive thickness vs initial loading G_{IC} comparison

The fracture surfaces for different configurations changed depending on the temperature, moisture and adhesive thickness. The SEM images of the grit blasted surface showed broken fibres on the surface of the adherend before the secondary bonding process. These broken fibres introduced a region of high stress concentration and potential path for crack propagation within the adherend surface 0° ply. For the 0.2mm adhesive thickness case, three different failure modes were observed for the three environmental conditions. The schematic in Figure 3.38 summarises the different crack propagation paths observed. The insert film was placed at the adhesive/composite interface for the 0.2mm adhesive thickness, and the failure mechanism was split into two, initiation and propagation.

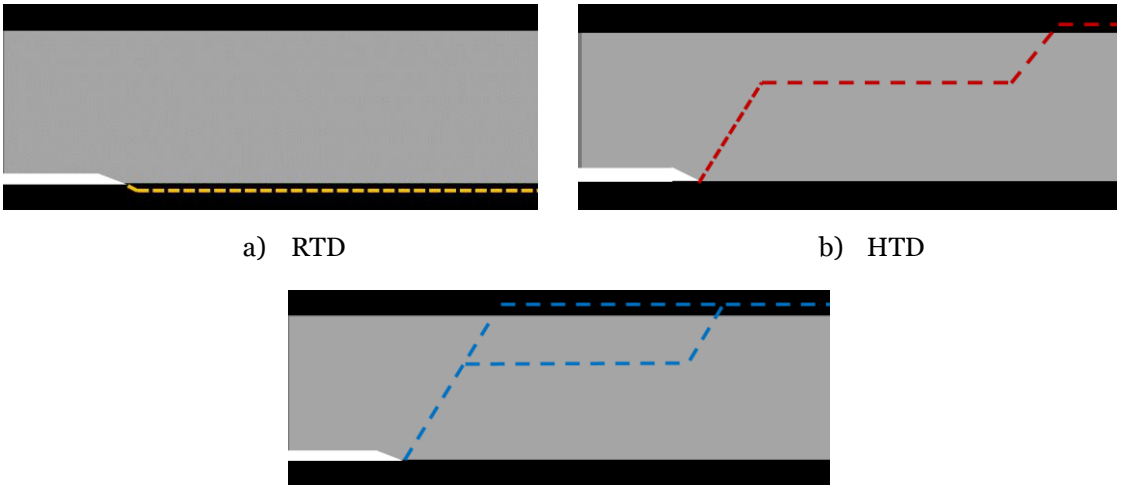

a) RTD b) HTD

c) HTW

Figure 3.38 - Failure schematic for 0.2mm adhesive thickness case

During crack initiation, at RTD, the high stress concentrations from the broken fibres at the composite surface facilitated the crack migration into the composite surface 0° ply before the adhesive could yield. This was shown in the force-displacement graph for the 0.2mm adhesive thickness RTD case, where a linear curve was seen before a sudden load drop. At HTD and HTW, the adhesive yield strength decreased significantly compared to the RTD case. Hence, during loading the adhesive started to yield at the adhesive/composite interface which was shown by the non-linearity in the 0.2mm HTD and HTW DCB force-displacement curves. The adhesive yielding resulted in failure initiation into the adhesive. During propagation, at HTD and HTW, the crack fully migrated into the composite after the initial cohesive failure. At RTD, the crack stayed within the composite during propagation.

All the failures observed for the thicker adhesive cases (0.4mm and 0.8mm) at all environmental conditions showed a similar failure mechanism. As the insert film was between the adhesive for these cases, crack initiation was always within the adhesive. Following the initiation, the crack propagated within the adhesive initially and then migrated into the 0° ply in the adherend surface. The final crack propagation path for all cases was into the composite 0° ply, as the composite was the least tough material and the broken fibres on the composite surface facilitated the crack migration.

3.11 Conclusions

The G_{IC} for adhesives and composite were measured for increasing adhesive thickness at different environmental conditions in this chapter. At RTD condition, G_{IC} increased with increasing adhesive thickness. The failure mode changed from delamination within the surface 0° ply (0.2mm adhesive thickness) to an initial cohesive failure followed by crack migration into the surface 0° ply of the adherend for the thicker adhesives (0.4mm and 0.8mm). Hence, the initial increase in G_{IC} from 0.2mm to 0.4mm adhesive thickness was due to the change in the crack initiation and propagation path. The increase from 0.4mm to 0.8mm adhesive thickness was due to the increased energy dissipation in the process zone through increased plastic straining which increased with increasing adhesive thickness, as the adhesive properties controlled the failure [21]. At HTD, the G_{IC} increased significantly compared to RTD for all adhesive thicknesses. For the 0.2mm adhesive thickness HTD case a change in failure mode was observed compared to the RTD case. An initial region of cohesive failure was followed by crack migration into the surface 0° ply. For the thicker adhesives at HTD, similar failure modes were observed compared to the RTD cases. The increased G_{IC} was due to the increased ductility of the adhesive due to the higher test temperatures. There was no significant difference in G_{IC} for all adhesive thicknesses between HTD and HTW conditions. The G_{IC} was controlled by the adhesive properties for all cases except the 0.2mm RTD condition. The composite G_{IC} also increased from RTD to HTW conditions.

Tensile tests using dog-bone specimens were conducted for the adhesive at HTD and HTW conditions. A significant decrease in strength and increase in strain was observed with the presence of moisture in the adhesive, due to the plasticisation of the adhesive during moisture conditioning.

CHAPTER 4

CHARACTERISATION OF MODE II FRACTURE TOUGHNESS AND SHEAR STRENGTH

4.1 Introduction

Three different nominal adhesive thicknesses of 0.2mm. 0.4mm and 0.8mm were tested at Room Temperature Dry (RTD), Hot Temperature Dry (HTD) and Hot Temperature Wet (HTW) conditions to determine the Mode II fracture toughness, G_{IIC} in this chapter. Similar to the Mode I specimen configurations, for the 0.2mm nominal adhesive thickness case the insert, was placed in between the adhesive and adherend interface. For the 0.4mm and 0.8mm cases the insert was placed in between the adhesive layers. The nominal adhesive thickness and actual measured adhesive thickness varied slightly due to leakage of the adhesive during the curing cycle, hence both nominal and actual thickness values were reported. End Notch Flexure (ENF) tests were conducted in a 3-point bending jig to determine the values following the ASTM standard (ASTM D7905) for unidirectional fibre-reinforced polymer matrix composites, using the Compliance Calibration Method (CCM) of data reduction, in which the relationship between the specimen compliance and the delamination length is determined before the fracture test. This is conducted through measurement of the compliance at multiple delamination lengths, 20mm, 30mm and 40mm as per the ASTM standard. Figure 4.1 shows the ENF test schematic according to the ASTM D7905 standard. The calculation of G_{IIC} for CCM is based on the cubic relationship

with the crack length, as shown in Equation 4.1. The coefficients m and A are calculated using least squares linear regression analysis, where C and a represent the compliance and crack length respectively.

$$C = A + ma^3 \tag{4.1}$$

G_{IIC} is calculated from Equation 4.2. Combining equations 4.1 and 4.2 gives G_{IIC} for the CCM in Equation 4.3, where P is the load and B is the specimen width. The fracture test was conducted with a crack length of 30mm

$$G_{IIC} = \frac{P^2}{2B}\frac{dC}{da} \tag{4.2}$$

$$G_{IIC} = \frac{2mP^2a^2}{2B} \tag{4.3}$$

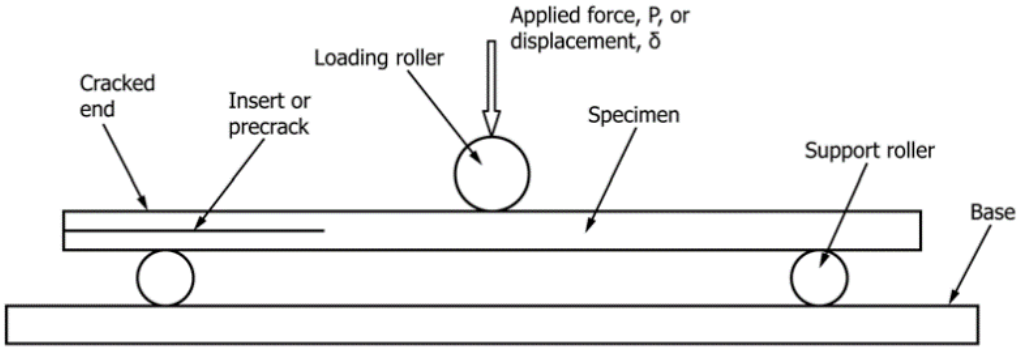

Figure 4.1 - ENF test schematic according to ASTM D7905

Figure 4.2 shows the typical ENF test setup. The NPC tests calculate the G_{IIC} from the pre-implanted insert, whereas the Pre-cracked (PC) test determine the G_{IIC} when the delamination had advanced from the pre-implanted insert. This chapter focuses on the Non-Pre-Cracked (NPC) results for all conditions for comparison. For RTD specimens, two tests were conducted, the NPC and PC. The PC RTD results are discussed in Appendix A.

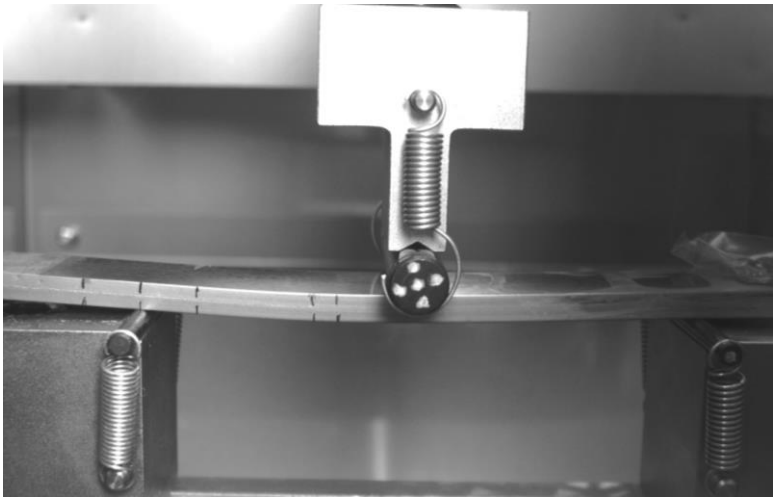

Figure 4.2 - ENF Test setup

Following the NPC tests, the new crack was marked by visual inspection of the specimen edge. It was found for some cases, the crack migrated from the adhesive into the composite during the NPC tests. Therefore, the crack was in the adhesive for the NPC tests and composite for the PC tests, giving G_{IIC} for different interfaces for most cases at all environmental conditions. For the HTD and HTW cases, separate composite ENF tests were conducted to calculate the composite G_{IIC} since literature data was not available. To observe the crack propagation during the NPC tests, white/gold paint was used on the edge of the specimen. Initially, the crack lengths were measured from both edges with a 0.2mm nominal adhesive thickness and were similar. Hence, the crack length was only measured at one edge with the 0.4mm and 0.8mm nominal adhesive thicknesses. The actual adhesive thickness was recorded for each specimen before testing. Similar to the Mode I cases, the G_{IIC} was calculated when the initial force- displacement deviates by 5% (P5%) and based on the maximum load (P_{max}). The P5% provides a lower bound value and is more appropriate for the G_{IIC} cases where significant non-linearity was present. For the HTW cases there was no apparent load drop, therefore no maximum load value was reached, and crack propagation occurred during the non-linear response. The large non-linearity particularly for the HTW cases also means that there could be a difference in the G_{IIC} value if the offset from the initial region was calculated at a different value than 5%. For consistency, comparisons for all cases are based on the NPC G_{IIC} from P5%. There was some variability in the force-displacement curves due to the variation in adhesive thickness for each specimen and due to the difficulty in identifying the insert film length (crack length for NPC/PC tests) prior to the tests accurately.

The same experimental configurations were used for the RTD, HTD and HTW tests. Similar to the Mode I testing section, the HTD tests were conducted at 80°C using a thermal chamber. A thermocouple was attached to the specimens to ensure the specimen temperature was consistent with the thermal chamber temperature. The HTW specimens were conditioned at 80°C at 85% Relative Humidity (RH) for 4 months. At least 3 specimens for each configuration were tested.

4.2 Mode II Fracture Energy: 0.2mm Nominal Adhesive Thickness

4.2.1 Experimental Configuration

For 0.2mm adhesive thickness configuration, the insert film was inserted between the adhesive and the composite layer as shown in Figure 4.3. For the ENF specimens used, the width, B was 20mm, specimen half-thickness, h was 2mm and the support length, L was 50mm. The insert (Flomfilm 100 cast PTFE film) had a thickness of 12μm and the insert length was 65mm. These dimensions were held constant for all the ENF tests conducted. The layup for a half specimen was $[0]_{16}$.

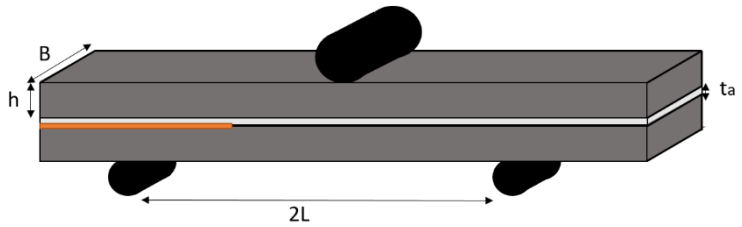

Figure 4.3 - Schematic of 0.2mm nominal adhesive thickness ENF specimen

4.2.2 Room Temperature Dry Case

The RTD was tested at 22°C. Figure 4.4 shows the load displacement graph for the NPC and PC tests respectively. For the NPC tests, once the peak load had been reached, a crack propagated stably from the adhesive/composite interface into the adhesive. The crack was allowed to propagate for 5mm before the NPC test was stopped.

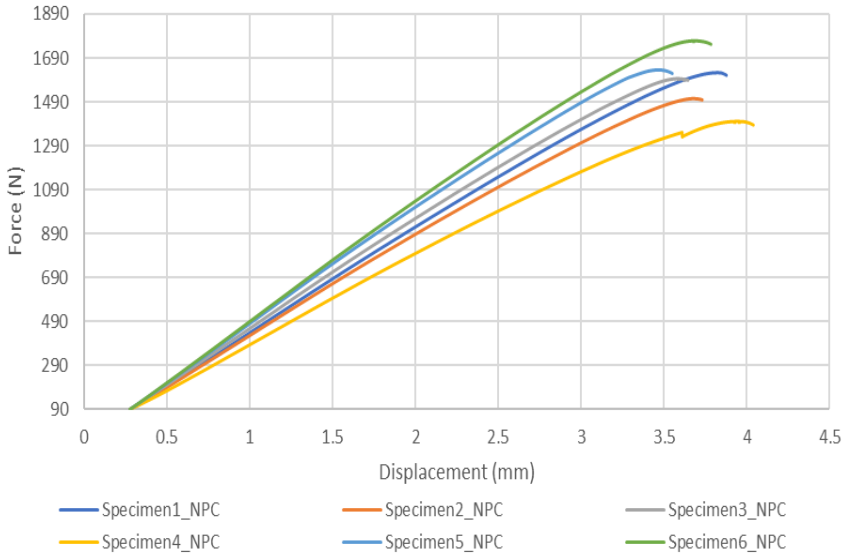

Figure 4.4 - Force-displacement curve during NPC for 0.2mm adhesive thickness at RTD conditions G_{IIC}

From the force-displacement curves, large non-linearity was observed before the peak load was reached. The new crack tip was marked after the NPC test, and the same procedure was done for the PC tests. During the PC tests, after an initial stable region, a load drop was observed indicating complete crack propagation into the composite.

Table 4.1 summarises the G_{IIC} results at RTD conditions. During the stable load-drop that occurred in the NPC test, an initial region of cohesive failure was observed with growing instances of fibres on the fracture surface as the crack propagated, as shown in Figure 4.5. The red dotted line indicates the end of the NPC test, and start of the PC test. For the PC tests, it is possible that the fibre bridging between the partially broken fibres and intact fibres increased the force required for crack propagation.

Table 4.1 - 0.2mm nominal thickness Mode II test summary at RTD conditions based on NPC

Specimen	**Adhesive Thickness (mm)**	**G_{IIC} (N/mm) (P5%)**
1	0.13	3.16
2	0.17	2.47
3	0.18	2.69
4	0.17	2.25
5	0.15	2.34
6	0.16	3.01
Mean *(CV)*	**0.16** *(9.6%)*	**2.65** *(13%)*

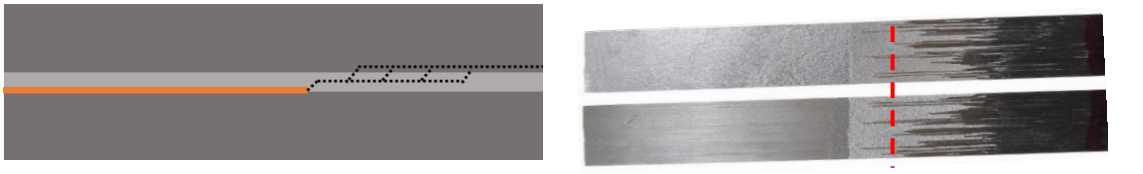

a) Failure Schematic b) Fracture Surface

Figure 4.5 – Failure schematic and fracture surfaces for 0.2mm ENF specimens at RTD conditions

4.2.3 Hot Temperature Dry Case

The HTD tests were conducted at 80°C. The force-displacement graphs are shown in Figure 4.6. Similar to the RTD case, the force-displacement graph shows that stable crack propagation occurred at the peak load for the NPC loading case. During the NPC tests, the crack was allowed to propagate for 5mm before unloading. Compared to the RTD case, there was much more non-linearity in the NPC force-displacement graph for the HTD case. The test results are summarised in Table 4.2. There was a significant decrease in G_{IIC} for the HTD condition compared to RTD.

The fracture surface in Figure 4.7 shows a cohesive failure for the NPC tests. Hence, from the insert at the adhesive/composite interface, the crack propagated into the adhesive. The red dotted line in Figure 4.7 indicates the starting position for the PC tests. When observing the fracture surface, the crack started to migrate into the composite gradually during the PC test, in a similar manner to the RTD case.

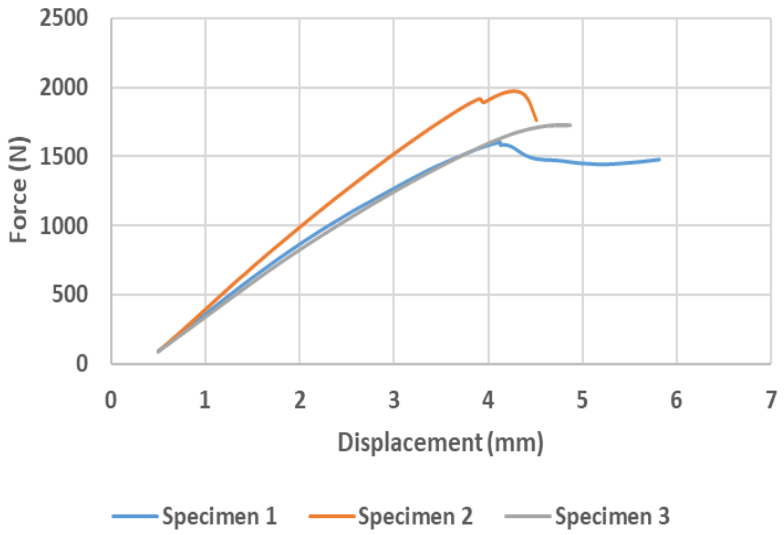

Figure 4.6 - Force-displacement curve during NPC for 0.2mm adhesive thickness at HTD conditions for G_{IIC}

Table 4.2 - 0.2mm nominal thickness Mode II test summary at HTD conditions based on NPC

Specimen	Adhesive Thickness (mm)	G_{IIC} (N/mm) (P5%)
1	0.23	1.17
2	0.19	1.24
3	0.20	1.56
Mean *(CV)*	**0.21** *(6%)*	**1.32** *(13%)*

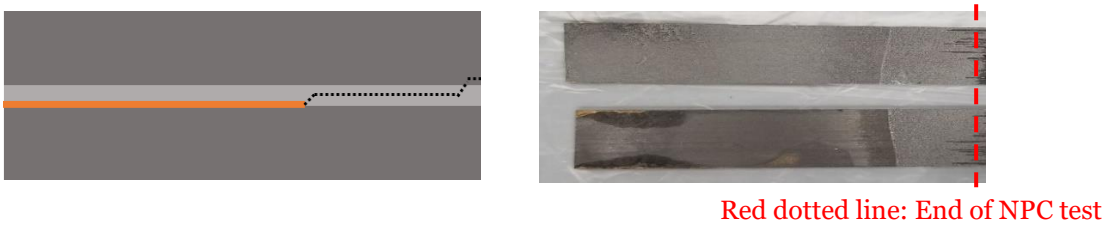

a) Failure Schematic b) Fracture Surface

Figure 4.7 - Failure schematic and fracture surfaces for 0.2mm ENF specimens at HTD conditions

4.2.4 Hot Temperature Wet Case

The HTW tests were conducted at 80°C for specimens conditioned at 80°C and 85% RH for 4 months. The force-displacement graphs are shown in Figure 4.8. The increase in weight due to moisture absorption (wt%) for each specimen was recorded before testing and shown in Table 4.3. The summary of the test results is presented in Table 4.3. The G_{IIC} decreases further with the presence of moisture.

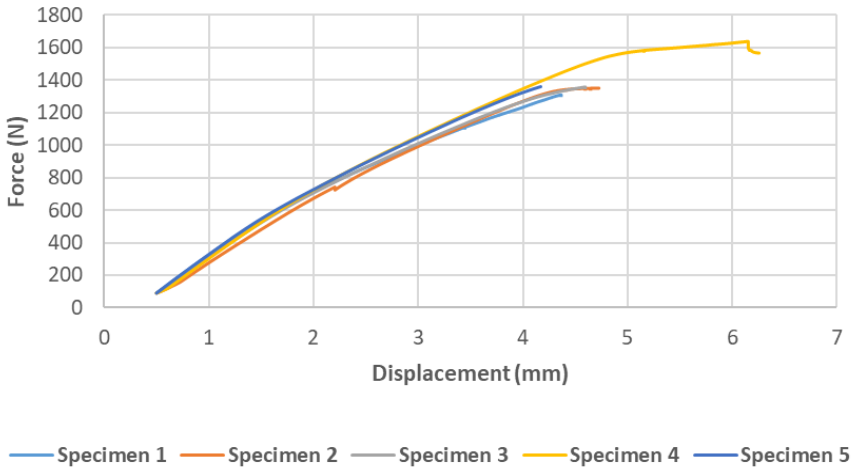

Figure 4.8 - Force-displacement curve during NPC for 0.2mm adhesive thickness at HTW conditions for G_{IIC}

Table 4.3 - 0.2mm nominal thickness Mode II test summary at HTW conditions based on NPC

Specimen	Adhesive Thickness (mm)	G_{IIC} (N/mm) (P5%)	Wt increase (%)
1	0.22	0.528	1.13
2	0.20	0.842	1.12
3	0.19	0.710	1.13
4	0.15	0.913	1.14
5	0.24	0.492	1.14
Mean *(CV)*	**0.20** *(16%)*	**0.697** *(24%)*	**1.13** *(0.7%)*

During the fracture ENF tests for the HTW condition, there was no indication of crack propagation from the force-displacement graphs. In previous ENF cases, from visual inspection it was observed that at a critical load the force started to either plateau indicating stable crack propagation or drop indicating crack migration into the adherend. Using a video gauge to capture the crack growth, it was found that the crack propagation occurred during the non-linear region of the force-displacement curve. Therefore, only the G_{IIC} based on the P5% was calculated for the HTW case, as it was a conservative and consistent approach which was applicable for all cases. For one specimen during the fracture test, the crack propagation was allowed to continue to observe whether a load-drop occurred at a later stage for the HTW condition. However, compression failure directly beneath the roller was seen at about 1600N. The premature compression failure was due to the reduced strength of the composite due to the conditioning process.

The fracture surfaces are compared for RTD, HTD and HTW conditions for the 0.2mm adhesive thickness in Figure 4.9. Cohesive failure became more dominant as the temperature and moisture increased. For the RTD case, an initial cohesive region was followed by stripes of fibres on the fracture surface, gradually increasing with the crack propagation, until the crack fully propagated into the composite. For the HTD case, the cohesive failure was more dominant. For the HTW case, clear cohesive failure was observed all the way before the test ended with compression failure at the roller.

a) Failure Schematic

b) Fracture Surface

1. RTD fracture surface and schematic

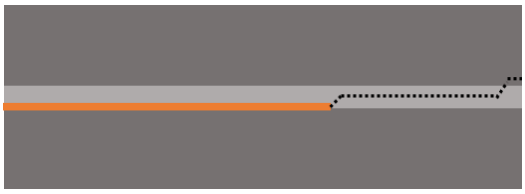

a) Failure Schematic

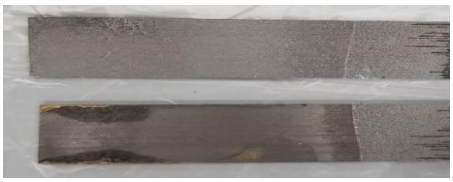

b) Fracture Surface

2. HTD fracture surface and schematic

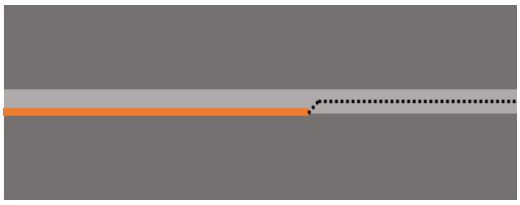

a) Failure Schematic

b) Fracture Surface

3. HTW fracture surface and schematic

Figure 4.9 - Comparison of failure schematics and fracture surfaces for 0.2mm adhesive thickness for G_{IIC}

Comparing the G_{IIC} for RTD, HTD and HTW for the 0.2mm adhesive thickness, a significant decrease in toughness was found as shown in Figure 4.10. The NPC G_{IIC} values were used for comparison.

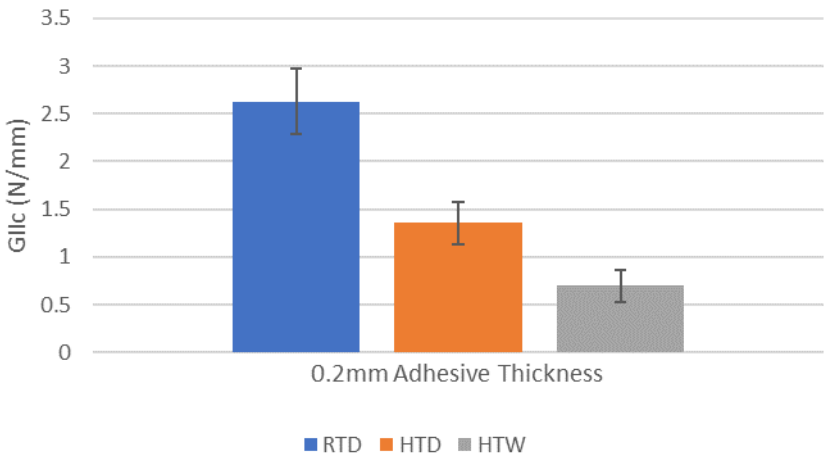

Figure 4.10 - Comparison of G_{IIC} based on P5% NPC for RTD, HTD and HTW for 0.2mm nominal adhesive thickness

4.3 Mode II Fracture Energy: 0.4mm Nominal Adhesive Thickness

4.3.1 Experimental Configuration

For the 0.4mm adhesive thickness tests, the pre-implanted insert was inserted between two adhesive layers as shown in Figure 4.11. The dimensions were the same as the 0.2mm nominal adhesive thickness case apart from t_a of 0.4mm.

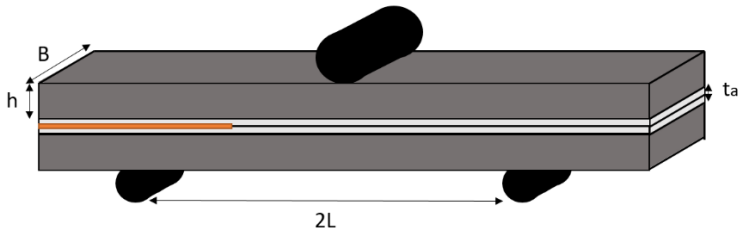

Figure 4.11 - Schematic of 0.4mm nominal adhesive thickness ENF specimen

4.3.2 Room Temperature Dry Case

Figure 4.12 shows the load displacement graph for the NPC and PC tests respectively. During the NPC tests, it was noted that once the maximum load was reached, an unstable crack propagation occurred, which was represented by the sharp load drop. After the load drop, the new crack tip was marked, and the PC test was conducted. The crack propagation during the PC test was also unstable.

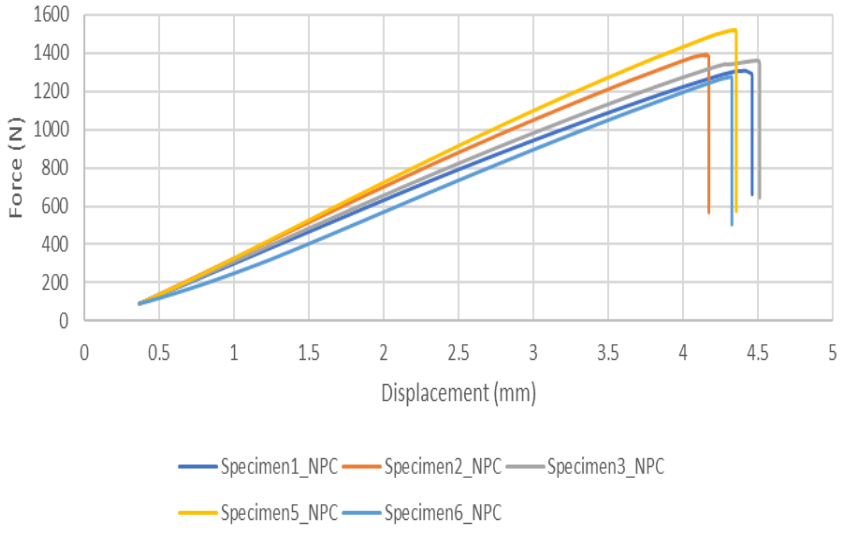

Figure 4.12 - Force-displacement curve during NPC for 0.4mm adhesive thickness at RTD conditions for G_{IIC}

Table 4.4 - 0.4mm nominal thickness Mode II test summary at RTD conditions based on NPC

Specimen	Adhesive Thickness (mm)	G_{IIC} (N/mm) (P5%)
1	0.27	3.47
2	0.33	3.28
3	0.26	2.82
5	0.29	4.00
6	0.28	3.75
Mean *(CV)*	**0.29** *(8%)*	**3.47** *(12%)*

Table 4.4 provides the summary for the G_{IIC} for 0.4mm adhesive thickness at RTD conditions. During the unstable crack propagation, the crack migrated into the composite interface and is represented by the red-dotted lines in Figure 4.13. Therefore, the interface at which the crack was present differed for the NPC and PC tests. Before the NPC, the film insert was in between two layers of adhesive whereas before the PC test the crack was in the composite. During the PC tests, the crack growth was unstable, similar to the NPC case.

Figure 4.13 shows the fracture surface for the 0.4mm nominal adhesive thickness case at RTD. The composite was visible on both fracture surfaces, right after the insert end, with shades of grey indicating some adhesive influence. It is different to the 0.2mm adhesive thickness case for the ENF specimen for which a clear initial cohesive failure was found.

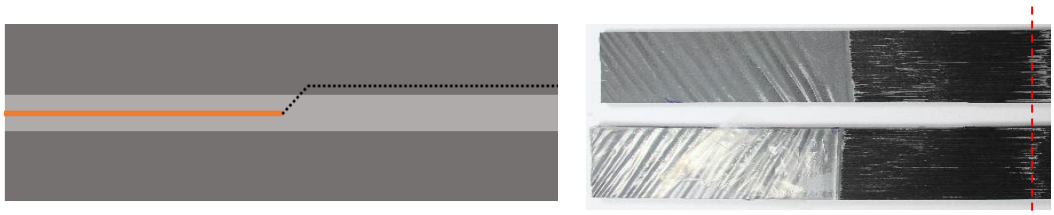

a) Failure Schematic b) Fracture Surface

Figure 4.13 – Failure schematic and fracture surface for 0.4mm ENF specimens at RTD conditions

4.3.3 Hot Temperature Dry Case

The force-displacement graph for the NPC case is shown in Figure 4.14. Compared to the RTD case, there was significant non-linearity in the force-displacement graph. At the end of the NPC tests, after the initial crack had propagated by 5mm, the test was paused to mark the new crack tip for the PC test. However, during the time where the

specimen was held under the constant load, unstable crack propagation occurred for specimens 1 and 2. For specimen 3 unstable crack propagation occurred before the test was paused. Hence, only the NPC tests were conducted for the HTD 0.4mm adhesive thickness case, as the crack propagated into the composite. Separate HTD tests for the composite were conducted. The results for the HTD case for 0.4mm adhesive thickness are summarised in Table 4.5.

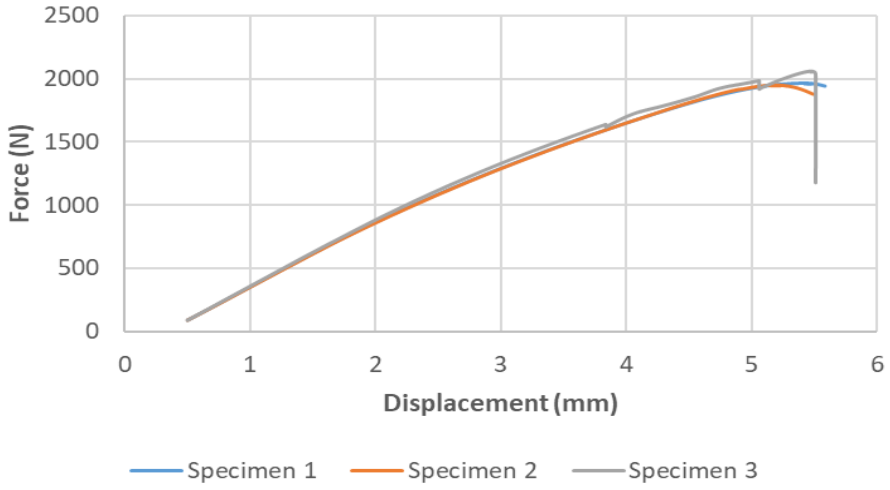

Figure 4.14 - Force-displacement curve during NPC for 0.4mm adhesive thickness at HTD conditions for G_{IIC}

Table 4.5 - 0.4mm nominal thickness Mode II test summary at HTD conditions based on NPC

Specimen	**Adhesive Thickness (mm)**	G_{IIC} **(N/mm) (P5%)**
1	0.30	1.43
2	0.33	1.31
3	0.33	1.83
Mean *(CV)*	**0.32** *(4%)*	**1.52** *(14%)*

A significant decrease in G_{IIC} was observed with increased temperature. The fracture surface shown in Figure 4.15 shows an initial region of cohesive failure before the crack propagated into the composite interface unstably. The unstable propagation is represented by the load drop in the force-displacement graph.

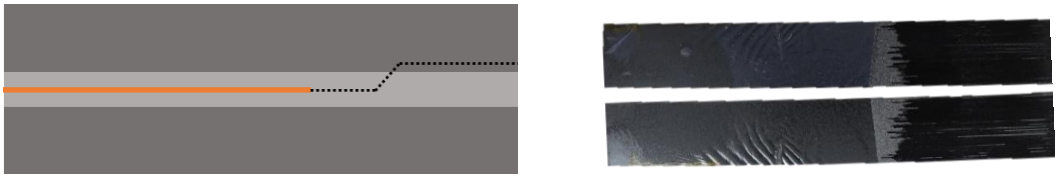

a) Failure Schematic b) Fracture Surface

Figure 4.15 - Failure schematic and fracture surfaces for 0.4mm ENF specimens at HTD conditions

4.3.4 Hot Temperature Wet Case

Following the HTD tests, HTW tests were conducted. Figure 4.16 shows the force-displacement graphs for the NPC loading. The HTW response for the 0.4mm adhesive thickness specimens were similar to the 0.2mm adhesive thickness case. Large non-linearity was observed from the tests and represented in the force-displacement graphs. The crack propagation occurred during the non-linear stage of the loading. The only case where a load drop was observed was due to the composite failure under compression from the rollers (Specimen 4). Table 4.6 summaries the test results.

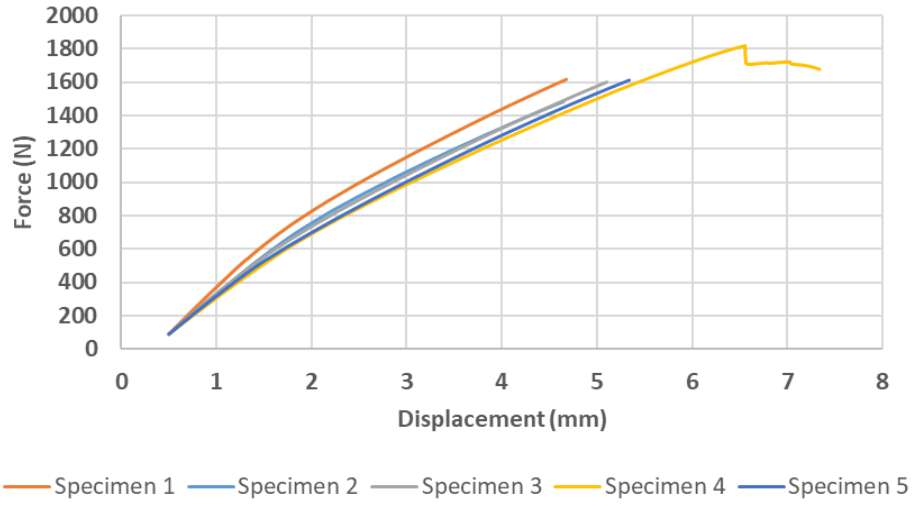

Figure 4.16 - Force-displacement curve during NPC for 0.4mm adhesive thickness at HTW conditions for G_{IIC}

Table 4.6 - 0.4mm nominal thickness Mode II test summary at HTW conditions based on NPC

Specimen	Adhesive Thickness (mm)	G_{IIC} (N/mm) (P5%)	*Wt increase (%)*
1	0.52	0.547	1.25
2	0.41	0.881	1.22
3	0.41	0.637	1.20
4	0.38	0.760	1.27
5	0.51	0.551	1.22
Mean *(CV)*	**0.45** *(13%)*	**0.675** *(19%)*	**1.23** *(2%)*

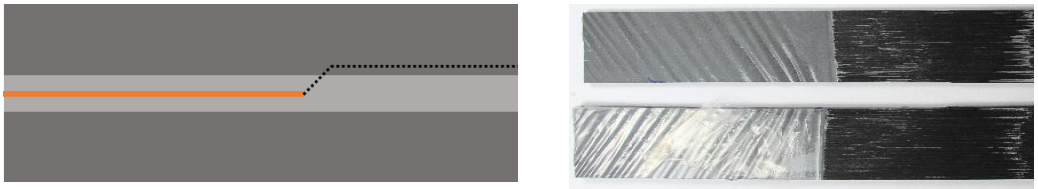

a) Failure Schematic b) Fracture Surface

1. RTD fracture surface and schematic

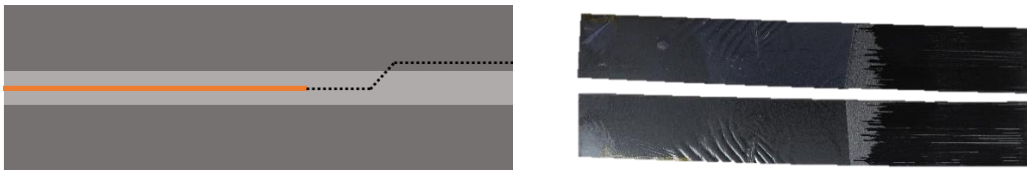

a) Failure Schematic b) Fracture Surface

2. HTD fracture surface and schematic

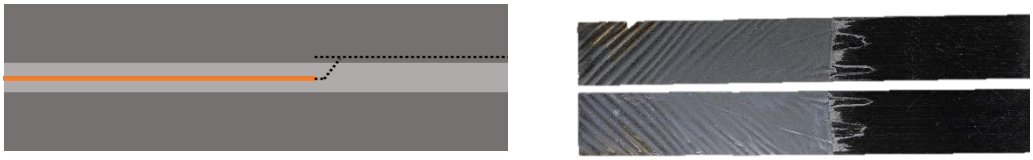

a) Failure Schematic b) Fracture Surface

3. HTW fracture surface and schematic

Figure 4.17 - Comparison of failure schematic and fracture surfaces for 0.4mm adhesive thickness for G_{IIC}

The fracture surface for the RTD, HTD and HTW cases are shown in Figure 4.17. Increasing the temperature and moisture resulted in a greater influence of adhesive on the fracture surface. However, for all cases the final migration path for the crack was into the composite. The fracture surfaces for the 0.2mm adhesive thickness case also had a growing influence of adhesive with temperature and moisture. However, for the 0.2mm adhesive thickness HTW case, there was clear cohesive failure, in which the crack initiated at the adhesive/composite interface and then propagated into the adhesive. For the HTD and HTW cases for the 0.4mm thickness, there was an initial

region of cohesive failure before the crack propagated through the adhesive and into the composite. The difference between the 0.2mm and the thicker adhesive (0.4mm) was that the insert was present in between the adhesive layer for the thicker adhesive, whereas for the 0.2mm adhesive thickness the insert was placed at the adhesive/adherend interface. The decrease in G_{IIC} with increased temperature and moisture for the 0.4mm adhesive thickness was consistent with the trend observed for the 0.2mm adhesive thickness case as shown in Figure 4.18.

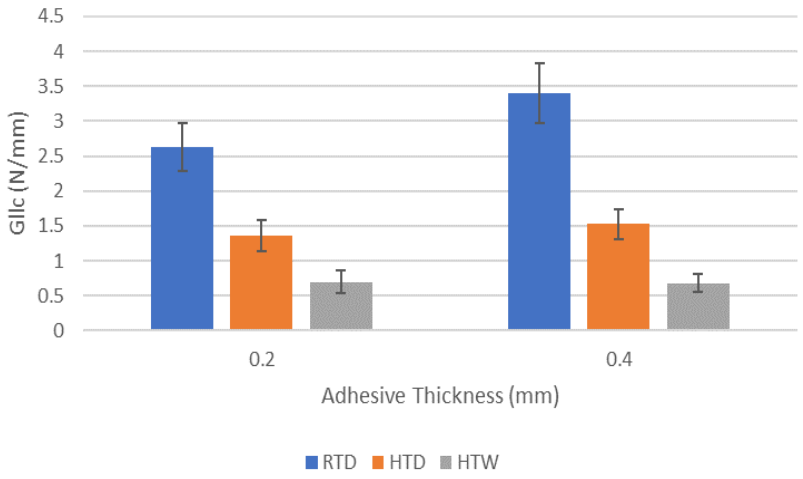

Figure 4.18 - Comparison of G_{IIC} based on P5% NPC for RTD, HTD and HTW for 0.2mm and 0.4mm adhesive thickness

4.4 Mode II Fracture Energy: 0.8mm Nominal Adhesive Thickness

4.4.1 Experimental Configuration

The 0.8mm adhesive thickness was manufactured by placing 2 layers of film adhesive either side of the insert as shown in the schematic in Figure 4.19.

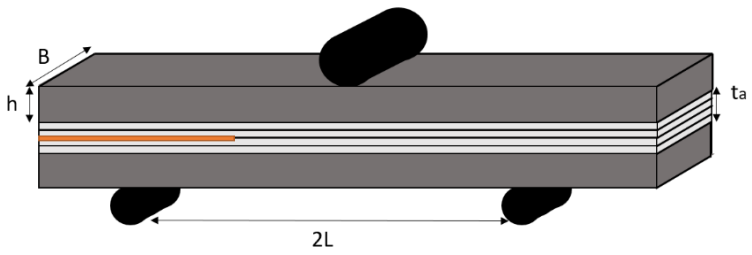

Figure 4.19 - Schematic of 0.8mm nominal adhesive thickness ENF specimen

4.4.2 Room Temperature Dry Case

Figure 4.20 shows the typical load displacement curves for the ENF NPC and PC cases. All NPC tests failed by a large propagation in crack length resulting in a sudden load drop at the maximum load. During the load drop, the crack propagated from the adhesive into the composite unstably. The new crack tip in the composite interface was then marked, and the PC tests were conducted.

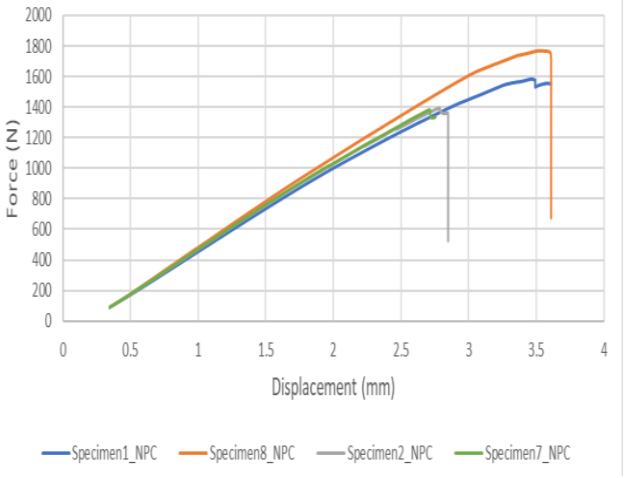

Figure 4.20 - Force-displacement curve during NPC for 0.8mm adhesive thickness at RTD conditions for G_{IIC}

Table 4.7 - 0.8mm nominal thickness Mode II test summary at RTD conditions based on NPC

Specimen	Adhesive Thickness (mm)	G_{IIC} (N/mm) (P5%)
1	0.57	2.25
2	0.67	2.31
7	0.69	2.25
8	0.65	3.16
Mean *(CV)*	**0.68** *(12%)*	**2.49** *(15%)*

Table 4.7 summarises the test results. The G_{IIC} decreased for the 0.8mm adhesive thickness compared to the 0.4mm adhesive thickness for the RTD condition. The type of failure observed was similar to the 0.4mm adhesive thickness case, in which during the NPC tests, the crack propagated from the adhesive into the composite as shown in Figure *4.21*. A larger unstable crack propagation was observed for the 0.8mm adhesive thickness NPC tests.

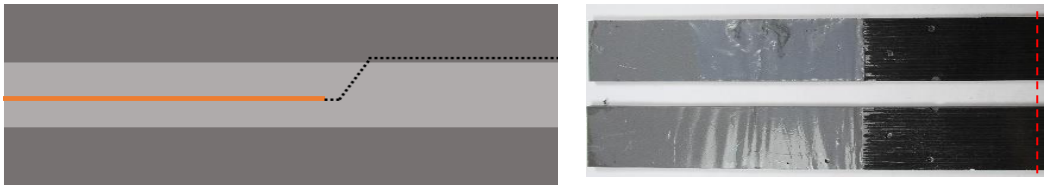

a) Failure Schematic

b) Fracture Surface

Red dotted line: End of NPC test

Figure 4.21 - Failure schematic and fracture surfaces for 0.8mm ENF specimens at RTD conditions

4.4.3 Hot Temperature Dry Case

The force displacement graphs for the HTD NPC case are shown in Figure 4.22. Like the 0.4mm adhesive thickness HTD tests, only the NPC tests were conducted for this configuration, as the crack propagated into the composite interface unstably during the NPC tests. Significant non-linearity was observed in the force-displacement graphs, similar to the other HTD cases tested.

Table 4.8 summarises the test results. The fracture surface in Figure 4.23 shows fragments of adhesive and growing instances of broken fibres, similar to the RTD 0.2mm adhesive thickness case. The fibre bridging effects due to the broken fibres as crack propagation occurred could be why the G_{IIC} increased for the 0.8mm adhesive thickness compared to the other HTD cases.

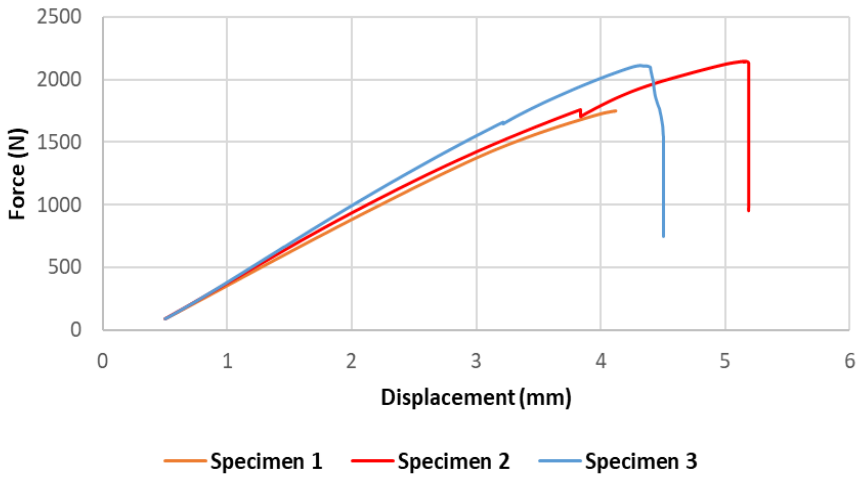

Figure 4.22 - Force-displacement curve during NPC for 0.8mm adhesive thickness at HTD NPC conditions for G_{IIC}

Table 4.8 - 0.8mm nominal thickness Mode II test summary at HTD conditions based on NPC

Specimen	Adhesive Thickness (mm)	G_{IIC} (N/mm) (P5%)
1	0.59	2.85
2	0.81	2.56
3	0.66	2.88
Mean *(CV)*	**0.69** *(13%)*	**2.76** *(5%)*

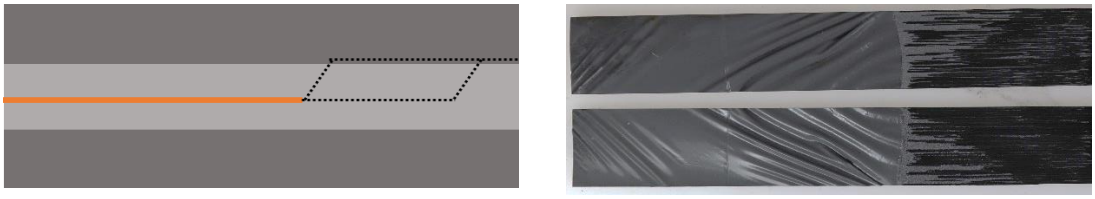

a) Failure Schematic b) Fracture Surface

Figure 4.23 - Failure schematic and fracture surfaces for 0.8mm ENF specimens at HTD conditions

4.4.4 Hot Temperature Wet Case

The HTW force-displacement graph is shown in Figure 4.24 for the NPC case. Similar to the 0.2mm and 0.4mm adhesive thickness cases, the HTW force-displacement graph shows large non-linearity and no load drop to indicate crack propagation.

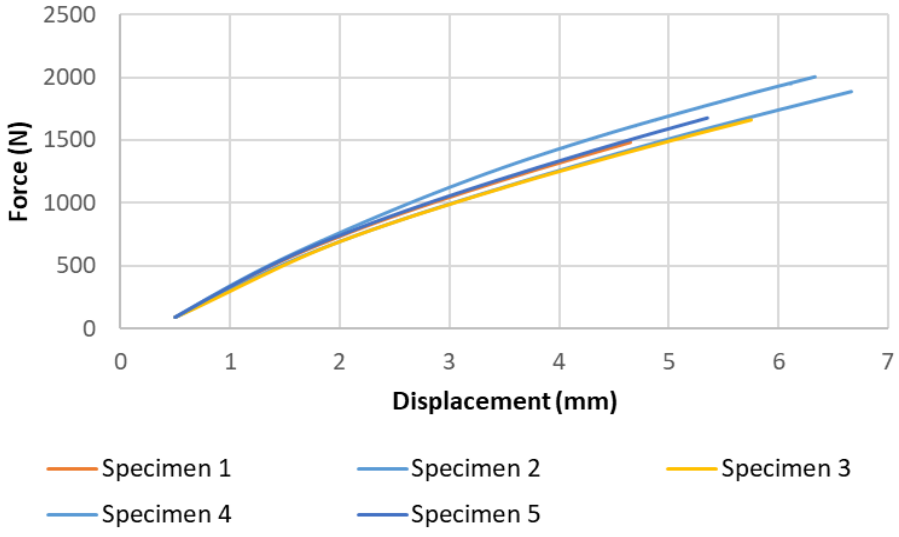

Figure 4.24 - Force-displacement curve during NPC for 0.8mm adhesive thickness at HTW NPC conditions for G_{IIC}

Table 4.9 summarises the test results. The fracture surface in Figure 4.25 shows the composite interface visible at both surfaces. Hence, during the non-linear stage of the force-displacement curve, the crack propagated into the composite directly from the insert, which was placed in between the adhesive. For the 0.4mm and 0.8mm adhesive thickness, where the insert was present in between the adhesive, the crack propagated unstably during the NPC tests for the RTD and HTD cases and was represented by a load drop. For the HTW cases, when the crack propagated into the composite interface, it was a gradual process, which occurred during the non-linear stage of the force-displacement curve. There was no initial region of cohesive failure visible for the 0.8mm adhesive thickness HTW case, unlike all the HTD and HTW cases.

Table 4.9 - 0.8mm nominal thickness Mode II test summary at HTW conditions based on NPC

Specimen	**Adhesive Thickness (mm)**	**G_{IIC} (N/mm) (P5%)**	***wt%***
1	1.01	0.665	1.38
2	0.97	0.848	1.35
3	0.83	1.056	1.30
4	1.07	0.757	1.44
5	1.02	0.697	1.42
Mean *(CV)*	**0.98** *(8%)*	**0.804** *(17%)*	**1.38** *(4.0%)*

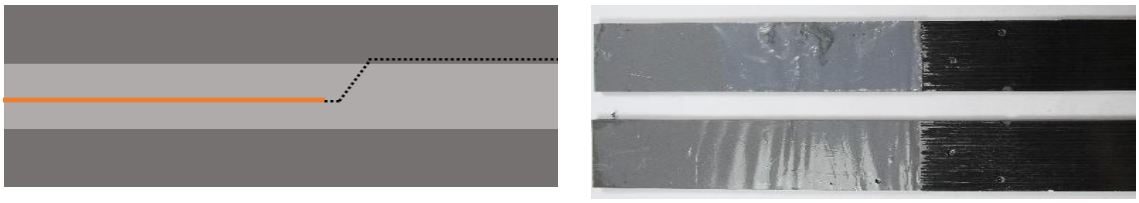

a) Failure Schematic b) Fracture Surface

1. RTD fracture surface and schematic

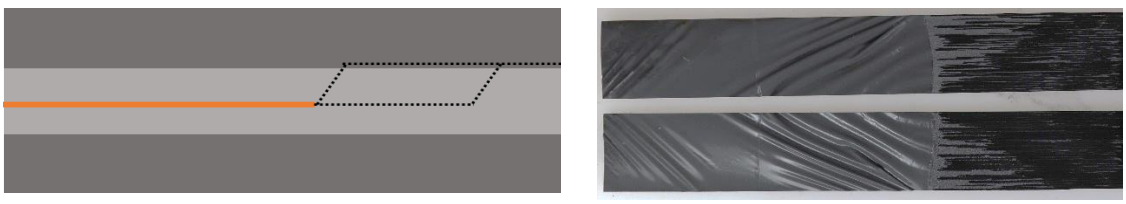

a) Failure Schematic b) Fracture Surface

2. HTD fracture surface and schematic

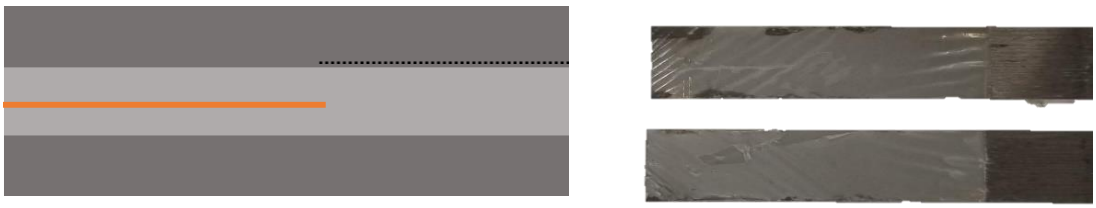

a) Failure Schematic b) Fracture Surface

3. HTW fracture surface and schematic

Figure 4.25 - Comparison of failure schematic and fracture surfaces for 0.8mm adhesive thickness for G_{IIC}

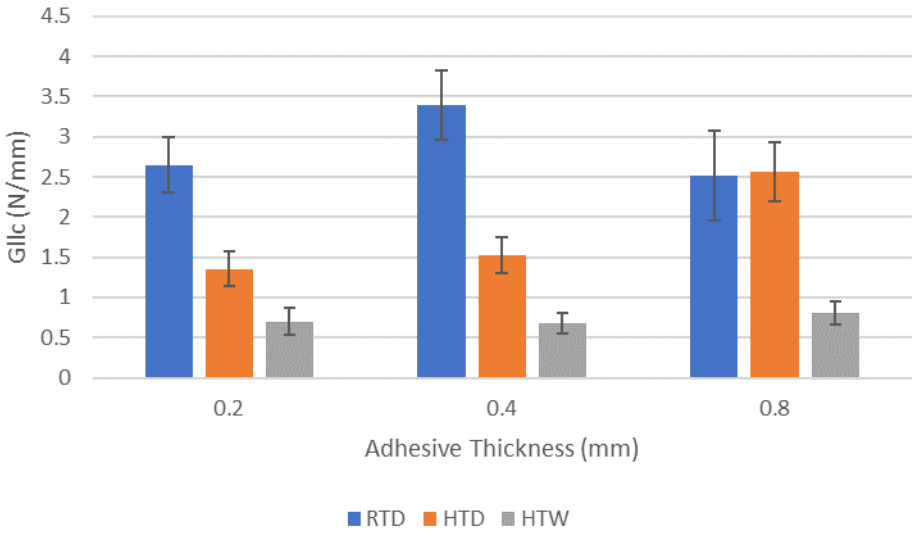

Figure 4.26 - Comparison of G_{IIC} based on P5% NPC for RTD, HTD and HTW for 0.2mm, 0.4mm and 0.8mm adhesive thickness

Figure 4.26 compares the G_{IIC} for all adhesive thicknesses. For the 0.8mm case, there was no significant difference in the RTD and HTD cases, but a sharp drop in G_{IIC} for the HTW case.

4.5 Effects of Insert Film Placement on G_{IIC}

A qualitative study was conducted to understand the effects of the position of the insert film at the adhesive/adherend interface for ENF loading at RTD conditions. The nominal adhesive thickness used for these tests was 0.8mm. All other dimensions were similar to the previous ENF tests. The schematic for the two configurations is shown in Figure 4.27. Two specimens from each configuration were tested and the failure

mechanism from the insert film for each configuration is shown in Figure 4.28. All samples failure unstably. As discussed in Chapter 3 (Section 3.7), the surface preparation of grit-blasting induced microscopic regions of broken fibres on the composite 0° surface prior to the secondary bonding process.

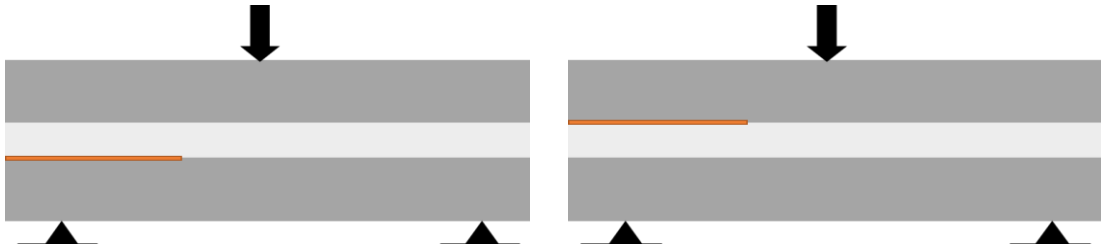

a) Configuration A: insert film placed on the lower adherend/adhesive interface

b) Configuration B: insert film placed on the lower adherend/adhesive interface

Figure 4.27 - Schematic of different insert film placement specimens

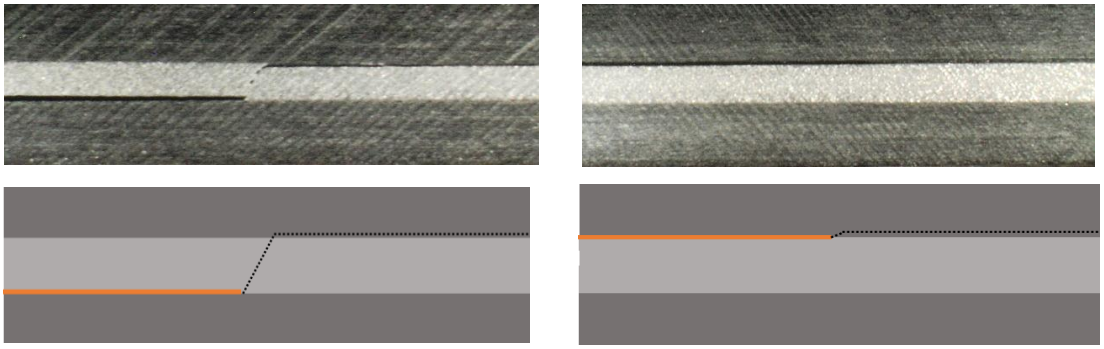

a) Configuration A

b) Configuration B

Figure 4.28 - Crack propagation for different configurations

For configuration A, where the insert film was placed on the lower adherend/adhesive interface the G_{IIC} value was 2.7 N/mm (12%). For configuration B, the G_{IIC} value was 1.2 N/mm (13%). Although only two specimens for each batch were tested, the tests showed that the placement of the insert film can have a significant effect on the G_{IIC} and failure mode for the ENF case. Depending on the direction of the applied bending, tensile cracks initiate at 45° from the insert film due to the shear. For configuration A, when the insert film was placed at the lower adherend/adhesive interface, the path for crack propagation due to the shear, i.e. tensile stresses at 45°, resulted in propagation

through the adhesive and a high G_{IIC}. The final crack propagation path was through the upper adhered surface 0° ply. When the insert film was placed at the upper adhered/adhesive interface the direction of the maximum principal stresses due to shear caused crack propagation within the adherend, through the broken fibres present from grit blasting. Hence, at RTD the shear crack propagation was controlled by the tensile stresses at 45°.

4.6 Mode II Fracture Energy: IM7/8552

4.6.1 Hot Temperature Dry Case

The G_{IIC} for IM7/8552 was characterised at HTD conditions. The tests were conducted at 80°C, consistent with the HTD tests for the adhesive. The insert film was placed within the mid-plane of the composite during the lay-up process. Figure 4.29 shows the ENF composite configuration used for testing. The specimen configuration was similar to the previous ENF tests, in which B was 20mm, specimen half-thickness, h was 2mm and the support length, *L* was 50mm. The insert length was 65mm and the layup for a half specimen was $[0]_{16}$.

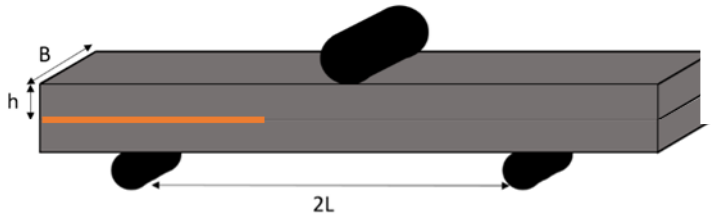

Figure 4.29 - Schematic of Composite ENF specimen

The force-displacement graphs are shown in Figure 4.30. During the fracture tests, once the maximum load was reached unstable crack propagation (>10mm) was observed, which was represented by the load drop. Due to the large crack propagation the PC tests were not possible and hence only the NPC values are reported. Only the G_{IIC} based on the P_{max} was reported as the force did not vary from linearity before the load drop. The test results are summarised in Table 4.10.

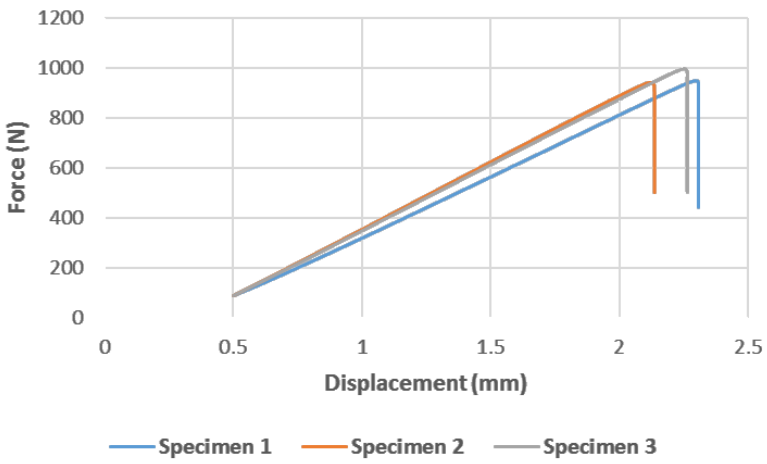

Figure 4.30 - Force-displacement curve for HTD IM7/8552 (NPC)

Table 4.10 - IM7/8552 Mode II test summary at HTD condition

Specimen	**G_{IIC} (N/mm) (Pmax) - NPC**
1	0.902
2	0.877
3	1.040
Mean *(CV)*	**0.940** *(8%)*

4.6.2 Hot Temperature Wet Case

The G_{IIC} at HTW for IM7/8552 was also characterised. The specimen configuration was same as the HTD composite case. Figure 4.31 shows the force-displacement graphs. Like the HTD case, a load drop was observed resulting in unstable crack propagation of greater than 10mm. Hence only the NPC tests were conducted for the HTW tests. Also, only the P_{max} values were reported as the force varied by less than 5% from the initial region of linearity before the load drop.

Table *4.11* summarises the experimental results, including the wt% increase due to moisture for each specimen tested.

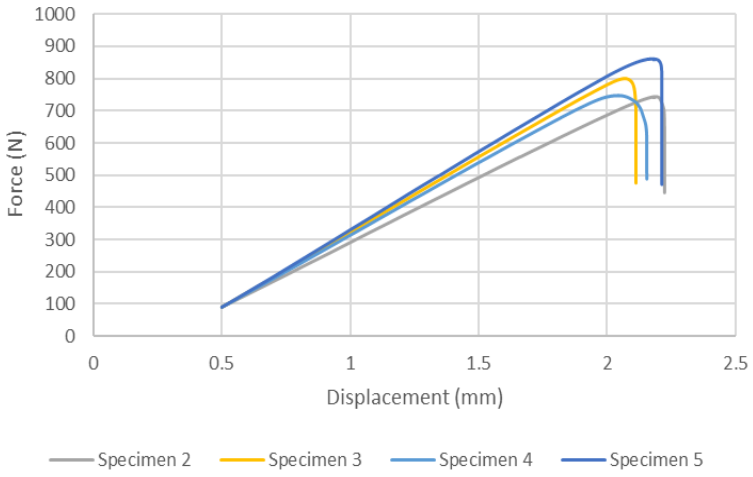

Figure 4.31 - Force-displacement curve for HTW IM7/8552 (NPC)

Table 4.11 - IM7/8552 Mode II test summary at HTW condition

Specimen	**G_{IIC} (N/mm) (Pmax) - NPC**	***wt%***
1	0.753	0.98
2	0.882	0.98
3	0.764	0.97
4	0.713	0.98
Mean *(CV)*	**0.778** *(8%)*	**0.98** *(0.5%)*

From Figure 4.32 the G_{IIC} decreases with increasing temperature and moisture for IM7/8552. The RTD value was obtained from literature [92]. The trend observed was similar to the adhesive under increasing temperature and moisture, although the magnitude of the effect was reduced.

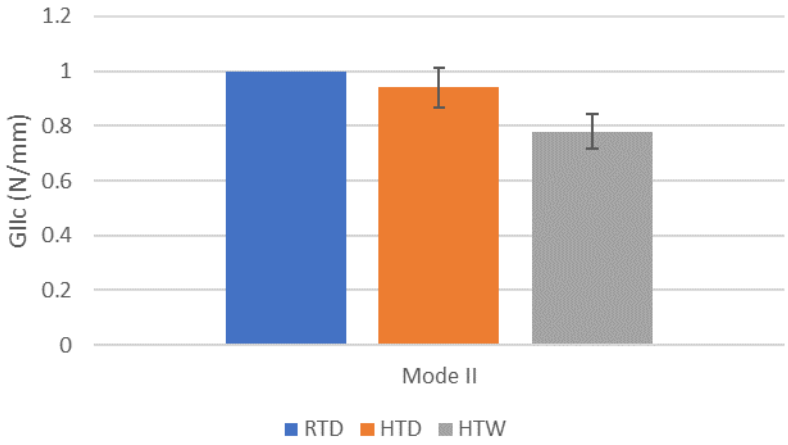

Figure 4.32 - Comparison of G_{IIC} (NPC) based of Pmax for RTD, HTD and HTW for IM7/8552

4.7 Discussion of Environmental and Adhesive Thickness Effects on Mode II Fracture Toughness

4.7.1 Overall Effects

Figure 4.33 compares the effects of adhesive thickness and environmental conditions on the G_{IIC}. The data points in solid indicate cohesive failure, dashed lines indicate initial cohesive failure followed by delamination and empty blocks indicate delamination within the composite. There was a drop in toughness from RTD to HTW conditions for all thicknesses. The factors affecting the fracture energy are the stress at which the material yields, the strain and the size of the plastic zone. The reduction in shear yield stress is likely to be the predominant factor explaining these trends.

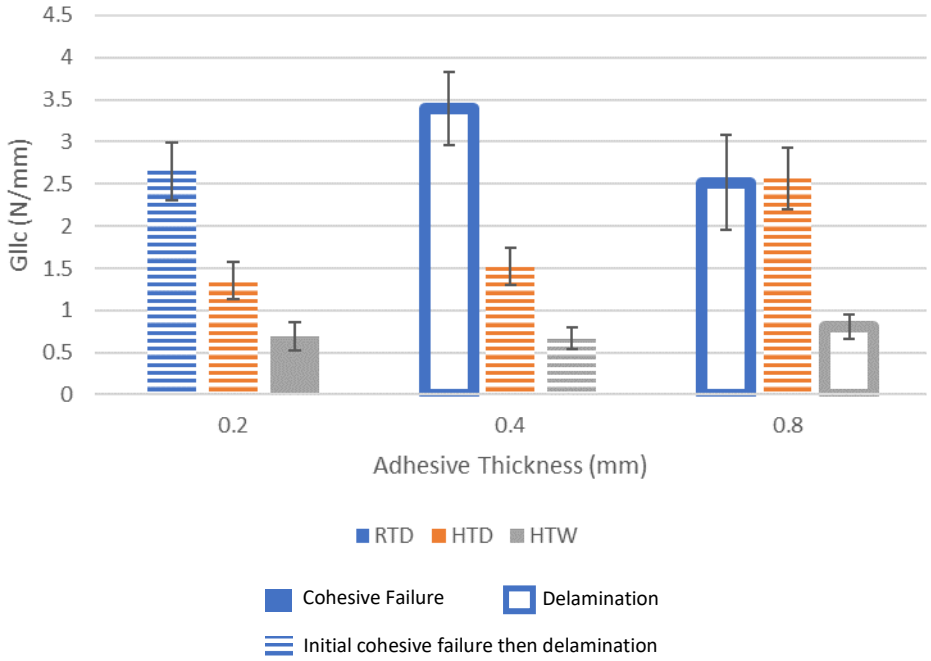

Figure 4.33 – G_{IIC} (NPC-P5%) vs adhesive thickness from RTD, HTD and HTW

For the RTD cases, the G_{IIC} increased initially between 0.2mm and 0.4mm adhesive thickness. The peak G_{IIC} occurred at 0.4mm adhesive thickness and then decreased for the 0.8mm adhesive thickness. This could be due to the constraint effects [21], [94] from the adherend, which was present and influenced the plastic zone size of the adhesive as reported in different cases form the literature. The size of the plastic zone for the adhesive may be different for the bulk material and when constrained in a joint. Initially, increasing the adhesive thickness increased the plastic zone. At 0.4mm adhesive thickness, the constraint effect influenced the plastic zone size, increasing

G_{IIC}. When the adhesive thickness was further increased the constraint effect was lost, and the plastic zone was smaller.

The HTD case shows the G_{IIC} was similar for both 0.2mm and 0.4mm adhesive thickness and increased for 0.8mm adhesive thickness. The plastic zone increased with temperature. For the 0.2mm and 0.4mm adhesive thickness cases, as the G_{IIC} were similar it can be assumed the constraint effects were present for both these cases. The G_{IIC} then increased for the 0.8mm adhesive thickness case at HTD. The fracture surface for this case (Figure 4.32) shows the insert film was wrinkled for the 0.8mm HTD batch, which resulted in increased friction due to the sliding constraint under ENF loading, which resulted in a 82% increase in G_{IIC}. This is discussed in Section 4.7.2. This could be why the G_{IIC} increased for the 0.8mm adhesive thickness at HTD. All HTW G_{IIC} values were similar and were not significantly different from the composite G_{IIC} at HTW.

Figure 4.34 summarises the different crack propagation paths observed for the 0.2mm adhesive thickness ENF cases at different environmental conditions. The crack initiation occurred at an angle from the insert film at the adhesive/composite interface. For all 0.2mm cases, the ENF specimens were loaded such that the insert film was placed on the lower composite interface, so that crack propagation would occur in the direction into the adhesive as found in Section 4.5. At RTD and HTD, multiple crack propagation paths are shown in the schematic. This represents the stable crack migration from the adhesive into the composites at multiple paths during the ENF test, as observed from the fracture surfaces of the specimens. It was found from Chapter 3 (Section 3.7) that from the grit blasted surface treatment, microscopic regions of broken fibres were present on the composite surface ply. This region effectively provided a potential path for crack propagation. The schematics for the 0.2mm adhesive thickness cases show that at RTD and HTD, the crack migrated from the adhesive into the composite, as the composite was the least tough path for propagation. The broken fibres on the composite surface plies facilitated the crack migration. At HTW, a stable cohesive failure was observed and shown in the schematics. As there was no significant difference in the composite and adhesive G_{IIC} at HTW, migration into the composite from the adhesive did not occur.

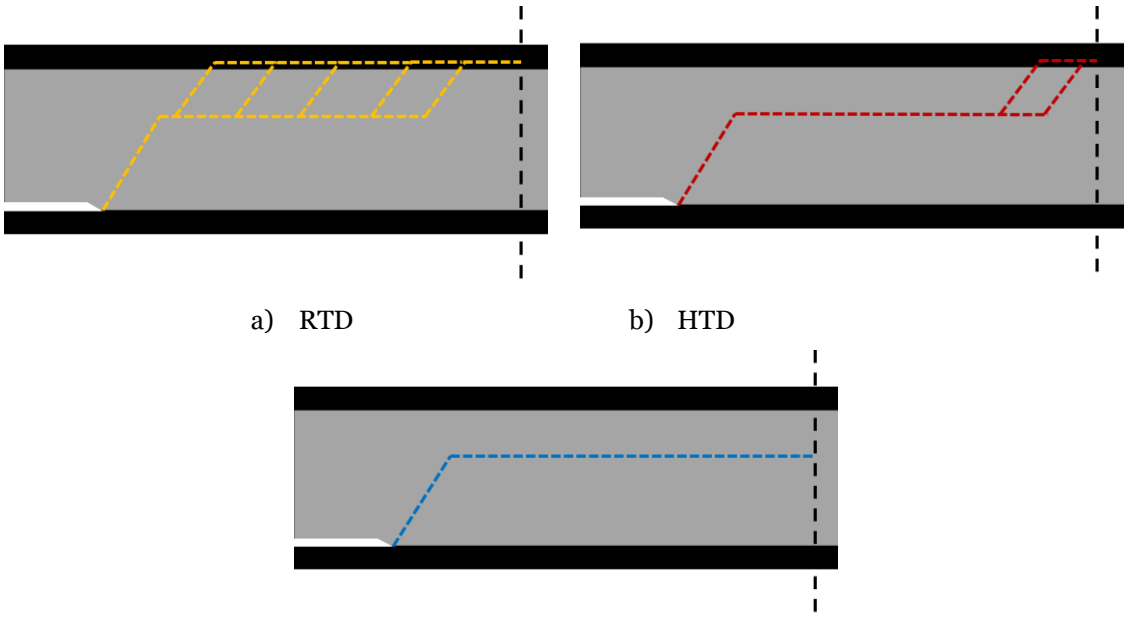

a) RTD b) HTD

c) HTW

Figure 4.34 - Crack propagation paths for 0.2mmm adhesive thickness

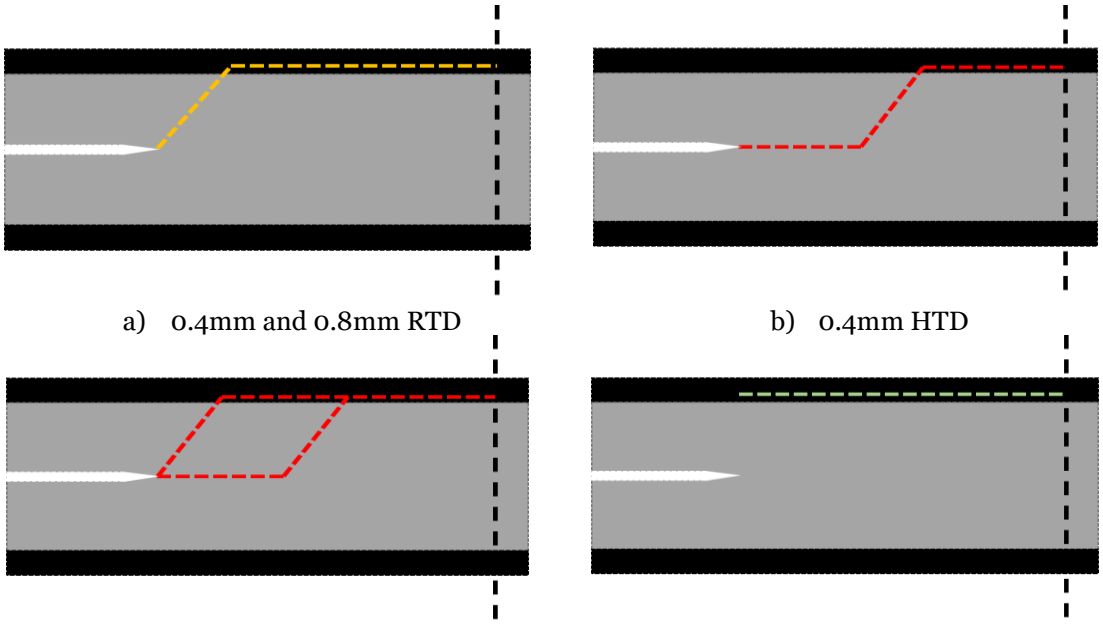

a) 0.4mm and 0.8mm RTD b) 0.4mm HTD

c) 0.8mm HTD (fibre bridging) d) 0.4mm and 0.8mm HTW

Figure 4.35 - ENF Crack propagation for thicker adhesives at different conditions

The schematics of the crack propagation for the thicker adhesives is summarised in Figure 4.35. From the fracture schematics, three different crack paths were observed. One, at an angle from the insert into the composite surface ply, two, on the maximum shear stress plane (i.e. mid-line of ENF sample) and three, crack initiating away from the insert film at the composite surface ply. For all RTD cases and the 0.8mm HTD

case, the crack initiated at an angle from the insert film. These cases had a high G_{IIC} and the fracture schematics show crack migration from the adhesive to composite interface, at 45° angle, corresponding to the maximum tensile stresses. For the HTD 0.4mm adhesive thickness case, an initial stable cohesive failure within the adhesive was observed. This case had a lower G_{IIC} compared to the RTD and the 0.8mm HTD cases. For this case, stable initial propagation occurred within the adhesive at the ENF specimen mid-plane, followed by migration into the composite.

For the thicker HTW cases, crack propagation within the adherend was observed away from the insert film as shown in Figure 4.36. At these conditions, the plastic zone under Mode II loading increased significantly compared to RTD and HTD conditions due to plasticisation of the adhesive and increased thickness. As the plastic zone interacted with the composite adherends, it was possible that the initial propagation during the NPC tests initiated at the broken fibres in composite, away from the insert film.

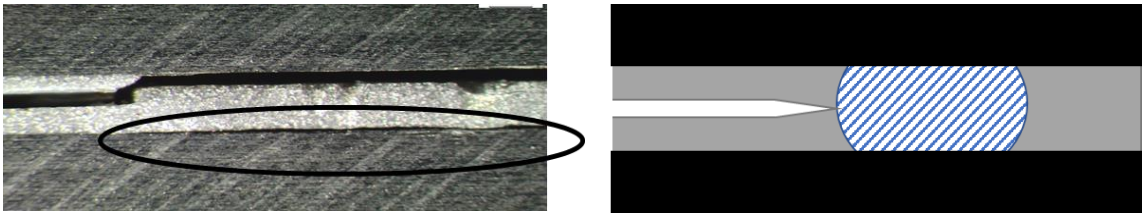

a) Microscopy of failed specimen b) Schematic of plastic zone

Figure 4.36 -Thicker adhesive ENF specimen at HTW

4.7.2 Effects of PTFE film Wrinkles for Thicker Adhesive Cases

During the manufacturing process for the ENF specimens, PTFE film inserts were used to represent an initial crack. The lower viscosity of the adhesives at higher temperatures allowed the PTFE film insert to move during curing. This resulted in the wrinkles observed within the adhesive layer, between the two crack interfaces, as represented by the schematic in Figure 4.37 (HTD case). These wrinkles were only present for the thicker adhesive cases.

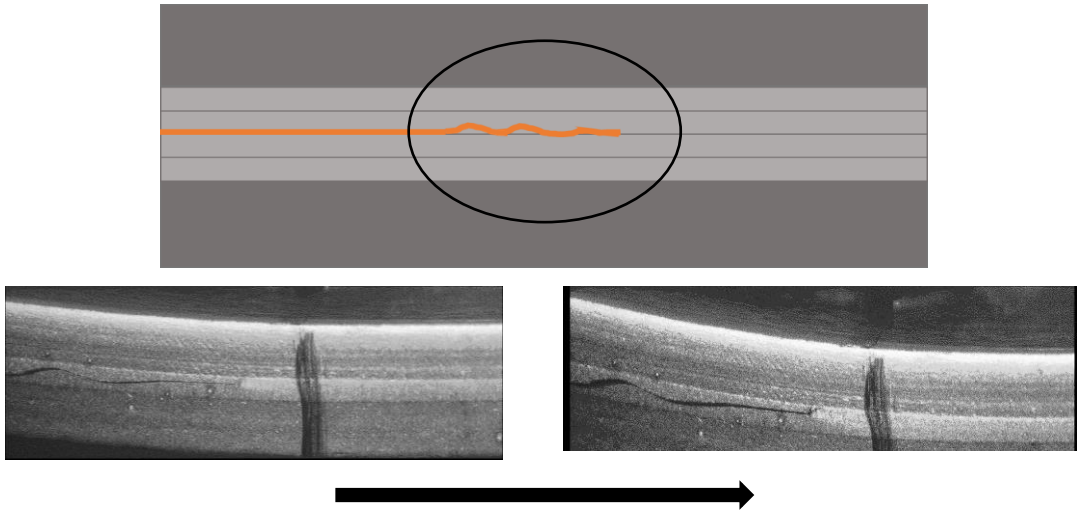

Figure 4.37 - Effects of PTFE film wrinkles on mode II loading

The wrinkles increased the friction between the two layers during the fracture tests due to the sliding constraint introduced and could also cause additional plastic deformation. It is possible that unstable crack propagation was due to build up during loading and the sudden release in energy due to the release of this constraint, which resulted in an 82% increase in G_{IIC}.

4.8 Shear Strength of Adhesive

4.8.1 Experimental Configuration

The adhesive shear characteristic for different thicknesses was studied by conducting shear tests for 3 nominal adhesive thicknesses of 0.2mm, 0.4mm and 0.8mm. The shear test schematic is shown in Figure 4.38. A similar test configuration was used by Jeenjtkaew [93]. The shear samples were connected to a test fixture through loading pins and placed vertically and loaded under tension. The tensile strength of the adhesive was characterised at RTD, HTD and HTW conditions in Chapter 3 (Section 3.9). The shear tests were conducted at RTD and HTW conditions. Tests were not conducted at HTD due to the extensive test program and time schedule.

Mild steel adherends were used for the RTD case to bond the film adhesive because their high stiffness can reduce the peel stresses at the end of the overlap. For HTW tests stainless steel was used due to the rusting of the mild steel when placed in the conditioning chamber. Imetrum optical based video extensometer systems were used

for displacement and strain measurements. These video gauges were used to measure the average shear strains during testing. This was done by tracking the relative vertical rigid body motion between the steel adherends during testing. The lateral motion of the steel adherends was very small.

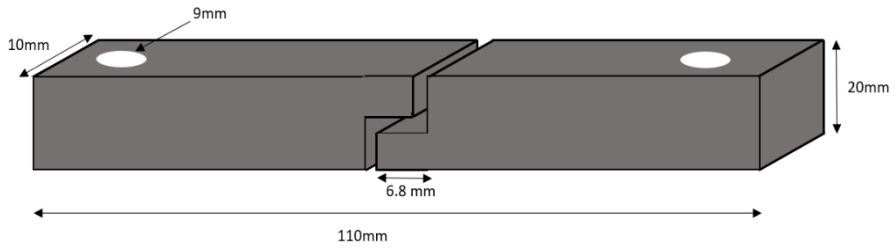

Figure 4.38 - Schematic of the shear test specimen

4.8.2 Room Temperature Dry Case

Table 4.12 provides a summary of the results for the shear tests at different adhesive thicknesses. Figure 4.39 shows the typical failure surface. A cohesive failure was observed for the adhesive shear tests. Although the 0.2 mm case gave a higher mean value, there was considerable scatter in the results and the difference in the shear strength of the adhesive with increasing thickness was not statistically significant. The scatter could be due to the variable actual adhesive thickness for each nominal thickness.

Table 4.12 - Adhesive shear test summary under RTD conditions

	0.2mm	**0.4mm**	**0.8mm**
Mean (MPa) (C.V. %)	51.2 (9.0%)	43.4 (11%)	44.0 (7.7%)
Number of Samples	10	6	10

Figure 4.39 - Cohesive failure for shear test at RTD using mild steel adherends

4.8.3 Hot Temperature Wet Case

Shear strength tests at HTW were conducted to understand the effects of temperature and moisture on the adhesive. The specimens were conditioned at 80°C and 85% RH and tested at 80°C. From the literature [95] it was found that interfacial failure is a common failure mode for conditioned metallic bonded joints due to the weakening of the interface properties because of moisture absorption. To try to avoid interfacial failure, shear samples were manufactured using acid etch surface treatment based on the literature [96]. Acid etching is an active surface treatment which modifies the boundary layer of the surface to be stronger, more stable and resistant to environmental attacks [93]. A 10% solution of nitric acid was mixed with 90% solution of ethanol and the specimen were soaked for 15 minutes and then bonded. To avoid rusting of the specimen, stainless steel was used.

Although these extra precautions were taken to avoid interfacial failure, all HTW shear samples did in fact fail at the interface. Figure 4.40 shows a typical failure surface for the shear test samples. The properties therefore are not representative of the adhesive at HTW conditions and reflect rather the interfacial strength. Table 4.13 summarises the test results for the different adhesive thickness' at HTW. Figure 4.41 compares the shear strength at RTD and HTW.

Figure 4.40 - Interfacial failure for shear test at HTW using stainless steel adherends

Table 4.13 - Adhesive shear test summary under HTW conditions

	0.2mm	0.4mm	0.8mm
Mean (MPa) (C.V. %)	11.39 (23%)	12.07 (14%)	8.93 (23%)
Number of Samples	5	5	5

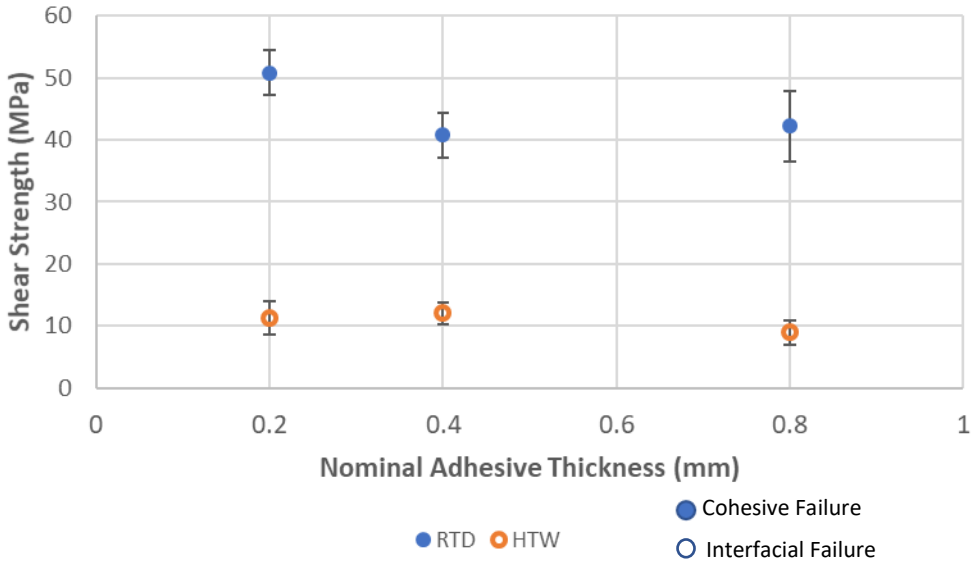

Figure 4.41 - Summary of shear strength vs adhesive thickness at RTD and HTW conditions

4.9 Conclusions

The effects of the increasing adhesive thickness, temperature and moisture on G_{IIC} were measured from adhesively bonded composite joints. For RTD, G_{IIC} initially increased and then decreased. The peak G_{IIC} occurred at an intermediate thickness (0.4mm). Increasing the adhesive thickness increased G_{IIC} at HTD, whereas at HTW all G_{IIC} values were similar as different failure modes were observed for these conditions. Analysing the fracture surfaces for the thicker HTW specimens, it was found that crack initiation occurred away from the insert film crack tip and at the composite surface 0° ply. The experimental results showed that the G_{IIC} decreased with increasing moisture and temperature for all adhesives thicknesses. This trend was also observed when measuring the composite G_{IIC} at increased temperature and moisture content. The reduction in shear yield stress is likely to be the predominant factor explaining these trends.

The shear strength of Redux 319 was measured at RTD and HTW conditions. There was no significant difference in the RTD shear strength with increasing adhesive thickness. Although additional surface treatment was applied on the HTW stainless steel adherends, an interfacial failure was observed during the test.

CHAPTER 5

EFFECTS OF ENVIRONMENTAL CONDITIONS ON PRISTINE DOUBLE LAP JOINT STRENGTH: EXPERIMENTAL RESULTS

5.1 Introduction

Following the characterisation of mechanical properties of both adhesive and composite, Double Lap Joints (DLJ) are tested at different environmental and geometrical conditions to understand the effects of temperature and moisture on the DLJ strength. This chapter describes the manufacturing, specimen and testing configuration for the DLJ at different environmental conditions. The experimental results are presented, looking into the effects of overlap length and composite inner adherend (adherend) thickness at Room Temperature Dry (RTD), Hot Temperature Dry (HTD) and Hot Temperature Wet (HTW) conditions. The effects of increasing adhesive thickness on the DLJ strength are studied at RTD and HTW conditions. Further tests looking into the effects of adhesive fillets and surface ply orientation at RTD are also conducted. Two types of failure modes are observed during the pristine DLJ tests and explained in this chapter.

Following the experimental results, simple analytical failure criteria are used to understand what controls the failure for each pristine DLJ case in Chapter 6. The introduction to the numerical model and initial sensitivity analysis on the material parameters are also conducted in Chapter 6. After an understanding and criteria to

distinguish the failure modes have been established, Chapter 7 discusses all the results and trends observed, followed by analysis to see whether the numerical models can accurately predict the failure for the DLJ at different conditions.

5.2 Manufacturing and Specimen Configuration

Figure 5.1 shows the typical DLJ specimen configuration. The material for the composite adherends used was the IM7/8552 carbon/epoxy prepreg with a nominal thickness of 0.125mm. The adhesive used was the Hexcel Redux 319 film adhesive with a nominal thickness of 0.2mm and no carrier. The specimen width was held constant at 25mm for all DLJ tests. The baseline stacking sequence was quasi-isotropic (QI), $[0/45/90/-45]_{ns}$ (ns means multiple layers of repeated stacking sequence symmetric about the midplane) with surface 0° plies with the intention to stop delamination migration into the composite. This was based on the initial focus to investigate the failure of the adhesive. However, it was found that delamination occurred within the surface 0° ply at the inner adherend and controlled the failure for several configurations. Adhesive fillets were not deliberately introduced but were formed during manufacturing and the precise geometry was variable. The expectation was that the numerical models would give a conservative prediction without considering the adhesive fillet. As described in Chapter 3 (Section 3.7) the grit blasted surface treatment introduced microscopic regions of broken fibres on the surface 0° ply, providing a path for delamination.

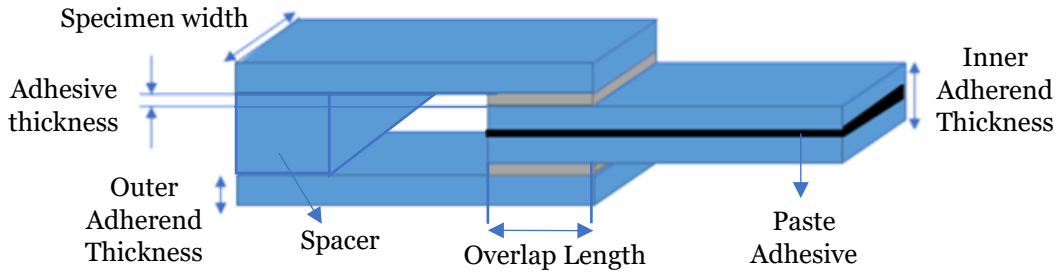

Figure 5.1 - Schematic of the double lap joint

The HTD tests were tested at 80°C. The HTW samples were conditioned for 4 months at 80°C and 85% RH and also tested at 80°C, consistent with the characterisation tests. For all HTW samples, the wt% increases due to moisture absorption were recorded before test. At least three specimens of each configuration were tested. The RTD tests were conducted using a hydraulic-driven test machine, while the HTD and HTW tests were conducted using a screw-driven test machine in a universal thermal chamber. Tensile testing of the double lap joints was conducted under displacement control at a loading rate of 0.5mm/min.

5.2.1 Double Lap Joints Manufacturing

Secondary bonding was used to manufacture the DLJ. The layup of the IM7/8552 laminates was done first. The curing cycle for the laminates was in two stages. The autoclave was heated up to 125˚C at a ramp-up rate of 2˚C/min and held at this temperature for 100 minutes, followed by a ramp to 185˚C at 2˚C/min and held for 165 minutes. The pressure was increased at 69kPa per minute to 690kPa, which was kept throughout the cycle. The adhesive was bonded using a secondary bonding technique. To achieve optimal bonding properties, surface treatment methods were used. A macroscopically rough surface was obtained by grit blasting, until the fibres were visible. The size of the grit used was 1.8µm. Care was taken to ensure no debris were left after grit blasting by concentrated high pressure air and cleaning with a micro-fibre towel, as it can have a critical effect on the bond strength. Liquid degreasing with acetone was subsequently used to remove oils and other potential organic contaminants from the surfaces immediately prior to bonding. Analysing the Scanning Electron Microscope (SEM) images of the grit blasted surface showed broken fibres at a microscopic scale on the composite surface, prior to bonding. This was discussed in Chapter 3, Section 3.7.

After the surface treatment of the QI laminates, they were bonded with the film adhesive in the configuration shown in Figure 5.2. The schematic shows two half joints bonded with the film adhesive. Spacers made of the same material were used to ensure constant adhesive thickness was achieved throughout the joint and minimum leakage of adhesive during the curing process, and to allow flat tooling. The spacers were not pre-cured and were bonded with a layer of adhesive and separated by the release film, which is highlighted in red in Figure 5.2. The release film ensured that after the curing process, the spacers could be separated from the adherends. The adhesive was cured

at 175˚C for 1 hour at 690kPa. The ramp-up rate specified in the data sheet was 5˚C/min. Gaps can arise due to dimensional tolerances in the composite cutting process. During the curing process, the adhesive can flow away from the bond-line if there are gaps between the laminates and spacers as highlighted in Figure 5.2. The fillet formation was not controlled for the DLJ cases and the fillet sizes were variable.

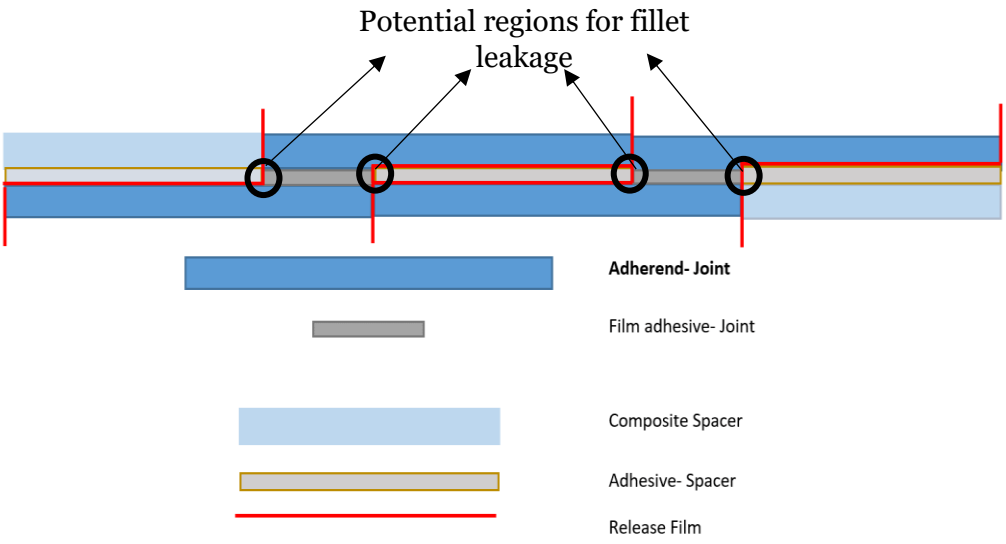

Figure 5.2 - Schematic of the bonding configuration

After the secondary bonding process was completed, Huntsman Araldite® 2014-1 paste adhesive was used to bond the two symmetrical half joints obtained, as shown in Figure 5.1, where the black block represents the paste adhesive. The curing cycle used for the paste adhesive was 80˚C for 1 hour with use of gentle clamping at the standard atmospheric pressure. The HTD test temperature was also at 80˚C, but failure was not expected at the region where the paste adhesive was applied.

5.3 Experimental Results

5.3.1 Introduction

All experimental results for the pristine DLJ are summarised in this section. Tests looking into the overlap effects at different environmental conditions for both 2mm and 4mm inner adherend thickness are shown in Table 5.1. Due to the extensive test program and time constraints only the 36mm overlap length was tested for the 2mm

inner adherend at HTD. The effects of increasing adhesive thickness on the DLJ strength were also studied at RTD and HTW conditions. The results are discussed in Chapter 7. The DLJ strength is defined as the experimental failure load per unit width.

Table 5.1 - DLJ tests comparing environmental effects

	2mm Inner Adherend			4mm Inner Adherend	
Overlap Length	**12mm**	**24mm**	**36mm**	**12mm**	**36mm**
RTD	✓	✓	✓	✓	✓
HTD			✓	✓	✓
HTW	✓	✓	✓	✓	✓

5.3.2 Room Temperature Dry

At RTD, the effects of increasing overlap length, inner adherend thickness and adhesive thickness on the DLJ strength were studied. Additional tests looking into the adhesive fillet and surface ply orientation were also conducted.

Table 5.2 presents the effects of increasing overlap length on DLJ strength for the 2mm inner adherend case, showing no significant difference in strength. For the 24mm overlap length case, the effects of increasing adhesive thickness on the DLJ strength is shown in Table 5.3. The results show that although the 0.8mm adhesive thickness had a higher strength, it was not statistically significant due to the high scatter in results. Increasing the overlap length for the 4mm inner adherend case increased the DLJ strength as shown in Table 5.4. Table 5.5 shows that increasing the adhesive thickness for the 36mm overlap length case did not have a significant effect on the DLJ strength. Comparing the 2mm and 4mm inner adherend cases show that increasing adherend thickness increased the DLJ strength.

Table 5.2 - Overlap length effects at RTD for 2mm inner adherend case

Inner Adherend Thickness (mm)	Lap Length (mm)	Nominal Adhesive Thickness (mm)	Failure load/unit width (N/mm) (C.V%)	Shear Stress (MPa) (C.V. %)	Number of Specimens
2	12	0.2	691 (13%)	27.32 (11%)	4
2	24	0.2	651 (7%)	13.16 (8%)	4
2	36	0.2	713 (7%)	9.90 (7%)	3

Table 5.3 – Adhesive thickness effects at RTD for 2mm inner adherend case

Inner Adherend Thickness (mm)	Lap Length (mm)	Nominal Adhesive Thickness (mm)	Failure load/unit width (N/mm) (C.V%)	Shear Stress (MPa) (C.V. %)	Number of Specimens
2	24	0.2	651 (7%)	13.16 (8%)	4
2	24	0.8	761 (18%)	15.88 (20%)	5

Table 5.4 - Overlap length effects at RTD for 4mm inner adherend case

Inner Adherend Thickness (mm)	Lap Length (mm)	Nominal Adhesive Thickness (mm)	Failure load/unit width (N/mm) (C.V%)	Shear Stress (MPa) (C.V. %)	Number of Specimens
4	12	0.2	945 (6%)	41.32 (6%)	4
4	36	0.2	1332 (5%)	18.76 (6%)	4

Table 5.5 - Adhesive thickness effects at RTD for 4mm inner adherend case

Inner Adherend Thickness (mm)	Lap Length (mm)	Nominal Adhesive Thickness (mm)	Failure load/unit width (N/mm) (C.V%)	Shear Stress (MPa) (C.V. %)	Number of Specimens
4	36	0.2	1332 (5%)	18.76 (6%)	4
4	36	0.8	1289 (8%)	17.71 (8%)	5

To understand the effects of the adhesive fillet on the strength, DLJ with minimal adhesive fillets were manufactured and tested. The result is compared to the case with the uncontrolled adhesive fillets and shown in Table 5.6 for the 4mm inner adherend case. The case with the uncontrolled adhesive fillet was significantly stronger than the minimal fillet case.

Table 5.6 – Uncontrolled vs minimal fillet summary

Fillet Geometry	Lap Length (mm)	Nominal Adhesive Thickness (mm)	Failure load/unit width (kN/mm) (C.V%)	Shear Stress (MPa) (C.V. %)	Number of Specimens
Uncontrolled	36	0.2	1332 (5%)	18.76 (6%)	4
Minimal	36	0.2	1014 (10%)	14.22 (9%)	4

Two QI stacking sequences with a different surface ply were tested. Changing the surface ply orientation for the QI stacking sequence from 0° to 45° decreased the DLJ

strength significantly as shown in Table 5.7. The fillets were not controlled for the 45° surface ply case.

Table 5.7 – QI 45° surface test results summary for 0.2mm adhesive thickness

Inner Adherend Thickness (mm)	Stacking Sequence	Lap Length (mm)	Failure load/unit width (mm) (C.V%)	Shear Stress (MPa) (C.V.%)	Number of Specimens
4	$[0/45/90/-45]_{ns}$	36	1332 (5%)	18.76 (6%)	4
4	$[45/90/-45/0]_{ns}$	36	1051 (8%)	14.60 (8%)	5

5.3.3 Hot Temperature Dry

The effects of increasing overlap length and inner adherend thickness were studied at HTD conditions. Table 5.8 shows that increasing the inner adherend thickness from 2mm to 4mm resulted in a significant increase in DLJ strength. Increasing the overlap length for the 4mm inner adherend case also significantly increased the DLJ strength.

Table 5.8 - Overlap length effects at HTD for 4mm inner adherend case

Inner Adherend Thickness (mm)	Lap Length (mm)	Nominal Adhesive Thickness (mm)	Failure load/unit width (N/mm) (C.V%)	Shear Stress (MPa) (C.V. %)	Number of Specimens
2	36	0.2	908 (8%)	12.61 (8%)	3
4	12	0.2	602 (7%)	25.07 (7%)	4
4	36	0.2	1369 (5%)	19.01 (5%)	3

5.3.4 Hot Temperature Wet

A similar study to the RTD case was conducted at HTW. Increasing the overlap length for the 2mm inner adherend case at HTW increased the DLJ strength as shown in Table 5.9. Increasing the adhesive thickness at HTW had no significant effect on the DLJ strength (Table 5.10). Similar to the 2mm case, Table 5.11 shows that for the 4mm inner adherend case at HTW, increasing the overlap length increased the DLJ strength. Increasing adhesive thickness did not have a significant effect on the DLJ strength (Table 5.12). For the 4mm inner adherend, 0.8mm adhesive thickness case at HTW, the overall thickness of the DLJ case was at the upper limit for the mechanical grips,

and a couple of specimens were damaged when placed in the grips. Only 2 specimens gave valid results for the HTW.

Table 5.9 - Overlap length effects at HTW for 2mm inner adherend case

Inner Adherend Thickness (mm)	Lap Length (mm)	Nominal Adhesive Thickness (mm)	Failure load/unit width (N/mm) (C.V%)	Shear Stress (MPa) (C.V. %)	Number of Specimens
2	12	0.2	536 (10%)	22.32 (10%)	5
2	24	0.2	833 (3%)	17.35 (3%)	4
2	36	0.2	1008 (6%)	14.00 (6%)	4

Table 5.10 - Adhesive thickness effects at HTW for 2mm inner adherend case

Inner Adherend Thickness (mm)	Lap Length (mm)	Nominal Adhesive Thickness (mm)	Failure load/unit width (N/mm) (C.V%)	Shear Stress (MPa) (C.V. %)	Number of Specimens
2	24	0.2	833 (3%)	17.35 (3%)	4
2	24	0.8	761 (8%)	15.85 (8%)	6

Table 5.11 - Overlap length effects at HTW for 4mm inner adherend case

Inner Adherend Thickness (mm)	Lap Length (mm)	Nominal Adhesive Thickness (mm)	Failure load/unit width (N/mm) (C.V%)	Shear Stress (MPa) (C.V. %)	Number of Specimens
4	12	0.2	531 (4%)	22.14 (4%)	5
4	36	0.2	1436 (3%)	19.95 (3%)	4

Table 5.12 - Adhesive thickness effects at HTW for 4mm inner adherend case

Inner Adherend Thickness (mm)	Lap Length (mm)	Nominal Adhesive Thickness (mm)	Failure load/unit width (N/mm) (C.V%)	Shear Stress (MPa) (C.V. %)	Number of Specimens
4	36	0.2	1436 (3%)	19.95 (3%)	4
4	36	0.8	1330 (2%)	18.47 (2%)	2

This section shows all the experimental results for the DLJ. Chapter 7 discusses and explains the results and trends in more detail.

5.4 Failure Modes for Pristine Double Lap Joints

5.4.1 Introduction

During the pristine DLJ tests at different environmental conditions, two types of failure modes were observed. They are defined as F1 and F2 failure modes for this thesis. A baseline case for the F1 and F2 is analysed and the failure mechanism is explained in this section.

5.4.2 Failure Modes for Pristine Double Lap Joints – F1, Fracture Controlled Failure

The 4mm inner adherend, 36mm overlap length case at RTD was chosen as the baseline case to explain the F1 failure mode. The adhesive fillets for this case were not controlled during the manufacturing process. A linear force-displacement curve was observed before sudden and catastrophic failure. The fracture surface and corresponding failure schematic is shown in Figure 5.3, where the dotted line in the schematic represents the primary crack propagation path during failure. The fracture surface image shows the two bonded inner adherend/outer adherend interfaces. The images shown are post failure of the whole bondline, hence includes secondary mechanisms such as the 'jump' as discussed later. The primary failure mechanism is explained based on images obtained from a Photron high-speed camera as shown in Figure 5.4. The high-speed camera video was taken at 80,000 frames per second.

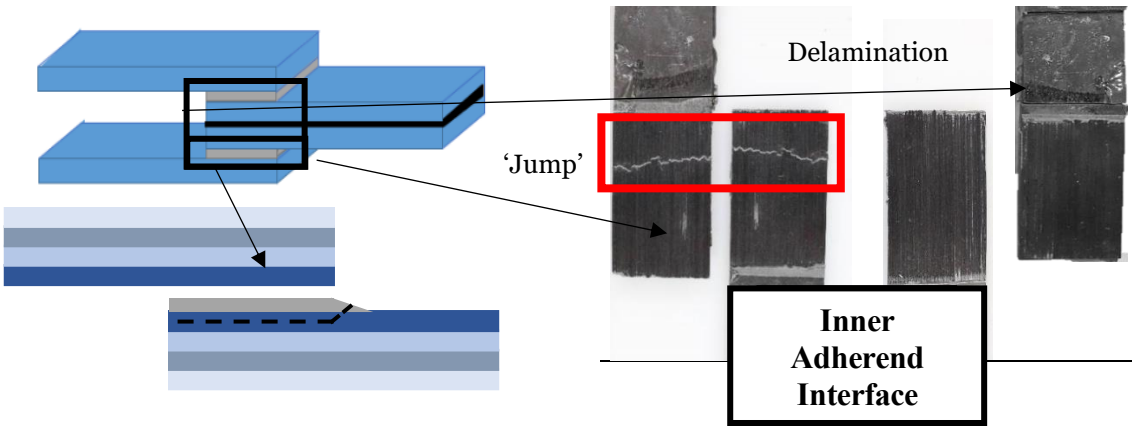

a) Schematic b) Fracture surface

Figure 5.3 - Failure schematic and fracture surface for failure within composite, F1

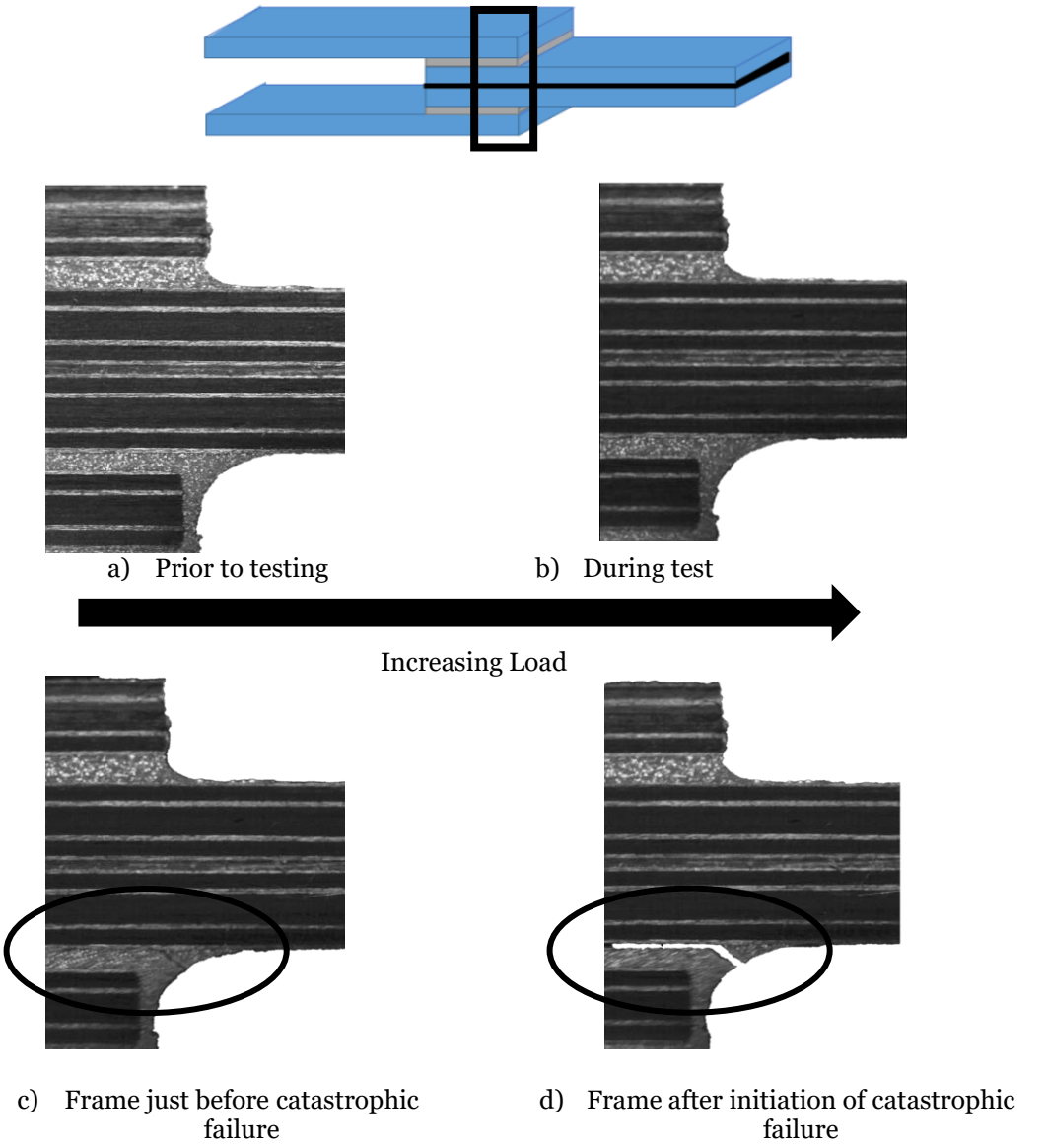

Figure 5.4 – High-speed camera images of F1 failure

The high-speed camera images do not show any indication of crack initiation during the initial stages of loading. Analysing the frame before catastrophic failure, cracks visible are within the adhesive fillet and on the surface 0° ply of the composite inner adherend. It was not clear whether the crack initiated within the adhesive or composite first, as cracks appeared in both materials simultaneously. As the failure was sudden and catastrophic and the high-speed camera did not pick up the failure sequence, it was postulated that the crack initiated at the adhesive fillets due to the high peel component at the leading edges of the DLJ. The crack then migrated into the surface 0° ply in the inner adherend as shown in Figure 5.4.

Figure 5.3 shows a 'jump' pattern on the fracture surface. Why this occurred is explained through analysing the failure from the high-speed camera. The DLJ has two inner adherend/outer adherend interfaces as labelled in Figure 5.5. The primary failure mechanism is represented by 1 in the schematic in Figure 5.5. During the primary failure mechanism, due to asymmetry formed by the initial crack propagation, delamination started to initiate and propagate within the surface 0° plies. These cracks were present at the outer adherend at the trailing edge of the second bonded interface and also at the forward adhesive/inner adherend interface, represented by 2 in Figure 5.5. When the delamination path from the inner adherend leading edge and outer adherend trailing edge at the second interface approached each other, the cracks joined up by fracture of the adhesive (3 in Figure 5.5). This is represented by the 'jump' pattern on the fracture surface as highlighted in Figure 5.3.

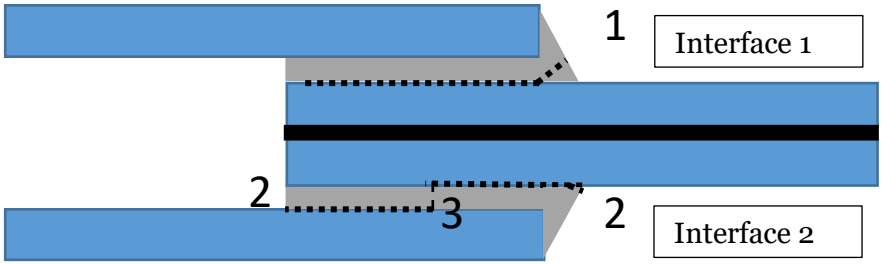

Figure 5.5 - Failure process schematic

5.4.3 Failure Modes for Pristine Double Lap Joints – F2, Strength Controlled Failure

Next, the failure controlled by the adhesive properties is discussed, referred to as F2. For this case, the 4mm inner adherend, 12mm overlap length at HTW was used as the baseline to explain the failure mechanism. The failure was sudden and catastrophic. The typical fracture surface and corresponding failure schematic for this case are shown in Figure 5.6. The fracture surface shows the post failure surface of the whole bondline and does not indicate the sequence of the failure. The failure schematic shows the primary failure mechanism within the adhesive. For this case, patches of adhesive and 0° fibres were visible on both the fracture surfaces, different to the F1 failure mode fracture surfaces, where only the 0° fibres were visible clearly, which suggests that the adhesive in the bondline influenced the failure for this case.

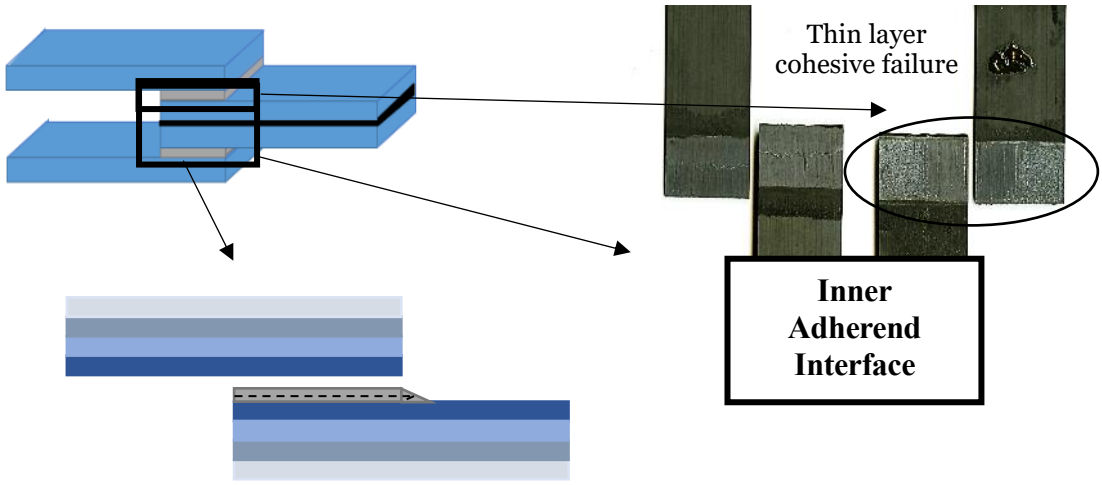

a) Schematic b) Fracture surface

Figure 5.6 - Failure schematic and fracture surface for failure within adhesive and composite, F2

5.5 Conclusions

This chapter introduced the pristine DLJ configuration used to test at RTD, HTD and HTW conditions. The manufacturing and testing process were described. The experimental results for the pristine DLJ at different environmental and geometrical conditions were reported in this chapter, with a brief description of the results.

The two different types of failure modes that were observed for pristine DLJ were analysed. The first, was postulated as failure that initiated at the adhesive fillets and then migrated into the surface 0° ply in the inner adherend (F1), and second, failure influenced by the adhesive bondline (F2). Two baseline cases showing these failure modes are described.

CHAPTER 6

EFFECTS OF ENVIRONMENTAL CONDITIONS ON PRISTINE DOUBLE LAP JOINT STRENGTH: INTRODUCTION TO ANALYTICAL AND NUMERICAL MODELS

6.1 Introduction

An introduction into the analytical and numerical modelling techniques for the pristine Double Lap Joint (DLJ) is discussed in this chapter. The analytical model is based on simple shear strength and fracture propagation criteria. These criteria are explained and applied to the baseline test results from Chapter 5 to help understand what controls the failure for each case. Using ABAQUS/Explicit, a Finite Elements (FE) numerical model for the DLJ is created and explained using the Cohesive Zone Model (CZM) approach. From the characterisation test results obtained from the previous chapters (Chapter 3 and 4), the input parameters for the CZM were obtained. Initial modelling results on the baseline cases are presented and discussed, analysing the accuracy of the model in predicting the joint strength. The purposes of the numerical model are to accurately predict the failure of the DLJ, understand the DLJ behaviour and input parameter sensitivity for different configurations.

The DLJ were tested at different environmental conditions to understand the effects of temperature and moisture and summarised in Chapter 5. Table 6.1 summarises the main pristine Double Lap Joint (DLJ) pristine tests conducted for the 0.2mm adhesive thickness case at different environmental conditions. The numerical models created are based on Table 6.1.

Table 6.1 - Experimental Summary of DLJ tests for 0.2mm adhesive thickness

	2mm Inner Adherend			**4mm Inner Adherend**	
Overlap Length	**12mm**	**24mm**	**36mm**	**12mm**	**36mm**
RTD	✓	✓	✓	✓	✓
HTD			✓	✓	✓
HTW	✓	✓	✓	✓	✓

6.2 Analytical Model

6.2.1 Introduction to Simple Analytical Model

The simple analytical failure criteria were applied on the DLJ to help determine the failure mode at different environmental and geometrical conditions. This section introduces these criteria. This is a simple qualitative analysis to estimate the relative importance of the stress and energy.

Equations 6.1 was used to calculate the average shear stress at failure where τ is the shear stress, P the applied load and A the bonded area. This equation assumes the adhesive deforms in shear and the other stress components in the DLJ do not affect the failure. It also assumes a constant adhesive shear stress throughout each bondline and the adherend to be rigid. The shear strength of the adhesive was used for the calculations as this was weaker than the composite for all conditions. The properties are summarised in Section 6.2.2.

$$\boldsymbol{\tau = \frac{P}{A}} \tag{6.1}$$

To obtain the estimated failure load for failure based on fracture propagation, a stress-based criterion would be difficult to use due to the induced singular stress fields as a result of the geometric discontinuities in the joint. Hence, a fracture mechanics approach based on the strain energy release rate (G) and the fracture energy (G_c) was used. Equation 6.2 ([97]) represents the change of elastic strain energy per unit area and is used to understand the strain energy release rate during delamination propagation for DLJ with a crack growth. G is defined as the difference between the external work done and the change in internal strain energy per unit area. As all force-displacement graphs during the DLJ tests were linear before catastrophic failure, justifying the linear elastic assumptions.

$$\boldsymbol{G = \frac{\sigma^2 h t}{4E(h - t)}} \tag{6.2}$$

The Young's Modulus in the loading direction is represented by E and the applied stress on the overall thickness is σ. The terms h and t are the overall specimen thickness and total thickness of the outer adherend respectively as shown in Figure 6.1. The advantage of this method is that the effects of the local stress field around the crack tip do not affect the strain energy release rate when the delamination propagates as the stress field moves along the specimen [98] [97].

Figure 6.1 – Schematic defining terms for fracture energy equation

The experimental results in Chapter 5, Section 5.3.2 shows that the inclusion of the adhesive fillet significantly influenced the DLJ strength. A high peel component is present at the leading edges of the DLJ due to bending moments that arise as a result of the eccentric loading. As adhesive fillets are present at the leading edges this can lead to failure initiation due to the peel, i.e. Mode I component in the adhesive, as seen

for the F1 failure mode, as described in Chapter 5. For the simple analytical calculations, the expected failure load based on the Mode I fracture energy of the adhesive is obtained using Equation 6.2. The failure load per unit width is obtained by multiplying the predicted applied stress by the specimen thickness.

6.2.2 Material Properties for Double Lap Joint Model

The elastic properties for the composite and adhesive are summarised in Table 6.2. These data were obtained from literature for IM7/8552 [92] and Redux 319 [93]. Homogenized properties were given to the 45°/-45° plies according to Classical Laminate Theory as shown in Table 6.2. The elastic properties were assumed not to change at different environmental conditions. The bulk adhesive for the adhesive fillets was modelled using linear-elastic assumptions (small region in comparison to bond-line), with cohesive elements beneath the adhesive fillet. The fillet geometry of 65° was used based on the typical fillet geometries from the experimental analysis.

Table 6.2 - Elastic properties for adhesive and composite

Adhesive	E (GPa)	G (GPa)	η			
	3.76	1.41	0.33			
Composite 0°	E_{11} **(GPa)**	$E_{22}=E_{33}$ **(GPa)**	$G_{12}=G_{13}$ **(GPa)**	G_{23} **(GPa)**	$\upsilon_{12}=\upsilon_{13}$	υ_{23}
	161	11.4	5.17	3.98	0.320	0.436
	$E_{xx} = E_{yy}$ **(GPa)**	E_{zz} **(GPa)**	G_{xy} **(GPa)**	$G_{zx} = G_{yz}$ **(GPa)**	υ_{12}	$\upsilon_{13}= \upsilon_{23}$
45°	18.6	13.5	41.6	4.5	0.79	0.093

The fracture and strength properties are summarised below. The values are used for the cohesive zone model which is described in Section 6.3.2. The fracture toughness values of the adhesive (Redux 319) at Hot Temperature Dry (HTD) and HTW conditions were obtained from the characterisation tests in Chapter 3 and 4. The RTD toughness value was obtained from literature [93] as the experimental results showed that the failure was controlled by the composite properties (Section 3.3.2). The Non-Pre-Crack (NPC) values based on 5% offset from linear load line were used for consistency across all cases. This was done because during some NPC tests the crack

migrated into the composite surface ply, hence during the Pre-Cracked test the results would not represent the adhesive fracture properties. The RTD toughness values for the composite (IM7/8552) was available from the literature [92]. The composite HTD and HTW toughness values were tested and presented in the previous chapters.

The experimental values from Chapter 3 and 4 include the adhesive tensile strength, at HTD and HTW. The tensile strength for the adhesive at RTD was obtained from the maximum applied stress derived from fixed arm peel tests from the previous literature [99]. The adhesive shear strength, S_{13} at RTD was measured experimentally. The shear strength test at HTW was conducted but failed at the interface between the adhesive and metal adherend, hence not representing the adhesive properties. The data for the shear strength at HTD (80°C) was not available. Hence, the adhesive shear strengths at HTD and HTW were estimated, using linear interpolation from the datasheet values at 22°C and 150°C. The HTW strength values were estimated using HTD data at 120°C. This approach was taken as the glass transition temperature (Tg) of a material decreases with moisture. Hence, it was postulated that the difference between the test temperature (80°C) and Tg at wet conditions would be similar to the HTD data at 120°C and Tg at dry conditions. This assumption was based on comparison of the tensile strength data at 80°C for conditioned samples (HTW) and at 120°C (HTD) (Appendix A). As these values correlated well for the tensile case, a similar assumption was made for the shear strength. The values based on these assumptions were used as this was a qualitative analysis to gain an understanding into what controls the failure for separate cases. It was later found from the numerical analysis conducted on all DLJ, that using these parameters in the FE model gave reasonable predictions.

Table 6.3 – Fracture and strength properties of composite and adhesive (used for cohesive elements)

	Conditions	G_{IC} **(N/mm)**	G_{IIC} **(N/mm)**	S_{33} **(MPa)**	S_{13} **(MPa)**
0.2 mm Adhesive	RTD	0.85 [93]	2.65	44	51
	HTD	1.05	1.36	36	35[1]
	HTW	1.13	0.70	7.5	28[1]
Composite	RTD	0.20 [92]	1.00 [92]	60 [92]	90 [92]
	HTD	0.25	0.94	45[1]	60[1]
	HTW	0.34	0.78	24	38

1 Estimated Values

The strength values used for the cohesive elements for IM7/8552 at RTD and HTW were available from the literature ([92], [100]). The temperature used for the HTW tests from this source was 120°C, higher than the 80°C used in this study. The HTD data was not available. In the absence of the HTD data, a crude estimate was taken as the average between the strengths at RTD and HTW conditions. From the literature it was found that the temperature decreased the strength of the composite, while the presence of temperature and moisture further decreased the strengths. The sensitivity analysis of different material parameters on the strength of the DLJ (discussed in Chapter 7) showed that varying the composite through thickness tensile strength did not have a significant effect on the DLJ strength compared to the other material parameters, hence this estimated value was used.

6.2.3 Analytical Model for Double Lap Joint

This section applies the simple analytical failure criteria to the baseline cases for the F1 and F2 failure modes as discussed in Chapter 5. This was a simple qualitative analysis to estimate the relative importance of the stress and energy for each of the failure modes observed. For F1 failure mode, the baseline case was the 4mm inner adherend, 36mm overlap length and 0.2mm adhesive thickness at RTD. The baseline case for F2 failure mode was the 4mm inner adherend, 12mm overlap length at HTW.

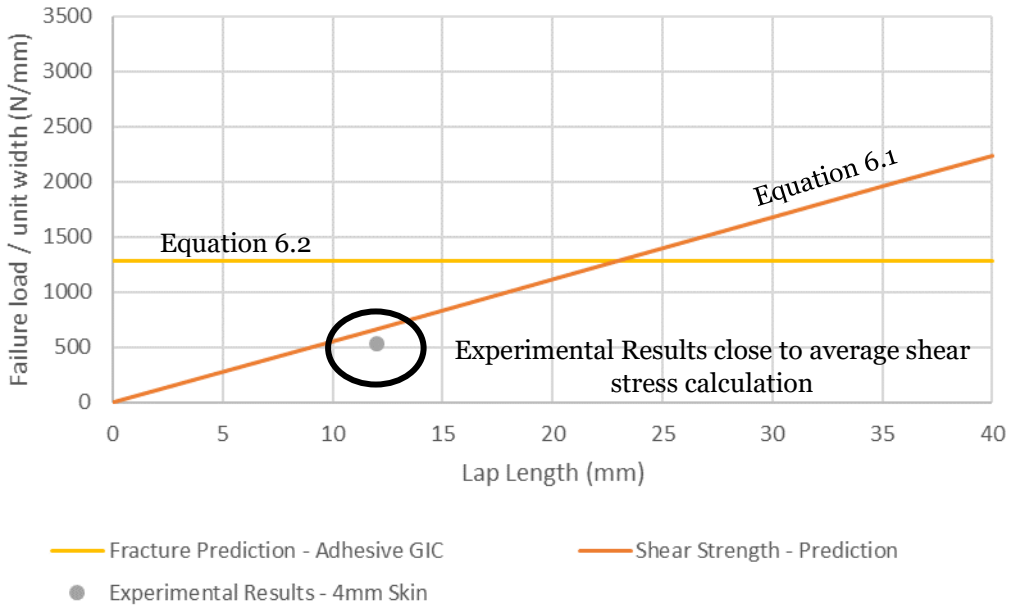

Figure 6.2 - Failure prediction using simple criteria at HTW for F2 (strength controlled) failure mode

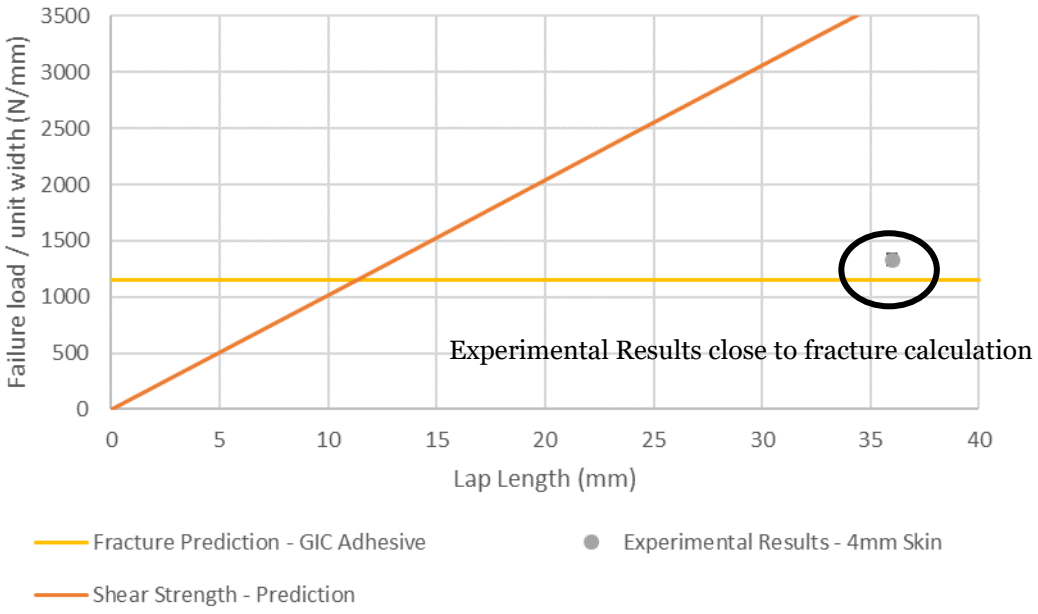

Figure 6.3 - Failure prediction using simple criteria at RTD for F1 (Fracture controlled) failure mode

The simple analytical failure criteria were based on the shear strength and the Mode I fracture energy of the adhesive. These results are presented in Figure 6.2 and Figure 6.3. The input shear strength of the adhesive and HTW G_{IC} was obtained from Table 6.3. The adhesive G_{IC} at RTD was 0.85 N/mm [93]. The line in orange represents the failure load based on the shear strength and the yellow line gave the expected failure load based on the G_{IC} of the adhesive.

The results in Figure 6.2 suggest that the failure for the 4mm inner adherend, 12mm overlap length case at HTW, i.e. F2 failure mode, was controlled by the shear strength of the adhesive as it was approaching the shear strength predicted failure criterion. For the F1 failure mode (4mm inner adherend, 36mm overlap length at RTD), the test result in Figure 6.3 was a long way from the shear strength line, but close to the failure load based on the fracture energy, which suggested the failure was fracture dominated.

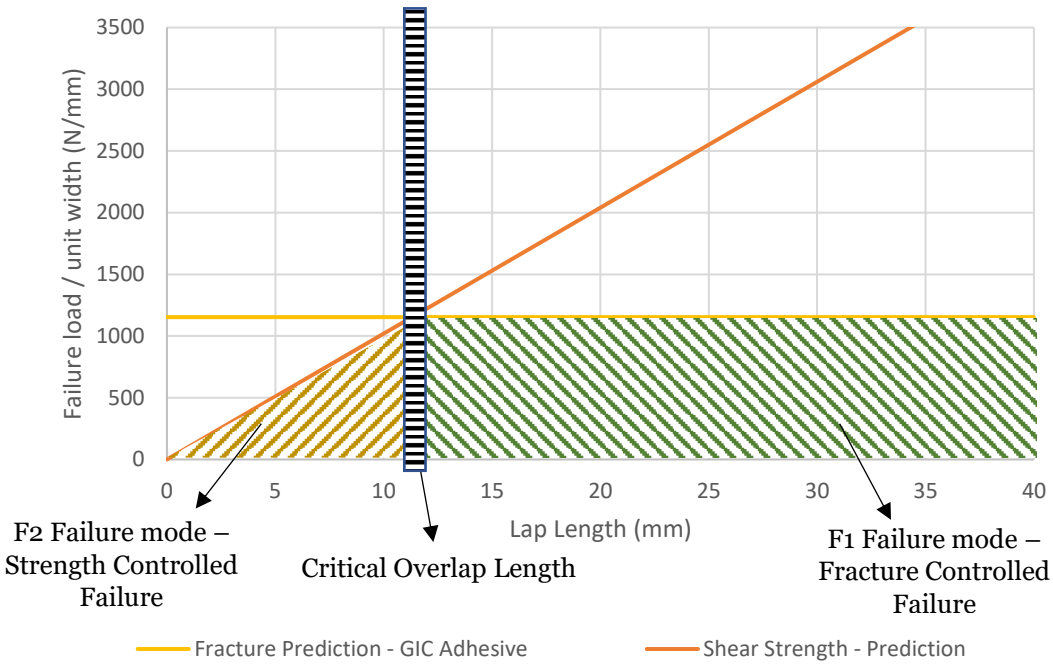

Figure 6.4 - Analytical simple criteria to determine failure mode (example shown using RTD properties)

These simple criteria gave an indication of what was likely to control the failure for the DLJ. At a specific overlap length, the expected failure mode for the pristine DLJ can be determined, as shown in Figure 6.4 (example using RTD properties). For shorter overlap lengths, a F2 failure mode where the failure was controlled by the adhesive shear strength properties is expected, up until a critical overlap length. At this point, the failure mode is expected to change from a strength to fracture controlled failure, i.e. an F1 failure mode where crack propagation initiated within the adhesive fillets followed by propagation within the composite. These criteria are applied to the experimental results and discussed in Chapter 7.

6.3 Numerical Model

6.3.1 Introduction to Numerical Model

Numerical models were created to accurately predict the DLJ failure at different conditions more accurately relative to the analytical model. A typical model is shown

in Figure 6.5. A ply-by-ply 2D slice was modelled by 3D solid elements with plane-strain assumptions and boundary conditions in ABAQUS/Explicit, based on the assumption that the stress and damage evolution is uniform across the specimen width.

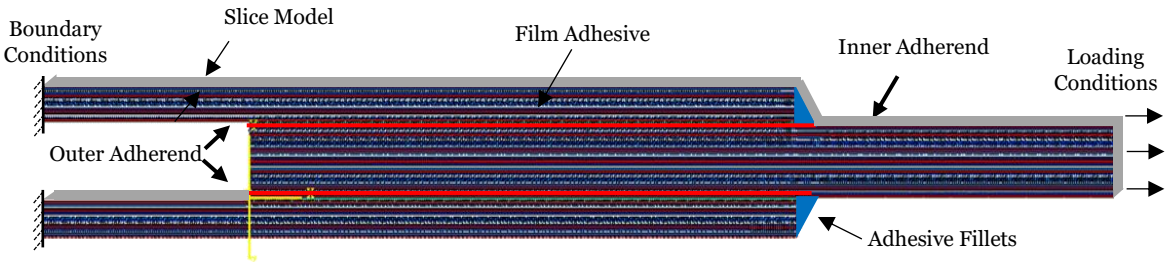

Figure 6.5 – A typical double lap joint model using 2D plane strain assumptions

The mesh size was constant at 0.125 mm. The 2D slice model was 0.125 mm wide with one element across the model width. 8-node C3D8 solid elements were used with one element through each ply thickness (0.125 mm). The 3D analysis was used to capture the shear stresses and through-thickness stresses in the ply-by-ply analysis accurately. All the nodes at the front and back faces were fixed in the width direction to simulate a plane-strain stress state. As 0° plies were present next to the adhesive bondline, 3D effects such as edge effects and 45˚ ply cracks were not expected to be critical. The nodes at one end were fixed, with uniform displacements applied to the nodes at the other end horizontally. Finite thickness cohesive elements using the ABAQUS built-in COH3D8 elements were used to represent the potential failure path. The finite thickness cohesive elements were 0.2 mm thick, taking the adhesive thickness loading offset into account. The adhesive thickness did not have a significant effect on the DLJ strength as found in Chapter 5, hence only one thickness was modelled. The material properties are summarised below. Cohesive elements were place between the outer adherends and the inner adherend and also beneath the simplified adhesive fillets. The adhesive fillets were assumed to be linear elastic for simplicity and the cracking within the adhesive fillets was not modelled explicitly but represented by the line of cohesive element between them. Such a simplification is reasonable since the fillet geometry was uncontrolled and cracking within adhesive is quite complex. This thesis mainly looks into joint failures and how they can be predicted based on basis material properties, rather than different fillet geometries which is nevertheless an interesting topic on its own right and will be looked at later with a parametric study.

6.3.2 Cohesive Zone Model

A mixed-mode bi-linear traction separation law was applied for the cohesive elements based on two criteria. The first was the stress-based criterion for damage initiation, assuming a quadratic interaction between the through thickness tensile stress and interlaminar shear stress, as shown by the damage initiation locus in Figure 6.6. The second criterion was energy based for damage propagation. A linear interaction between the Mode I strain energy release rate and Mode II strain energy release rate was assumed for this model. Figure 6.6 summarises the cohesive zone model used for the current numerical prediction (alpha = 1 for linear interaction).

The penalty stiffness (K) value was chosen after a sensitivity analysis on different K values as shown in Figure 6.7 on the baseline DLJ model. The results for K = 10,000 N/mm^3, 100,000 N/mm^3 and 1,000,000 N/mm^3 are shown, and it was concluded that the model was relatively insensitive to the penalty stiffness parameter. Hence, a penalty stiffness value of K = 100,000 N/mm^3 was used for the cohesive elements for the DLJ model. The properties of cohesive elements for both the composite and adhesive are shown in Table 6.3.

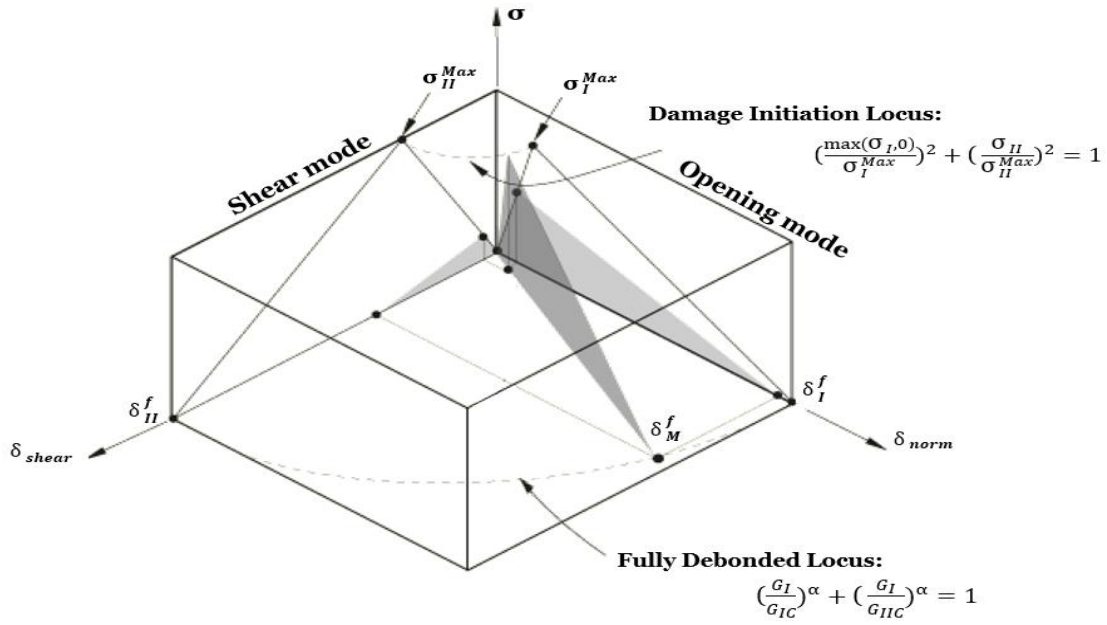

Figure 6.6 - Mixed-mode traction separation relationship for cohesive elements

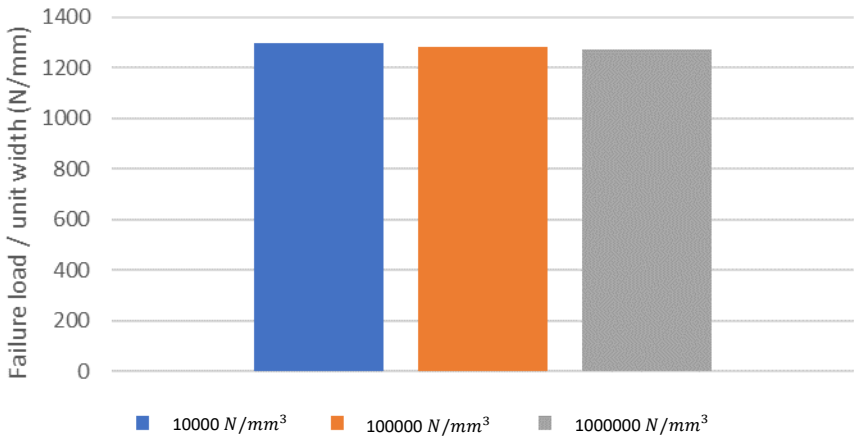

Figure 6.7 - Effects of penalty stiffness on joint strength

6.3.3 Sensitivity Analysis on ABAQUS Model

An explicit analysis was used based on the initial expectation to capture the progressive damage and non-linear response of the DLJ. The optimum values for the density and loading rate used in the explicit analysis were obtained from a sensitivity analysis comparing these values, to understand the effects of mass scaling on the model.

Mass scaling is a technique where nonphysical mass is added to a structure. Mass scaling increases the density of the elements which reduces the wave propagation speed and increases the maximum stable time step, hence decreasing the computation time. A lower density and higher loading rate result in lower computational time but can lead to artificial dynamic effects. Figure 6.8 summarises the results, checking the effects of density and loading rate on the failure load for the 4mm inner adherend, 36mm overlap length DLJ configuration. A high density and loading rate had a significant effect on the DLJ strength prediction compared to the lower density and loading rates. The sensitivity analysis shows that increasing the density of the elements during the explicit analysis resulted in an increase in kinetic energy in the model, which has artificial effects on the DLJ strength, giving inaccurate results. To avoid these effects, the loading rate and density values chosen for the numerical model needs to be in the range that does not artificially increase the DLJ strength.

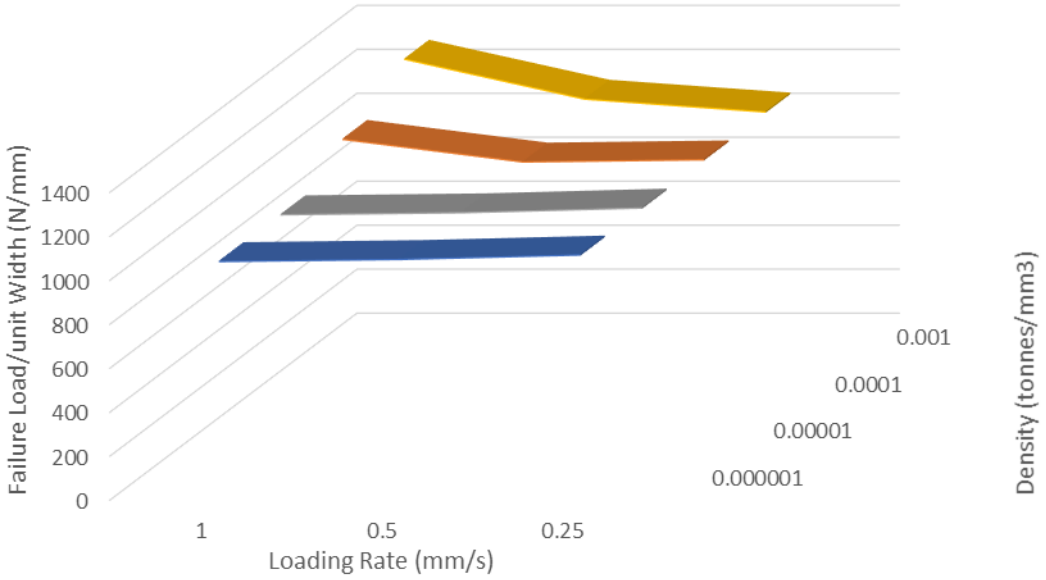

Figure 6.8 - Effects of density and loading rate

The values used for the analysis were a loading rate of 1 mm/s and a density of 1E-5 ton/mm^3 as these gave the shortest computational time while avoiding the artificial dynamic effect.

6.3.4 Pristine Double Lap Joint Numerical Model

For the pristine model, the bondline was represented by a layer of cohesive elements as shown in Figure 6.9. Two failure modes were observed in the joint tests, which were summarised in Section 5.4.2 and 5.4.3. These were crack propagation that initiated within the adhesive fillets followed by migration into the composite (F1) and failure controlled by the shear strength of the adhesive (F2). Therefore, the joints with different failure modes were modelled differently as shown in Figure 6.9b and c. The choice of which model to use for the pristine cases was determined using the analytical criteria.

For cases controlled by fracture propagation (F1), composite properties were used for the cohesive elements beneath the bondline and adhesive properties used beneath the fillet. For cases controlled by the shear strength (F2), adhesive properties were used for the cohesive elements throughout the bondline and fillets. For all pristine models

the adhesive fillet geometry was simplified and modelled at 65° with cohesive elements with adhesive properties beneath the fillet based.

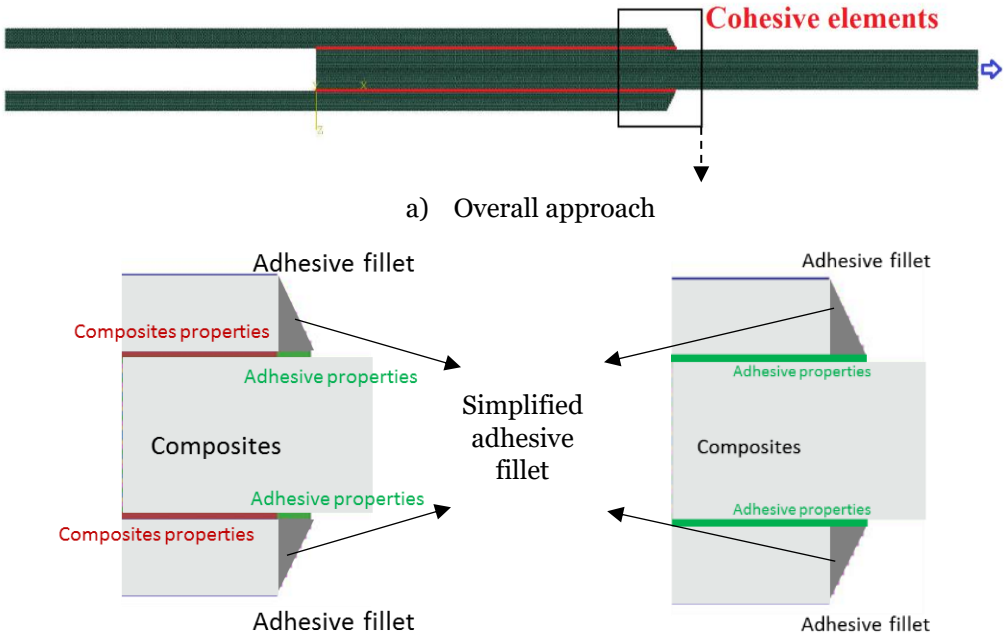

a) Overall approach

b) Adhesive bondline with composite properties – delamination failure (F1)

c) Adhesive bondline with adhesive properties – cohesive failure (F2)

Figure 6.9 – Pristine DLJ with adhesive fillets modelled with a 65° angle

6.3.5 Pristine Double Lap Joint Numerical Results

The pristine numerical models were compared to the experimental baseline cases discussed in Section 5.4 for F1 and F2 failure modes. A typical predicted load-displacement curve from the model is shown in Figure 6.10. The load was the failure load per unit width for the baseline (4mm inner adherend, 36mm overlap length, RTD) case. The response was linear up to the peak load followed by a sharp load drop when one inner adherend/outer adherend interface fails, which was then followed by failure in the other inner adherend/outer adherend interface. The peak load was defined as the failure load, and the predicted failure load was normalised by the model width.

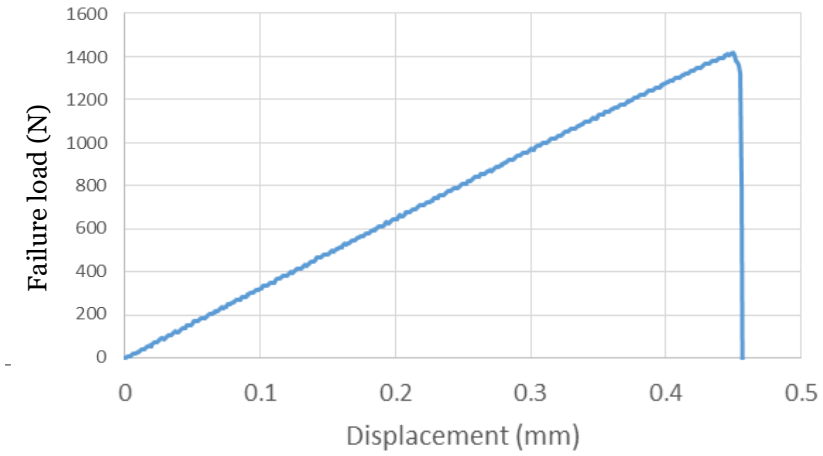

Figure 6.10 - Typical force-displacement response for baseline numerical DLJ model for unit width

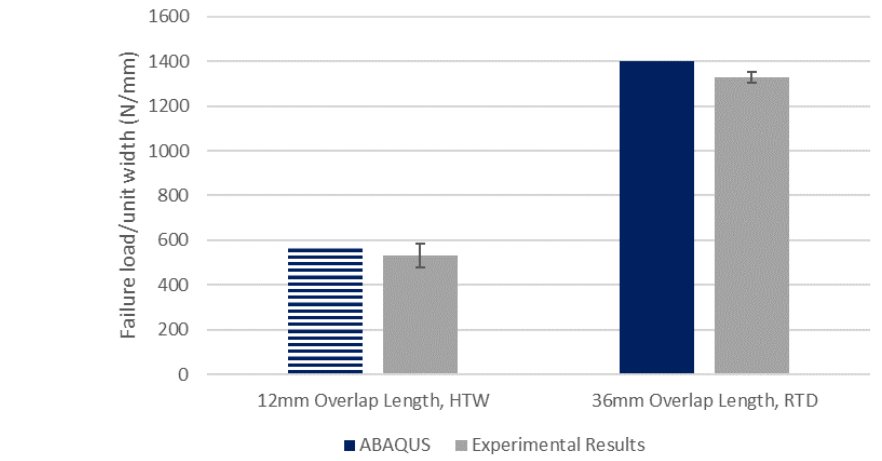

F1, Adhesive properties beneath fillet, composite beneath bondline

F2, Adhesive properties only

Figure 6.11 - Comparison of experimental results to numerical model

Figure 6.11 compares the experimental results to the numerical model and shows very good agreement, showing this approach can accurately capture the failure process. Using the F1 numerical model for a F2 failure mode, or vice-versa overpredicted the experimental results.

6.4 Conclusions

This chapter introduced the analytical and numerical models used for the pristine DLJ. From the experimental analysis in Chapter 5, two types of failure modes were observed, F1 and F2. The first, described as failure occurring by crack initiation within the adhesive fillets followed by migration into the composite (F1), and the second, failure controlled by shear strength of the adhesive (F2). Analytical criteria were created in this chapter to determine whether the failure was controlled by the strength (F2) or fracture properties (F1). Following this, numerical models were created using ABAQUS/Explicit. The numerical model used CZM, for which the input parameters were obtained from the characterisation tests in Chapter 3 and 4, literature and some estimates where data was lacking. Two types of models were created. The first model was based on the F1 failure mode, where cohesive elements were placed with adhesive properties at the region beneath the adhesive fillet and then composite properties at the bondline. For the second model based on F2, elements with adhesive properties were used throughout the bondline. Initial modelling results showed good correlation to the experimental results. The analytical model was used to determine the expected failure mode and the numerical models are used for the DLJ prediction at different environmental conditions in Chapter 7.

CHAPTER 7

EFFECTS OF ENVIRONMENTAL CONDITIONS ON PRISTINE DOUBLE LAP JOINT STRENGTH: DISCUSSION

7.1 Introduction

The pristine Double Lap Joints (DLJ) experimental results were presented in Chapter 5, and the analytical and numerical models were introduced in Chapter 6. This chapter discusses the DLJ behaviour and trends at different environmental and geometrical conditions based on the experimental results. Two types of failure modes were observed and explained in previous chapters. F1, defined as initial failure within the adhesive fillet followed by migration into the inner adherend surface 0° ply, and was controlled by the fracture energy. F2, defined as failure controlled by the shear strength of the adhesive. Simple analytical calculations were used to determine the failure mode. The numerical models are then used to predict the DLJ strength for the test cases taking account of the expected failure mode. The analytical model is not used as a predictive tool as it can only approximately address the initial failure within the adhesive for the F1 failure mode and is based on simple assumptions. Whereas the numerical model can address both initial failure within the adhesive and followed by the migration into the composite for the F1 failure mode, capturing the failure sequence. Figure 7.1 shows the schematic of a typical DLJ used.

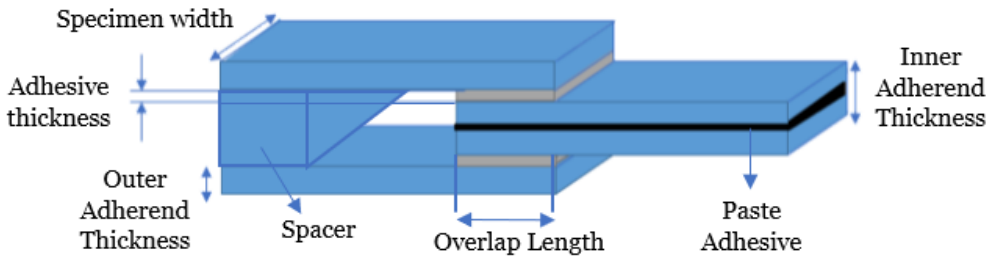

Figure 7.1 - Schematic of the double lap joint

7.2 Room Temperature Dry – Results and Discussion

7.2.1 Introduction to Test Cases

The section discusses the effects of overlap length, inner adherend thickness and adhesive thickness on the DLJ strength at RTD conditions. Table 7.1 summarises the tests conducted at RTD. The simple analytical failure criteria were applied to understand the expected failure mode and the numerical modelling results are presented and discussed based on the models presented in Chapter 6. The simple analytical model calculations were based on the shear strength and Mode I fracture energy of the adhesive, which were 51MPa and 0.85 N/mm respectively at RTD. These values were discussed in Chapter 6.

Table 7.1 - RTD test summary

	2mm Inner Adherend				**4mm Inner Adherend**	
Adhesive Thickness (mm)	12mm	24mm	36mm		12mm	36mm
0.2	✓	✓	✓		✓	✓
0.8		✓				✓

7.2.2 Effects of Overlap Length on the Double Lap Joint Strength

Figure 7.2 summarises the results for the 2mm inner adherend case and Figure 7.3 show the fracture surfaces of the whole bondline presenting the two inner adherend/outer adherend interfaces for the DLJ after failure.

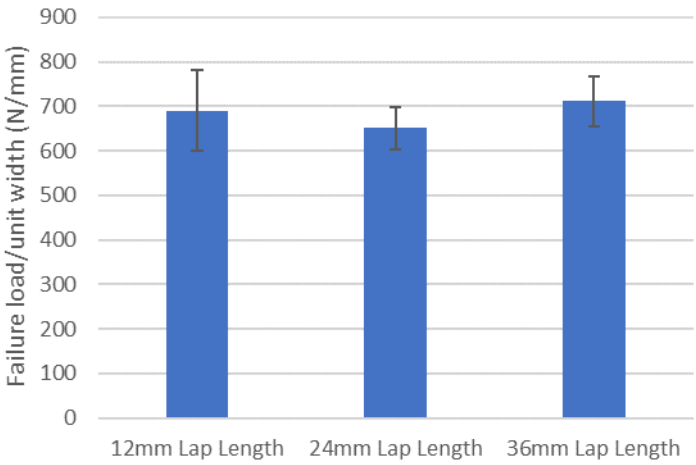

Figure 7.2 - Effects of increasing overlap length on DLJ strength for 2mm inner adherend at RTD

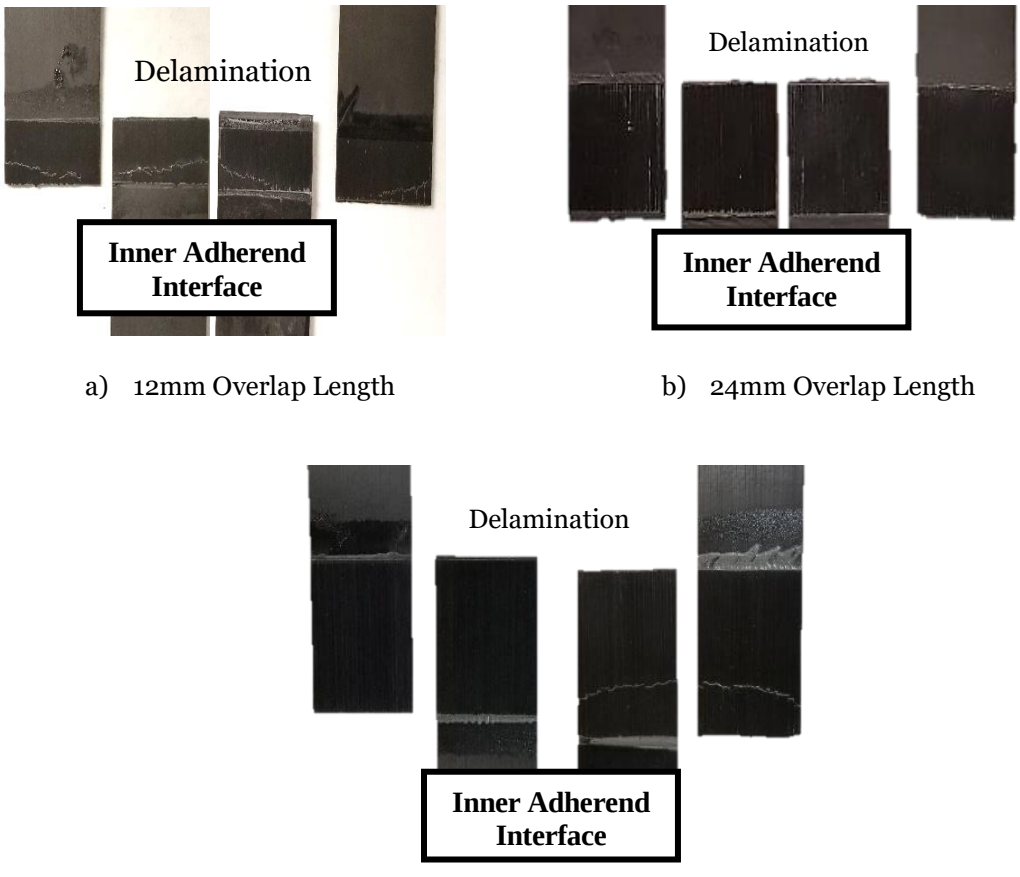

a) 12mm Overlap Length

b) 24mm Overlap Length

c) 36mm Overlap Length

Figure 7.3 - Fracture surfaces for 2mm inner adherend cases at RTD

For all 2mm inner adherend cases, the fracture surfaces show the 0° ply visible across all 4 fracture surfaces. Analysing the 2mm inner adherend results show that there was no significant difference in strength for the three overlap lengths tested. For all 2mm inner adherend RTD cases, the crack initiated at the adhesive fillets and then migrated into the composite surface ply, i.e. a F1 failure mode.

The 2mm inner adherend results are compared against the simple criteria (introduced in Chapter 6) in Figure 7.4. Analysing the results shows that at RTD, all overlap lengths fall within the area of expected failure based on fracture energy, hence explains why the strengths were similar.

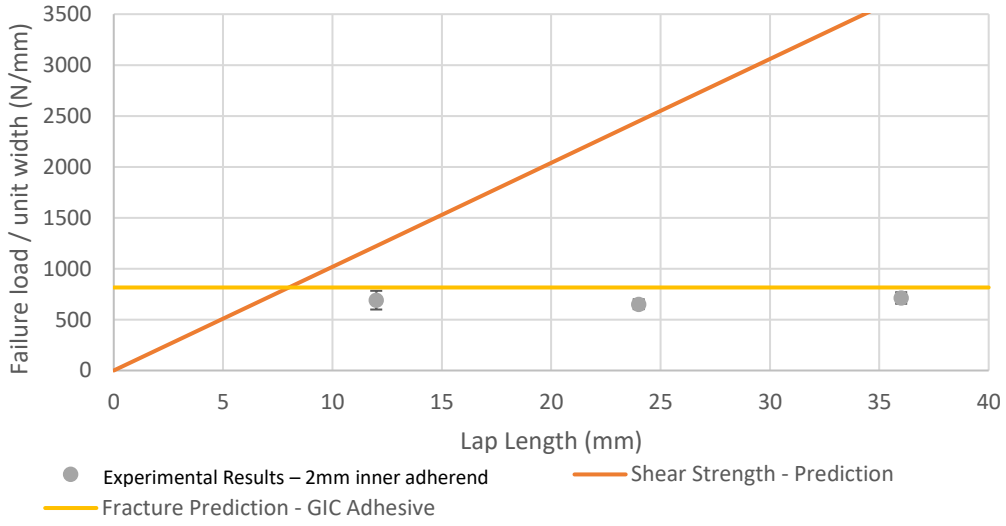

Figure 7.4 - Analytical simple criteria for 2mm inner adherend at RTD

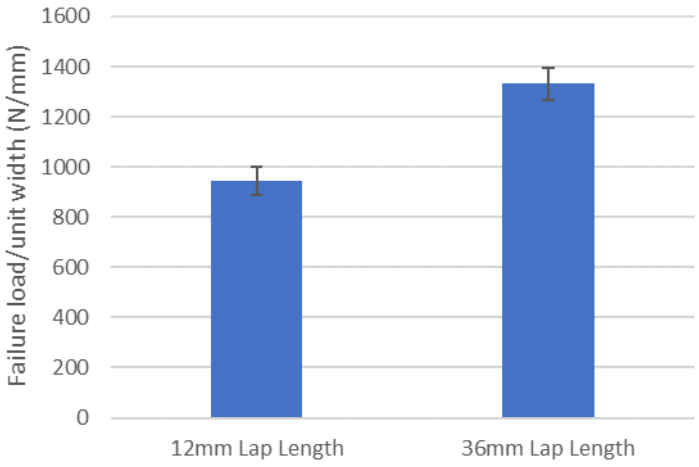

Figure 7.5 - Effects of increasing overlap length on DLJ strength for 4mm inner adherend at RTD

For the 4mm inner adherend, the DLJ strength increased with increasing overlap length as shown in Figure 7.5. The fracture surface images (Figure 7.6) show that the 12mm overlap length case had very small fragments of adhesive on the fracture surface and the failure mode was not conclusive based on this observation. The 36mm overlap length fracture surfaces show the surface 0° plies across all inner adherend/outer adherend interfaces, similar to the 2mm case, i.e. F1 failure mode.

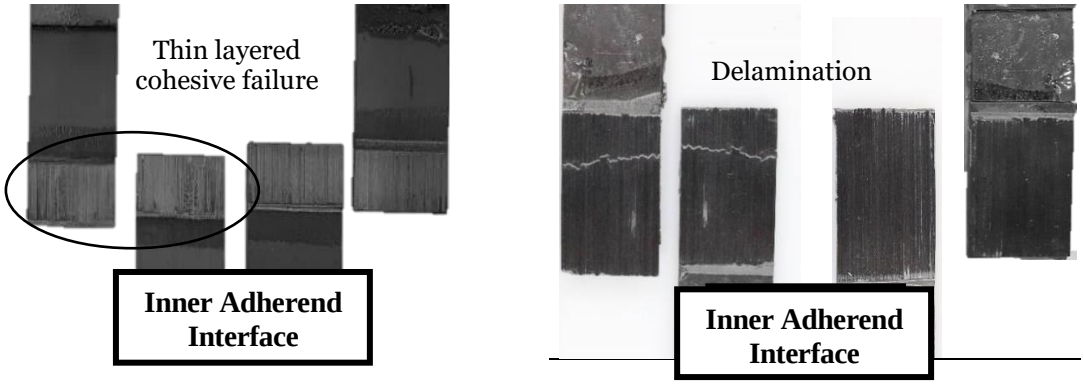

a) 12mm Overlap Length b) 36mm Overlap Length

Figure 7.6 - Fracture surfaces for 4mm inner adherend cases at RTD

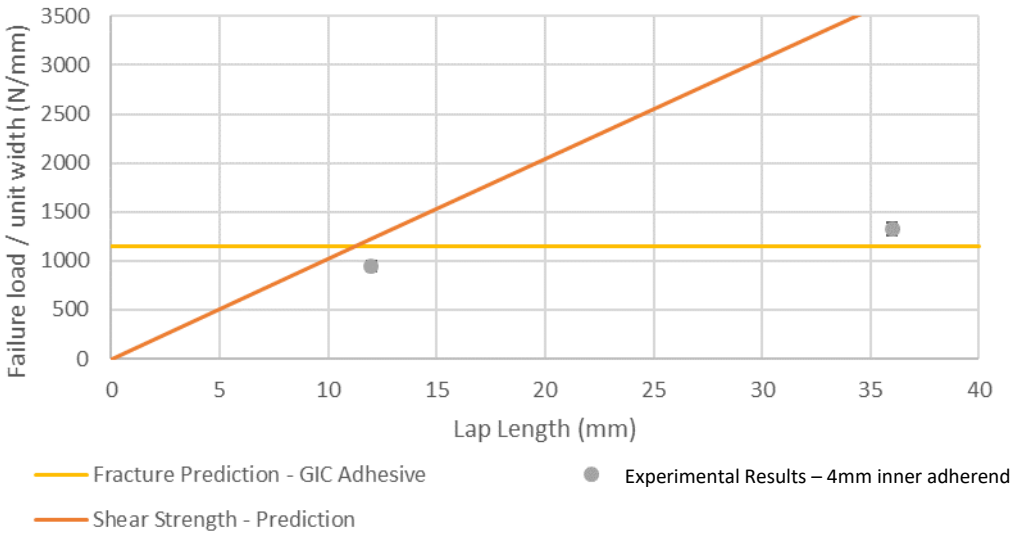

Figure 7.7 Analytical simple criteria for 4mm inner adherend at RTD

The simple failure criteria were applied to the 4mm inner adherend cases as shown in Figure 7.7. The results show that the 12mm overlap length result was close to both the strength and fracture lines. This suggests the 12mm overlap length case was at the critical overlap length between the F1 and F2 failure modes. The longer 36mm overlap

length was fracture dominated as it approaches the fracture prediction lines in Figure 7.7.

7.2.3 Effects of Inner Adherend Thickness on the Double Lap Joint Strength

Figure 7.8 compares the 12mm and 36mm cases for both 2mm and 4mm inner adherend cases. For both overlap lengths, increasing the inner adherend thickness increased the DLJ strength. The increase in strength was greater for the 36mm overlap length case.

Considering the shorter overlap length case, for the 2mm inner adherend the failure was expected to be fracture dominated. The expected failure mode for the 4mm inner adherend case was at the critical overlap length from a strength controlled failure to a fracture controlled as shown in the simple failure criteria. For both 2mm and 4mm inner adherend, the 36mm overlap length cases were fracture dominated. Hence, the increase in specimen thickness resulted in the increased failure load.

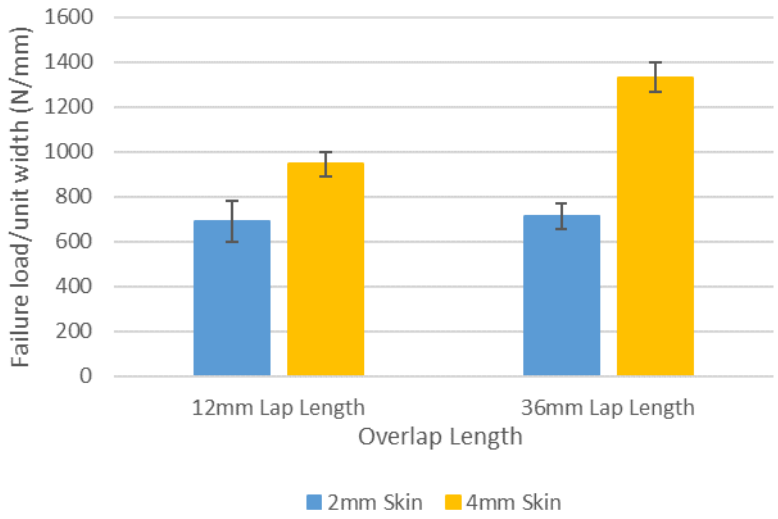

Figure 7.8 - Comparison of increasing adherend thickness on DLJ strength at RTD

According to Equation 6.2, doubling the inner adherend thickness should increase the strength by a factor of $\sqrt{2}$ for fracture controlled cases. However, this is not directly applicable to these cases as it assumes a constant mixed-mode ratio for both inner adherend thicknesses. It also does not factor the effects of the adhesive fillets, which had a greater effect on the 4mm inner adherend case than the 2mm case. The 4mm

inner adherend had a higher peel component at the leading edges due to greater offset from the DLJ mid-plane resulting in larger bending moments.

7.2.4 Effects of Adhesive Thickness on the Double Lap Joint Strength

For the thicker adhesive tests, an overlap length of 24mm was used for the 2mm inner adherend case, while for the 4mm inner adherend case 36mm overlap length was used to compare 0.2mm and 0.8mm nominal adhesive thicknesses. The same overlap length was not used for both inner adherend thickness because initial numerical analysis on the 2mm inner adherend assuming a cohesive failure (i.e. using adhesive properties for the cohesive elements) showed potential fibre failure for the 36mm overlap length case. However, during the tests, it was found that the failure for all 2mm inner adherend cases occurred by delamination within the surface 0° ply of the composite.

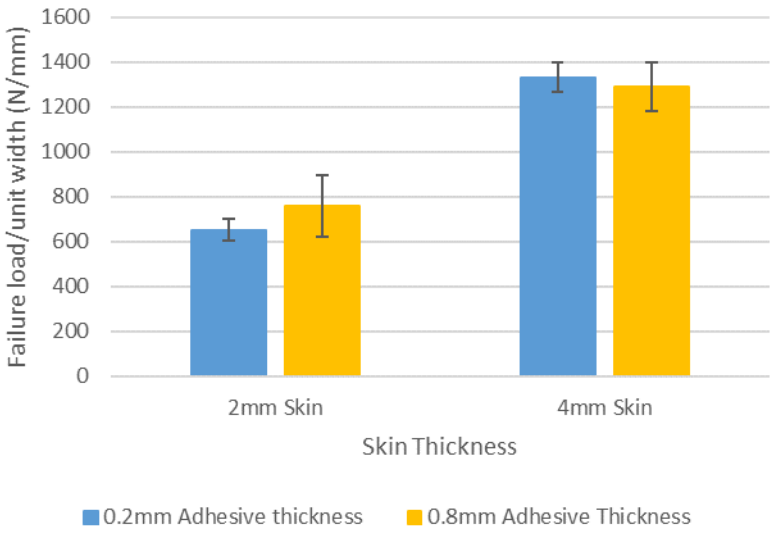

Figure 7.9 - Effects of increasing adhesive thickness on DLJ strength at RTD

Figure 7.9 summarises the experimental results and compares them to the 0.2mm adhesive thickness cases. For the 2mm inner adherend case, the failure modes for both thicknesses were similar, in which the crack initiated at the fillets and propagated into the surface 0° ply. Statistically there was no significant difference in DLJ strength with increased adhesive thickness. However, the 0.8mm adhesive thickness case had considerable scatter due to the variation in adhesive thickness during manufacturing, (thicker adhesive in comparison to 0.2mm adhesive thickness) as the adhesive thickness was not controlled. For the 4mm inner adherends case, the failure mode

observed was also similar for both the 0.2mm and 0.8 adhesive thickness cases. The results show no significant difference in the DLJ strength for the 4mm inner adherend, as for both cases the crack initiated at the fillets and propagation occurred within the surface 0° ply, with little influence of the adhesive at the bondline.

7.2.5 Numerical Modelling Correlation

This section summarises the results from the numerical analysis. The input parameters for the CZM and the different pristine models for F1 and F2 failure modes were discussed in Chapter 6. The numerical modelling results show good correlation with the experimental results as shown in Figure 7.10.

These results were obtained when using the CZM properties in accordance with the simple criterion based on shear strength and fracture energy. When the failure was expected to be controlled by the shear strength of the adhesive, adhesive properties were given for all cohesive elements (F2). When the failure was controlled by the fracture energy, adhesive properties were used for the cohesive elements beneath the fillet and composite properties for the bondline (F1).

At RTD, all 2mm inner adherend cases were fracture dominated, and a good correlation for all overlap lengths was achieved. Modelling using only the adhesive properties significantly overestimated the results. The expected failure mode for the 12mm overlap length for the 4mm inner adherend case was inconclusive, so both models based on the F1 and F2 failure modes were analysed. The numerical results using both methods were similar, confirming the results of the simple analysis and showing that in such cases the lower result from both assumptions could be used. The 36mm overlap length case was fracture dominated and correlated well to the numerical results. Modelling using only the adhesive properties overestimated the results for the 4mm inner adherend, 36mm overlap length case.

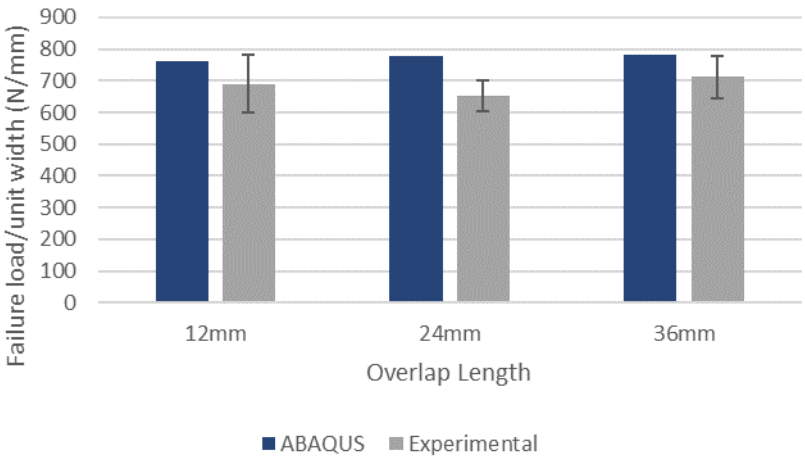

a) 2mm Inner Adherend - RTD

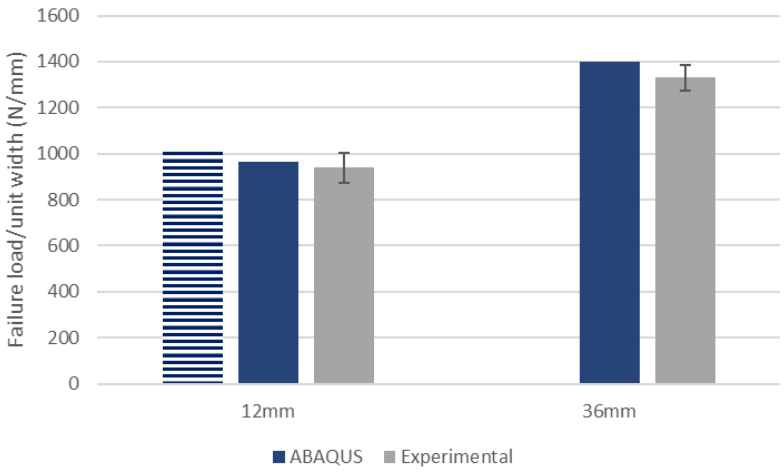

b) 4mm Inner Adherend - RTD

F1, Adhesive properties beneath fillet, composite beneath bondline

F2, Adhesive properties only

Figure 7.10 - Numerical results correlation to experimental results at RTD

7.2.6 Effects of Adhesive Fillet on the Double Lap Joint Strength

Figure 7.11a shows the typical adhesive fillets present for the 4mm inner adherend, 36mm overlap length case where the fillets were not controlled during manufacturing. Another batch of the same configuration (minimal fillet) was manufactured, but with flash tapes around the bondline to constrain the adhesive flow within the bondline. Figure 7.11b shows the resulting fillet formation for this case. As seen, there was a very small area of fillet present. These configurations were tested under in-plane tension at

RTD conditions to understand the effects of the adhesive fillet on the DLJ strength. The longer overlap length case was used for comparison as at RTD these cases were expected to be fracture dominated.

Figure 7.12 shows a significant difference in the failure load/unit width for the uncontrolled vs minimal fillet cases. For the uncontrolled fillet case, the crack initiated from the adhesive fillets. For the minimum fillet case, the crack initiated from the sharp corner at the end of the outer adherend directly into the composite. For both cases, the final failure was influenced by the fracture properties of the composite, i.e. delamination in the surface 0° plies. Hence, the presence of the adhesive fillet significantly increased the DLJ strength for this failure mode (F1) by delaying the initiation of fracture.

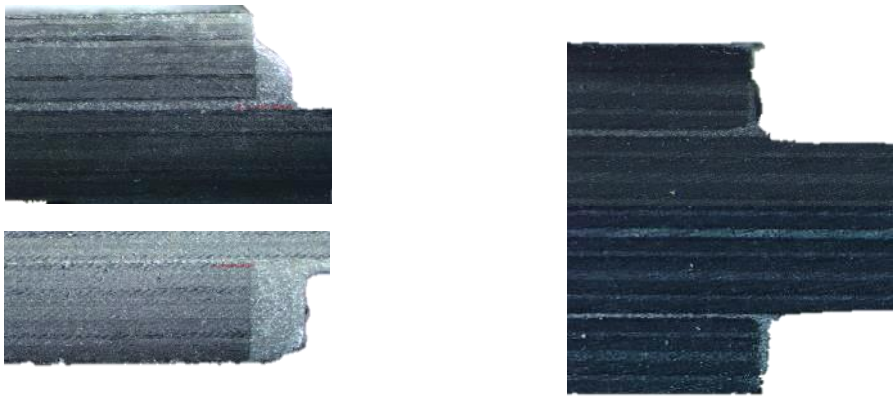

a) Uncontrolled Fillet b) Minimal Fillet

Figure 7.11 - Typical fillet geometry

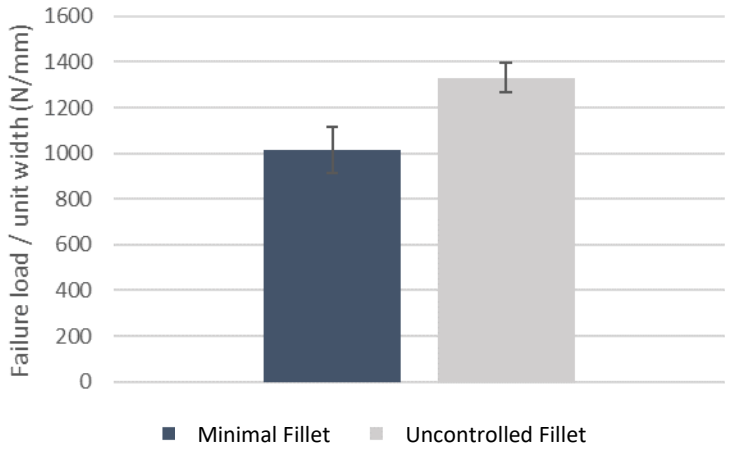

Figure 7.12 - Comparison between uncontrolled vs controlled minimal adhesive fillet for 4mm inner adherend

A numerical analysis on the minimal fillet case was also conducted and compared to the experimental results as shown in Figure 7.13. Modelling the F1 failure mode for cases with fillets, adhesive fillets were modelled with cohesive elements beneath the fillet with adhesive properties. Beneath the bondline, cohesive elements with composite properties were used. For the minimal fillet case, the adhesive fillet and cohesive elements beneath the fillet were removed. The numerical results show good comparison to the experimental results, capturing the failure sequence.

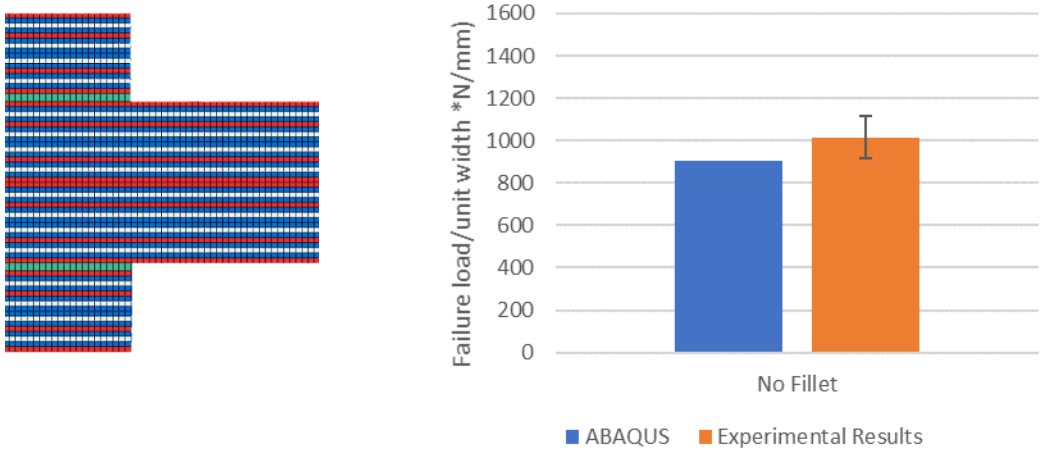

a) No-Fillet model geometry used for numerical analysis

b) Results comparison

Figure 7.13 - Minimal fillet numerical modelling vs experimental results

7.2.7 Stacking Sequence Effects on the Double Lap Joint Strength

A QI stacking sequence of $[45/90/-45/0]_{ns}$ with 45° surface ply orientation was tested for the 4mm inner adherend case and 36mm overlap length. The fillet geometry was not controlled. Figure 7.14 shows the fracture surface for the 45° surface ply case.

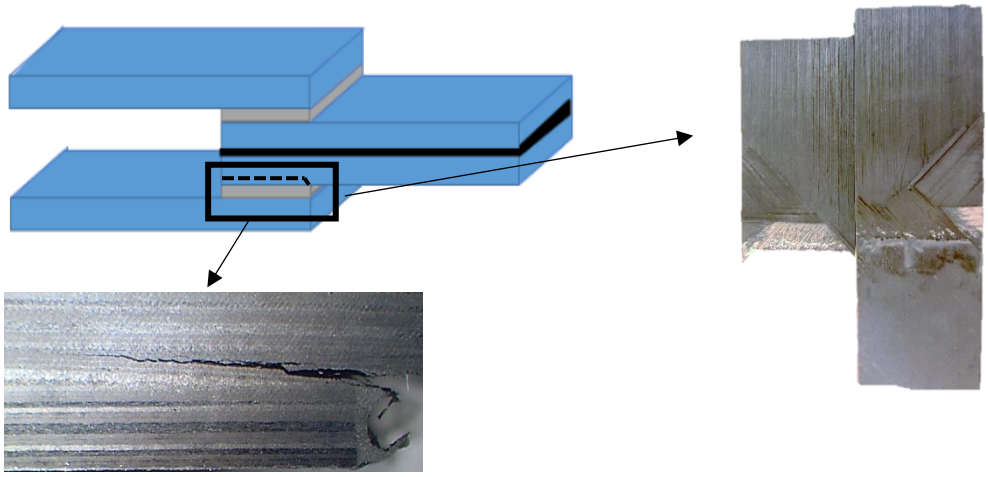

Figure 7.14 - Fracture surface and schematic for 45° QI DLJ

The failure was controlled by delamination in the composite, as the delamination initiated from matrix cracks in the surface ply and migrated into the 45°/90° ply interface as shown in Figure 7.14, with little influence of the adhesive fillet. The 45° surface ply case was compared to the 4mm 0° surface ply QI with and without the fillets as shown in Figure 7.15. The fillets for the 45° surface joints were not controlled. Both the 45° surface ply and 0° surface ply no fillet cases gave similar strengths, lower than the 0° ply with fillets. This was because delamination in the composite could occur from the transverse cracks in the first case, and from the sharp discontinuity in the second case without any delay, due to the lack of adhesive fillets.

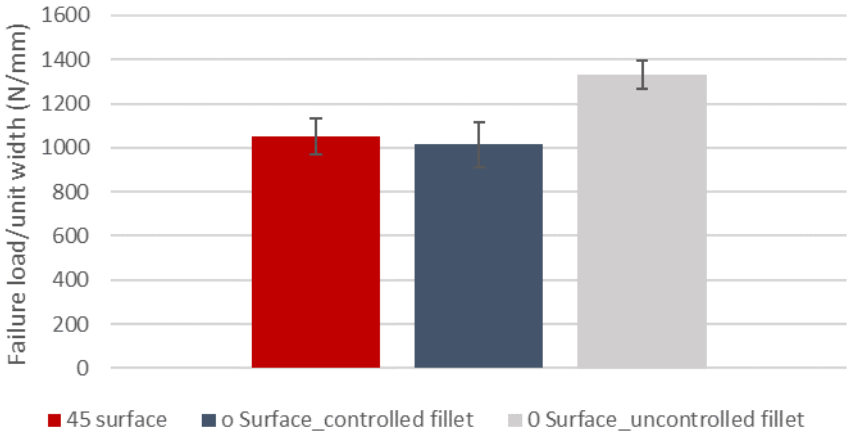

Figure 7.15 - Comparison of QI 45° and 0° surface ply cases

7.3 Hot Temperature Dry – Results and Discussion

7.3.1 Introduction to Test Cases

This section analyses the pristine DLJ results at HTD conditions. The effects of increasing overlap length and inner adherend thickness are discussed. Table 7.2 summarises the experiments conducted at HTD. Consistent with the previous RTD section, the experimental results are explained with simple failure criteria and numerical analysis. For the simple analytical model, the adhesive shear strength was estimated based on linear interpolation (Chapter 6), giving a value of 35MPa. The adhesive G_{IC} used was measured experimentally in Chapter 3, giving a value of 1.05 N/mm.

Table 7.2 - HTD test summary

	2mm Inner Adherend				**4mm Inner Adherend**	
Adhesive Thickness (mm)	12mm	24mm	36mm		12mm	36mm
0.2			✓		✓	✓

7.3.2 Effects of Overlap Length on the Double Lap Joint Strength

At HTD, the effects of increasing overlap length were studied for the 4mm inner adherend case at 12mm and 36mm overlap lengths. Figure 7.16 compares the experimental results.

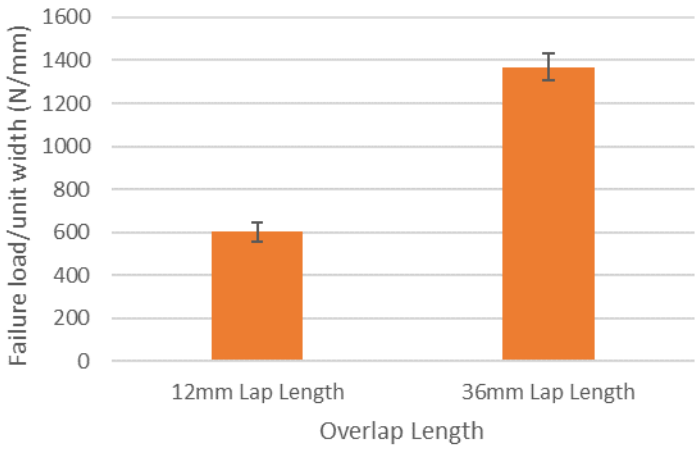

Figure 7.16 - Effects of increasing overlap length on DLJ strength for 4mm inner adherend at HTD

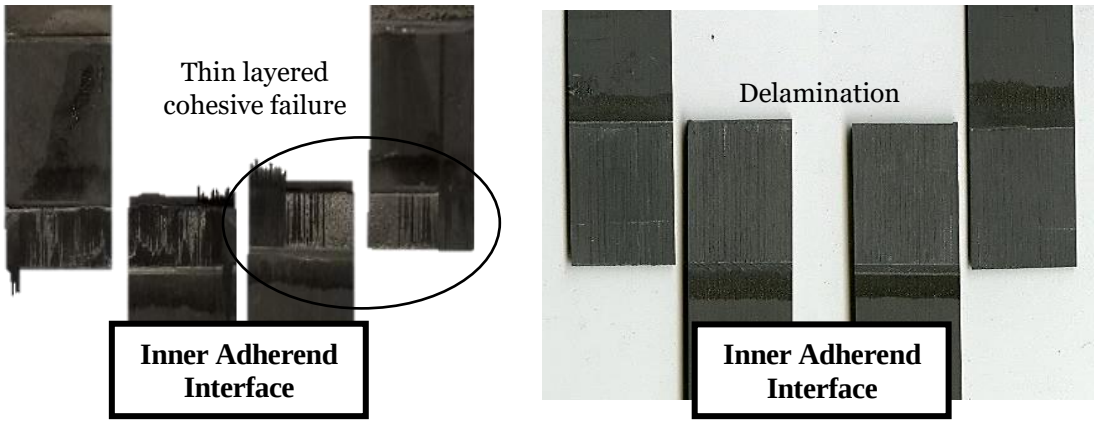

a) 12mm Overlap Length b) 36mm Overlap Length

Figure 7.17 - Fracture surfaces for 4mm inner adherend cases at HTD

The fracture surfaces for these cases are shown in Figure 7.17. The 4mm inner adherend with 12mm overlap length had patches of adhesive on the fracture surface, indicating an F2 failure mode. Whereas for the 36mm overlap length, only the composite surface 0° plies were visible on the fracture surface, indicating a F1 failure mode. Figure 7.18 compares the experimental results to the simple shear and fracture failure criteria.

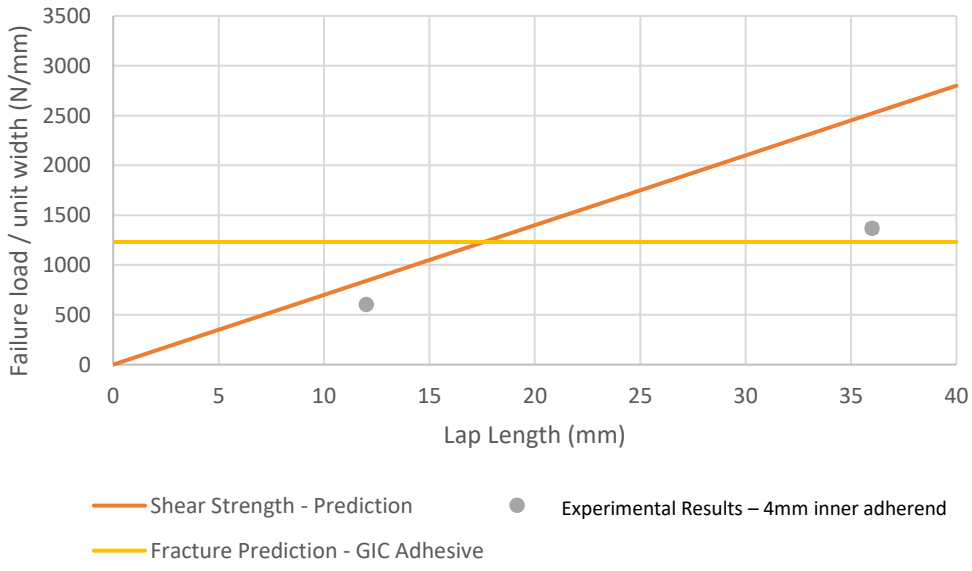

Figure 7.18 - Analytical simple criteria for 4mm inner adherend at HTD

The simple analysis results suggest that the shorter overlap length case was controlled by the shear strength of the adhesive, consistent with the fracture surface for this case. The longer overlap length was fracture dominated, close to the fracture energy calculation based on the adhesive $G_{IC.}$ This suggested the adhesive fillets had a significant effect on the DLJ strength for the longer overlap length case, consistent with the RTD longer overlap length case. The decrease in DLJ strength from the 36mm to 12mm overlap length was due to the change in failure mode, from fracture to strength controlled failure.

7.3.3 Effects of Inner Adherend Thickness on the Double Lap Joint Strength

Figure 7.19 summarises the test results for the 36mm overlap length at HTD. Both 2mm inner adherend and 4mm inner adherend cases failed by fracture propagation in the surface 0° plies as shown in Figure 7.17b and Figure 7.20. Similar to the RTD cases, the 4mm inner adherend thickness case was higher than the 2mm case. Both cases were controlled by the fracture properties, i.e. F1 failure mode. Hence, the increase in specimen thickness resulted in an increased failure load.

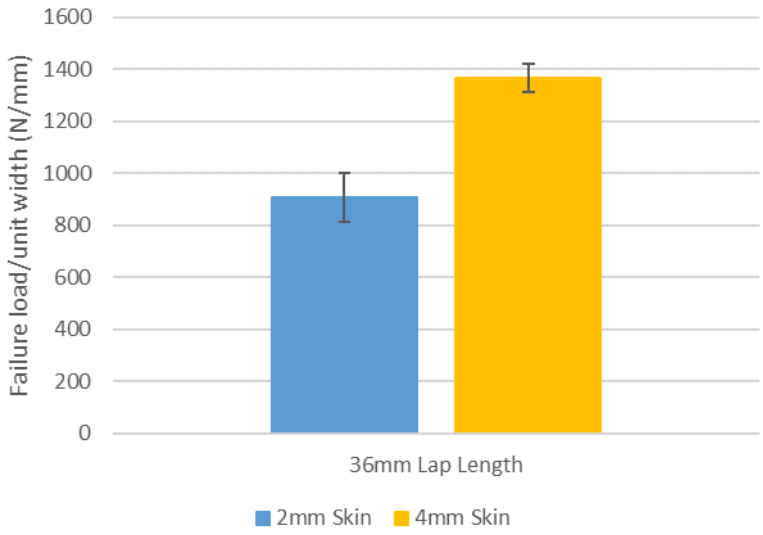

Figure 7.19 - Comparison of increasing adherend thickness on DLJ strength at HTD

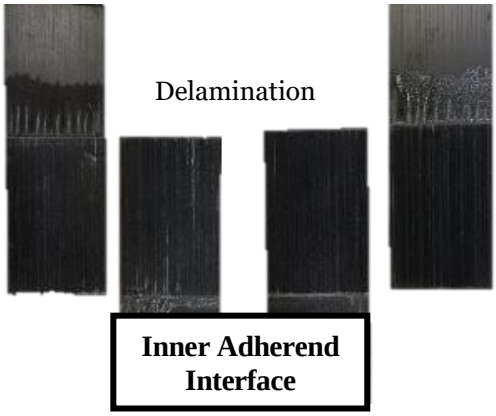

Figure 7.20 - Fracture surface for 2mm inner adherend, 36mm overlap length at HTD

7.3.4 Numerical Modelling Correlation

The experimental results are correlated to the numerical model in this section. As described previously, the numerical models use CZM. Based on the material input parameters at HTD which were described in Chapter 6 the results were compared. The cohesive elements were based on the expected failure mode from the simple analytical criteria. Figure 7.21 compares the experimental results to the numerical analysis.

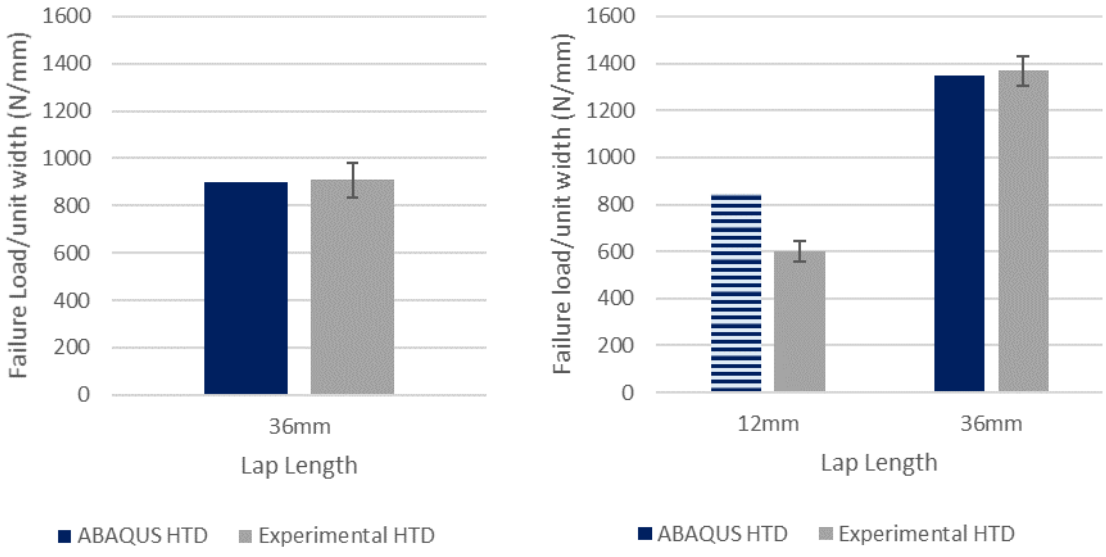

a) 2mm Inner Adherend - HTD

b) 4mm Inner Adherend - HTD

F1, Adhesive properties beneath fillet, composite beneath bondline

F2, Adhesive properties only

Figure 7.21 - Numerical results correlation to experimental results at HTD

The results show good correlation for the longer overlap length when the failure was controlled by the fracture properties (F1). The model overpredicts the 12mm overlap length for the 4mm inner adherend thickness. This could be because the shear strength for the adhesive was estimated as discussed in Chapter 6. The longer overlap length cases were not as sensitive to the adhesive shear strength compared to the shorter overlap length cases, as found from the sensitivity analysis later.

7.4 Hot Temperature Wet – Results and Discussion

7.4.1 Introduction to Test Cases

The effects of overlap length, inner adherend and adhesive thickness on the DLJ strength at HTW are discussed in this section. Table 7.3 summarises the tests conducted at HTW for the pristine DLJ. As with the previous RTD and HTD cases, the experimental results are explained using the simple shear and fracture criteria and numerical models. The input parameter for the analytical model for the adhesive shear strength was estimated and discussed in Chapter 6, giving a value of 28MPa. The adhesive G_{IC} used was 1.13 N/mm, measured experimentally in Chapter 3.

Table 7.3 - HTW test summary

	2mm Inner Adherend				**4mm Inner Adherend**	
Adhesive Thickness (mm)	12mm	24mm	36mm		12mm	36mm
0.2	✓	✓	✓		✓	✓
0.8		✓				✓

7.4.2 Effects of Overlap Length on the Double Lap Joint Strength

Figure 7.22 summarises the experimental results for the 2mm inner adherend case. Increasing the overlap length increased the DLJ strength for the 2mm inner adherend case. Figure 7.23 shows the fracture surfaces for these cases. The 12mm overlap length case had patches of adhesive visible in the fracture surface, indicating a F2 failure

mode. For the 24mm and 36mm overlap length cases, only the surface 0° plies were visible on the fracture surfaces, indicating a F1 failure mode.

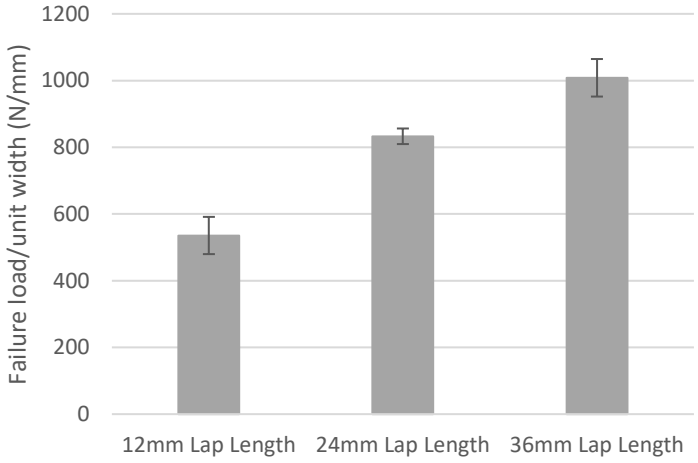

Figure 7.22 - Effects of increasing overlap length on DLJ strength for 2mm inner adherend at HTW

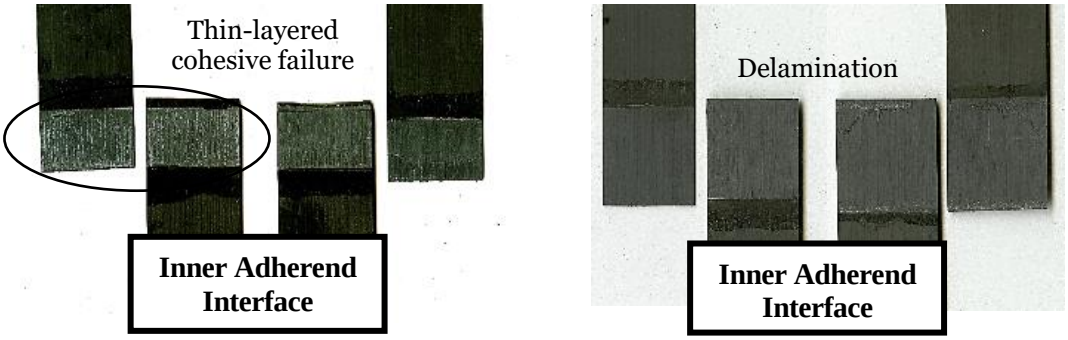

a) 12mm Overlap Length b) 24mm Overlap Length

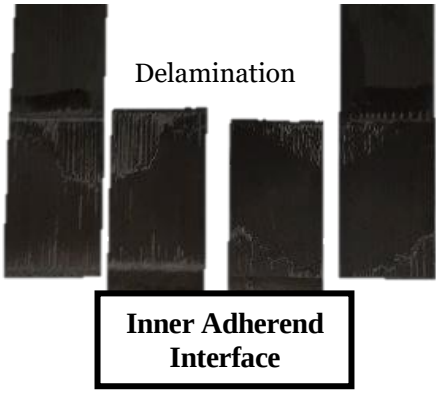

c) 36mm Overlap Length

Figure 7.23 - Fracture surfaces for 2mm inner adherend cases at HTW

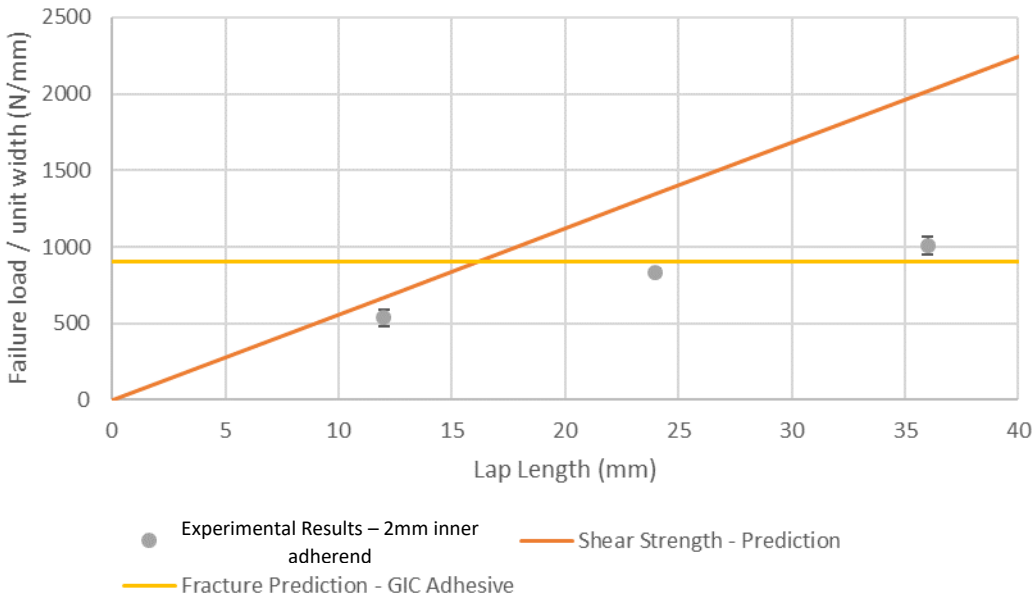

Figure 7.24 - Analytical simple criteria for 2mm inner adherend at HTW

The analytical model based on the shear strength and fracture energy is shown in Figure 7.24. Analysing the results shows that the 12mm overlap length case approached the criterion based on the adhesive shear strength (F2). The longer overlap lengths were close to the criterion based on the fracture energy, i.e. adhesive G_{IC} (F1).

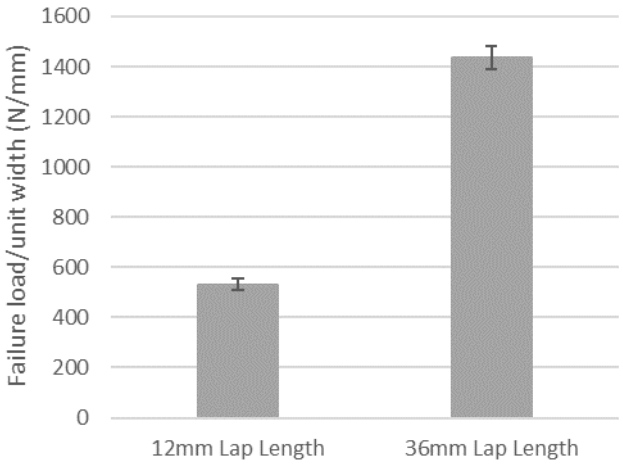

Figure 7.25 - Effects of increasing overlap length on DLJ strength for 4mm inner adherend at HTW

Similarly, for the 4mm inner adherend case, increasing the overlap length increased the DLJ strength at HTW (Figure 7.25). The fracture surfaces, shown in Figure 7.26 show patches of adhesive on the bondline for the 12mm overlap length case, whereas

for the 36mm overlap length case, 0° plies were visible across the inner adherend/outer adherend interfaces.

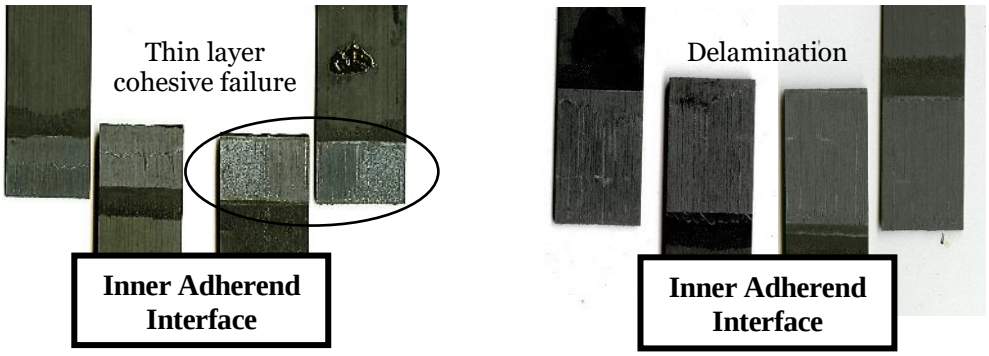

a) 12mm Overlap Length b) 36mm Overlap Length

Figure 7.26 - Fracture surfaces for 4mm inner adherend cases at HTW

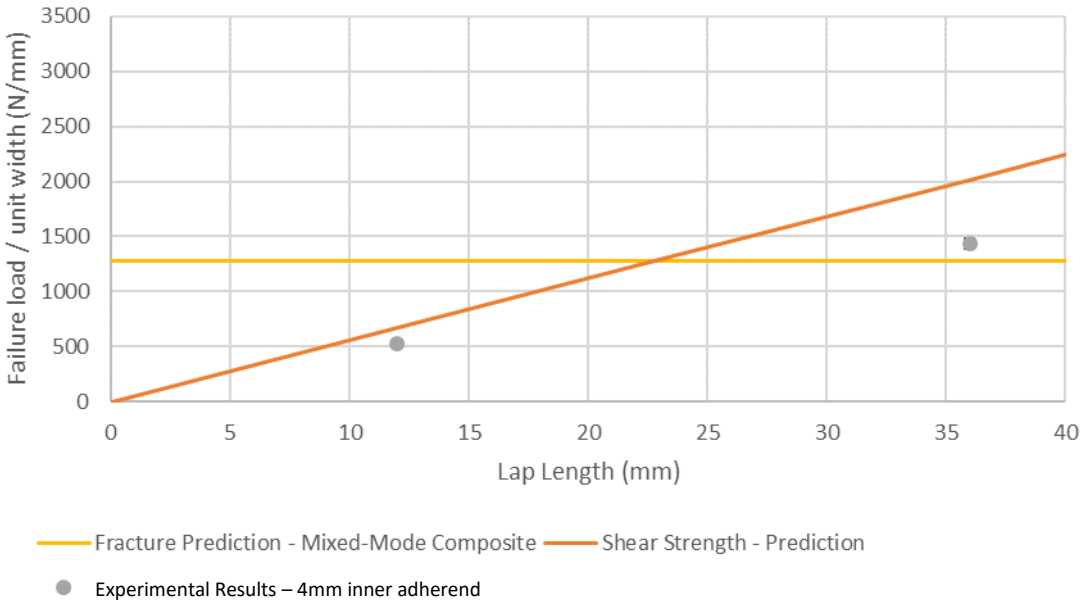

Figure 7.27 - Analytical simple criteria for 4mm inner adherend at HTW

Figure 7.27 compares the experimental results to the analytical model based on shear strength and fracture energy. The shorter overlap length was controlled by the shear strength of the adhesive (F2), whereas the longer overlap length was controlled by the fracture energy (F1). Consistent with the previous RTD and HTD cases, the longer overlap length with the adhesive fillets approaches the fracture energy calculation based on the adhesive G_{IC}, due to the influence of the adhesive fillet on the F1 failure mode. For both inner adherend thickness, the DLJ strength increased with overlap

length. But the increase was not linear with the overlap length as the failure mode changed from shear controlled to fracture controlled failure.

7.4.3 Effects of Inner Adherend Thickness on the Double Lap Joint Strength

The results are presented in Figure 7.28. For the 12mm overlap length case, the DLJ strengths for both 2mm and 4mm inner adherend cases were similar (within experimental scatter) as for both cases the failure mode was thin layered cohesive, i.e. controlled by the adhesive (F2). The failures for both these cases were shear strength dominated, as analysed by comparing the experimental results to the simple shear strength failure criterion in the previous section. This shows that if the failure of the DLJ was controlled by the shear strength of the adhesive, the DLJ strength would be relatively insensitive to the inner adherend thickness.

Comparing the 36mm overlap length cases shows a significant increase in DLJ strength from 2mm to 4mm inner adherend thickness. As both these failures were controlled by fracture properties, the increased specimen thickness resulted in increased failure load.

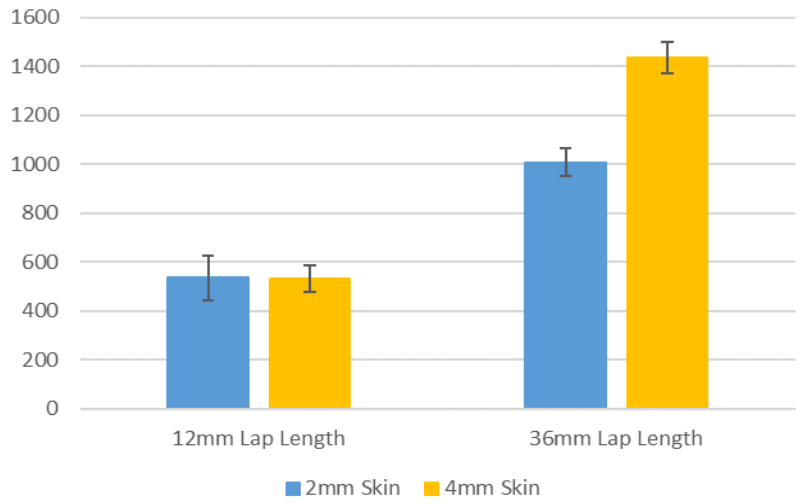

Figure 7.28 - Comparison of increasing adherend thickness on DLJ strength at HTW

7.4.4 Effects of Adhesive Thickness on the Double Lap Joint Strength

Figure 7.29 summarises the test results for both 2mm and 4mm inner adherend cases. As with the RTD case, the overlap length used for the 2mm case was 24mm, while a 36mm overlap length was used for the 4mm case. For the 4mm case, the overall

thickness of the DLJ for the 0.8mm adhesive thickness case was at the upper limit for the mechanical grips, and a couple of specimens were damaged when placed in the grips. Only 2 specimens gave valid results.

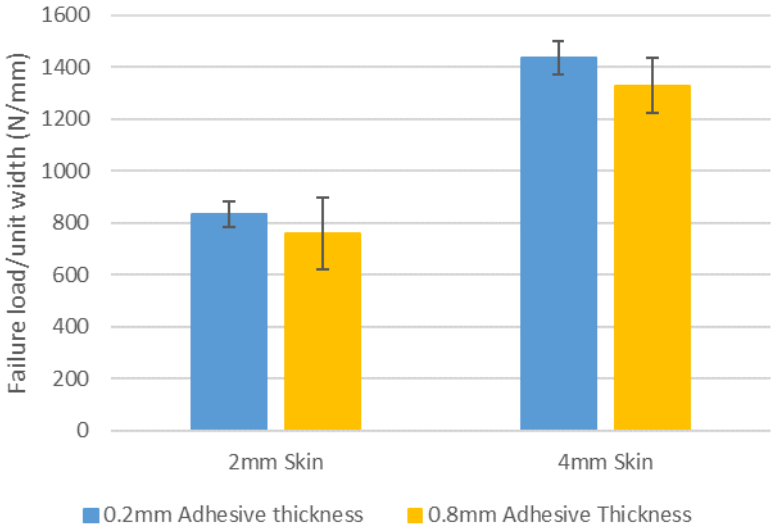

Figure 7.29 - Effects of increasing adhesive thickness on DLJ strength at HTW

For both the 2mm and 4mm inner adherend, no significant difference in the DLJ strength was observed comparing the 0.2mm and 0.8mm adhesive thickness. The failure was controlled by crack propagation within the adhesive fillet followed by migration into the surface 0° ply (F1) for both cases. This was consistent with the 0.2mm adhesive thickness case. Hence, as the crack propagation occurred within the surface plies of the inner adherend without the influence of the adhesive bondline, the DLJ was insensitive to increase in adhesive thickness.

7.4.5 Numerical Modelling Correlation

The experimental results are correlated to the numerical models for the HTW conditions in this section. Figure 7.30 summarises the numerical results and compares them to the experimental cases. Consistent with the previous section, based on the analytical failure criteria, adhesive properties were given for the cases controlled by the shear strength and is represented by the striped pattern. For failure due to fracture propagation, adhesive properties were given to the cohesive elements beneath the fillet, and composite properties beneath the bondline.

The numerical comparison shows good correlation to the experimental results at HTW for the shorter and intermediate overlap length cases. For the longer overlap length (F1 failure mode), the numerical model slightly underpredicts the failure load. This could be due to the significant increase in plastic deformation of the adhesive at HTW.

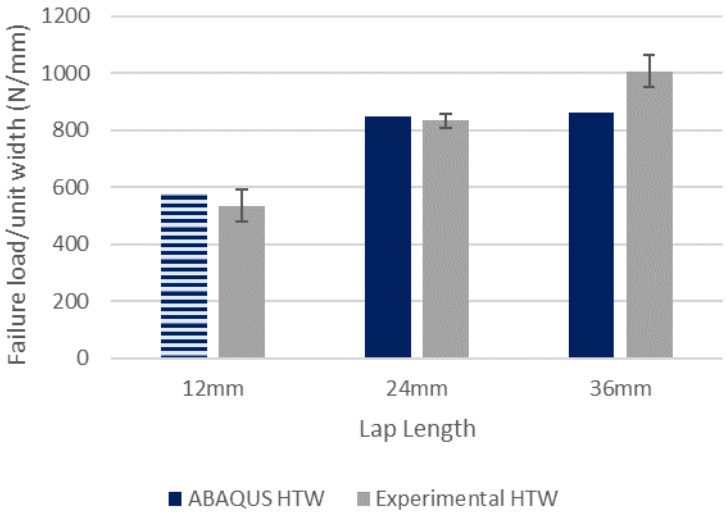

a) 2mm Inner Adherend -HTW

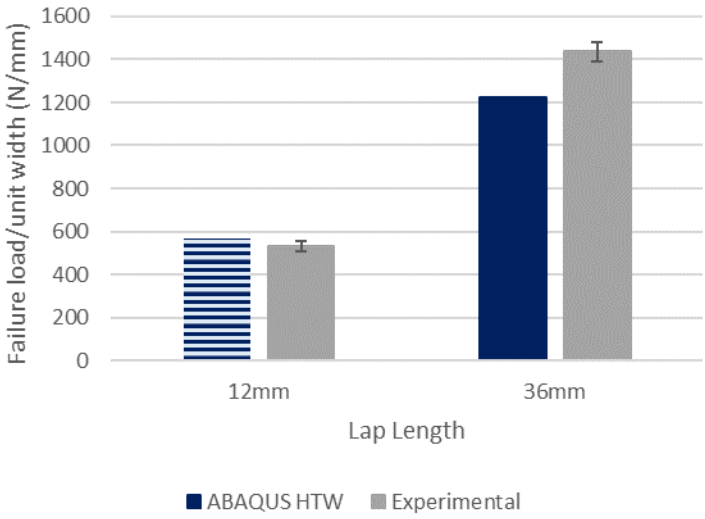

b) 4mm Inner Adherend – HTW

F1, Adhesive properties beneath fillet, composite beneath bondline

F2, Adhesive properties only

Figure 7.30 - Numerical results correlation to experimental results at HTW

7.5 Environmental Effects on Pristine Double Lap Joints Discussion

7.5.1 Sensitivity Analysis

The simple analytical model was used to understand the failure modes for different DLJ cases. However, it is not a predictive model based on the assumptions used for the criteria and complex failure modes, such as crack migration from the adhesive fillets which can influence the failure.

To understand the key material parameters that influenced the failure for the different pristine test cases, a sensitivity analysis on the cohesive element input properties was conducted on the numerical models. The through-thickness tensile strength (Sigma33), shear strength (Sigma13), Mode I (G_{IC}) and Mode II (G_{IIC}) fracture energies for the cohesive elements were varied by ±50% for the F1 failure mode. The results are shown as a percentage increase/decrease from the baseline value for each configuration. The values highlighted in red show a large decrease, whereas the values highlighted in green show a large increase in DLJ strength. Results in yellow meant the values were not sensitive to the change in input properties. The sensitivity analysis is presented in the discussion section below and used as an aid during discussion when comparing the experimental trends.

7.5.2 Overlap Length Discussion for 2mm Inner Adherend

Figure 7.31 compares the DLJ strength for the three overlap lengths tested for the 2mm inner adherend case at RTD, HTD and HTW conditions. For the 12mm overlap length case, with increased temperature and moisture the DLJ strength decreased. For the longer overlap lengths, increasing temperature and moisture increased the DLJ strength.

The reduced DLJ strength for the 12mm overlap length cases between RTD and HTW was due to the change in failure mode. At RTD, the failure was controlled by fracture propagation (F1) whereas at HTW the failure was controlled by the shear strength of the adhesive (F2). This was because the adhesive strength properties reduced significantly due to the increased temperature and moisture, hence making this the preferred mode for failure at HTW for the shorter overlap length cases.

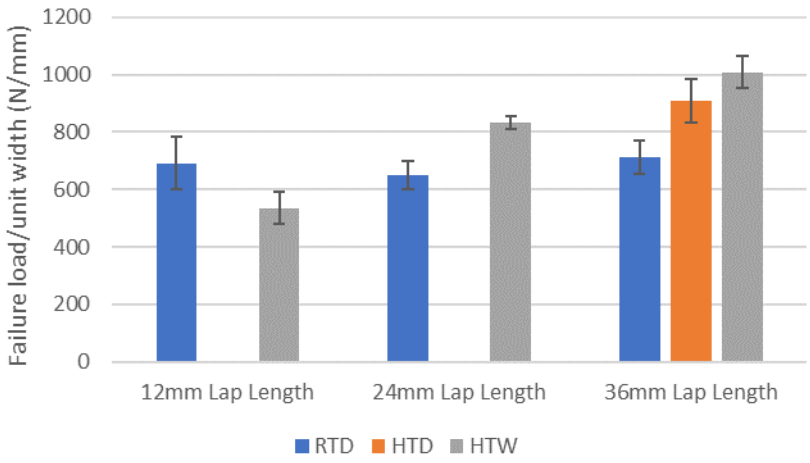

Figure 7.31 - 2mm inner adherend overlap length summary

Adhesive

	+50%	*-50%*
S33	-1.3	-4.4
S13	1.4	-3.6
G_{IC}	4.6	-13.3
G_{IIC}	0.7	-0.6

a) % increase/ decrease for 2mm inner adherend, 36mm overlap length, adhesive properties

Composite

	+50%	*-50%*
S33	-0.4	0.6
S13	3.1	-0.4
G_{IC}	9.0	-13.2
G_{IIC}	3.2	-7.6

b) % increase/ decrease 2mm inner adherend, 36mm overlap length, composite properties

Figure 7.32 - Sensitivity analysis for F1 failure – For 2mm inner adherend, 36mm overlap length at RTD

The failures for the longer overlap length cases were fracture dominated, and for these cases the DLJ strength increased with increasing temperature and moisture. This was consistent with the increase in Mode I fracture toughness from RTD to HTW as found from the characterisation tests (Chapter 3 and 4). All other parameters such as the strengths and G_{IIC} decreased from RTD to HTW for both composite and adhesive. Hence, the increase in DLJ strength for the 2mm inner adherend with temperature and moisture was because the longer overlap length cases were more influenced by the G_{IC} parameter than other material parameters. A sensitivity analysis was conducted on the 2mm inner adherend case (Figure 7.32), based on the F1 failure mode on the

36mm overlap length case at RTD. Both the adhesive CZM properties beneath the cohesive elements and composite properties in the bondline were varied by +/-50%. The results show that G_{IC} of both adhesive and composite were the most sensitive parameters.

7.5.3 Overlap Length Summary for 4mm Inner Adherend

Figure 7.33 compares the failure load/unit width of the 12mm and 36mm overlap length for the 4mm inner adherend case. For the shorter overlap length, a significant drop in DLJ strength was observed from the RTD to HTD and HTW cases. There was no significant difference in the DLJ strength for the longer overlap length cases for all three conditions.

A change in fracture surface was also visible for the specimens tested at hot temperatures. At RTD, for the 12mm overlap length case, the failure mode was at the critical overlap length of being controlled by strength and fracture. The fracture surfaces for the HTD and HTW 12mm overlap length cases show patches of adhesive visible and the simple analytical criterion indicated the failure was controlled by the shear strength of the adhesive (F2). The decrease in the shear strength with increased temperature and moisture explains why a reduction in DLJ strength was observed for the 12mm overlap length case.

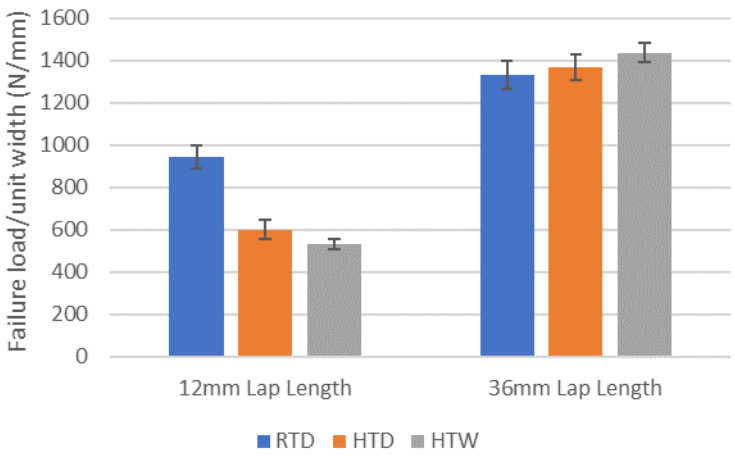

Figure 7.33 - 4mm inner adherend overlap length summary

For the longer overlap length, the failure was fracture dominated and controlled by an initial region of adhesive and composite properties as discussed in the earlier sections.

From the characterisation test results, it was found that the G_{IC} increased and G_{IIC} decreased with temperature and moisture for both the composite and adhesive. There was a slight increase in DLJ strength, but results were within the experimental scatter for the 36mm overlap length. The sensitivity analysis (Figure 7.34) shows that the 4mm inner adherend, 36mm overlap length was primarily sensitive to G_{IC} of both the composite and adhesive. The model also showed that this case was more sensitive to the shear strength of the composite, than the 2mm inner adherend case. Hence, the increase in G_{IC} and decrease in strengths cancelled each other out for the 4mm inner adherend case, resulting in no significant difference in DLJ strength from RTD to HTW.

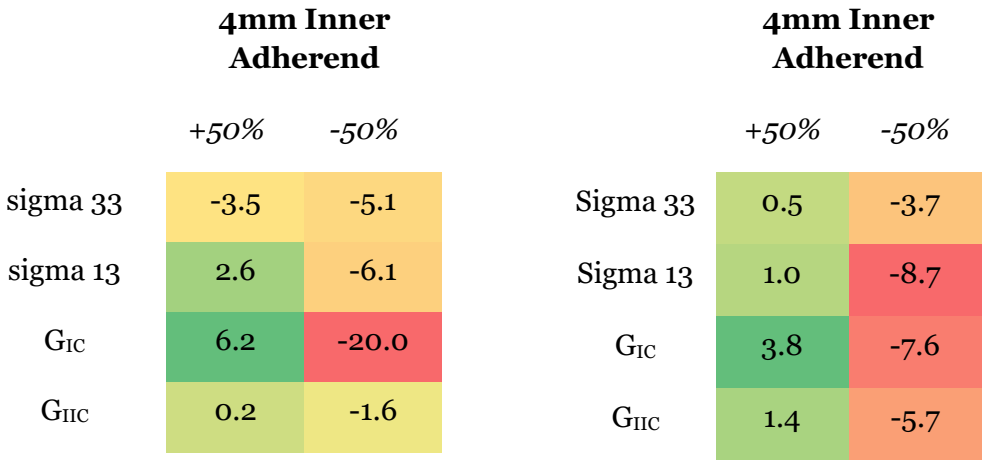

a) % increase/ decrease for 4mm inner adherend, 36mm overlap length, adhesive properties

b) % increase/ decrease 4mm inner adherend, 36mm overlap length, composite properties

Figure 7.34 - Sensitivity analysis for F1 failure – For 4mm inner adherend, 36mm overlap length at RTD

7.5.4 Inner Adherend Thickness Effects Summary

This section compares the adherend thickness effects to understand how the DLJ strength varies for the 2mm and 4mm inner adherend cases at different environmental conditions. Figure 7.35 shows the DLJ strength for the 12mm overlap length at RTD and HTW. For both inner adherend thicknesses, the DLJ strength was higher at RTD.

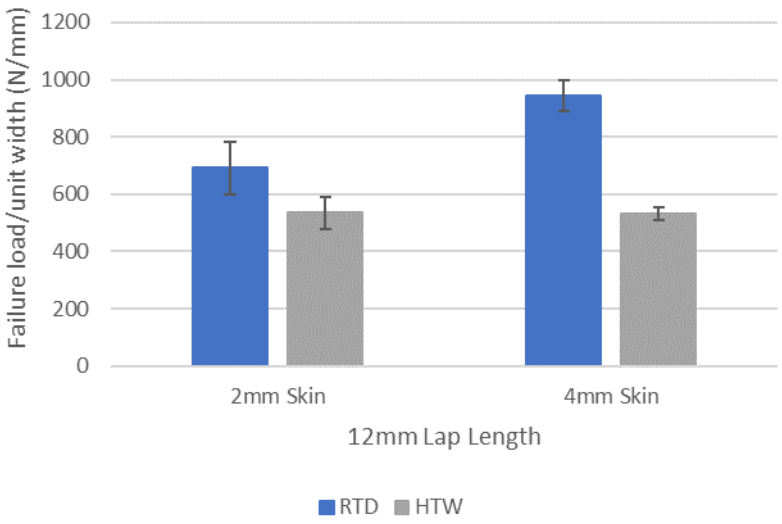

Figure 7.35 - Comparison for 12mm overlap length with different inner adherend thicknesses

The relative decrease in DLJ strength from RTD to HTW was greater for the 4mm inner adherend case than the 2mm inner adherend case. For the 2mm case, as explained previously, a change in failure mode was observed, from an F1 failure at RTD controlled by fracture energy to F2 failure at HTW controlled by the shear strength. For the 4mm inner adherend, 12mm overlap length case at RTD the failure was at the critical overlap length between a strength and fracture controlled failure. At HTW, the failure was controlled by the shear strength of the adhesive, i.e. an F2 failure mode. As the 4mm RTD case approached the shear strength of the adhesive, the decrease in DLJ strength corresponds to the decrease in shear strength of the adhesive from RTD to HTW.

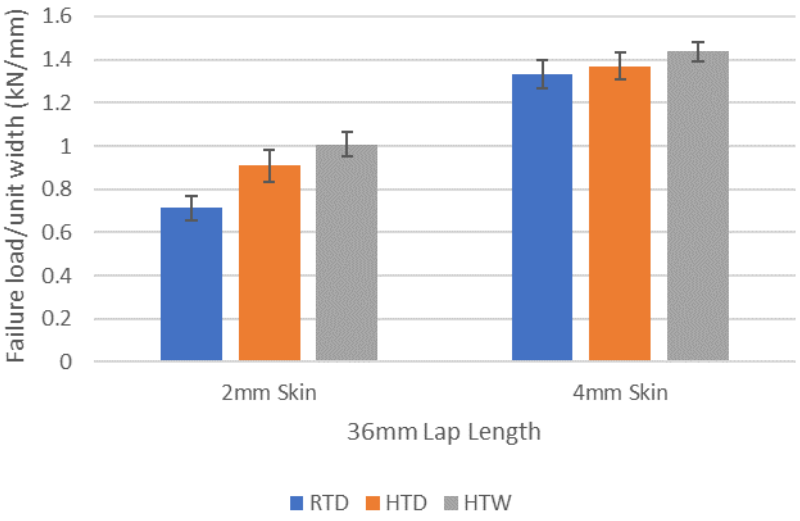

Figure 7.36 - Comparison for 36mm overlap length with different inner adherend thicknesses

The 36mm overlap length results for 2mm and 4mm inner adherends are compared in Figure 7.36. An opposite trend to the 12mm overlap length was observed in that the joint strengths increased with temperature and moisture, as the failure for all cases was more fracture rather than strength dominated. The increase in DLJ strength was more distinct for the 2mm inner adherend case compared to the 4mm inner adherend. As only G_{IC} increased with temperature and moisture, this suggests that the 2mm inner adherend was more sensitive to G_{IC}. The sensitivity analysis in Figure 7.32 and Figure 7.34 at RTD showed that the 2mm inner adherend was more sensitive to the composite G_{IC} than the 4mm inner adherend, while being insensitive to the composite strength parameters. The 4mm inner adherend case was more sensitive to the composite shear strength and G_{IIC} values, which decreased at HTD and HTW from RTD. Hence the 2mm inner adherend case had an increase in DLJ strength with increased temperature and moisture.

7.6 Conclusions

The effects of environmental conditions on the DLJ strength was studied for different geometrical configurations. At RTD for the 2mm inner adherend, the DLJ strength was similar from 12mm to 36mm overlap length. This was because all cases were controlled by fracture propagation within the adhesive and composite. For the 4mm inner adherend case, the DLJ strength increased from 12mm to 36mm overlap length. The failure for the shorter overlap length case was close to the critical overlap length at which the failure mode would be expected to change from being controlled by the strength properties to the fracture properties. The longer overlap length was fracture dominated.

For both 2mm and 4mm inner adherend thicknesses, increasing the temperature and moisture decreased the DLJ strength for the shorter overlap length as these cases were strength dominated. The strength properties of both composite and adhesive decreased at high temperature and moisture. For the longer overlap length cases, the failure was mainly fracture dominated, hence the DLJ was dependent on the combined effects of the fracture properties of the adhesive and composite (G_{IC} increased, while G_{IIC} decreased with temperature and moisture). The effect of increasing adhesive thickness was also studied at different environmental conditions for the longer overlap

length case. As the failure was fracture dominated, with crack initiating at the adhesive fillets and migrating into the composite for the longer overlap lengths, i.e. with no influence of the bondline adhesive, there was no significant difference in DLJ strength.

The effects of adhesive fillets were studied in this chapter. The tests comparing the uncontrolled and minimal fillet cases showed a significant difference in joint strength. This was due to the failure mode present at RTD conditions for the baseline configuration, where the failure was initially controlled by the region of adhesive at the adhesive fillet. For the minimal fillet case, this region was not present, hence significantly decreased the joint strength. The effect of changing surface ply orientation for the QI stacking sequence on the joint strength was also studied at RTD condition. The 45° surface ply case was compared to the 0° surface ply case with and without the adhesive fillet. Both the 45° surface ply and 0° surface no fillet cases gave similar strengths, lower than with fillets.

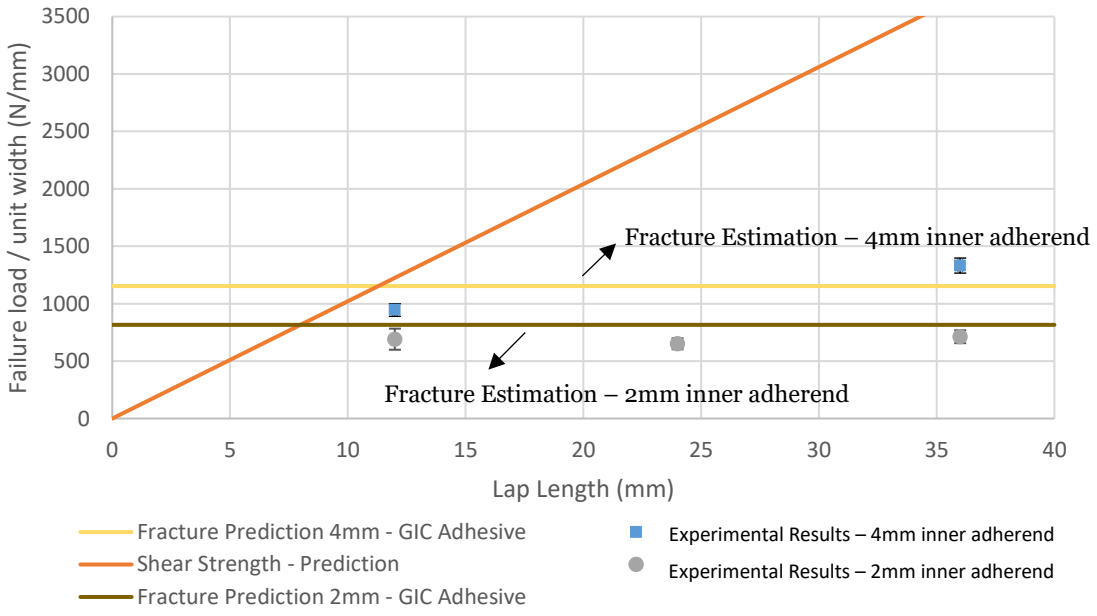

a. Summary of analytical criteria at RTD

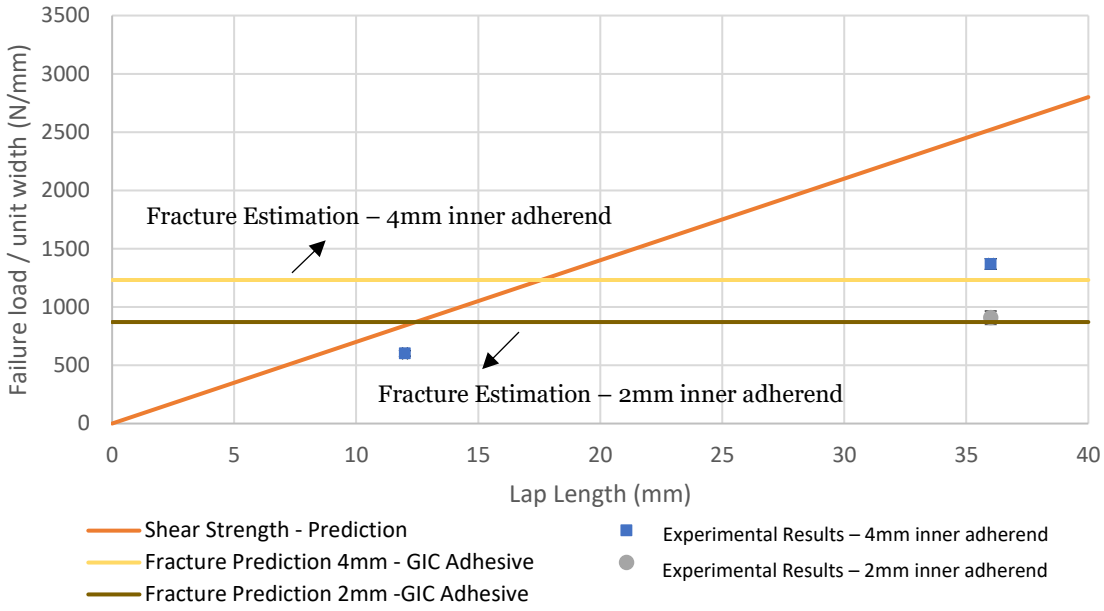

b. Summary of analytical criteria at HTD

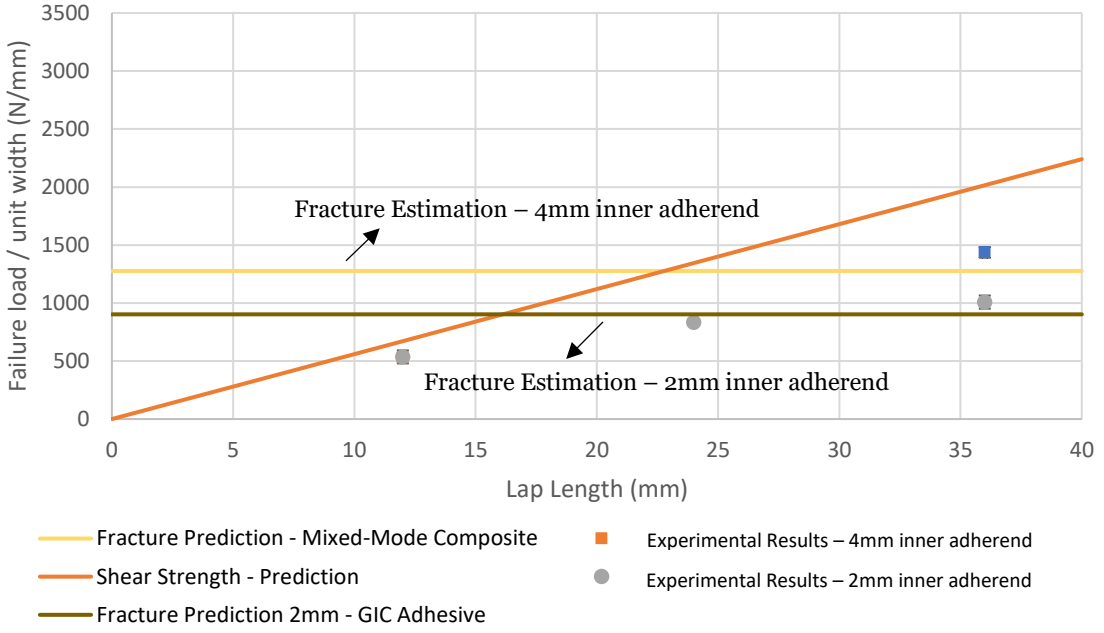

c. Summary of analytical criteria at HTW

Figure 7.37 – Summary of the analytical simple criteria to determine failure mode for all experimental results

Analytical calculations based on shear strength and fracture energy were also conducted and compared to the experimental results to understand what controls the different failure modes observed. Figure 7.37 summarises all the test results with the analytical criteria. Depending on the input properties, at a critical lap length, the

failure mode changed from a failure controlled by the shear strength of the adhesive (F2) to failure controlled by fracture propagation within the adhesive and composite (F1). This was not a truly predictive model, for example, for the F1 failure, the analytical fracture energy criterion assumed only the adhesive G_{IC} to control failure, but from the numerical sensitivity analysis it was found that the adhesive and composite properties combined influenced the failure. The analytical model gives a better understanding of the DLJ behaviour and failure modes of the pristine DLJ.

Table 7.4 - Comparison of Experimental results to Numerical Model

Environmental Conditions	Inner Adherend Thickness (mm)	Overlap Length (mm)	Experimental Result (N/mm) C.V %	ABAQUS Prediction (N/mm)	% difference
RTD	2	12	691 (13%)	757	9.2
		24	651 (7%)	773	17.2
		36	713 (7%)	777	8.7
	4	12	945 (6%)	963	2.3
		36	1332 (5%)	1401	5.2
HTD	2	36	908 (8%)	901	-0.9
	4	12	602 (7%)	833	32.3
		36	1369 (5%)	1350	-1.4
HTW	2	12	536 (10%)	579	7.7
		24	833 (3%)	848	1.8
		36	1008 (6%)	864	-15.4
	4	12	531 (4%)	569	6.9
		36	1436 (3%)	1226	-15.8

Numerical models were created by ABAQUS/Explicit for the pristine cases for the two failure modes observed, F1 and F2. Based on the analytical criteria in Figure 7.37, the input parameters for the CZM were decided. The experimental results were compared with the numerical predictions and a good correlation was achieved for most cases. The summary of the correlation between the experimental results and ABAQUS numerical modelling results is shown in Table 7.4. An average difference of 9.6% was achieved comparing all the cases.

Only the fracture propagation criterion based on the adhesive G_{IC} is used for the simple analysis in this thesis. This was because adhesive fillets were present for all DLJ tested at different environmental conditions, and these fillets which were mainly subjected to Mode I loading and had a significant effect on DLJ strengths. For cases without adhesive fillets (minimal fillet cases) the failure occurred within the surface 0° ply without the influence of the adhesive. This type of failure was also observed for the 45° surface ply cases at RTD. Hence, for a conservative prediction, the mixed-mode DLJ G_C could be used for the failure criterion based on fracture energy.

CHAPTER 8

EFFECTS OF ENVIRONMENTAL CONDITIONS ON DOUBLE LAP JOINTS WITH IMPACT AND DISBOND

8.1 Introduction

This chapter analyses the effect of through thickness impact on the residual strength of the Double Lap Joint (DLJ) and the effect of an artificial defect, i.e. a disbond on the strength of the DLJ at different environmental conditions. The environmental conditions for Hot Temperature Dry (HTD) and Hot Temperature Wet (HTW) are consistent with the previous sections. The Hexcel HexPly IM7/8552 carbon/epoxy pre-preg and the Hexcel Redux 319 film adhesive with a 0.2mm nominal thickness are used for impact and disbond DLJ tests. A Quasi-isotropic (QI) stacking sequence with a surface 0° ply of $[0/45/90/-45]_{4s}$ is used for the inner adherend with an overlap length of 36mm. The manufacturing and the surface preparation methods used are similar to the pristine DLJ. The artificial defect for the disbond cases is inserted during the manufacturing process using Flomfilm 100 cast PTFE film of 12µm thickness, the same material used for the insert film in the characterisation tests.

The residual tensile strength after impact is studied for two impact energy levels of 2J and 3J at Room Temperature Dry (RTD) conditions. After the impact, the damage for each case is characterised before the residual tensile test. For HTD and HTW conditions, the residual tensile tests on only the 2J impact energy case are conducted. The artificial defect lengths for the disbond cases are chosen to be similar to the impact

damage lengths at 2J and 3J, to directly compare the DLJ strength after impact and disbond cases. Two disbond lengths at the inner adherend (inner adherend)/adhesive interface are tested for RTD, HTD and HTW conditions. The effect of changing the position of the disbond with respect to the adhesive film is also studied at RTD conditions, for the same disbond lengths at the outer adherend/adhesive interface. An analytical failure criterion based on fracture energy is applied to understand the failure mode. Numerical models using Cohesive Zone Models (CZM) are used to understand the disbond DLJ performance at different environmental conditions through sensitivity analysis.

8.2 Residual Tensile Tests after Impact

8.2.1 Impact Testing Configuration

The DLJ configuration used for the impact tests had an inner adherend thickness of 4mm, a nominal adhesive thickness of 0.2mm and the lap length was 36mm. The typical impact test set-up and schematic is shown in Figure 8.1.

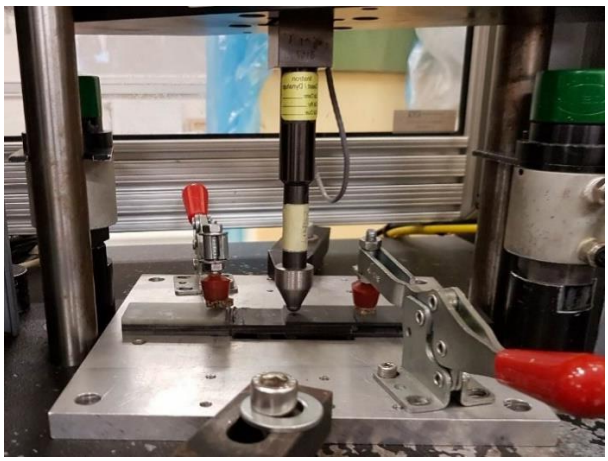

a) Joint was gently clamped on the metallic frame in the impact tower

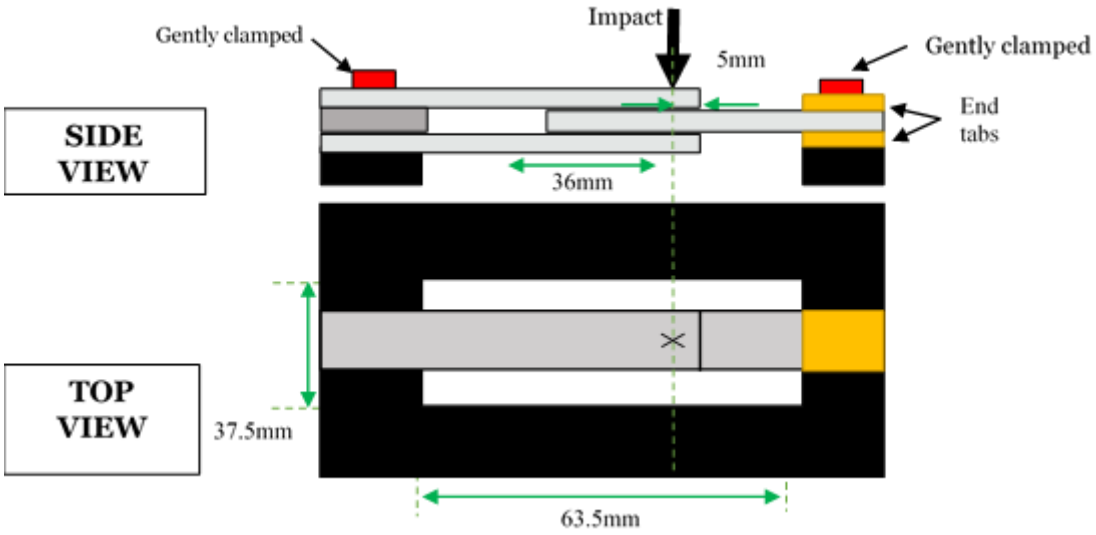

b) Schematic of impact test set-up

Figure 8.1 – Impact set-up

The impact location was chosen to be 5mm from the leading edge of the specimen, as from the literature review it was found that this location presented the most critical case. Another point to note is that a beam configuration was used, where only the two ends of the beam were supported. The window in which the specimens were placed was 37.5mm×63.5mm and the indenter tip diameter used was 8mm. The impactor weighed 4.9kg and the impact height varied from 30mm to 40mm depending on the impact energy. The impact velocity was measured just before impact application.

8.2.2 Trial Static Indentation Tests

A static indentation test was initially conducted to understand the response of the DLJ under through thickness loading. The test was stopped when a load drop was observed at a force of around 2kN and no visible damage was observed on the specimen. To understand the failure mechanisms and damage occurring in more detail, X-ray Computed Tomography (CT) scan images of the specimen were taken as shown in Figure 8.2.

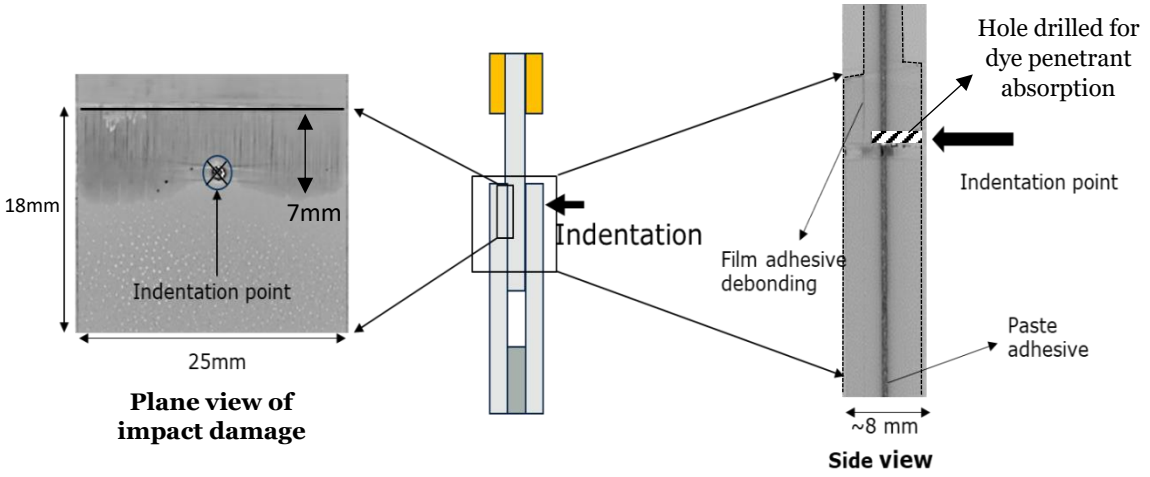

Figure 8.2 – CT scan images from the indentation test

To prepare the specimen for the CT scan, a hole was drilled (1mm diameter) at the indentation point so that dye penetrant could be absorbed through the specimen thickness to show any damage within the composite. The dye is absorbed by discontinuities within the DLJ due to the impact damage. From the CT scan debonding was observed at the adherend/adhesive interface near the inner adherend, as shown in Figure 8.2. For pure laminates, a higher load is required to create damage within the composite. However, for the DLJ, the failure initiated due to the high peel component at the edges of the DLJ, microscopic cracks due to grit blasting combined with the simple support along two edges, lead to delamination within the sub-laminate surface ply (0° plies visible from CT scan plane view). No damage was found in the paste adhesive. The damage length for the first load drop was about 7mm. The crack propagation was sudden when the energy reached a certain value.

8.2.3 Through-thickness Impact Tests

Through trial impact tests, it was found that a similar force to that in the static indentation test was achieved at 2J energy. A higher energy level (3J) was also tested. All impact tests were conducted at RTD conditions. The impact velocity ranged from 0.986 m/s (2J case) to 1.04 m/s (3J case). The residual tensile tests for the 2J impact case were conducted at RTD, HTD and HTW conditions. To analyse the damage, ultrasonic C scans were used using the DolphiCam, a handheld, mobile NDT scanning device. For one specimen for each impact energy case, CT scans were also taken which were then compared to the C-scan images. A good correlation was found, hence for all

the impacted specimens, the C scan images were used to quantify the amount of damage. The CT scan images for the impact case revealed that the damage pattern was similar to that in the indentation case, with debonding occurring at the adherend/adhesive interface near the inner adherend.

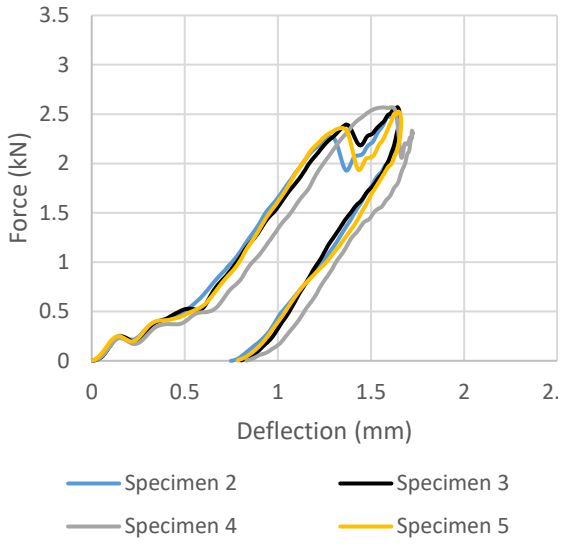

Figure 8.3 – 2J Impact force-displacement

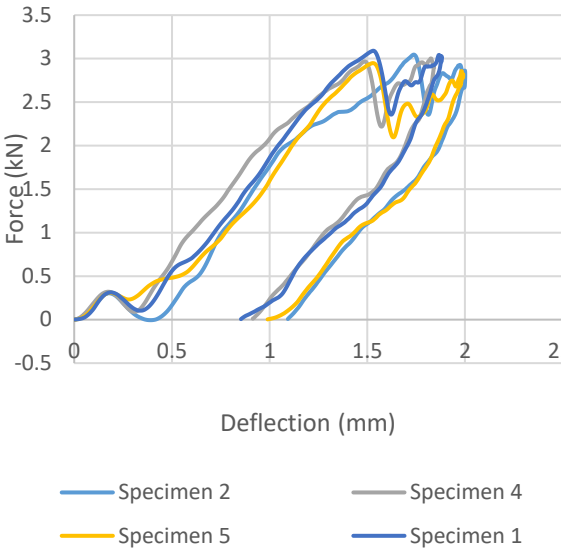

Figure 8.4 – 3J impact force-displacement

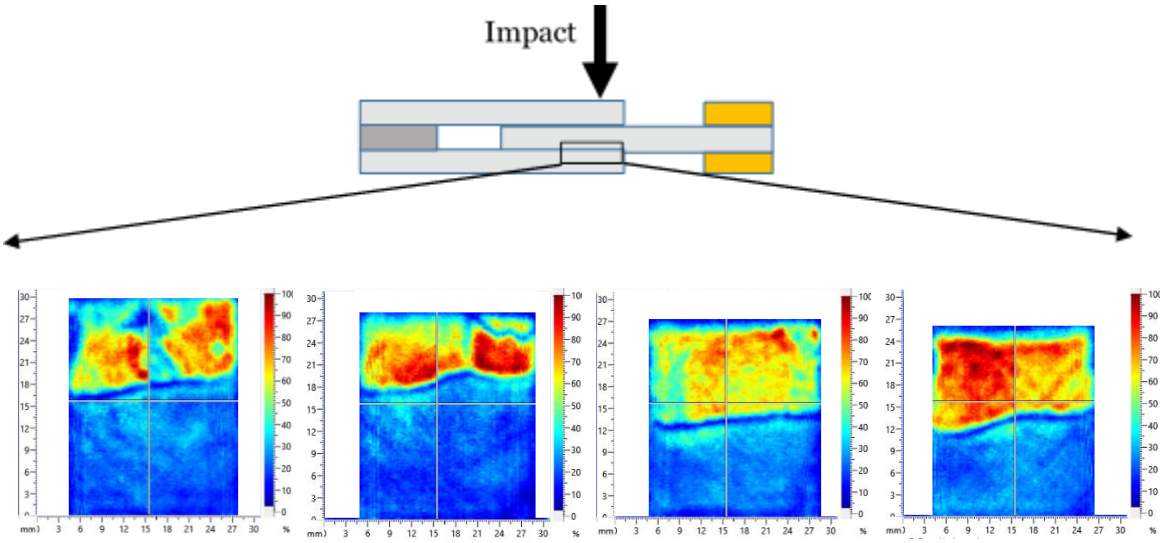

Specimen 1 Specimen 2 Specimen 3 Specimen 4

Figure 8.5 – 2J impact C scan images

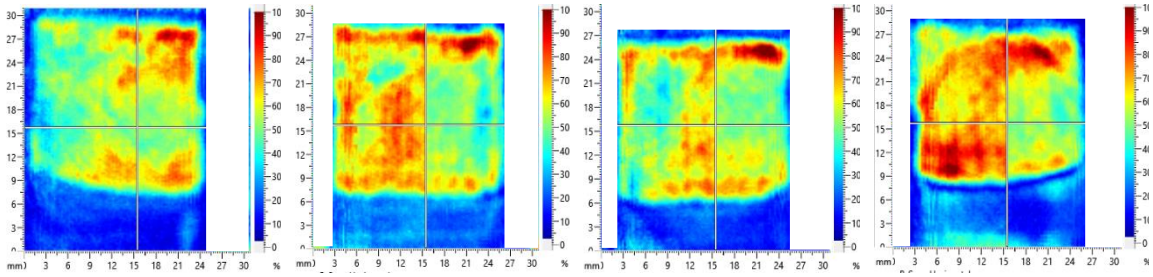

Specimen 1 Specimen 2 Specimen 3 Specimen 4

Figure 8.6 – 3J impact C scan images

The impact force vs deflection for the 2J and 3J cases at RTD conditions is shown in Figure 8.3 and Figure 8.4 respectively. The load drops, when they occur, were at a similar level for both impact energies tested, and represented the points when damage occurred. For some 2J cases, there were no load drops and no debonding observed from the C scan image, suggesting no damage. This implied that 2J was close to the threshold impact energy in which failure occurred in the joint. The C scan images for the two cases at RTD are shown in Figure 8.5 and Figure 8.6 respectively. For the RTD case, the average damage length for the 2J case was 13mm, which represented approximately a third of the overlap length (36mm), while for the 3J case the average debonding length was 22mm, approximately two thirds of the overall overlap length. The damage occurred in the inner adherend/adhesive interface, opposite to the side at which the impact was applied, similar to the indentation case.

8.2.4 Residual Tensile Tests after Impact – Room Temperature Dry

Following the impact tests, the specimens were tested under tension to understand how the impact damage affects tensile strength. Table 8.1 shows the residual tensile results for the two impacted energy cases at RTD condition.

Table 8.1 – Residual tensile test results at RTD

Impact Energy (J)	De-bonding Length (mm)	Failure Load/unit Width (N/mm) *(CV)*	Number of Specimens
0 (Baseline)	0	1332 (5%)	4
1.94 (0.2%)	12.70 (7%)	681 (9%)	4
2.92 (0.4%)	22.00 (3%)	567 (3%)	3

8.2.5 Residual Tensile Tests after Impact – Hot Temperature Dry and Hot Temperature Wet

For the HTD and HTW configurations, the impact tests were conducted at 2J at RTD condition. The residual tensile tests after impact were conducted at HTD and HTW. The results are summarised in Table 8.2. The impact damage for the HTD and HTW batch was slightly higher than the RTD batch, as the 2J impact case was at the threshold energy for impact damage.

Table 8.2 – Residual tensile test results at HTD and HTW

Condition	De-bonding Length (mm)	Failure Load/unit Width (N/mm) *(CV)*	Number of Specimens
HTD	13.7 (5%)	616 (5%)	4
HTW	13.5 (5%)	686 (16%)	4

8.2.6 Residual Tensile Tests after Impact – Discussion

Under impact the peel stresses at the bottom edge (i.e. the other side of the joint from where the impact load is applied) were high. This led to the debonding initiation and propagation at this interface, close to the adhesive bondline.

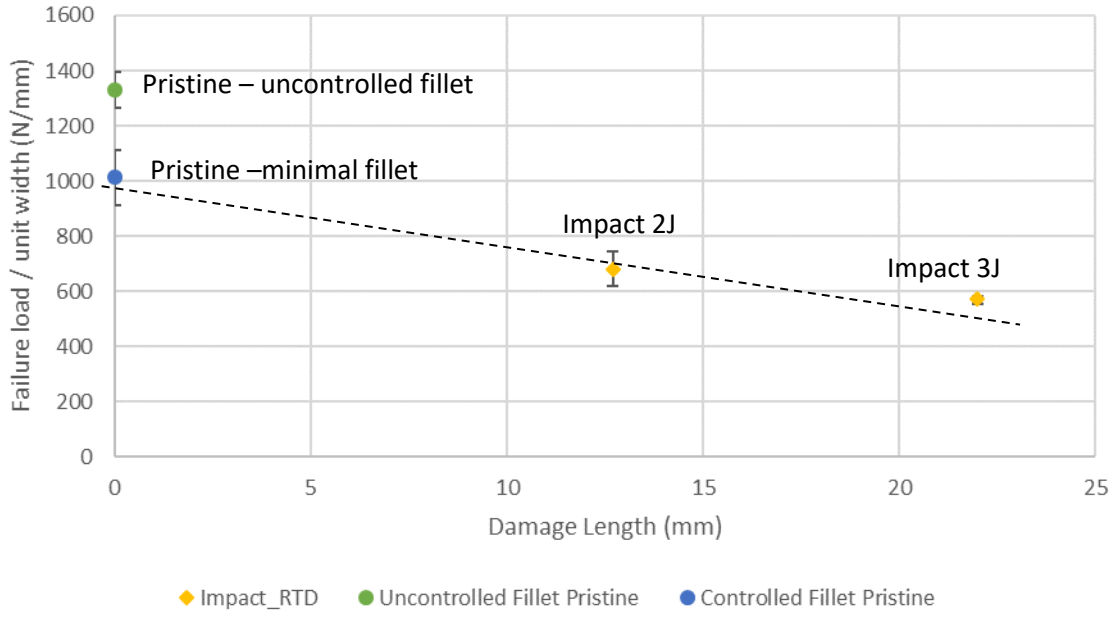

Figure 8.7 – Summary of impact and pristine DLJ strength at RTD

Increasing the impact energy from 2J to 3J resulted in a 42% increase in the debond length. The residual tensile strength was compared to both pristine DLJ cases with and without fillets in Figure 8.7. A linear force-displacement relationship was observed before catastrophic failure. When the impact damage was present, a significant knockdown in the failure load was observed when compared to the pristine case. A linear decrease in strength was observed when comparing the impact cases to the pristine case without fillets, whereas a greater decrease in strength was observed for the uncontrolled fillet case.

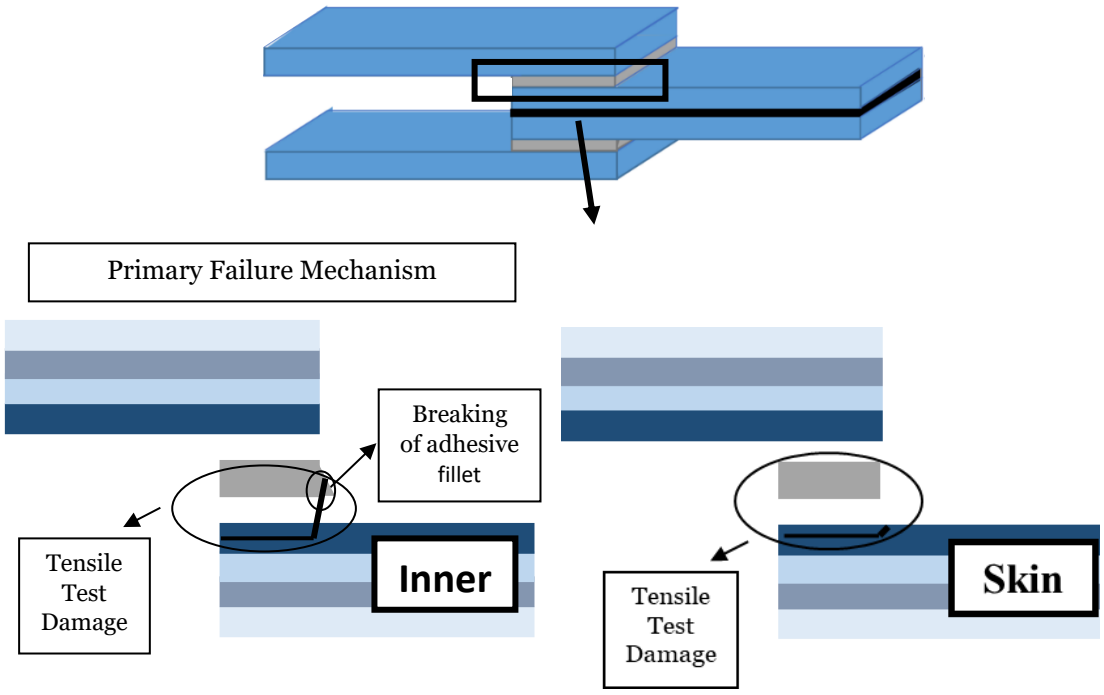

a) Pristine Case (uncontrolled fillets) b) Pristine Case (minimal fillets)

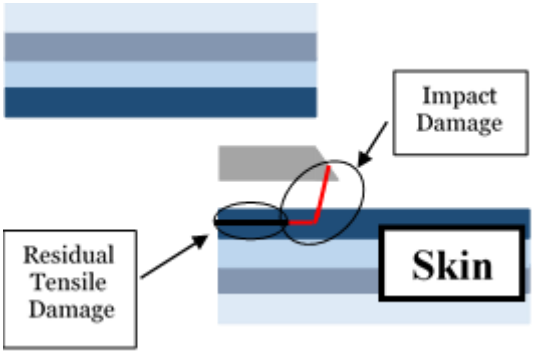

c) Impact Case

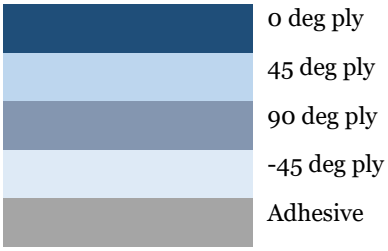

Figure 8.8 – Failure schematic for pristine and impact case

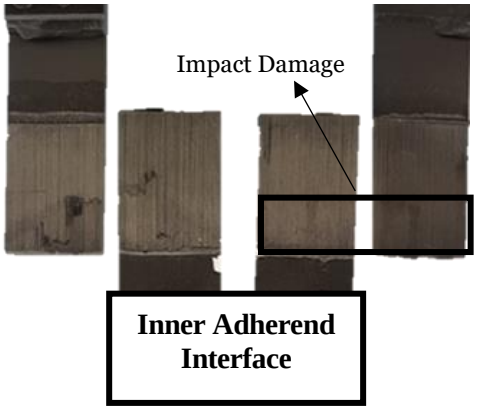

c) 2J Impact Case – RTD

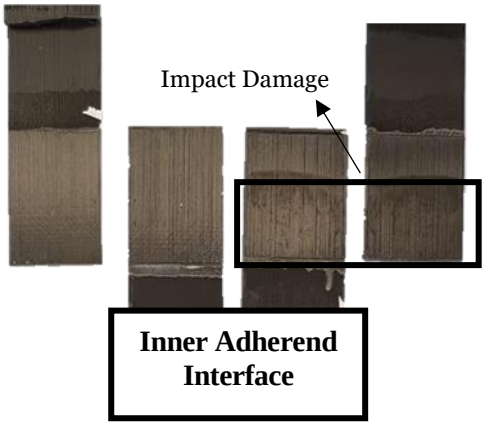

d) 3J Impact Case – RTD

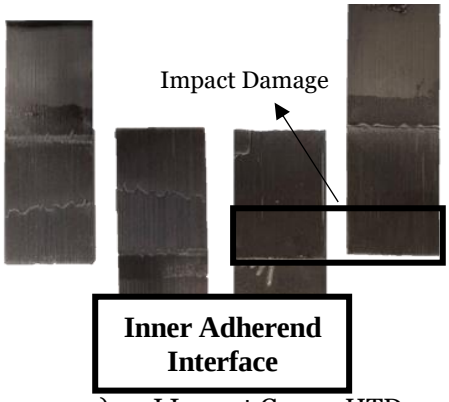

e) 2J Impact Case – HTD

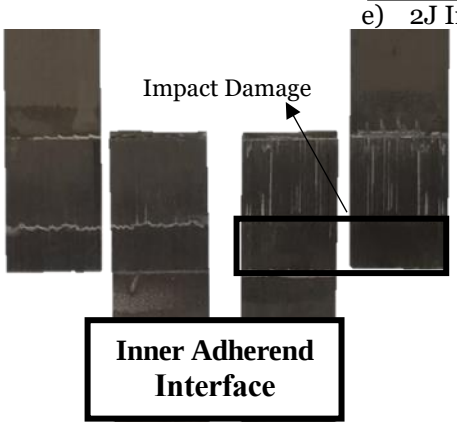

f) 2J Impact Case – HTW, patches of adhesive visible

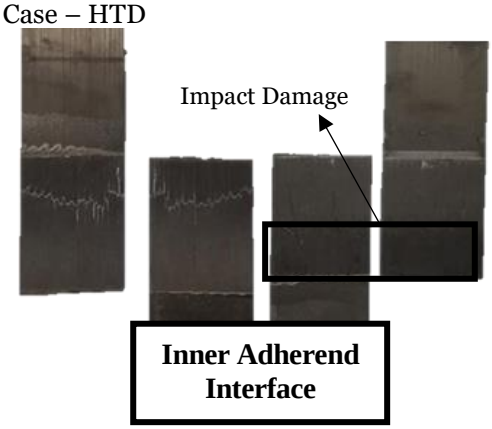

g) 2J Impact Case – HTW, no adhesive visible

Figure 8.9 – Fracture surfaces of impacted specimens after tensile test

The failure schematics for the pristine and impact cases are shown in Figure 8.8 and the fracture surfaces are shown in Figure 8.9. For the HTW configuration a high C.V% was measured. Analysing the fracture surfaces at HTW, two specimens had small regions of adhesive visible (Figure 8.9d) along with the 0° plies and resulted in a higher DLJ strength. The fracture surface for the other two specimens showed just the 0° plies across all interfaces (Figure 8.9e), similar to the RTD and HTD cases and resulted in a lower DLJ strength. The average strength for these cases resulted in a high C.V%.

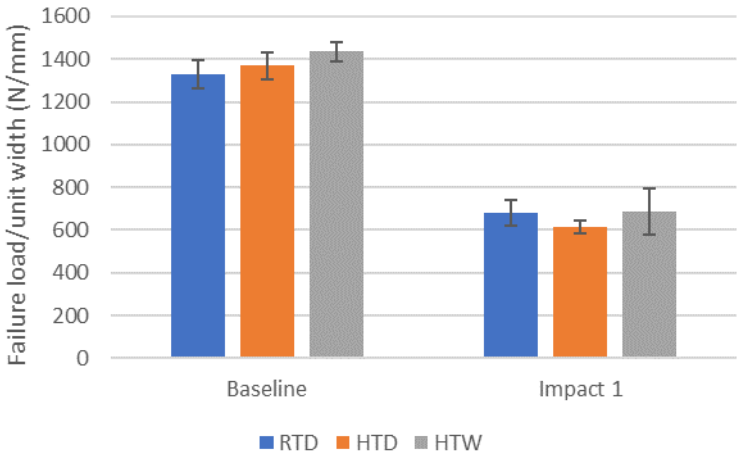

Figure 8.10 – Effects of environmental conditions on impact strength

For all environmental conditions, a significant drop in DLJ strength was observed with impact damage as shown in Figure 8.10. There was no significant difference in the residual tensile strength of the impacted joints with increased temperature and moisture. The impact tests at HTD and HTW were conducted at 2J, with a slightly larger impact damage length for the HTD and HTW batches. The HTD case was slightly lower, but statistically, not significantly different from the RTD and HTW cases.

The general failure modes for both the pristine and impact cases were similar for all environmental conditions. For the pristine uncontrolled fillet case, the crack initiated at the fillet before migration in the composite inner adherend 0° ply. For the minimal fillet case at RTD, the crack propagated into the composite 0° ply without the influence of the adhesive fillet. During the impact application, the crack initiated in the adhesive and then propagated into the 0° ply creating a sharp crack as shown schematically in Figure 8.8. When the following residual tensile tests were conducted, the crack continued to propagate within the 0° ply until failure. This showed that the final crack propagation path for both the pristine and impacted specimens under tensile loading

were similar. The load drop from the uncontrolled pristine case was due to the impact damage breaking the adhesive fillet and creating a sharp crack in the composite. Once the impact damage was present, along with the shear component acting on the DLJ, due to greater rotation from the asymmetric loading, a significant peel component was also present during tensile load application. Hence, the decrease in DLJ strength from the 2J impact to 3J impact case could be due to a change in mixed-mode ratio with increased Mode I due to the increased effective overlap length (overlap length minus impact damage length)

Figure 8.11 compares the residual tensile strength after impact at RTD, HTD and HTW against the analytical model based on the fracture propagation criterion as explained in Chapter 6, using the previously presented Equation 6.2

$$G = \frac{\sigma^2 ht}{4E(h-t)} \tag{6.2}$$

Table 8.3 – Composite fracture properties

G_{IC} (N/mm)	G_{IIC} (N/mm)	G_C (N/mm)
0.2	1	0.69

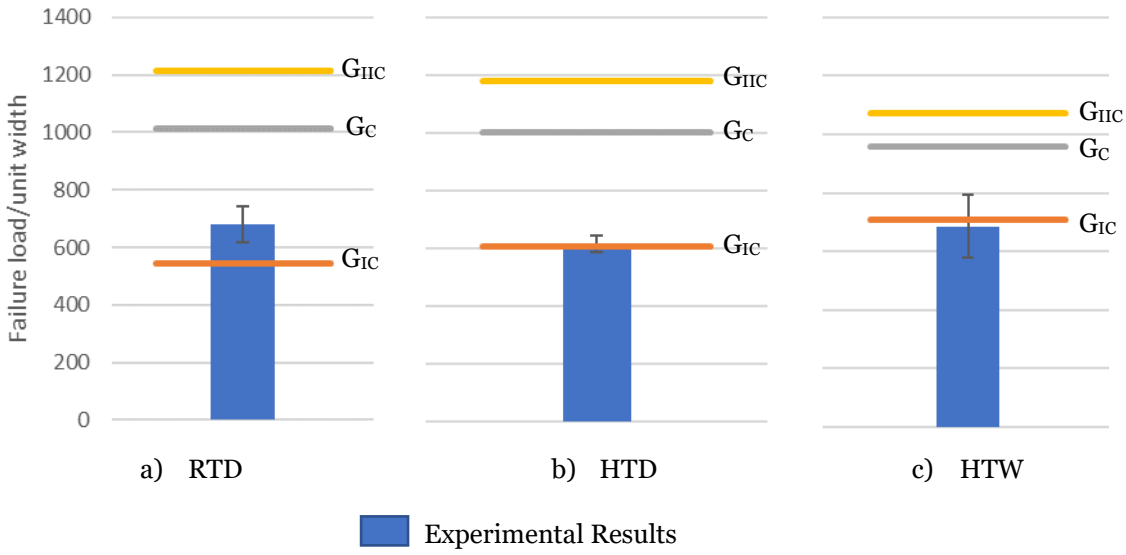

Figure 8.11 – Comparison of residual tensile strength against simple analytical calculations using composite properties

The failure based on a pure Mode I (orange line), Mode II (yellow line) and mixed-mode (for the minimal fillet pristine case) (grey line) fracture energies were calculated and presented in Figure 8.11. The composite properties were used for all cases as the crack propagated into the inner adherend surface 0° ply during impact. The material properties are given in Table 8.3. The G_C for the DLJ was calculated using the experimental minimal fillet result using Equation 6.2. The minimal fillet case was used to calculate G_C to ensure the adhesive fillet effects were not included in the calculations.

Both peel and shear components were present on the impacted DLJ during tensile loading. Based on the simple analytical calculations, the results suggest that the failure might be controlled by Mode I for the impact cases at all environmental conditions. This could be because the crack was already present in the composite during the tensile tests, combined with the low G_{IC} of the composite. The impact damage for the RTD batch was slightly lower than the HTD and HTW batch, hence why the RTD case had a slightly greater mixed-mode influence. As both peel and shear components are present in the impacted specimen during tensile tests, the was controlled by the weakest material property.

8.3 Disbond Tests

8.3.1 Experimental Configuration

Two different configurations for the artificial defect, i.e. disbond cases were considered for the baseline DLJ configuration. A full width disbond was used. The baseline DLJ configuration was with an overlap length of 36mm, adhesive thickness of 0.2mm and inner adherend thickness of 4mm. For the first disbond configuration, the disbond was placed at the interface between the outer adherend and the adhesive, while for the second configuration the disbond was placed between the inner adherend and the adhesive. An additional configuration was also tested where two disbond defects were present at both the outer adherend and inner adherend (Case C), to understand the effects of a double disbond. These cases are shown schematically in Figure 8.12. Two disbond lengths were tested for Case A, while three disbond lengths were tested for Case B.

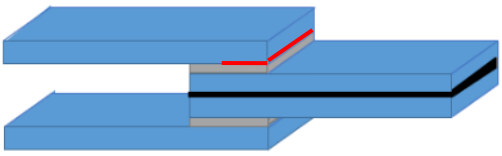

a) Disbond at outer adherend, Case A

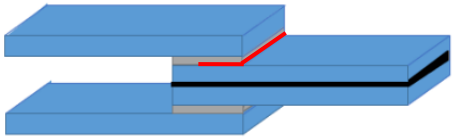

b) Disbond at Inner Adherend, Case B

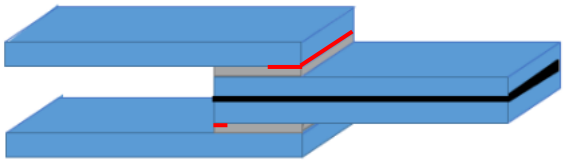

c) Disbond at inner adherend and outer adherend, Case C

Figure 8.12 – Schematic of disbond cases

8.3.2 Experimental Results

This section provides a summary of all the disbond experimental results at different environmental conditions.

Table 8.4 – Results for disbond tests summary for RTD conditions

Specimen	Disbond Length (mm)	Failure Load/unit Width (N/mm) *(CV)*	Number of Specimens
Case A	12	822 (7%)	5
Case A	24	727 (4%)	3

Specimen	Disbond Length (mm)	Failure Load/unit Width (N/mm) *(CV)*	Number of Specimens
Case B	5	801 (8%)	4
Case B	12	723 (5%)	4
Case B	24	524 (6%)	4

Specimen	Disbond Length at Outer Adherend (mm)	Disbond Length at Inner Adherend (mm)	Failure Load/unit Width (N/mm) *(CV)*	Number of Specimens
Case C	24	5.50	587 (8%)	5

Table 8.5 – Results for disbond tests summary for HTD conditions

Specimen	Disbond Length (mm)	Failure Load/unit Width (N/mm) *(CV)*	Number of Specimens
Case B	12	1385 (2%)	4
Case B	24	843 (2%)	4

Table 8.6 – Results for disbond tests summary for HTW conditions

Specimen	Disbond Length (mm)	Failure Load/unit Width (N/mm) *(CV)*	Number of Specimens
Case B	12	1067 (5%)	5
Case B	24	649 (10%)	5

8.3.3 Numerical Disbond Model using ABAQUS/Explicit

Following the experimental study on the different disbond configurations, a numerical analysis was conducted to further understand the disbond DLJ performance at different environmental conditions. Similar to the pristine model, the disbond cases were modelled using ABAQUS/Explicit. Further details on the numerical model are available in Chapter 6. The disbond defect in the numerical model was represented by deleting cohesive elements as shown in Figure 8.13. The selection of the input parameters for the cohesive elements at the disbond defect was in accordance with the failure mode. The material properties used for the model were given in Chapter 6 (Table 6.2 and Table 6.3).

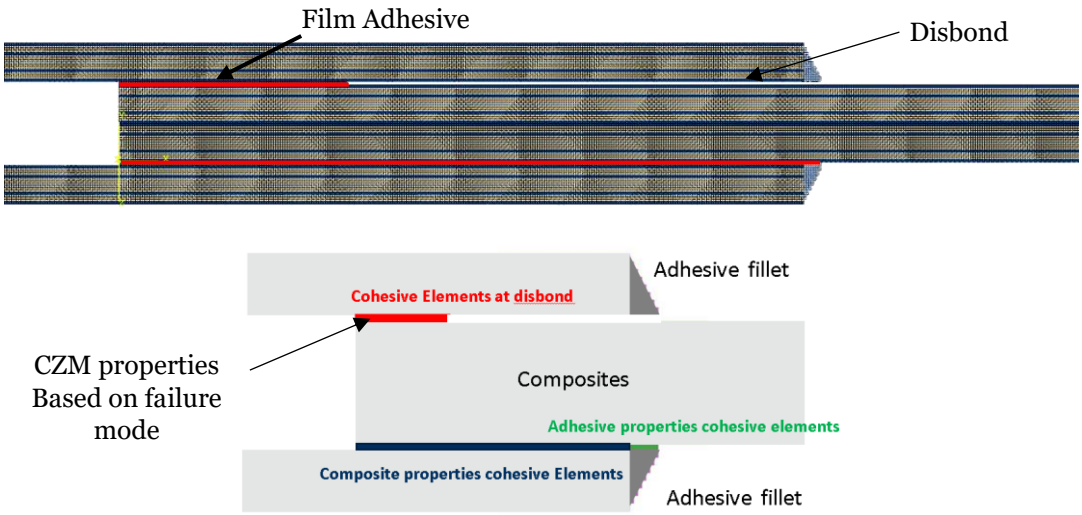

Figure 8.13 – Disbond model and material properties selection

From the experimental results it was found that for all RTD cases, the failure was controlled by the composite properties, i.e. the crack migrated into the surface 0° ply for all configurations tested. For the HTD and HTW cases, the failure was controlled by the adhesive properties as the adhesive was visible on the fracture surfaces. This is

discussed in detail in Section 8.4. Figure 8.14 presents the modelling results for the 12mm and 24mm disbond cases at RTD, HTD and HTW environmental conditions. The results in the striped pattern was obtained using adhesive properties, whereas the results in solid bars were modelled using composite properties for the cohesive elements at the disbond.

Comparing the results, an excellent correlation was achieved for the HTD and HTW cases, where failure was dominated by the adhesive properties. For the RTD case, particularly the 24mm disbond inner adherend, the numerical model overestimated the experimental result. For the RTD case, the crack migrated into the surface 0° ply of the inner adherend, for both inner adherend/adhesive interface and outer adherend/adhesive interface disbond cases. For the disbond placed at the outer adherend/adhesive interface, the strength was higher as the crack had to propagate through the adhesive before final migration at the surface 0° ply at the inner adherend. This is discussed in detail in Section 8.4.2. The current disbond model does not distinguish between the two disbond locations on either side of the adhesive, since there is only one layer of cohesive elements representing the adhesive and two interfaces. This could be the reason why it overpredicts the RTD results.

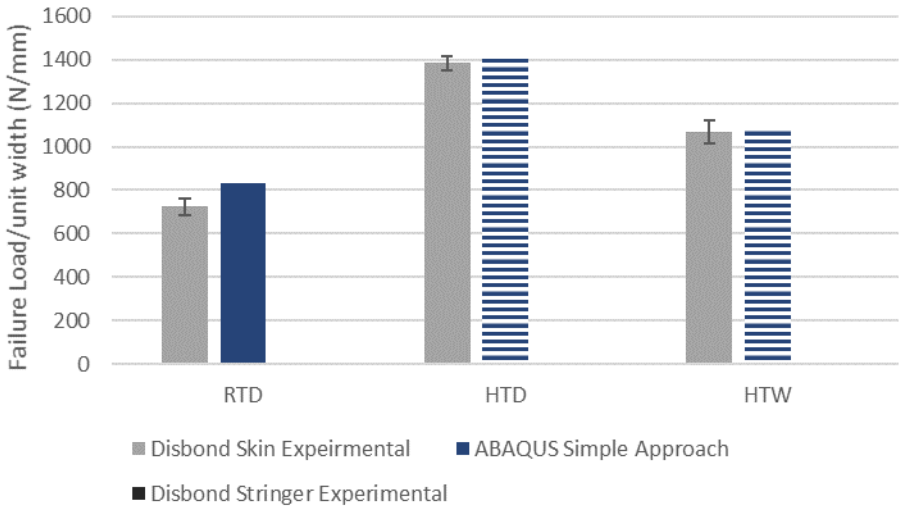

a) 12mm disbond modelling correlation

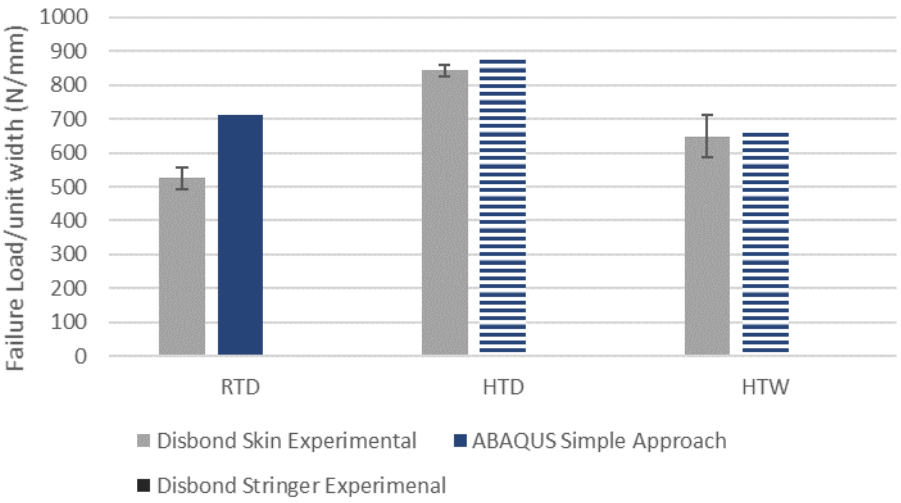

b) 24mm disbond modelling correlation

Composite properties only

Adhesive properties only

Figure 8.14 – Disbond experimental and modelling correlation

8.4 Discussion

8.4.1 Disbond Sensitivity Analysis

As a working model has been established and correlated with the experimental results, a sensitivity analysis was conducted. The aim of the sensitivity analysis is to understand the influence of the material parameters on the strength of the disbonded joints and help explain the DLJ performance at different conditions. This section gives a brief description of the sensitivity analysis and the results are shown in the discussion.

Two sets of sensitivity studies were conducted for the disbond cases, on the failure controlled by the composite properties (RTD) and on the failure controlled by the adhesive properties (HTD and HTW) in accordance with the experimental failure mode. For both configurations, the cohesive element properties were varied by +/- 50%. Like the pristine DLJ sensitivity analysis, the values highlighted in red show a large decrease, whereas the values highlighted in green show a large increase in DLJ

strength. Results in yellow mean the values are not sensitive to the change in input properties.

8.4.2 Room Temperature Dry Case

The experimental results for Case A, B and C were shown in Table 8.4. Figure 8.15 provides a summary for the disbond results compared against the pristine case with no damage. For both pristine and disbond cases, the force-displacement curves were linear before a sudden load drop. Comparing the pristine cases with the disbond cases, a reduction in strength was found even for a small defect, with further reductions for longer defects. The reduction in strength was enhanced when compared to the pristine uncontrolled fillet case due to the lack of a fillet in the disbond case.

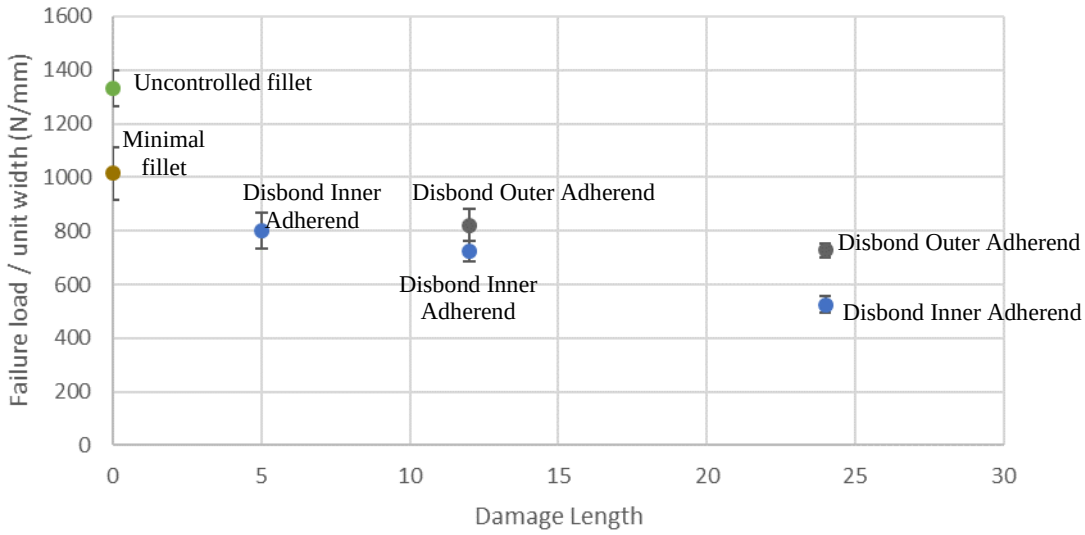

Figure 8.15 – Summary disbond and pristine results at RTD

High-speed camera images of the typical failure mechanism for the 24mm disbond at the inner adherend/adhesive interface are shown in Figure 8.17. The high-speed camera video output was dependent on the frame rate, resolution and trigger time which can be varied to achieve the optimum setting for different types of tests. The camera recorded continuously until the trigger button was clicked and the data was saved for the defined time interval. The trigger time was initiated manually once the final failure occurred, hence enough time was needed to activate the trigger time button after sudden failure. Increasing the frame rate decreased the resolution and trigger time. Hence, to achieve a high frame rate to capture the failure process in detail,

the high-speed camera was focused at the disbond location reducing the overall resolution and achieving a frame rate of 100,000 frames per second.

Analysing the high-speed camera images, no damage was visible prior to unstable failure, and the crack migration into the composite adherend was sudden. Chapter 3 (3.5) explains the effects of the grit blasted surface treatment, which resulted in microscopic regions of broken fibres. The high-speed camera images show no signs of adhesive yielding before failure which suggests that the crack propagated from the insert film directly into the surface 0° ply through the broken fibres. This could be because of the high stress concentrations due to the broken fibres facilitating crack migration directly from the insert film before the adhesive started to yield. The shear stress at failure using the effective overlap length was 22MPa, significantly lower than the shear strength at which the adhesive yields at RTD (45MPa). As the failure initiation occurred into the composite as observed from the high-speed camera, the failure was controlled by the composite properties. Figure 8.16 shows schematically that during the tensile tests with the disbond, both shear and peel components were present on the DLJ. The mode ratio at these conditions was hard to obtain through analytical calculations as the disbond cases were not symmetric.

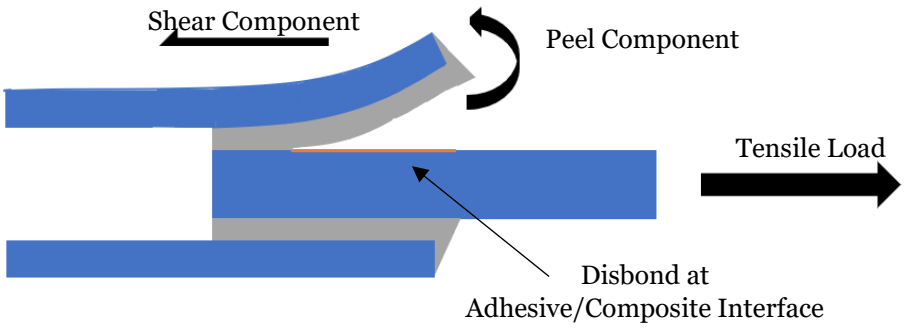

Figure 8.16 – Shear and peel component on Disbond DLJ

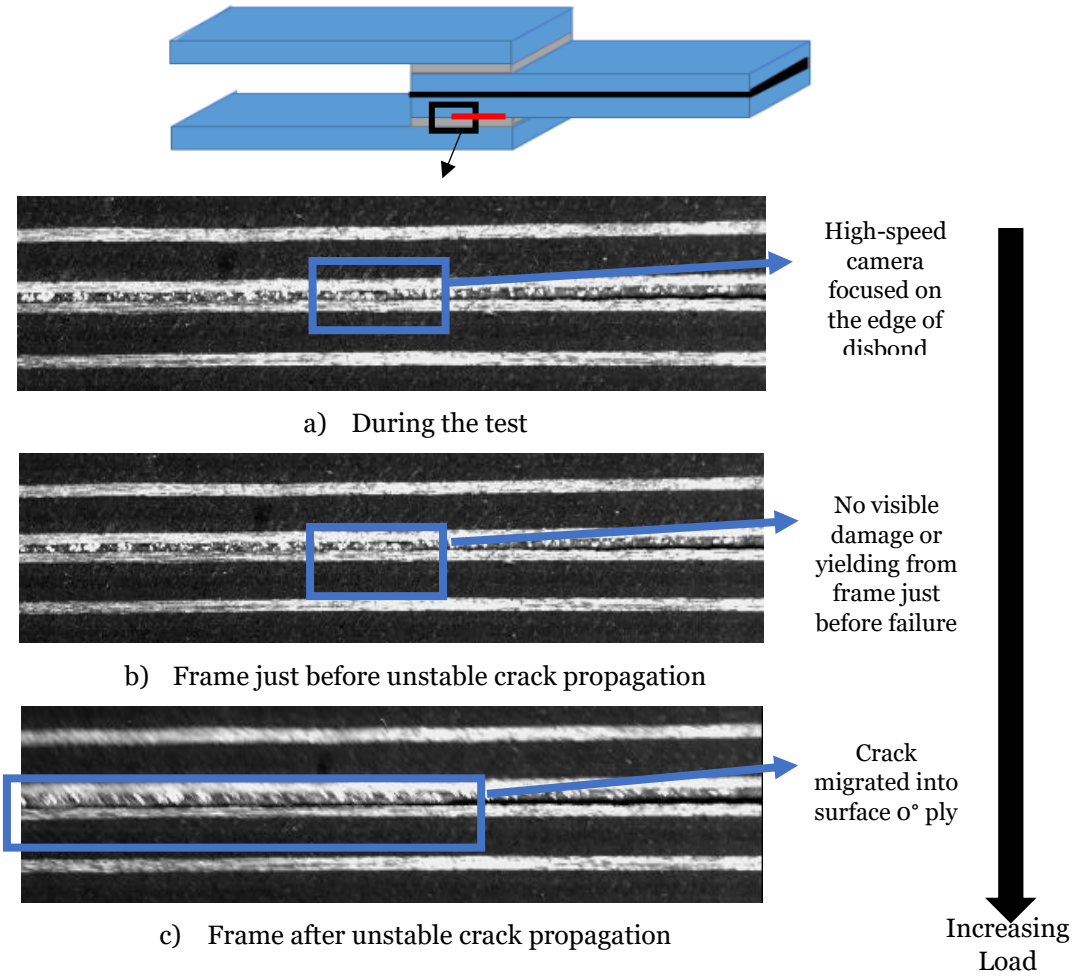

Figure 8.17 – Detailed high-speed camera of disbond inner adherend/adhesive interface

Figure 8.18 compares the disbond inner adherend experimental results to the analytical failure criterion based on fracture energy, which was introduced in Chapter 6 (Equation 6.2). As described earlier, the failure initiated into the composite, therefore the composite fracture properties were used for this analysis. The approximate failure based on fracture energy was done for three cases: one, assuming a pure Mode I failure (yellow line), two, assuming a pure Mode II failure (blue line) and three, assuming mixed-mode G_c based on the pristine DLJ case (4mm inner adherend, 36mm overlap length configuration for minimal fillet case). These input properties are summarised in Table 8.3. Analysing Figure 8.18, the longer disbond case approached the failure criterion based on G_{IC} of the composite, while the shorter disbond case was slightly higher than the failure estimation based on G_{IC}. This suggests that the G_{IC} of the composite may have influenced the failure at RTD, consistent with the sensitivity analysis shown in Figure 8.19 The sensitivity analysis also shows the

disbond cases were sensitive to G_{IIC}, but not as significant as G_{IC}. Both peel and shear components were present in the disbond DLJ, hence the failure was controlled by the weaker material property. As the crack initiated into the composite, combined with the low composite G_{IC} resulted in failure being controlled by this material property. The failure load increased with decreased disbond length potentially due to the slight change in mode ratio, i.e. lower peel component for the 12mm disbond case. The sensitivity analysis shows that the 12mm disbond case was more slightly more sensitive to G_{IIC} than the 24mm disbond case.

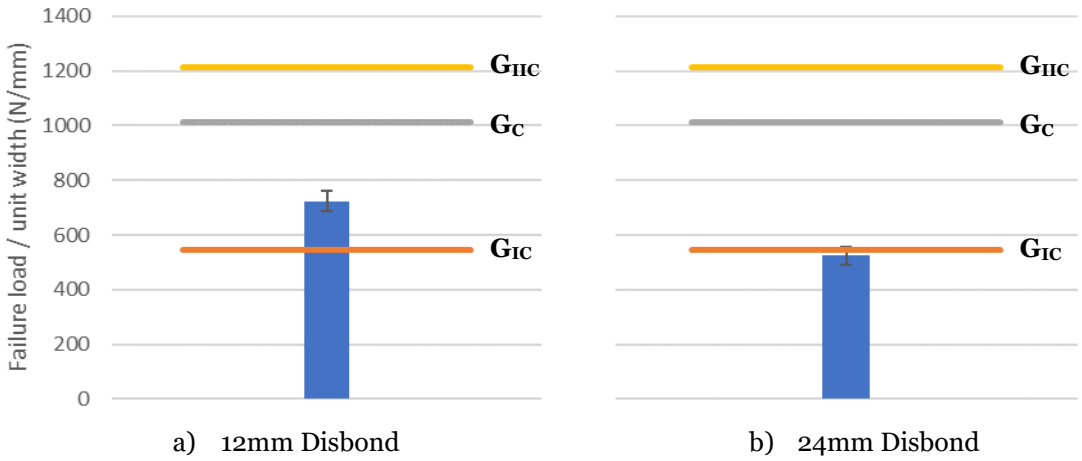

a) 12mm Disbond b) 24mm Disbond

Figure 8.18 – Comparison of disbond results against analytical criterion at RTD

Disbond 12mm

	+50%	-50%
Sigma 33	-2.4	5.7
Sigma 13	2.3	-5.0
G_{IC}	16.9	-25.0
G_{IIC}	3.1	-8.9

Disbond 24mm

	+50%	-50%
Sigma 33	-1.2	2.1
Sigma 13	1.7	-7.3
G_{IC}	18.2	-25.5
G_{IIC}	1.9	-7.4

Figure 8.19 - Sensitivity analysis results for disbond joints at RTD

When the position of the disbond changed from the inner adherend to the outer adherend (Figure 8.20), a significant difference in DLJ strength was observed. High-speed camera images at the initiation of the failure process were taken to understand the failure mechanisms occurring at a global view for both disbond cases to compare the behaviour. As a greater resolution was needed for the global view, the frame rate used was 25,000 frames per second. Analysing Figure 8.21, it can be seen that when

the disbond was at the outer adherend, the crack had to break the adhesive before it could 'jump' from the outer adherend interface into the inner adherend interface. When the disbond was at the inner adherend, the crack initiated and propagated straight into the inner adherend as summarised in the failure schematic in Figure 8.20. This 'jump' from the outer adherend interface, through the adhesive into the inner adherend 0° surface ply occurred because the loading path was through the inner adherend, and the less tough composite toughness results in the 'jump'. This was responsible for the higher failure load per unit width obtained with the disbond at the outer adherend foot rather than at the inner adherend. Analysing the fracture surface for these cases in Figure 8.22, a consistent failure surface was observed in which the crack propagated along the 0° surface ply at the inner adherend for both the impact and disbond cases. The effect of changing disbond position was only investigated at RTD condition.

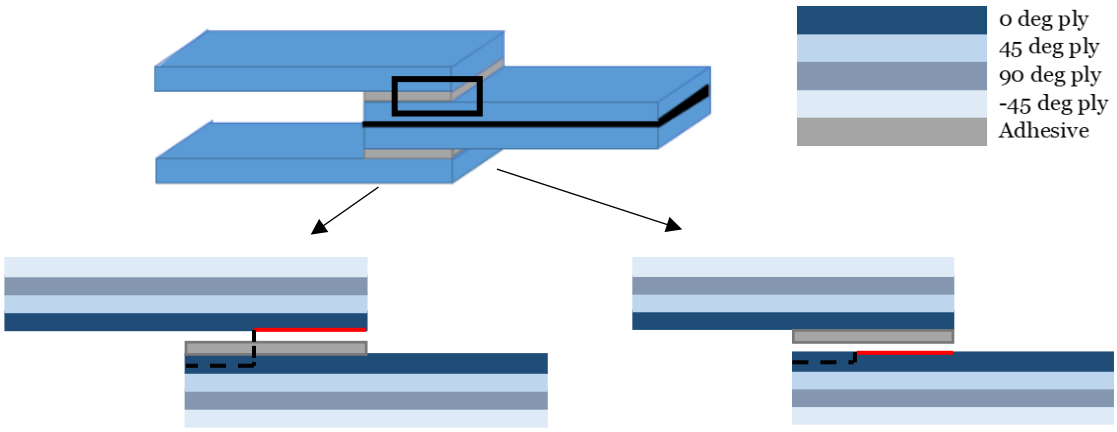

a) Disbond at Outer Adherend Foot b) Disbond at Inner Adherend

Figure 8.20 – Failure schematic for the disbond case

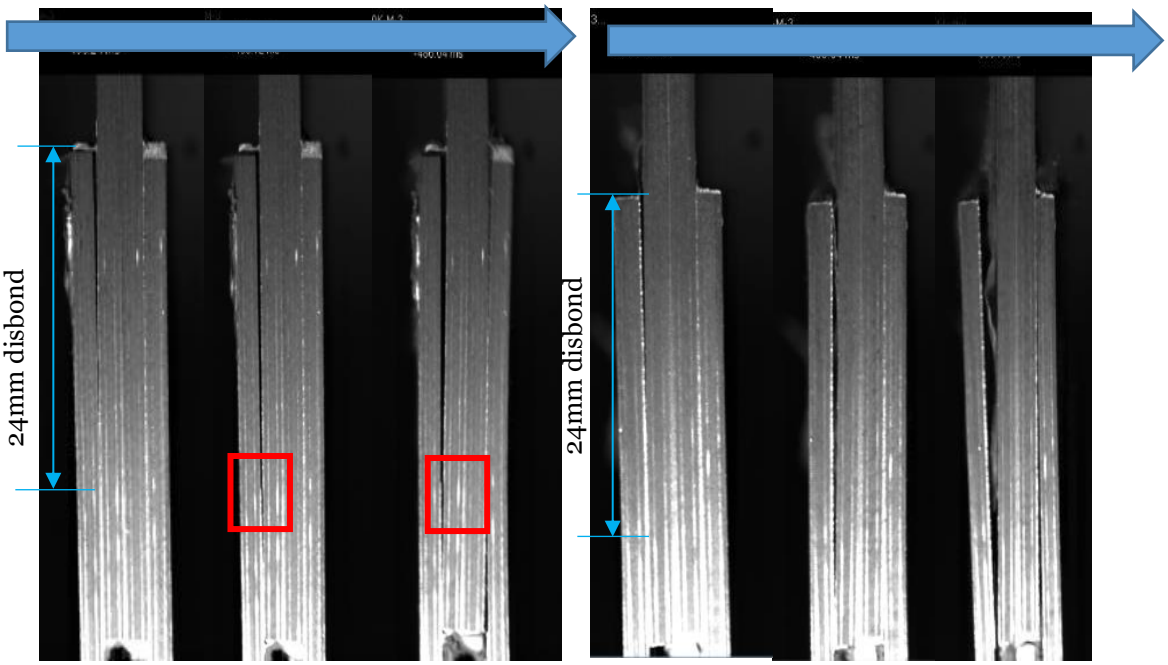

a) Case A, Disbond at Outer Adherend b) Case B, Disbond at Inner Adherend

Figure 8.21 – High-speed camera frames just before failure

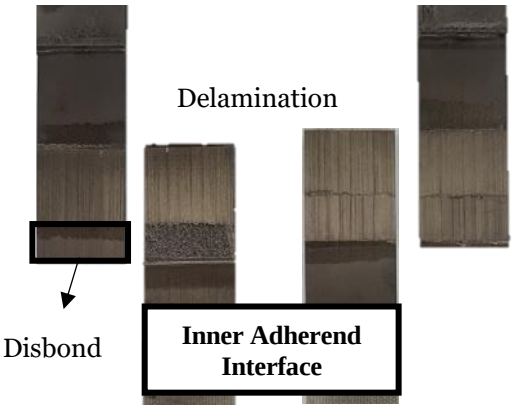

a) Disbond Outer Adherend, 12mm

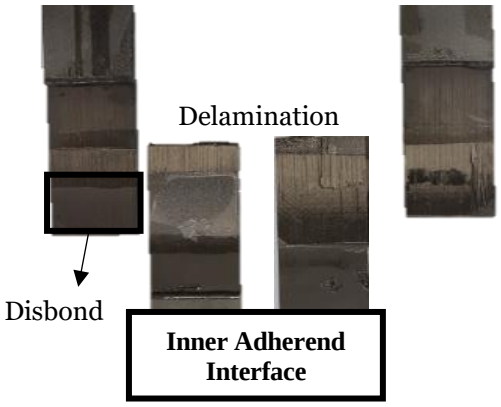

b) Disbond Outer Adherend, 24mm

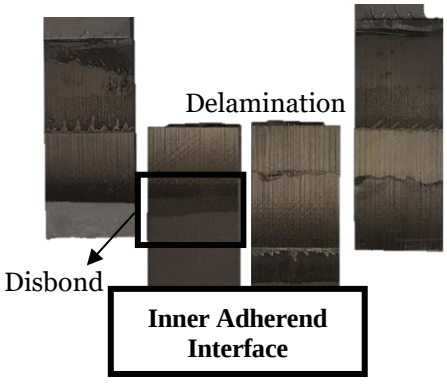

c) Disbond Inner Adherend, 12mm

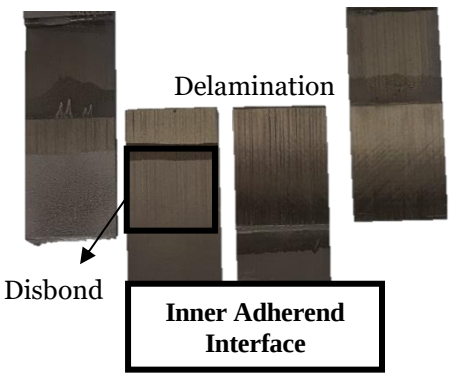

d) Disbond Inner Adherend, 24mm

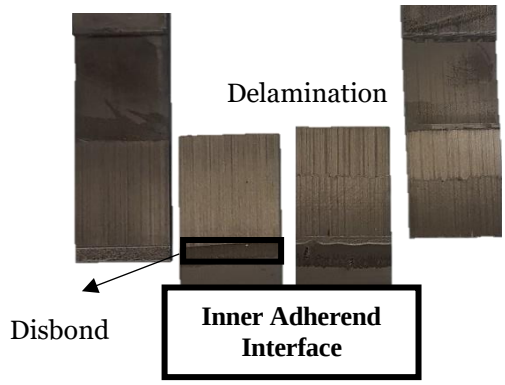

e) Disbond Inner Adherend, 5mm

Figure 8.22 - Fracture surfaces for RTD disbond cases

8.4.3 Hot Temperature Dry Case

The HTD tests were conducted for disbond lengths of 12mm and 24mm at the inner adherend/adhesive interface at 80°C. The disbond at the inner adherend/adhesive was the critical case for the RTD conditions and correlated well to the RTD impact case with similar damage length. Table 8.5 summarised the test results and Figure 8.23 compares the HTD disbond strengths. The failure was controlled by the initiation similar to the RTD case.

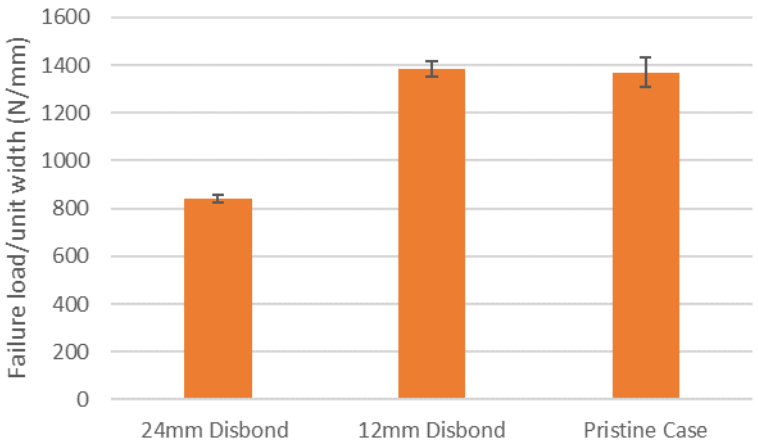

Figure 8.23 – Disbond inner adherend results compared to pristine at HTD conditions

The fracture surface for the disbond cases at HTD as shown in Figure 8.24. For the disbond cases, fragments of adhesive were visible on the fracture surface after the disbond, hence the failure initiation was controlled by the adhesive properties.

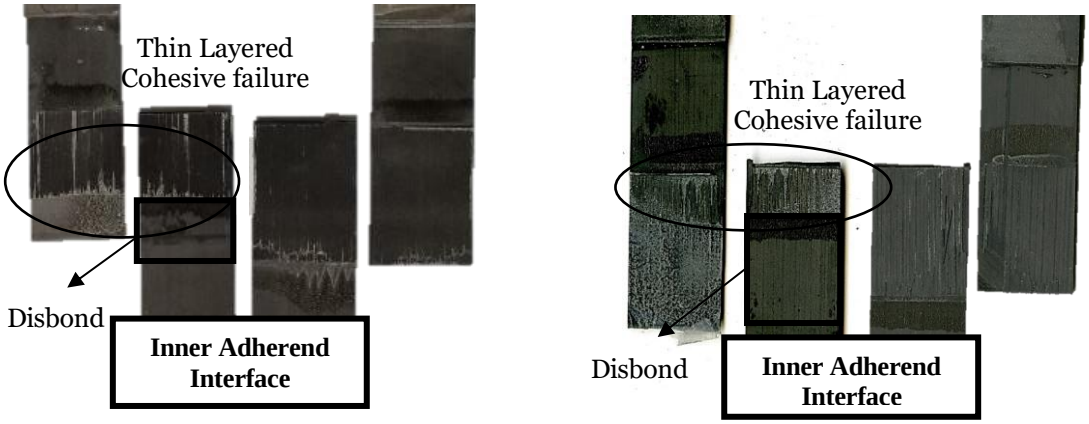

a) 12mm Disbond b) 24mm Disbond

Figure 8.24 – Fracture surfaces for HTD disbond cases

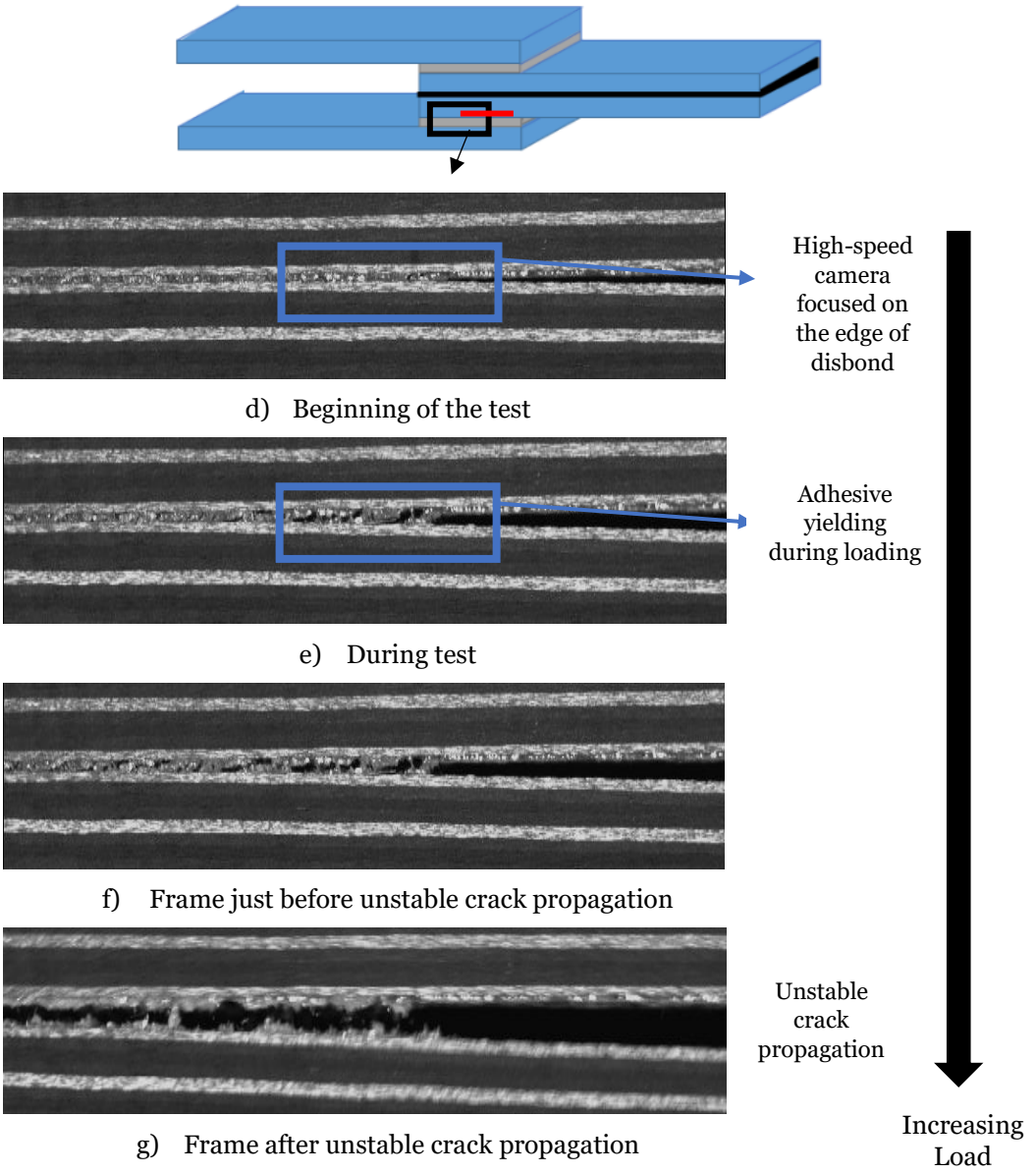

d) Beginning of the test

e) During test

f) Frame just before unstable crack propagation

g) Frame after unstable crack propagation

Figure 8.25 – Detailed high-speed camera images for disbond HTD

The failure process was captured using a high-speed camera and is shown in Figure 8.25. The camera was focused at the disbond, hence a frame rate of 100,000 was used due to the reduced resolution. The high-speed camera images show prior to catastrophic failure, the adhesive yielded, causing the failure to initiate into the adhesive. The adhesive ductility increased with temperature while the yield strength decreased as reported in the literature. Hence, the initiation was controlled by the adhesive properties. During the catastrophic failure, the crack migrated from the adhesive into the composite surface ply.

Analytical calculations based on the fracture energy criterion were conducted at HTD. As the initial failure occurred into the adhesive, adhesive properties were used for the analysis. The material properties are summarised in Table 8.7 and Figure 8.26 shows the results. The failure for the 12mm disbond case approached the failure load based on fracture propagation within the adhesive. The sensitivity analysis in Figure 8.27 shows that the 12mm disbond case was sensitive to both shear strength and G_{IIC} of the adhesive. Hence, this suggests the failure was close to the critical disbond length between a strength and fracture controlled failure.

Table 8.7 – Adhesive fracture properties at HTD

G_{IC} (N/mm)	G_{IIC} (N/mm)
1.05	1.36

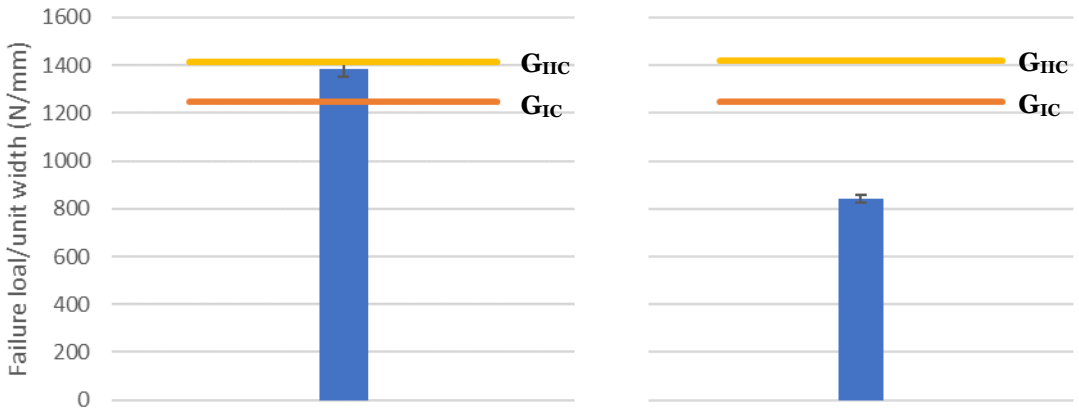

a) 12mm Disbond b) 24mm Disbond

Figure 8.26 – Comparison of disbond results against the analytical criterion at HTD

For the 24mm disbond case, the sensitivity analysis in Figure 8.27 shows that the shear strength of the adhesive was the most sensitive parameter. The analytical criterion based on fracture energy case did not correlate well and the sensitivity analysis showed that this case was relatively insensitive to variations in G_{IC} and G_{IIC} compared to the shear strength. Hence, the failure for the 24mm disbond case was controlled by the shear strength of the adhesive. The decrease in the disbond DLJ strength from 12mm to 24mm disbond cases was due to the increase in disbond length.

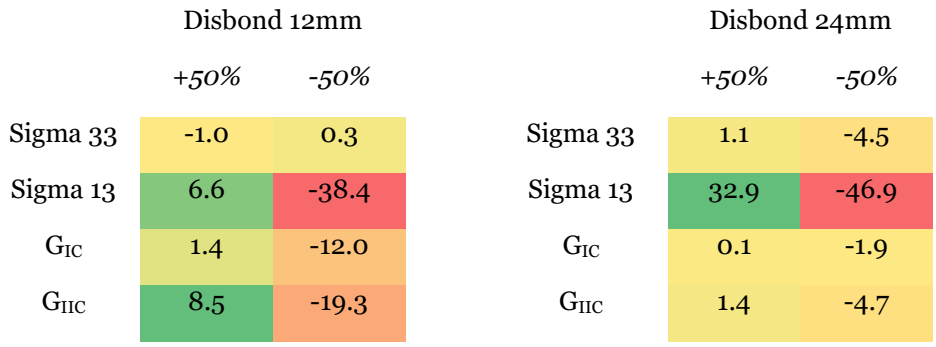

Figure 8.27 – Sensitivity analysis results for disbond joints at HTD

The pristine DLJ and 12mm disbond cases had the same strengths due to the change in failure mode. The pristine case failed with initial crack propagation within the adhesive fillet (controlled by G_{IC}) followed by crack migration into the surface 0° ply in the inner adherend. For the disbond 12mm case, the failure was influenced by the shear strength and G_{IIC} of the adhesive. As the G_{IC} and G_{IIC} of the adhesive were similar, this could be a reason why there was no significant difference in the pristine and 12mm disbond DLJ strength.

8.4.4 Hot Temperature Wet Case

HTW tests were conducted for disbond lengths of 12mm and 24mm at the inner adherend/adhesive interface at 80°C for specimens conditioned at 80°C and 85% RH. The results are summarised in Table 8.6. Figure 8.28 compares the disbond and pristine results at HTW conditions.

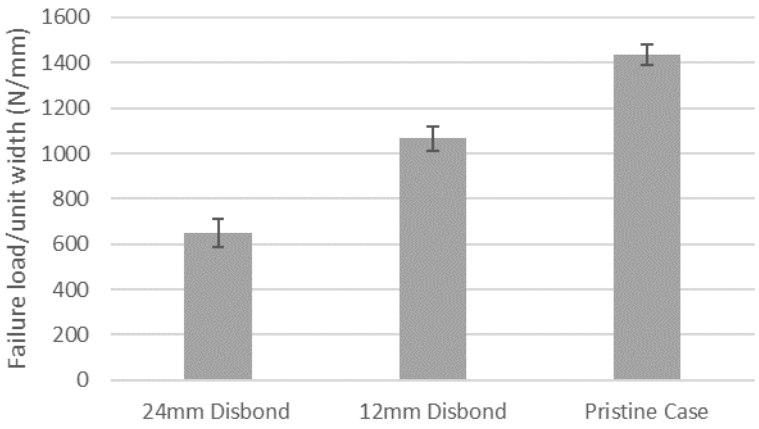

Figure 8.28 – Disbond inner adherend results compared to pristine at HTD conditions

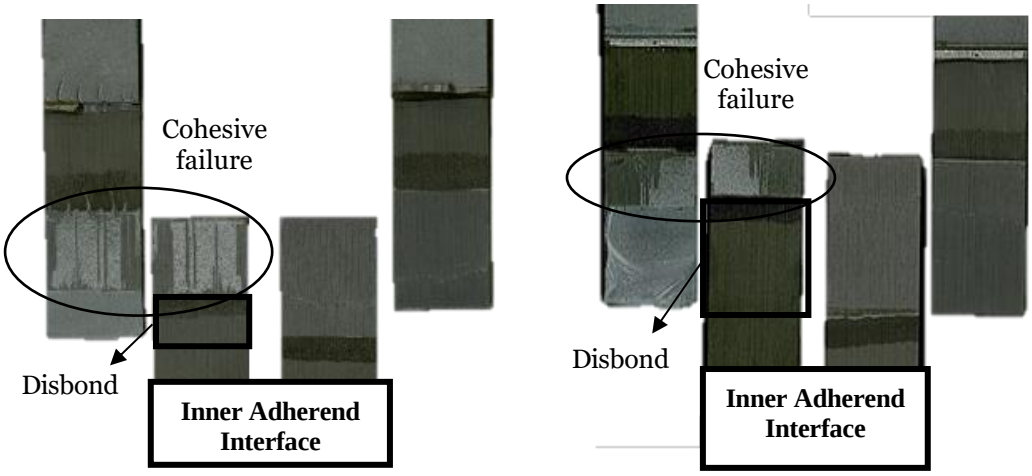

a) 12mm Disbond b) 24mm Disbond

Figure 8.29 – Fracture surfaces for HTW disbond cases

A significant decrease in DLJ strength was found with the presence of a disbond for the HTW condition. Analysing the fracture surfaces in Figure 8.29, the disbond cases had patches of adhesive on the fracture surface. Similar to the HTD case, the failure initiated into the adhesive from the insert film placed at the adhesive/composite interface. With increased temperature and moisture, the ductility of the adhesive increased, while the yield strength decreased significantly compared to the RTD case. Hence, during loading the adhesive yielded, causing failure initiation into the adhesive. The fracture surface at HTW shows more adhesive on the bondline compared to HTD, which could be due to greater yielding of the adhesive during loading at HTW. The final failure was catastrophic, and the crack migrated into the surface 0° ply.

Figure 8.30 compares the experimental results to the analytical equation based on the fracture energy. The material properties are summarised in Table 8.8. The adhesive properties were used for the calculations as the initial failure occurred into the adhesive. The results show that the 12mm disbond case approached the failure load based on the fracture energy criterion. The sensitivity analysis in Figure 8.31, shows the 12mm disbond case to be primarily sensitive to the adhesive shear strength, but also the G_{IIC} of the adhesive. This suggests this case could be at the boundary for the failure controlled by the adhesive shear strength or G_{IIC}. The disbond length may be the critical overlap from which the failure changes from a strength to fracture controlled failure at for the disbond case at HTW. The 24mm disbond case does not correlate with the analytical fracture energy criterion and the sensitivity analysis showed this case was sensitive to the shear strength of the adhesive. Hence, it can be concluded that the 24mm disbond case at HTW was controlled by the adhesive shear strength. The 24mm disbond case was also sensitive to the S33 parameter which suggests yielding due to the combination of both peel and sheer. The decrease in disbond DLJ strength was due to the increased disbond length.

Table 8.8 – Adhesive fracture properties at HTW

G_{IC} (N/mm)	G_{IIC} (N/mm)
1.13	0.70

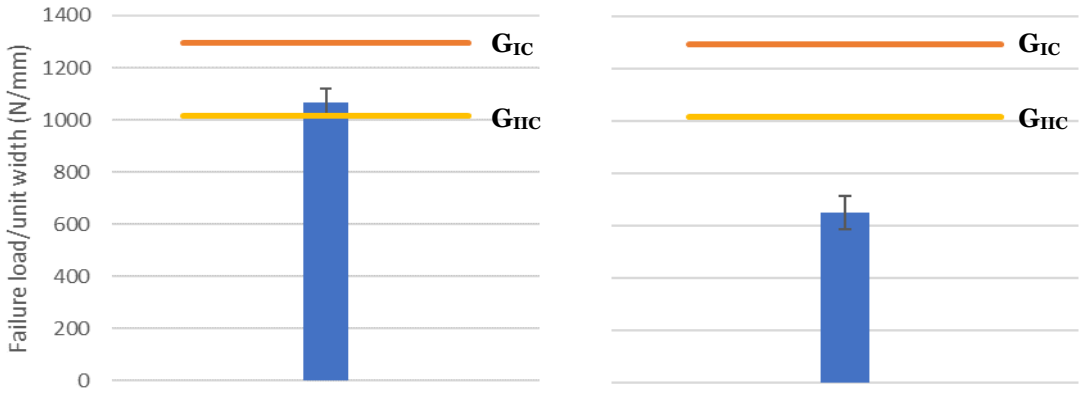

a) 12mm Disbond b) 24mm Disbond

Figure 8.30 – Comparison of disbond results against analytical criterion at HTW

	Disbond 12mm	
	+50%	*-50%*
Sigma 33	1.3	-5.6
Sigma 13	12.0	-36.7
G_{IC}	0.1	-0.6
G_{IIC}	8.4	-19.4

	Disbond 24mm	
	+50%	*-50%*
Sigma 33	10.1	-25.5
Sigma 13	21.1	-39.7
G_{IC}	0.6	-0.3
G_{IIC}	1.8	-4.4

Figure 8.31 – Sensitivity analysis results for disbond joints at HTW

The pristine cases were significantly stronger than the 12mm disbond case unlike at HTD. The pristine cases failed by crack initiation within the adhesive fillet (G_{IC} controlled) followed by migration into the composite surface 0° ply. The disbond 12mm case was at the boundary for failure controlled by the adhesive shear strength and G_{IIC}. The failure load estimation based on the failure controlled by the adhesive shear strength and G_{IIC} was significantly lower than that based on the adhesive G_{IC}. Hence, as the pristine case was influenced by the adhesive G_{IC}, and the disbond case influenced by the adhesive shear strength and G_{IIC}, this explains why the disbond DLJ strength was weaker than the pristine case at HTW.

8.4.5 Environmental Effects

Figure 8.32 compares the disbond strengths (at the inner adherend/adhesive interface) of the DLJ at RTD, HTD and HTW conditions. For consistency across all cases, the pristine cases with uncontrolled fillets were compared against the inner adherend interface disbond cases. For pristine cases at RTD, HTD and HTW, the failure was controlled by initial crack propagation within the adhesive followed by delamination within the surface 0° ply of the composite. The sensitivity analysis results are used to help explain the effects of environmental conditions on the disbond joint strength.

For the 12mm and 24mm disbond cases, there was a significant increase in DLJ disbond strength from RTD to HTD. The disbond DLJ strength then decreased from HTD to HTW conditions but was still higher than RTD. The increased disbond DLJ strength was due to the change in failure mode between from RTD to HTD and HTW.

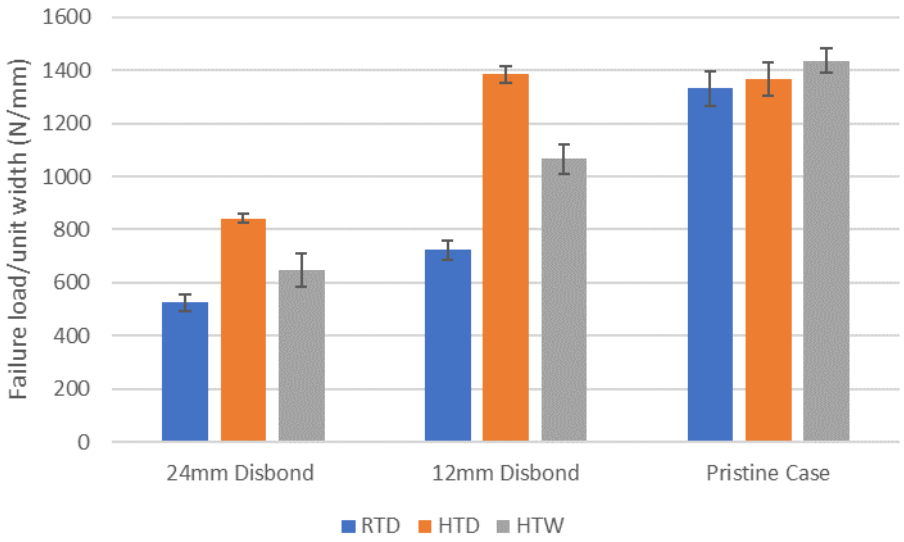

Figure 8.32 – Comparison of disbond cases vs pristine cases at different environmental conditions

At RTD, the crack migrated from the adhesive/composite interface into the composite before the adhesive started to yield. The broken fibres on the composite surface facilitated the crack migration from the interface into the composite, hence the failure was controlled by the composite properties. At HTD and HTW, the adhesive yielded significantly before final failure. The failure initiation occurred into the adhesive; hence the failure was controlled by the adhesive properties. Both shear and peel components were present on the disbond DLJ. As this was a complex case involving the strengths and ductility of the adhesive and composite at different environmental conditions, and lack of data comparing different material systems, a simple analytical criterion could not be confidently used to assess whether the initiation occurred into the adhesive or composite.

At HTW the DLJ disbond strengths decreased from the HTD case. From the characterisation tests and literature data, it was concluded that there was no significant difference in G_{IC} of the adhesive at HTD and HTW, whereas there was a significant decrease in G_{IIC}, tensile strength and shear strength of adhesives due to the presence of moisture. The sensitivity analysis showed that when the failure was controlled by the adhesive properties, the strengths and G_{IIC} were the critical parameters controlling failure. Hence, the reduction in the strengths and G_{IIC} of the adhesive with increased moisture explains why the HTW disbond strengths were significantly lower than the HTD disbond strengths.

8.4.6 Disbond vs Impact

Figure 8.33 compares the residual impact tensile test results for the 2J case with 13mm delamination (average across all environmental conditions) against the 12mm disbond inner adherend case for the three environmental conditions. Impact cases were tested to understand the effects of impact on the DLJ strength, while disbond tests were conducted to understand the effects of manufacturing defects on the DLJ strength. The impact and disbond cases are compared to understand whether an impact damage can be represented by a disbond for all environmental conditions. All impact tests were conducted at RTD conditions, where the crack propagation occurred at the composite 0° ply at the inner adherend/adhesive interface. The residual tensile tests after impact were conducted at RTD, HTD and HTW conditions. For the RTD case, the impact tensile tests compared well with the disbond inner adherend results. The failure mechanism was similar for the residual tensile test and disbond cases, where the crack migrated into the surface 0° ply of the inner adherend. When the failure was controlled by the composite properties, the G_{IC} was the weakest parameter as found from the sensitivity analysis, hence the weakest path controlling failure.

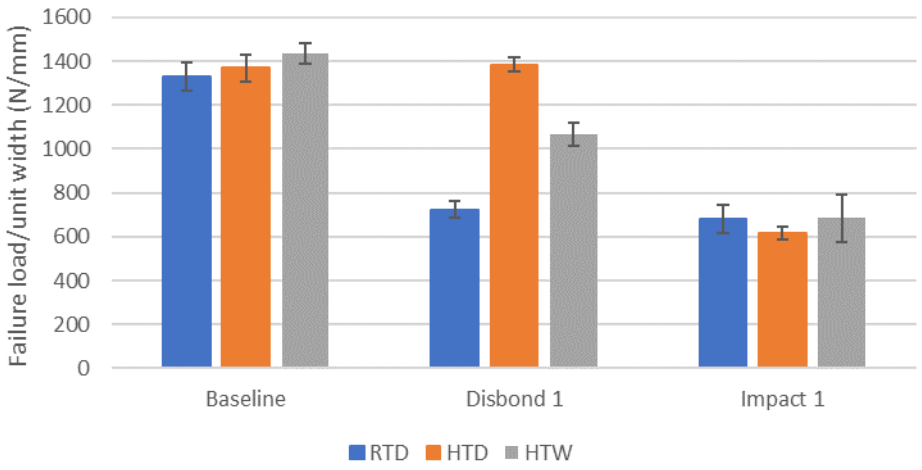

Figure 8.33 – Comparison of disbond vs impact at different environmental conditions

For the HTD cases, the failure mechanisms for the disbond and impact cases were different. When the impacted specimen was tested at the HTD condition, the crack propagation continued within the 0° ply. For the disbond HTD case, the failure mode changed to initial failure within the adhesive, i.e. initial cohesive failure. Hence, the failure was controlled by the adhesive properties. A similar response was also observed for the HTW disbond and impact cases. For the impacted specimen, the crack propagation path does not change once migration into the composite occurred (during

impact) as the crack was already in the composite and it was the least tough path for propagation.

8.5 Conclusions

This chapter studied the effects of impact and disbond on the strength of DLJ. The residual tensile strength after through thickness impact was studied for two impact energy levels of 2J and 3J at RTD. The impact damage occurred at the surface 0° ply at the inner adherend (inner adherend)/adhesive interface that initiated due to high peel stresses in the DLJ during impact. From the following residual tensile tests after impact, a significant decrease in DLJ strength was found from the pristine case and with increased impact damage length. This was due to the sharp crack formed within the surface 0° ply, the effects of the adhesive fillet delaying initiation for the pristine case and the possible change in mixed-mode ratio. The residual tensile tests were also conducted at HTD and HTW conditions for the 2J impacted specimen at RTD. As the damage was already present in the composite during the RTD impact, at HTD and HTW the crack propagation continued within the composite until final failure. There was no significant difference in the residual impact strength for the 2J case at different environmental conditions.

Following the impact tests, the artificial defect i.e. disbond cases were tested for the DLJ at different environmental conditions. Increasing the disbond length decreased the DLJ strength for all environmental conditions tested. At RTD, the crack migrated from the adhesive/composite interface into the surface 0° of the inner adherend during failure. All RTD cases were controlled by the fracture properties of the composite, particularly G_{IC}. Increasing the disbond length decreased the DLJ strength possibly due to the change in mixed-mode ratio. At HTD and HTW, a change in failure mode was observed from the RTD disbond cases and the failure was controlled by the adhesive properties. At both HTD and HTW conditions, the longer disbond case (shorter effective overlap length) was controlled by the shear strength of the adhesive, while the shorter disbond case (longer effective overlap length) was at the critical disbond length of being controlled by the shear strength and fracture (G_{IIC}). Hence, the increase in disbond length, resulted in decreased disbond DLJ strength. At HTW the disbond DLJ strengths decreased from the HTD case. This was because from HTD to HTW, the shear strength and G_{IIC} decreased significantly. Hence, as the failure was

controlled by these parameters, the reduction in shear strength and G_{IIC} at HTW decreased the disbond DLJ strength.

Numerical analysis was used to compare with the experimental results. The CZM properties were based on the failure mode, as failures controlled by both composite and adhesive were observed for the disbond cases. This method correlated the experimental and numerical results well, showing that the failure sequence was captured through the model accurately. However, further modelling including the yielding of the adhesive bondline and a corresponding failure criterion is needed to capture the crack initiation during the disbond cases. As a conservative approach, the lowest material properties (from the adhesive and composite) could be used for the CZM numerical model, but this may result in significant under prediction in DLJ strength for some cases.

CHAPTER 9

CONCLUSIONS

9.1 Introduction

The aim of this thesis was to investigate the effects of environmental conditions on the strength of Double Lap Joints (DLJ) of different geometrical conditions. The adhesive and composite were characterised at Room Temperature Dry (RTD), Hot Temperature Dry (HTD) and Hot Temperature Wet (HTW) conditions to understand how increasing temperature and moisture affected the mechanical properties of these materials. Following the material characterisation tests, pristine, impacted and disbonded DLJ were tested under tension at different environmental condition. Simple analytical models were used to understand what controlled the failure for each case, and based on the failure mode, numerical models using Cohesive Zone Models (CZM) were used to predict the joint behaviour. The major conclusions are summarised below.

9.2 Characterisation Tests Summary

The Mode I fracture energy increased with increased adhesive thickness for all environmental conditions tested. Increasing the temperature significantly increased G_{IC} for all adhesive thicknesses. The increase for the thinner adhesive from RTD to HTD was due to the change in failure mode, where the HTD case failed by an initial

region of cohesive failure followed by crack migration into the adherend. Whereas at RTD, the crack migrated straight into the composite. The failure modes for the thicker adhesives were similar at all environmental conditions, where an initial cohesive failure was followed by migration into the composite. The increased G_{IC} for these cases was because of the increased ductility of the adhesive at higher test temperatures. There was no significant difference in G_{IC} for all adhesive thicknesses between HTD and HTW conditions. For composites, the G_{IC} also increased from RTD to HTD to HTW.

For the Mode II fracture energy tests at RTD, G_{IIC} initially increased with thickness, thought to be due to the increased plastic zone with increasing thickness. The peak G_{IIC} occurred at an intermediate thickness (0.4mm) as the constraint effects from the composite adherend was present and increased the plastic zone size of the adhesive. For the thicker adhesive, the plastic zone present in the ENF specimen was similar to that of a bulk adhesive specimen as the constraint effect was lost, resulting in a lower G_{IIC}. At HTD, increasing adhesive thickness resulted in increased G_{IIC}. The failure mechanism was cohesive initially, followed by migration into the surface 0° ply of the composite. At HTW, all G_{IIC} values were similar. It was found that crack initiation occurred away from the insert film crack tip and at the composite surface 0° ply for the HTW cases. Increasing temperature and moisture decreased G_{IIC} for both the adhesive and composite.

9.3 Double Lap Joint Summary

9.3.1 Pristine Double Lap Joints

It was found that environmental conditions have a significant effect on the DLJ strength. The DLJ strength for the shorter overlap length cases decreased with increased temperature and moisture, whereas there was a slight increase in DLJ strength for the longer overlap lengths. This was because the shorter overlap length cases were strength dominated and the strength properties decreased significantly with increased temperature and moisture. For the longer overlap length cases, failure was fracture dominated where a limit is approached based on the energy required for fracture propagation. The increase in DLJ strength was much more significant for the thinner inner adherend cases compared to the thicker inner adherend for the longer

overlap length cases. Numerical models successfully predicted the DLJ strength at different conditions based on the failure modes determined from the simple analytical criteria.

Further tests looking into the effects of the adhesive fillets and surface ply orientation were conducted at RTD. A significant difference in joint strength was observed when comparing the uncontrolled (adhesive fillet present) and minimal fillet cases. This was because the failure mode at RTD was partially controlled by the initial region of cohesive failure at the adhesive fillet. For the minimal fillet case, this region was not present, hence it significantly decreased the joint strength. The typical DLJ stacking sequence used for the pristine and disbond tests was $[0/45/90/-45]_{ns}$. The DLJ strength for a 45° surface ply (Quasi-Isotropic (QI)) was lower than the typical DLJ stacking sequence with 0 surface ply and fillets. This was because delamination in the composite could occur from the transverse cracks for the 45° surface ply cases without the effects of the adhesive fillets.

9.3.2 Impact and Disbond Double Lap Joints

The impact damage occurred at the surface 0° ply at the inner adherend (inner adherend) /adhesive interface, opposite side to the impact application, and initiated due to high peel stresses in the DLJ.

From the following residual tensile test after impact, a significant decrease in DLJ strength was found with impact damage length compared to the pristine case. This was due to the sharp crack formed within the surface 0° ply and effects of the adhesive fillet delaying initiation for the pristine case. The residual tensile tests were also conducted at HTD and HTW conditions for the 2J impacted specimen at RTD. As the damage was already present in the composite during the RTD impact, at HTD and HTW the crack propagation continued along the surface 0° ply at the inner adherend until final failure. There was no significant difference in the residual impact strength for the 2J case at different environmental conditions.

For the disbond cases, increasing the disbond length decreased the DLJ strength for all environmental conditions tested. The disbond DLJ strength increased from RTD to HTD due to the change in failure mode, from the composite properties to adhesive properties controlling failure. The disbond DLJ strength then decreased from HTD to

HTW (HTW still significantly higher than RTD as failure controlled by adhesive) due to the decrease in adhesive shear strength and G_{IIC}.

9.4 Crack Migration

Microscopic regions of broken fibres were present on the surface composite ply before secondary bonding. These regions formed as a result of the grit-blasting surface treatment. The broken fibres provided a path for crack migration into the surface 0° plies. For all DLJ cases, the crack migrated into the surface 0° ply of the inner adherend, but the sequence of migration, i.e. initial failure or after the initial failure depended on the material properties and failure mode. For the DLJ tested throughout the thesis, 3 types of failures were observed. These are summarised below:

1) Failure initiating in the adhesive due to bondline yielding followed by migration into the composite

This type of failure occurred for the pristine shorter overlap lengths and disbond cases at HTD and HTW. At these conditions, the failure was controlled by the adhesive shear strength as found from the simple analytical and numerical sensitivity analysis. The failure initiated through the yielding of the adhesive bondline in shear. As the whole bondline yielded during the initiation, the adhesive properties controlled the failure for this case. This was followed by migration into the surface 0° ply, which was catastrophic and sudden, and a post failure effect.

2) Failure initiating in the adhesive fillet followed by migration into the composite

This type of failure occurred for the pristine longer overlap lengths at all conditions and during impact application. For the pristine cases, the crack initiated at the adhesive fillets and then migrated into the surface 0° ply in the inner adherend. As the initiation occurred at the small adhesive fillet region, and the crack migrated into the composite at the beginning of the bondline, both adhesive and composite properties controlled the failure. The failure initiated at the adhesive fillets due to the high peel

components at the edges of the DLJ. The crack then migrated into the composite 0° ply, through the broken fibres as this was the weakest path for crack propagation.

For the impact cases, the crack migration occurred during the impact application. When the through-thickness impact was applied, the crack initiated at the adhesive fillets and propagated into the surface 0° ply, similar to the pristine cases. The high peel stresses at the opposite edge to the impact application initiated this failure mode.

3) Crack migration into the surface 0° ply

This failure occurred for the pristine minimal fillet test at RTD and disbond cases at RTD. This is when the crack migrated directly into the composite surface ply without any influence of the adhesive. For the minimal fillet case, as the stresses were highest at the edges of the DLJ and no adhesive fillets were present, the crack initiated into the surface ply before the adhesive could yield. The high peel component, the low G_{IC} of the composite and stress concentration from the broken fibres facilitated the crack migration into the surface 0° ply. Similarly, for the disbond cases, past the insert film representing the disbond, the crack migration occurred directly into the surface ply before the adhesive could yield.

9.5 Design Analysis for Double Lap Joints

9.5.1 Pristine Double Lap Joint

From a design point of view, to predict the pristine DLJ strength, the following steps are recommended based on the conclusions of this thesis.

1) Material Characterisation

The material properties of both the composite and adhesive at the desired environmental conditions needs to be characterised. These tests need to be conducted using ASTM standard tests, e.g. Double Cantilever Beam (DCB) for Mode I and End Notch Flexure (ENF) for Mode II. To achieve the adhesive properties during the fracture tests, it is recommended to put the insert film in between the adhesives. If the

insert film is at the interface between the composite and adhesive, the material at which the crack initiates could vary depending on the composite and adhesive material properties.

2) Analytical Failure Criteria

For DLJ with adhesive fillets, two modes of failure occurred depending on the overlap length and inner adherend thickness. The first was failure controlled by the shear strength of the adhesive and second was failure initiating at the adhesive fillet, influenced by the adhesive G_{IC} followed by crack propagation within the composite.

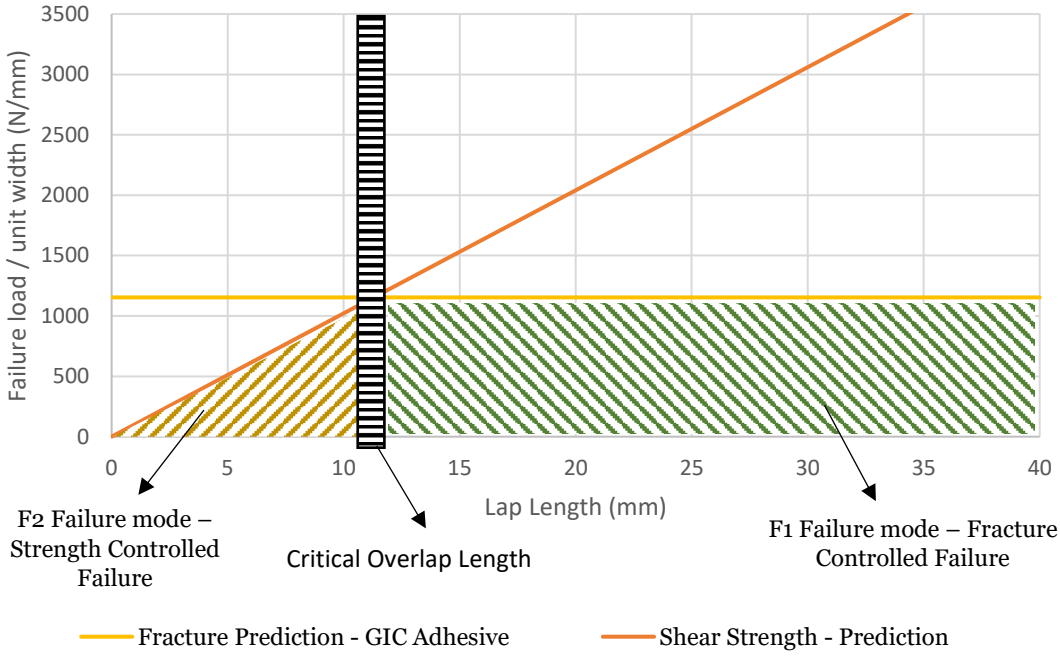

Figure 9.1 - Simple analytical calculations to predict failure mode

Based on this, simple analytical criteria using the adhesive shear strength and G_{IC} can be applied to determine the expected failure mode. This is a simple qualitative analysis to estimate the relative importance of the stress and energy. Figure 9.1 shows an example of the analytical criteria for the 4mm inner adherend, RTD case. Up until the critical overlap length, the failure is expected to be controlled by the shear strength of the adhesive (F2) and is represented by the orange line. After the critical overlap length, the failure changed from strength to fracture controlled. The failure initiated at the adhesive fillets and migrated into the composite surface 0° ply (F1). Hence, the

G_{IC} of the adhesive influenced the failure. The failure load based on adhesive G_{IC} was calculated and represented by the yellow line, giving the boundary for failure based on fracture.

3) Numerical Analysis

Once the expected failure mode was understood, Finite Element (FE) numerical models of the DLJ can be used as a predictive tool. The DLJ is modelled using a ply-by-ply analysis on a 3D slice model with Cohesive Element Modelling (CZM) for the interface. The properties for the CZM depend on the expected failure mode from the analytical study. If the failure is controlled by the shear strength of the adhesive, i.e. before the critical overlap length, all cohesive elements are given the adhesive properties. If the failure is fracture controlled, adhesive properties are given for the cohesive elements beneath the adhesive fillet and composite properties are given to elements in the bondline.

The design analysis above is based on uncontrolled adhesive fillets during manufacturing and QI DLJ with surface 0° plies. The approach using the adhesive G_{IC} for the fracture energy calculations gave good estimations for the analytical model for all pristine cases at different environmental conditions. For cases with no fillets or 45° surface ply, crack migration will occur directly into the surface 0° ply of the inner adherend, which is controlled by the fracture properties of the composite. Hence, for an estimation using the analytical model for these cases, the fracture energy calculations based on the DLJ mixed-mode G_C can be used. For this study, using the mixed-mode DLJ G_C was too conservative as the fillets had a significant effect on the DLJ strength.

9.5.2 Disbond/Impact Double Lap Joint

The disbond failure mode changed with environmental conditions. As discussed in the crack migration section, depending on the yield strength of the adhesive, the failure initiation can occur into the composite or adhesive. As the disbond case is asymmetric, and both peel and shear components affect the failure, a simple analytical criterion to predict the failure was not possible. At RTD, the disbond and impact cases correlated well. However, at HTD and HTW the disbond strengths were significantly higher than the impact cases as the failure initiated into the adhesive for disbond cases. For the

impacted specimen, as the damage was already present within the composite during the RTD impact application, at HTD and HTW tests, the crack propagation stayed within the composite. Therefore, from a design perspective, the best way for prediction is to design for the most critical case, which was the impact case which was influenced by the G_{IC} of the composite

9.6 Future Work

Although the current thesis covers a range of different studies, certain works were left for the future due to time constraints. These are summarised below:

1) Effects of surface preparation on failure modes

The surface preparation used for most of the characterisation tests and all DLJ test was grit blasting followed by liquid degreasing. An initial comparison study comparing grit blasted specimens to peel ply surface preparation for 0.2mm adhesive thickness was conducted on the Mode I fracture energy. As the insert film was placed at the adhesive/composite interface, the crack propagation occurred along this interface. This study could be expanded to analyse the effects of increasing adhesive thickness and environmental conditions on G_{IC} and observe whether a consistent failure mode can be achieved. This could also be applied to experimental DLJ tests to analyse if there would be a change in DLJ strength and failure mode.

A different surface preparation method could also be tested, e.g. plasma treatment to observe how this would affect the fracture toughness and DLJ strength for this adhesive adherend system.

2) Experimental study on tougher adherend/adhesive system

The main failure mechanism for most characterisation and DLJ test was through crack migration into the surface 0° ply of the adherend. Another study can explore the effects of a tougher adherend on the failure mode for both characterisation and DLJ tests using the same surface preparation as the one used for this project (grit-blasting) for comparison with this thesis study. This would help further understand the factors and

mechanisms that causes the crack migration into the adherend 0° ply. The recommended design analysis can be demonstrated on the different adherend /adhesive system.

3) Through-thickness Impact at HTD/HTW

The through-thickness impact tests for this project were conducted at RTD conditions. Further works can investigate the impact application at HTD and HTW to understand how the DLJ residual tensile strength and failure modes varies at these conditions. This can then be compared to the cases in this project to give a better understanding on the influence of impact conditions on the DLJ behaviour.

4) Detailed FE models

The current numerical model simplifies the damage zone with a single layer of Cohesive Zone Elements (CZM) representing both the adhesive and composite. As only one set of cohesive elements was used, the damage path was pre-defined and simplified. For the current project this was enough to simulate the joint behaviour. A more detailed numerical Finite Element (FE) analyses can be conducted as future work. This could be done through a more detailed model, incorporating multiple adhesive and composite cohesive elements throughout the bondline and using further techniques such as XEFM to define crack migration into the adherend. This can also be useful to capture the crack initiation during the disbond cases taking the shear and peel yield strengths of both the adhesive and composite.

APPENDIX A

A.1 Compliance Calibration Method Calculations (Mode I)

A typical example of the G_{IC} calculations based on the Modified Beam Theory (MBT) using Equation A1. is given in this section. The terms P, δ, b, a and Δ represent the load, displacement, specimen width, crack length and the correction factor. The correction factor (Δ) calculations were only possible for stable crack propagation as the compliance was needed at increasing delamination length. This was the case for the DCB tests for the composite at HTD and HTW. The force-displacement curves for the composite at HTD is shown in Figure A.*1*.

$$G_I = \frac{3P\delta}{2b(a + |\Delta|)} \qquad \textbf{(A1)}$$

The crack propagation during the DCB test for the composites were tracked using a video gauge. White paint was applied on the specimen edges to visualise the crack propagation. Lines were marked along the specimen edge from the crack tip at every 5mm intervals. Post processing the video gauge output, once the crack propagation approached the marked line, the force and displacement was recorded. Figure A.*2* and Figure A.*3* show the variation of G_{IC} with increasing delamination length for HTD and HTW. An increase in G_{IC} was observed with increased delamination length.

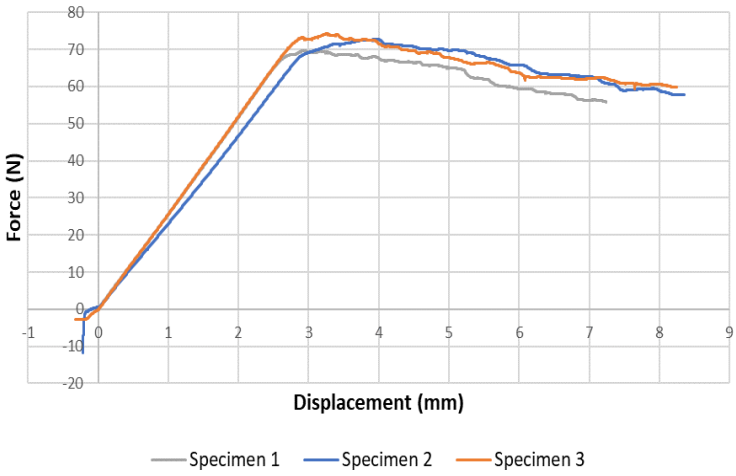

Figure A.1 - Reloading force-displacement curve for HTD IM7/8552

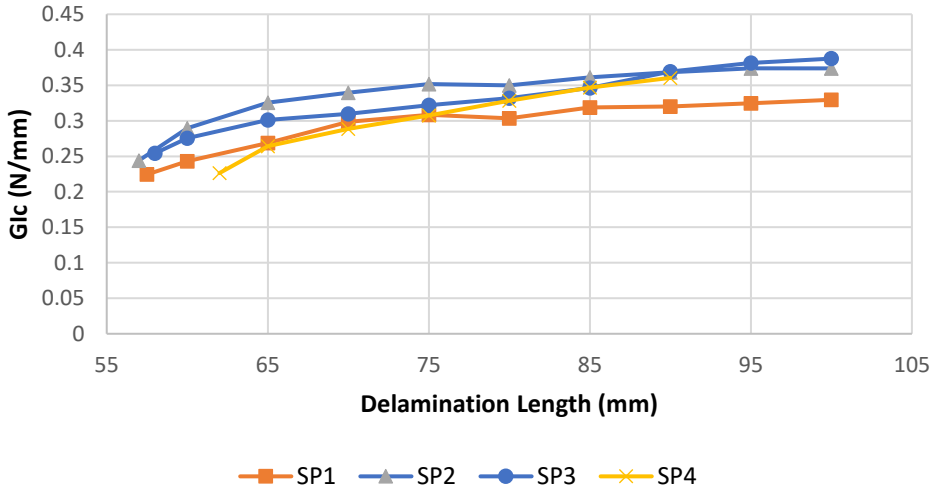

Figure A.2 - Change in G_{IC} with increasing delamination length for IM7/8552 at HTD

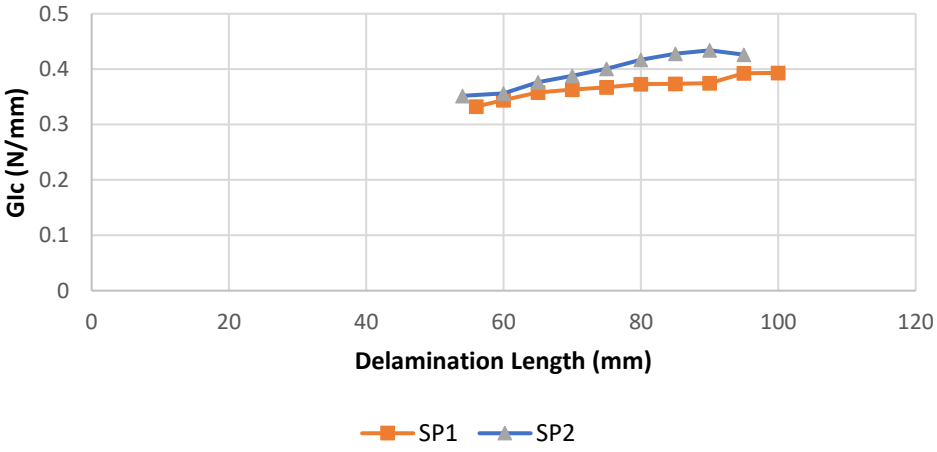

Figure A.3 - Change in G_{IC} with increasing delamination length for IM7/8552 at HTW

An example of the typical correction factor (Δ) calculation is summarised. Figure A.*4* shows the $C^{1/3}$ against the delamination length, a for a typical HTD composite DCB test, where C is defined as the compliance. The compliance was calculated at 5mm crack length intervals using the force and displacement values. This is plotted to calculate the correction factor (Δ) as illustrated in the Figure A.*4*.

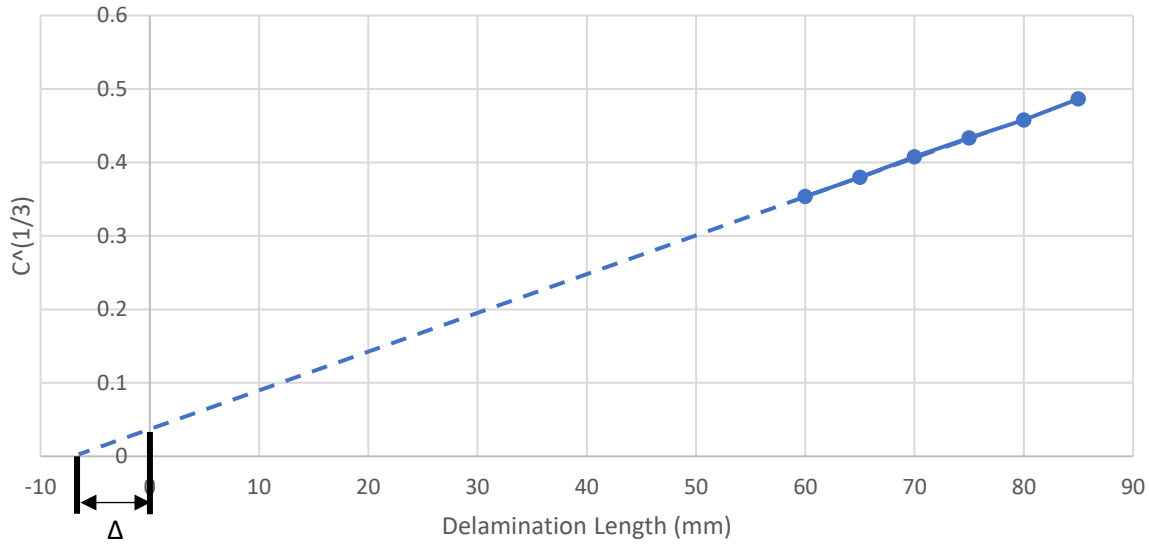

Figure A.4 – Cube root of compliance against delamination length curve to calculate correction factor

A.2 Mode I Reloading Tests

The reloading DCB tests for the adhesives were conducted at RTD even though unstable crack propagation occurred during the initial loading. This section summarises the reloading G_{IC} test and results at RTD. Figure A.5 shows the reloading results for the 0.2mm, 0.4mm and 0.8mm adhesive thickness cases at RTD conditions. The G_{IC} reloading values are presented in Table A.1.

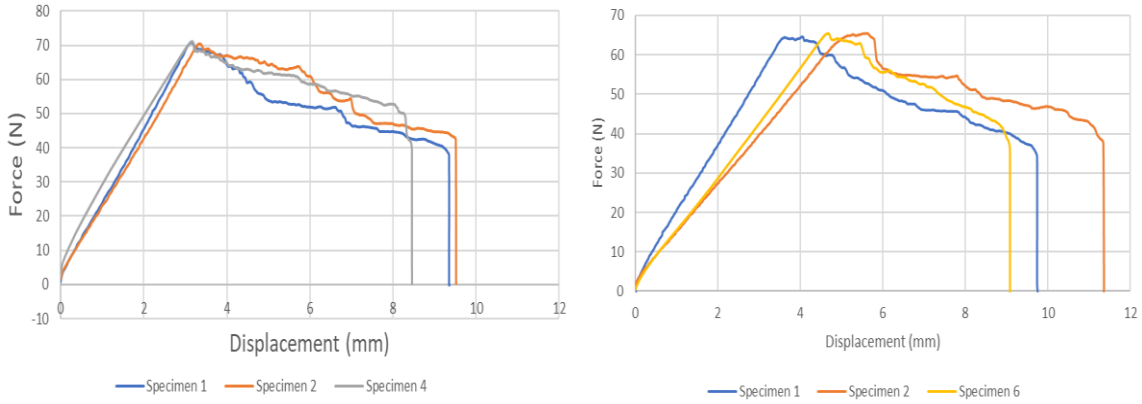

a) 0.2mm

b) 0.4mm

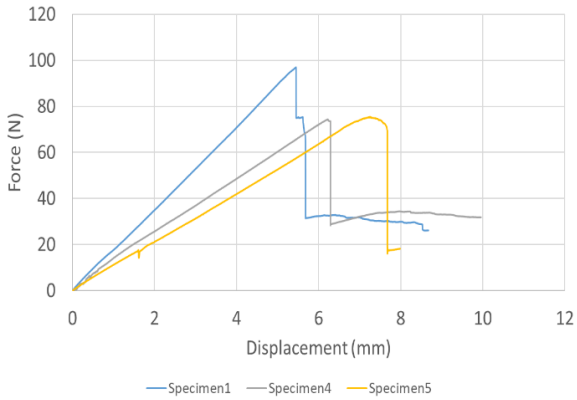

c) 0.8mm

Figure A.5 - Reloading force-displacement plot DCB tests

During the initial loading tests, unstable crack propagation occurred for all DCB RTD cases. For the 0.2mm case, the insert film was placed at the interface between the composite and adhesive. During the initial loading, the crack migrated unstably into the composite surface 0° ply directly from the interface. For the 0.4mm and 0.8mm cases, the insert film was between the adhesive. For these thicker cases, an initial cohesive failure occurred followed by migration into the surface 0° plies unstably during the initial loading. Hence for all reloading cases, the crack was present in the composite surface 0° ply before testing. The reloading G_{IC} value for the 0.2mm adhesive thickness at RTD was 0.28 N/mm. Due to the crack migration, the crack path was not at the mid-plane of the DCB specimen, hence some mixed-mode influence was present, which influenced the G_{IC} value calculated. As the adhesive thickness increased, the offset from the mid-plane, hence the mixed-mode effects increased.

The crack propagation during the initial loading was not controlled, hence the new delamination length, a, for each reloading case varied before the test. The explains the variability in the force-displacement curves for the reloading tests.

Table A.1 - G_{IC} reloading test results

Adhesive Thickness (mm)	**Mean Initiation- G_{IC} (N/mm) Reloading *(C.V%)***
0.2	0.28 *(1.1%)*
0.4	0.31 *(12.8%)*
0.8	0.60 *(6.6%)*

A.3 Mode II Reloading Tests

Chapter 4 summarised the Non Pre-Cracked (NPC) Mode II results for the adhesives. This section discusses the Pre-Cracked (PC) tests results for Mode II at RTD conditions. Figure A.*6* shows the force displacement plots for the three adhesive thickness and Table A.*2* summarises the test results.

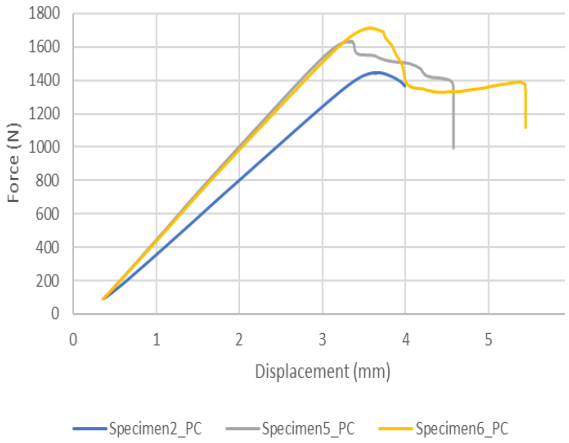

a) 0.2mm

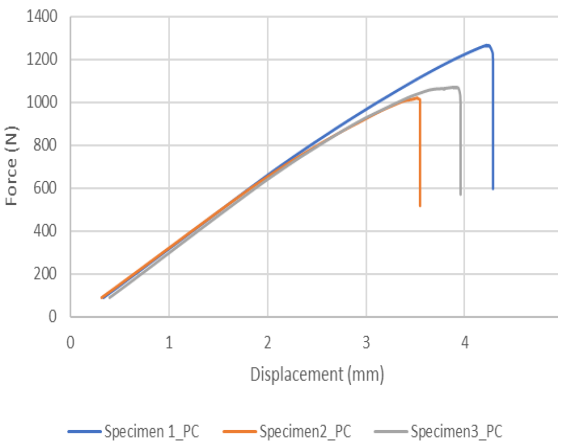

b) 0.4mm

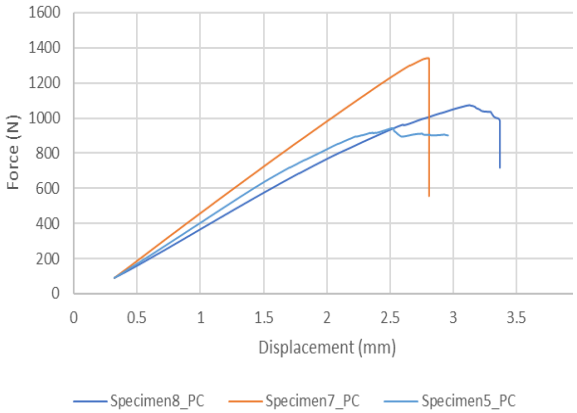

c) 0.8mm

Figure A.6 - PC force-displacement plot ENF tests

Table A.2 - G_{IIC} NPC test results

Adhesive Thickness (mm)	**Mean Initiation- G_{IC} (N/mm) PC *(C.V%)***
0.2	3.43 *(13%)*
0.4	2.85 *(15%)*
0.8	2.36 *(17%)*

As explained in Chapter 4, for the 0.2mm adhesive thickness ENF configuration, the insert film was placed at the composite adherend/adhesive interface. During the RTD NPC tests, once the peak load had been reached, the crack propagated stably for 3-5mm from the interface into adhesive before the NPC test was stopped. The new crack tip was marked, and the same procedure was done for the PC tests. Hence, the PC and NPC gave similar G_{IIC} values, as the initial failure was cohesive. During the PC tests, the crack then gradually jumped from the adhesive into the composite, more stably compared to the DCB case.

For the thicker 0.4mm and 0.8mm cases during the RTD NPC tests, the crack migrated from the insert film placed between the adhesive, into the composite surface 0° ply. Hence, for the PC tests, the crack was within the composite adherend. This meant that G_{IIC} was controlled by the toughness of the composite rather than the adhesive. The crack migrated away from the mid-plane during the unstable propagation, hence inducing mixed-mode effects. Also, due to the unstable propagation into the composite during the NPC tests, the new crack was not flat, but had a step 'jump' from the adhesive mid-plane to the composite during the NPC test. Therefore, shear sliding was

inhibited and there may be additional plastic deformation and friction. The combination of these effects could explain why the G_{IIC} values from the PC tests are higher than the IM7/8552 adherend G_{IIC} = 1 N/mm from the literature [92].

A.4 Tensile Strength of Redux 319

This section compares the tensile strength of the Redux 319 for two different conditions. One, at HTW conditions tested at 80°C for samples conditioned at 80°C and 85% Relative Humidity (RH) as explained in Section 3.9. The second condition was tested at 120°C for a dry specimen (no moisture), for which 3 specimens were tested. The specimen dimension is given in Figure 3.34.

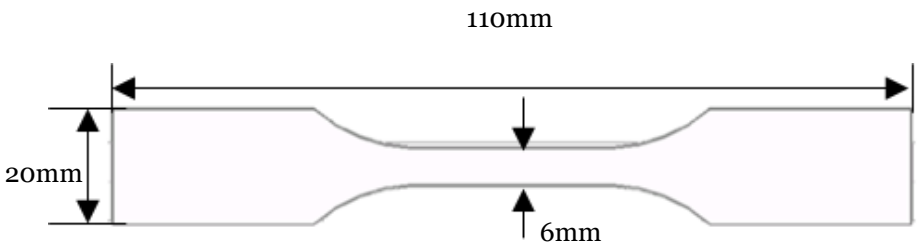

Figure A.7 - Schematic of dog-bone tensile specimen

The ultimate tensile strengths (UTS) for a dry specimen tested at 120°C and a conditioned specimen (80°C and 85% RH) tested at 80°C are shown in Figure A.8

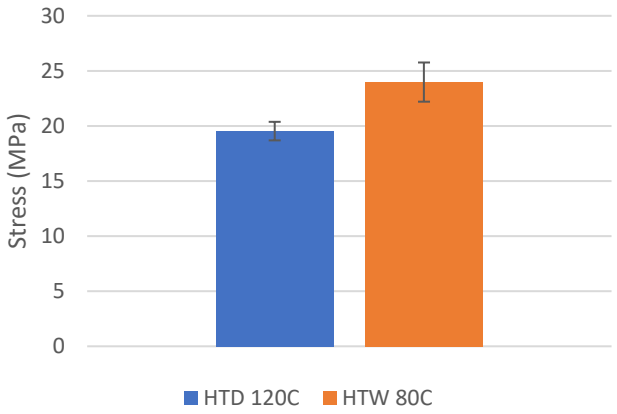

Figure A.8 – Bar chart comparing the UTS Redux 319 at HTD 120°C and HTW 80°C

REFERENCES

[1] S. Black, “Structural adhesives, Part I: Industrial,” 4 November 2016. [Online]. Available: http://www.compositesworld.com/articles/structural-adhesives-part-i-industrial. [Accessed 3 April 2017].

[2] R. Adams, J. Comyn and W. Wake, Structural adhesive joints in engineering, London: Chapman & Hall, 1997.

[3] K. N. Anyfantis, Analysis and Design of Composite-to-Metal Adhesively Bonded Joints, National Technical University of Athens: Thesis, 2012.

[4] L. da Silva, R. Carbas, G. Critchlow, M. Figueiredo and K. Brown, “Effect of material, geometry, surface treatment and environment on the shear strength of single lap joints,” *International Journal of Adhesion and Adhesives,* vol. 29, no. 6, pp. 621-632, 2009.

[5] E. Oterkus, C. Diyaroglu, D. De Meo and G. Allegri, “Fracture modes, damage tolerance and failure mitigation in marine composites,” in *Marine Applications of Advanced Fibre-Reinforced Composites*, Woodhead Publishing Series in Composites Science and Engineering, 2016, pp. 79-102.

[6] C. E. Inglis, “Stresses in a Plate Due to the Presence of Cracks and Sharp Corners,” *SPIE Milestone Series,* vol. 137, pp. 3-17, 1913.

[7] A. A. Griffith, “The Phenomena of Rupture and Flow in Solids,” *Philosophical Transactions of the Royal Society A: Mathematical, Physical and Engineering Sciences,* vol. 221, pp. 582-93, 1921.

[8] M. Tsai and J. Morton, “An investigation into the stresses in double-lap adhesive joints with laminated composite adherends,” *International Journal of Solids and Structures,* vol. 47, no. 24, p. 3317–3325, 2010.

[9] J. F. A. Leone, D. Girolamo and C. G. Dάvila, “Progressive Damage Analysis of Bonded Composite Joints,” National Aeronautics and Space Administration, Langley Research Center, Hampton, Virginia 23681-2199, 2012.

[10] C. Galliot, J. Rousseau and G. Verchery, “Drop weight tensile impact testing of adhesively bonded carbon/epoxy laminate joints,” *International Journal of Adhesion & Adhesives,* vol. 35, pp. 68-75, 2012.

[11] J. Li, Y. Yan, T. Zhang and Z. Liang, “Experimental study of adhesively bonded CFRP joints subjected to tensile loads,” *International Journal of Adhesion and Adhesives,* vol. 57, pp. 95-104, 2015.

[12] J. L. Gardon, “Peel Adhesion. I. Some Phenomenological Aspects of the Test,” *Journal of Applied Polymer Science,* vol. 7, no. 2, p. 625–641, 1963.

[13] W. D. Bascom, R. L. Cottington, R. L. Jones and P. Peyser, “The Fracture of Epoxy and Elastomer-Modified Epoxy Polymers in Bulk and as Adhesives,” *Journal of Applied Polymer Science,* vol. 19, no. 9, p. 2545–2562, 1975.

[14] H. Chai, “The effects of bond thickness, rate and temperature on the deformation and fracture of structural adhesives under shear loading,” *International Journal of Fracture,* vol. 130, no. 1, pp. 497-515, 2004.

[15] A. J. Kinloch and S. J. Shaw, “The Fracture Resistance of a Tough- ened Epoxy Adhesive,” *The Journal of Adhesion,* vol. 12, no. 1, p. 59–77, 1981.

[16] T. Ikeda, A. Yamashita, D. Lee and N. Miyazaki, “Failure of a ductile adhesive layer constrained by hard adherends,” *Journal of Engineering Materials and Technology,* vol. 122, no. 1, pp. 80-85, 2000.

[17] D.-B. Lee, T. Ikeda, N. Miyazaki and N.-S. Choi, “Effect of Bond Thickness on the Fracture Toughness of Adhesive Joints,” *Journal of Engineering Materials and Technology,* vol. 126, no. 1, pp. 14-18, 2004.

[18] L. F. M. da Silva, F. A. C. R. G. de Magalhães, F. J. P. Chaves and M. F. S. F. de Moura, “Mode II Fracture Toughness of a Brittle and a Ductile Adhesive as a Function of the Adhesive Thickness,” *The Journal of Adhesion,* vol. 86, no. 9, pp. 891-905, 2010.

[19] C. Sarrado, A. Turon, J. Costa and J. Renart, “An experimental analysis of the fracture behavior of composite bonded joints in terms of cohesive laws,” *Composites Part A: Applied Science and Manufacturing,* vol. 90, pp. 234-242, 2016.

[20] T. Pardoen, T. Ferracin, C. Landis and F. Delannay, “Constraint effects in adhesive joint fracture,” *Journal of the Mechanics and Physics of Solids,* vol. 53, no. 9, pp. 1951-83, 2005.

[21] J. P.-H. Belnoue and S. R. Hallett, “Cohesive/adhesive failure interaction in ductile adhesive joints Part I: A smeared-crack model for cohesive failure,” *International Journal of Adhesion and Adhesives,* vol. 68, pp. 359-368, 2016.

[22] L. F. M. da Silva, T. N. S. S. Rodrigues, M. A. V. Figueiredo, M. F. S. F. de Moura and J. A. G. Chousal, “Effect of Adhesive Type and Thickness on the Lap Shear Strength,” *The Journal of Adhesion,* vol. 82, no. 11, pp. 1091-1115, 2006.

[23] P. Davies, L. Sohier, J.-Y. Cognard, A. Bourmaud, D. Choqueuse, E. Rinnert and R. Cre´ac’hcadec, “Influence of adhesive bond line thickness on joint strength,” *International Journal of Adhesion and Adhesives,* vol. 29, no. 7, pp. 724-736, 2009.

[24] J. A. Harris and R. D. Adams, “An assessment of the impact performance of bonded joints for use in high energy absorbing structures.,” *Proceedings of the Institution of Mechanical Engineers, Part C: Journal of Mechanical Engineering Science,* vol. 199, no. 2, pp. 121-131, 1985.

[25] A. Beevers and M. Ellis, “Impact behaviour of bonded mild steel lap joints,” *International Journal of Adhesion and Adhesives,* vol. 4, no. 1, pp. 13-16, 1984.

[26] K. Kihara, H. Isono, H. Yamabe and T. Sugibayashi, “A study and evaluation of the shear strength of adhesive layers subjected to impact loads,” *International Journal of Adhesion and Adhesives,* vol. 23, no. 4, pp. 253-259, 2003.

[27] I. Higuchi, T. Sawa, H. Okuno and S. Kato, “Three-dimensional finite element analysis of stress response in adhesive butt joints subjected to impact bending moments,” *The Journal of Adhesion,* vol. 79, no. 11, pp. 1017-1039, 2003.

[28] P. N. B. Reis, J. A. M. Ferreira, A. M. Pereira and F. J. V. Antunes, “Influence of Superposition Length on Transverse Impact Response of Single-Strap Adhesive Joints,” *The Journal of Adhesion,* vol. 90, no. 1, pp. 65-79, 2014.

[29] I. Farrow, K. D. Potter, A. Fisher and M. Kelly, “Impact of adhesively bonded composite joints with edge effect,” *Advanced Composite Letters, 9: 397-408.,* vol. 9, pp. 397-408, 2000.

[30] U. Vaidya, A. Gautam, M. Hosur and P. Dutta, “Experimental–numerical studies of transverse impact response of adhesively bonded lap joints in composite structures,” *International Journal of Adhesion and Adhesives,* vol. 26, no. 3, pp. 184-198, 2006.

[31] P. Li, P. Lee-Sullivan and R. Thring, “Nonlinear finite element analysis of stress and strain distributions across the adhesive thickness in composite single-lap joints,” *Composite Structures,* vol. 46, no. 4, pp. 395-403, 1999.

[32] H. Kim, T. Kayir and S. L. Mousseau, “Mechanisms of Damage Formation in Transversely Impacted Glass-Epoxy Bonded Lap Joints,” *Journal of Composite Materials,* vol. 39, no. 22, pp. 2039-2052, 2005.

[33] H. Park and H. Kim, “Damage resistance of single lap adhesive composite jointsby transverse ice impact,” *International Journal of Impact Engineering,* vol. 37, no. 2, pp. 177-184, 2010.

[34] W. Wu, Q. Liu, Z. Zong, G. Sun and Q. Li, “Experimental investigation into transverse crashworthiness of CFRP adhesively bonded joints in vehicle structure,” *Composite Structures,* vol. 106, pp. 581-589, 2013.

[35] H. Nie and J. Xu, “Tensile behaviors after impact of composite scarf joints,” in *7th International Conference on Mechanical and Aerospace Engineering*, London, UK, 2016.

[36] F. Ribeiro, R. Campilho, R. Carbas and L. da Silva, “Strength and damage growth in composite bonded joints with defects,” *Composites Part B,* vol. 100, pp. 91-100, 2016.

[37] Y. Liu, S. Lemanski, X. Zhang, D. Ayre and H. Y. Nezhad, “A finite element study of fatigue crack propagation in single lap bonded joint with process-induced disbond,” *International Journal of Adhesion and Adhesives,* vol. 87, pp. 164-172, 2018.

[38] O. Volkensen, “ Die niektraftverteiling in zugbeansprunchten mit konstanten laschenquerscritten,” *Luftfahrforsch,* vol. 15, pp. 41-47, 1938.

[39] M. Goland and E. Reissner, “The stresses in cemented joints,” *Journal of Applied Mechanics,* vol. 11, no. 1, pp. A17-A27, 1944.

[40] L. da Silva, A. Öchsner, R. Adams and (eds.), Handbook of Adhesion Technology., Heidelberg: Springer, 2011.

[41] L. Hart-Smith, “Adhesive-bonded single-lap joints,” Technical report, NASA CR-112236., 1973.

[42] D. W. Oplinger, “Effects of adherend deflections in single lap joints,” *International Journal of Solids and Structures,* vol. 31, pp. 2565-87, 1994.

[43] M. Tsai, D. Oplinger and J. Morton, “Improved Theoretical Solutions for Adhesive Lap Joints,” *Internation Journal of Solid Structures,* vol. 35, no. 12, pp. 1163-85, 1997.

[44] R. Adams and J. Harris, “Strength prediction of bonded single lap joints by nonlinear finite element methods,” *International Journal of Adhesion and Adhesives,* vol. 4, pp. 65-78, 1984.

[45] L. Greenwood, The Strength of a Lap Joint, in Aspects of Adhesion-5, ed. by D. Alner, London: University of London Press, 1969.

[46] S. Lee and D. Lee, “Development of a failure model for the adhesively bonded tubular single lap joint,” *Journal of Adhesion,* vol. 40, pp. 1-14, 1992.

[47] Z. P. Bažant and J. Planas, “Fracture and Size Effect in Concrete and Other Quasibrittle Materials,” CRC Press, London, 1998.

[48] Q. Yang and M. Thouless, “Mixed-mode fracture analyses of plastically-deforming adhesive joints,” *International Journal of Fracture,* vol. 110, pp. 175-187, 2001.

[49] S. Li, M. Thouless, A. Waas, J. Schroeder and P. Zavattieri, “Competing failure mechanisms in mixed-mode fracture of an adhesively bonded polymer-matrix composite,” *International Journal of Adhesion and Adhesives,* vol. 26, pp. 609-606, 2006.

[50] C. Landis, T. Pardoen and J. Hutchinson, “Crack velocity dependent toughness in rate dependent materials,” *Mechanics of Materials,* vol. 32, p. 663–678, 2000.

[51] H. Khoramishad, A. Crocombe, K. Katnam and I. Ashcroft, “Predicting fatigue damage in adhesively bonded joints using a cohesive zone model,” *International Journal of Fatigue,* vol. 32, p. 1146–1158, 2010.

[52] C. Sarrado, F. A. Leone and A. Turon, “Finite-thickness cohesive elements for modeling thick adhesives,” *Engineering Fracture Mechanics,* vol. 168, no. Part B, pp. 105-113, 2016.

[53] V. Tvergaard and J. Hutchinson, “On the toughness of ductile adhesive joints,” *Journal of the Mechanics and Physics of Solids,* vol. 44, pp. 789-800, 1996.

[54] K. Anyfantis and N. Tsouvalis, “A novel traction–separation law for the prediction of the mixed mode response of ductile adhesive joints,” *International Journal of Solids and Structures,* vol. 49, pp. 213-226, 2012.

[55] V. Tvergaard and J. Hutchinson, “Toughness of an interface along a thin ductile layer joining elastic solids,” *Philosophical Magazine A,* vol. 70, pp. 641-656, 1994.

[56] K. S. Madhusudhana and R. Narasimhan, “Experimental and numerical investigations of mixed mode crack growth resistance of a ductile adhesive joint,” *Engineering Fracture Mechanics,* vol. 69, no. 7, pp. 865-883, 2002.

[57] C. Sarrado, Experimental characterization and numerical simulation of composite adhesive joints using the cohesive zone model approach, University of Girona, 2015.

[58] P. Harper and S. Hallett, “Cohesive zone length in numerical simulations of composite delamination,” *Engineering Fracture Mechanics,* vol. 75, no. 16, pp. 4774-4792, 2008.

[59] A. Soto, E. González, P. Maimí, A. Turon, J. Sainz de Aja and F. de la Escalera, “Cohesive zone length of orthotropic materials undergoing delamination,” *Engineering Fracture Mechanics,* vol. 159, pp. 174-188, 2016.

[60] T. Breitzman, E. Iarve, B. Cook, G. Schoeppner and R. Lipton, “ Optimization of a composite scarf repair patch under tensile loading,” *Composites Part A: Applied Science and Manufacturing,* vol. 40, no. 12, pp. 1921-30, 2009.

[61] M. Wang, A. Liu and Z. Liu, “Effect of hot humid environmental exposure on fatigue crack growth of adhesive bonded aluminum A356 joints,” *International Journal of Adhesion and Adhesives,* vol. 40, pp. 1-10, 2013.

[62] A. ASTM D5229/D5229M, “Standard Test Method for Moisture Absorption Properties and Equilibrium Conditioning of Polymer Matrix Composite Materials,” ASTM Committee on Lamina and Laminate Test Methods, 2014.

[63] R. Pethrick, “Design and ageing of adhesives for structural adhesive bonding - A review.,” *Proceedings of the Institution of Mechanical Engineers,* vol. 229, pp. 349-379, 2015.

[64] G. Viana, M. Costa, M. Banea and L. da Silva, “A review on the temperature and moisture degradation of adhesive joints,” *Proceedings of the Institution of Mechanical Engineers, Part L: Journal of Materials: Design and Applications,,* vol. 231, no. 5, pp. 488-501, 2017.

[65] M. Adamson, “Thermal-expansion and swelling of cured epoxy-resin used in graphite-epoxy composite-materials.,” *Journal of Materials Science,* vol. 15, pp. 1736-1745, 1980.

[66] C. Liljedahl, A. Crocombe and F. Gauntlett, “Characterising moisture ingress in adhesively bonded joints using nuclear reaction analysis,” *International Journal of Adhesion and Adhesives,* vol. 29, pp. 356-360, 2009.

[67] C. Liljedahl, A. Crocombe and M. Wahab, “The effect of residual strains on the progressive damage modelling of environmentally degraded adhesive joints.,” *Journal of Adhesion Science and Technology,* vol. 19, pp. 525-547, 2005.

[68] W. Loh, A. Crocombe and M. Wahab, “Modelling anomalous moisture uptake, swelling and thermal characteristics of a rubber toughened epoxy adhesive,” *International Journal of Adhesion and Adhesives,* vol. 25, pp. 1-12, 2005.

[69] Y. Lin and X. Chen, “Moisture sorption-desorption-resorption characteristics and its effect on the mechanical behavior of the epoxy system,” *Polymer,* vol. 46, pp. 11994-12003, 2005.

[70] M. Zannideffarges and M. Shanahan, “Diffusion of water into an epoxy adhesive - comparison between bulk behavior and adhesive joints,” *International Journal of Adhesion and Adhesives,* vol. 15, pp. 137-142, 1995.

[71] A. Kinloch, M. Little and J. Watts, “The role of the interphase in the environmental failure of adhesive joints.,” *Acta Mater,* vol. 48, pp. 4543-4553, 2000.

[72] L. F. M. da Silva and R. D. Adams, “Measurement of the mechanical properties of structural adhesives in tension and shear over a wide range of temperatures,” *Journal of Adhesion Science and Technology,* vol. 19, no. 2, pp. 109-141, 2005.

[73] M. Banea, L. da Silva and R. Campilho, “Mode I fracture toughness of adhesively bonded joints as a function of temperature: Experimental and numerical study,” *International Journal of Adhesion and Adhesives,* vol. 31, no. 5, pp. 273-279, 2011.

[74] M. D. Banea, L. F. M. da Silva and R. D. S. G. Campilho, “Mode II Fracture Toughness of Adhesively Bonded Joints as a Function of Temperature: Experimental and Numerical Study,” *The Journal of Adhesion,* Vols. 4-6, no. 534-551, p. 88, 2012.

[75] S. Sugiman, A. Crocombe and I. Aschroft, “Experimental and numerical investigation of the static response of environmentally aged adhesively bonded joints,” *International Journal of Adhesion and Adhesives,* vol. 40, pp. 224-237, 2013.

[76] W. Loh, A. Crocombe and M. Wahab, “Environmental degradation of the interfacial fracture energy in an adhesively bonded joint.,” *Engineering Fracture Mechanics,* vol. 69, pp. 2113-2128, 2002.

[77] M. Costa, G. Viana, L. d. Silva and R. Campilho, “Effect of humidity on the mechanical properties of adhesively bonded aluminium joints.,” *Proceedings of*

the Institution of Mechanical Engineers, Part L: Journal of Materials: Design and Applications, vol. 232, no. 9, pp. 733-742, 2018.

[78] P. Fernandes, G. Viana, R. Carbas, M. Costa, L. da Silva and M. Banea, "The influence of water on the fracture envelope of an adhesive joint," *Theoretical and Applied Fracture Mechanics,* vol. 89, pp. 1-15, 2017.

[79] G. Viana, M. Costa, B. M.D. and L. F. M. da Silva, "Behaviour of environmentally degraded epoxy adhesives as a function of temperature," *The Journal of Adhesion,* vol. 93, no. 2, pp. 95-112, 2017.

[80] D. Vaezie, J. Qu and J. Lindsay, "Durability of Adhesive Joints Subject to Elavated Temeprature Aging," in *Recent Develepments in Durability Analysis of Composite Systems*, Rotterdam, 2000.

[81] C. Shen and G. Springer, "Moisture absorption and desorption of composite materials. Environmental effects on composite materials," Westport, CT: Technomic., 1981.

[82] B. DeNève and M. Shanahan, "Water absorption by an epoxy resin and its effect on the mechanical properties and infra-red spectra," *Polymer,* vol. 34, no. 24, pp. 5099-5105, 1993.

[83] M. Akay, S. Kong Ah Mun and A. Stanley, "Influence of moisture on the thermal and mechanical properties of autoclaved and oven-cured Kevlar-49/epoxy laminates," *Composites Science and Technology,* vol. 57, no. 5, pp. 565-571, 1997.

[84] S. Grant and L. Bradley, "In-situ Observations in SEM of Degradation of Graphite/Epoxy Composite Materials Due to Seawater Immersion," *Journal of Composite Materials,* vol. 29, no. 7, pp. 853-867, 1995.

[85] P. Choqueuse, F. Davies and R. Baizeau, "Aging of Composites in Water: Comparison of Five Materials in Terms of Absorption Kinetics and Evolution of Mechanical Properties," *High Temperature and Environmental Effects on Polymeric Composites, ASTM STP 1302,* vol. 2, pp. 73-97, 1997.

[86] R. Rao, N. Balasubramanian and M. Chanda, "Factors affecting moisture absorption in polymer composites," *Journal of Reinforced Plastics and Composites,* vol. 3, pp. 232-245, 1984.

[87] L. M, "Temperature and Moisture Effects on Composite Matericals for Wind Turbine Blades," Montana State University - Bozeman, Bozeman, Montana, 2000.

[88] K. J. Wong, Moisture absorption characteristics and effects on mechanical behaviour of carbon/epoxy composite : application to bonded patch repairs of composite structures, University de Bourgogne (Thesis), 2013.

[89] P. Coronado, A. Argüelles, J. Viña, V. Mollón and I. Viña, "Influence of temperature on a carbon–fibre epoxy composite subjected to static and fatigue loading under mode-I delamination," vol. 49, no. 21, 2012.

[90] R. Bossi, R. Carlsen, F. J. Boerio and G. Dillingham, "Composite surface preparation QA for bonding," in *SAMPE* , Long Beach CA - May 1-5 / 2005, 2005.

[91] U. D. o. Transportation, “The Effect of Peel-Ply Surface Preparation Variables on Bond Quality,” Office of Aviation Research and Development, Washington, DC 20591 , 2006.

[92] S. Hallett, B. Green, W. Jiang and M. Wisnom, “An experimental and numerical investigation into the damage mechanisms in notched composites,” *Composites Part A: Applied Science and Manufacturing,* vol. 40, no. 5, pp. 613-624, 2009.

[93] C. Jeenjitkaew, Kissing Bonds in Adhesive Joints: A Holistic Approach for Surface Chemistry and Joint Mechanics, School of Engineering and Materials Science Queen Mary, University of London, 2011.

[94] A. Kinloch and S. Shaw, “The fracture resistance of a toughened epoxy adhesive,” *The Journal of Adhesion,* vol. 12, no. 1, pp. 59-77, 1981.

[95] G. Viana, M. Costa, M. D. Banea and L. F. M. da Silva, “Moisture and temperature degradation of double cantilever beam adhesive joints,” *Journal of Adhesion Science and Technology,* vol. 31, no. 16, pp. 1824-1838, 2017.

[96] D. Lee, K. Kim and Y. Im, “An Experimental Study of Fatigue Strength for Adhesively Bonded Tubular Single Lap Joints,” *The Journal of Adhesion,* vol. 35, no. 1, pp. 39-53, 1991.

[97] M. Wisnom, “On the Increase in Fracture Energy with Thickness in Delamination of Unidirectional Glass Fibre-Epoxy with Cut Central Plies,” *Journal of Reinforced Plastics and Composites,* vol. 11, no. 8, pp. 897-909, 1992.

[98] A. Kinloch and S. Shaw, “A fracture mechanics approach to the failure of structural joints,” *Developments in adhesives- 2.(A 82-28576 13-39) London, Applied Science Publishers,* pp. 83-124, 1981.

[99] C. Jeenjitkaew, Kissing bonds in adhesive joints: a holistic approach for surface chemistry and joint mechanics, London, UK: Queen Mary, University of London (Thesis), 2011.

[100] “NCAMP test report number: CAM-RP-2009-028 NC”.

[101] H. R. Daghyani, L. Ye and Y. W. Mai, “Mode I Fracture Behavior of Adhesive Joints. Part I. Relationship between Fracture Energy and Bond Thickness,” *The Journal of Adhesion,* vol. 53, no. 3-4, p. 149–162, 1995.

[102] A. Turon, P. Camanho, J. Costa and J. Renart, “Accurate simulation of delamination growth under mixed-mode loading using cohesive elements: definition of interlaminar strengths and elastic stiffness,” *Composite Structures,* vol. 92, no. 8, pp. 1857-1864, 2010.